The Power Balance Method For Aerodynamic Performance Assessment

by

Sho Sato

S.B., Aeronautical Engineering, Massachusetts Institute of Technology, 2007
S.M., Aeronautical Engineering, Massachusetts Institute of Technology, 2008

Submitted to the Department of Aeronautics and Astronautics
in partial fulfillment of the requirements for the degree of

Doctor of Philosophy in Aerospace Engineering

at the

MASSACHUSETTS INSTITUTE OF TECHNOLOGY

June 2012

Author . . . .
Department of Aeronautics and Astronautics
May 11th, 2012

Certified by . . . .
Edward M. Greitzer
H.N. Slater Professor of Aeronautics and Astronautics
Thesis Committee Chairman

Certified by . . . .
Mark Drela
Terry J. Kohler Professor of Fluid Dynamics
Thesis Supervisor

Certified by . . . .
Elena De la Rosa Blanco
Research Engineer at MIT
Thesis Committee

Certified by . . . .
Zoltan S. Spakovszky
Associate Professor of Aeronautics and Astronautics
Thesis Committee

Accepted by . . . .
Eytan H. Modiano
Professor of Aeronautics and Astronautics
Chair, Committee on Graduate Students

The Power Balance Method
For Aerodynamic Performance Assessment

by

Sho Sato

Submitted to the Department of Aeronautics and Astronautics
on May 11th, 2012, in partial fulfillment of the
requirements for the degree of
Doctor of Philosophy in Aerospace Engineering

Abstract

This thesis describes the use of the power balance method for performance estimation of aircraft configurations. In this method, mechanical power production and mechanical power consumption of the aircraft are balanced, rather than forces as in the conventional thrust and drag approach to aircraft performance estimation. It is shown that an approach based on mechanical power provides a substantial advantage in accuracy and a wider range of applicability for integrated configurations such as boundary layer ingesting (BLI) aircraft.

The thesis provides evidence of the major benefits of the power balance method, and descriptions of its limitations, for three applications: 1) derivation of an analytic expression of profile drag estimates for conceptual design applications, 2) aerodynamic performance estimation for three canonical integrated configurations, and 3) performance quantification of a hybrid wing body (HWB) with BLI propulsion system.

In the first application, an analytical expression for the form factor used in the wetted area method (a profile drag correlation employed in conceptual design, which is heavily based on empiricism) is derived from the power balance method. The developed estimation method uses only potential-flow surface velocities, and it can be applied to new geometries for which experimental drag data is not available. The accuracy of this analytical expression and its limitations are presented in terms of quantitative results and analysis of physical effects for two-dimensional and axisymmetric geometries in incompressible and transonic flows.

In the second application, the mechanical energy loss is evaluated for three integrated configurations: a fuselage with a propelling fan at the rear, a nacelle-fan combination, and two interfering airfoils. Using the boundary layer mechanical energy equation, it is shown that the profile mechanical loss from potential field (pressure) interference scales according to $\rho_e U_e^3 \left(1 + \frac{\gamma-1}{2} M_e^2\right)^r$. The scaling is confirmed using computational fluid dynamics (CFD) calculations. The scaling is accurate to within 10% for configurations for which the average boundary layer kinematic shape parameter increases by no more than 0.04 from non-interfering to interfering configuration. The physical mechanisms responsible for the breakdown in accuracy are analyzed.

The power balance method is also applied to a system-level optimization of fuel burn for an HWB with BLI propulsion system. The fuel burn of the HWB is shown to decrease monotonically with increasing BLI, up to a maximum fuel burn improvement of 11% compared to a non-BLI aircraft.

Thesis Committee Chairman: Edward M. Greitzer
Title: H.N. Slater Professor of Aeronautics and Astronautics

Thesis Supervisor: Mark Drela
Title: Terry J. Kohler Professor of Fluid Dynamics

Thesis Committee: Elena De la Rosa Blanco
Title: Research Engineer at MIT

Thesis Committee: Zoltan S. Spakovszky
Title: Associate Professor of Aeronautics and Astronautics

Acknowledgments

Since I came here as a freshman, I have spent one-third of my entire life at MIT. The experience that I have gained over this period certainly makes up more than one-third of myself. The people that I have met—shared part of life—have had a tremendously positive influence on me. It has been a pleasure for me to get to know the wonderful people at MIT.

First, I would like to thank Prof. Edward Greitzer, for his teachings and guidance, not just advising me in my research, but in my life. I am extremely grateful for your caring for and dedication to the students, guiding me and many other students through the ups and down of MIT.

Prof. Mark Drela has taught me many important skills for aerospace engineers, from tips to win the Unified aircraft design competition to the power balance method. I have great admiration for your knowledge and enthusiasm in the field of aeronautical engineering.

I would also like to thank Prof. Zoltan Spakovszky for his guidance and enthusiasm in teaching and advising me. Without your thermodynamics class, I would not have made the decision to join the Gas Turbine Lab, and would have missed the opportunity to work on the wonderful projects taking place at GTL.

The work on the hybrid wing body owes a lot to Dr. Elena De la Rosa Blanco, who gave me much valuable advice in the analysis. I was saved and encouraged many times by your energy and interest in this research.

This thesis greatly benefited from the valuable feedbacks from my readers, Prof. David Darmofal and Dr. Robert Liebeck. Your comments are greatly appreciated.

I would like to thank Prof. Nick Cumpsty for giving me feedback and advice throughout my research. The meetings that I had with you helped me tremendously in organizing my thoughts that got entangled at times.

I am grateful for the support of the NASA Subsonic Fixed Wing N+3 project, which funded this research, as well as those involved in the project. I would like to thank in particular Dr. James Hileman and Pritesh Mody, for working together with me in developing the HWB design optimization program.

I would like to acknowledge David Hall, with whom I had many constructive discussions on my research. You are one of the very few students who speak the language of "power balance"; hopefully, by the time you graduate, everybody in GTL will be speaking "power

balance".

My thanks also go to Alejandra Uranga, who was very kind to take her precious time to go through my thesis and presentation. You gave me valuable feedback.

I owe many thanks, as well, to the students of the Gas Turbine Lab, for making life at GTL more exciting. In particular, I would like to thank Jeff for introducing me to hockey, which has become one of my favorite sports, and my officemates Andreas and Jon, with whom I shared some rough times at MIT.

Thank you, Ken; it is too bad we will not be able to play basketball as often as we used to. Thank you, Takuto, I had so much fun talking to you. Thank you everybody in the Japanese Association of MIT for your hospitality. Arisa, thank you very much for your support; without you I would not have been able to come this far.

Last, but not least, I would like to thank my family—Mom, Dad, Saki and Yuki—for your love and support. Without you, I would not have had the opportunity to come to such a wonderful place, and have such a fulfilling experience.

Contents

List of Figures

List of Tables

Nomenclature

Latin Letters

a	speed of sound
c	airfoil chord length
$C_{\mathcal{D}}$	dissipation coefficient
$c_{\mathcal{D}}$	local dissipation coefficient
$\bar{C}_{\mathcal{D}}$	average dissipation coefficient
$C^*_{\mathcal{D}}$	corrected dissipation coefficient
$c^*_{\mathcal{D}}$	local corrected dissipation coefficient
$\bar{C}^*_{\mathcal{D}}$	average corrected dissipation coefficient
C_D	drag coefficient
$\bar{C}_D$	average drag coefficient
C_d	spanwise drag coefficient
$\bar{C}_d$	average spanwise drag coefficient
C_f	skin friction coefficient
c_f	local skin friction coefficient
$\bar{C}_f$	average skin friction coefficient
C_L	lift coefficient
C_ℓ	spanwise lift coefficient
C_p	pressure coefficient
C_{pt}	total pressure coefficient
C_{Φ^*}	ME loss coefficient
$\bar{C}_{\Phi^*}$	average mechanical loss coefficient
C_T	thrust coefficient

C_{Th}	propulsor disk loading
$\mathbf{D}$	Density flux defect
D	drag
D_i	induced drag
D_p	profile drag
D_w	wave drag
d	diameter
d	streamwise separation
$\mathcal{D}$	Dissipation
DVC	drag variation coefficient
${}^{D}/_{Dt}$	substantial derivative
$\mathbf{E}$	Potential Mixing Dissipation
e	internal energy
e	error
$\dot{E}_a$	streamwise KE deposition rate
$\dot{E}_p$	wake pressure-defect work rate
$\dot{E}_v$	transverse KE deposition rate
$\dot{\mathcal{E}}$	kinetic energy flux
$\dot{E}_w$	wave pressure-work and kinetic energy outflow rate
F	force
F_f	force due to field effect
g	gravitational acceleration
h	enthalpy
h	vertical separation
H	boundary layer shape parameter
H_k	boundary layer kinematic shape parameter
$\bar{H}_k$	average boundary layer kinematic shape parameter
H^*	kinetic energy shape parameter
$\dot{h}$	aircraft climb rate
h_f	fuel heating value

$\hat{\imath}$, $\hat{\jmath}$, $\hat{k}$	locally-Cartesian unit vectors
$\mathbf{K}$	Kinetic energy defect
k	wall roughness height
k^+	wall effective roughness height
K_f	form factor
K_τ	skin friction compressible correction factor
l	length
ℓ, $d\ell$	spanwise integration variable
LVC	loss variation coefficient
m	mass
M	Mach number
$\mathbf{M}$	Mass defect
$\hat{n}$	normal unit vector
p	pressure
P_K	net propulsor mechanical power
P_P	net propulsive power
P_S	net propulsive shaft power
P_V	net pressure volume power
PFEI	payload fuel energy efficiency
Pr	Prandtl number
PSC	power saving coefficient
PSFC	propulsive power specific fuel consumption
$\mathbf{P_x}$	x-momentum defect
$\mathbf{P_z}$	z-momentum defect
$\boldsymbol{q}$	heat flux vector $(q_x\hat{\imath} + q_y\hat{\jmath} + q_z\hat{k})$
$\dot{Q}$	internal heat addition per unit mass
$\mathcal{R}$	$\equiv r\frac{\gamma-1}{2}M_e^2$
R	range
r	Temperature recovery parameter $(= \sqrt{Pr})$
R	wake recovery parameter
Re	Reynolds number
S	area

s	entropy
s, ds	streamwise integration variable
$\mathcal{S}$, $d\mathcal{S}$	surface integration variable
S_{ref}	reference area
S_{wet}	wetted area
T	temperature
t	airfoil thickness
T	thrust
u, v, w	velocity in locally-Cartesian coordinate
$\tilde{u}$, $\tilde{v}$, $\tilde{w}$	perturbation velocity
$\boldsymbol{U}$	in-plane velocity $(u\hat{\imath} + w\hat{k})$
$\boldsymbol{V}$	velocity $(u\hat{x} + v\hat{y} + w\hat{z})$
$\boldsymbol{V}_\infty$	freestream velocity $(V_\infty\hat{x})$
$\mathcal{V}$, $d\mathcal{V}$	volume integration variable
W	weight
W_E	empty weight
W_P	payload weight
W_R	reserve fuel weight
X, Y, Z	globally-Cartesian coordinates
$\hat{X}$, $\hat{Y}$, $\hat{Z}$	global Cartesian unit vectors
x, y, z	locally-Cartesian surface coordinates

Greek Letters

α	angle of attack
β	ingested to total surface dissipation ratio
∇	Space-gradient operator
$\bar{\nabla}$	Surface-gradient operator $(= \frac{\partial}{\partial x}\hat{\imath} + \frac{\partial}{\partial z}\hat{k})$
δ	boundary layer thickness
δ^*	displacement thickness
η_{BLI}	BLI efficiency
η_{prop}	propulsive efficiency

η_{th}	thermal efficiency
Φ	dissipation
Φ^*	mechanical loss
γ	aircraft climb angle
Λ	Wing sweep angle
μ	viscosity
ν	kinematic viscosity
ρ	density
φ	ingested to total profile ME loss ratio
$\boldsymbol{\tau}$	shear stress vector $\left(=\overline{\overline{\tau}}\cdot\hat{\jmath}\right)$
θ	momentum thickness
$\overline{\overline{\tau}}$	shear stress tensor
θ^*	kinetic energy thickness

Superscripts

$()'$	Quantity for integrated (or BLI) configuration
$()^{SC}$	side cylinder quantity
$()^{TP}$	Trefftz plane quantity

Subscripts

$()_0$	initial quantity
$()_\infty$	free stream quantity
$()_{act.}$	actual quantity
$()_B$	body surface quantity
$()_{des.}$	design quantity
$()_e$	BL edge quantity
$()_{est.}$	estimated quantity
$()_f$	final quantity
$()_{FP}$	flat plate quantity
$()_i$	EIF quantity

$()_O$	outer boundary quantity
$()_\perp$	perpendicular flow quantity
$()_t$	total quantity
$()_w$	wall quantity
$()_x$	x-component
$()_z$	z-component

Chapter 1

Introduction

In air-vehicle conceptual design optimization, rapid estimation of the aerodynamic performance of an aircraft configuration is critical, because its performance will be evaluated thousands of times during the optimization process. Performance has been traditionally estimated through a well-established methodology based on a momentum balance, where the drag force on an airframe is matched against the thrust generated by a propulsor.

The need for further performance improvement, however, has pushed aircraft design toward configurations in which the airframe and the propulsion system are tightly integrated. A consequence can be the presence of boundary layer ingestion (BLI) in which the engines take in the airframe boundary layer. Evaluation of such integrated configuration is challenging because the conventional performance metric, which assumes non-interacting airframe and propulsor, is not directly applicable. For example, the pressure drag cannot be obtained by integrating the pressure forces around the airframe as an isolated body, because interactions between the airframe and propulsion system pressure fields create a substantial change in pressure on the airframe.

The power balance method is an alternative approach for performance estimation of aircraft configurations. This method is directly applicable to configurations with BLI and has utility in performance estimation for many other configurations.

In the power balance method, the aircraft mechanical energy production and its consumption are balanced. Unlike momentum, the mechanical power is not explicitly affected by pressure forces, allowing:

- Evaluation of the aerodynamic body performance using a global quantity that is not affected by the local pressure field;

- Quantification of the increase in drag or dissipation due to potential-flow interactions between components, which traditionally has been labeled as "interference" drag;
- Expression of the boundary layer mechanical energy loss using the boundary layer edge velocity and the dissipation coefficient; and
- Calculation of the aerodynamic performance using the dissipation coefficient instead of skin friction coefficient. The former varies much less than the latter with boundary layer shape factor, and therefore gives more accurate estimates of the performance in a conceptual design stage.

This thesis provides evidence of the major benefits of the power balance method listed above from three different applications: 1) derivation of analytical expression of profile drag estimates for conceptual design applications, 2) aerodynamic performance estimation for three canonical integrated configurations, and 3) performance quantification of a hybrid wing body (HWB) with BLI propulsion system.

1.1 The Power Balance Method

This section presents an introduction of the power balance method, together with the definition of various terms involved in the formulation. The detailed derivation of the power balance method is presented by Drela [9]. The concept of the power balance method can be introduced through an analogy with solving problems in dynamics using the principle of energy conservation. A number of problems can be solved more easily through application

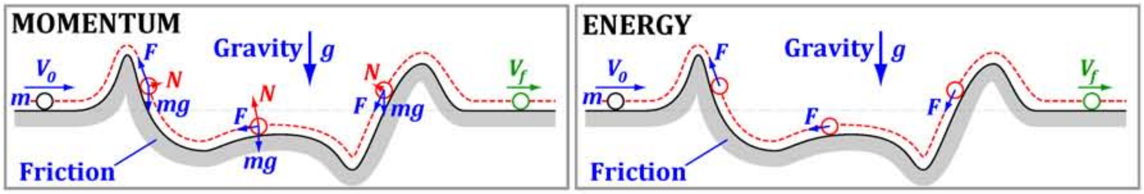

Figure 1-1: Example dynamics problem illustrating the difference between momentum (left) and energy (right) conservation approach. To obtain the final velocity of the ball, conservation of momentum involves integration of the horizontal components of tangential friction forces and normal contact forces over entire path, while conservation of energy only requires the integration of friction force magnitudes.

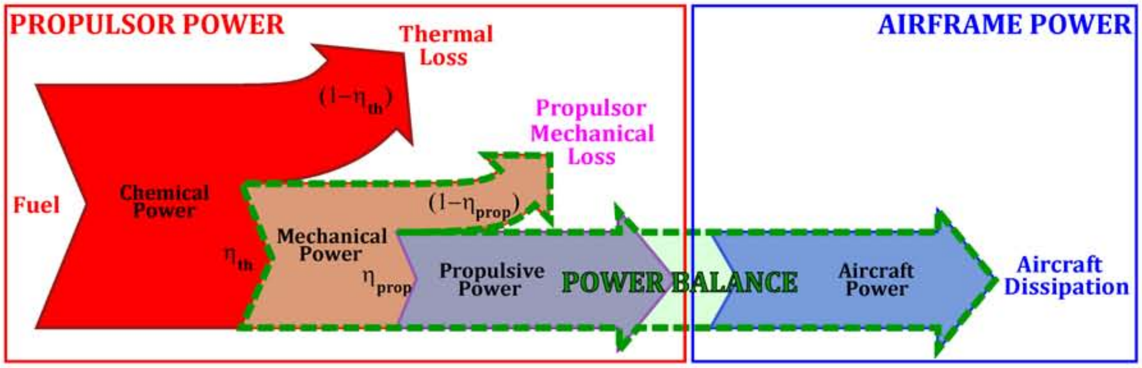

Figure 1-2: Power conversion process from fuel to aircraft power. The power balance method addresses the power conversion after chemical power is converted to mechanical power.

of conservation of energy rather than momentum considerations. An illustration is given in Figure 1-1, which shows a ball of mass m traveling over a non-uniform surface with friction. We are interested in obtaining the final velocity of the ball V_f, from the known quantities, shown in blue. To obtain this quantity using conservation of momentum, the horizontal components of the tangential (friction) and normal contact forces need to be integrated over the entire path. The normal force is a function of the orientation of the surface and the acceleration of the ball, which requires solving for the dynamics of the ball through the entire process. Using conservation of energy, only the tangential friction needs to be integrated, as normal forces do not do any work. The amount of information needed for the conservation of energy relation is less than for the conservation of momentum, and the application of conservation of energy thus simplifies the calculation. (This is even more the case when there are no friction forces as the energy method reduces to knowledge of the difference in height.) The power balance method is essentially conservation of mechanical energy applied to fluid dynamics.

A general formulation of the conservation of mechanical energy in a flow field was introduced by Tsien in 1945 [12]. This concept of mechanical energy and losses has also been employed extensively in the field of turbomachinery, as examplified by the work of Denton [6], which presents an in-depth analysis on turbomachine stage performance from the perspective of loss generation. There have not been, however, to the author's knowledge, any work that proposed the application of the concept of power balance to aircraft design other than that of Drela [9], which provides a starting point for the current research.

An important performance metric in aircraft design is fuel consumption. Figure 1-2 describes the conversion process from fuel chemical power to the mechanical power needed to propel an aircraft. The chemical power released from the combustion of fuel is first converted into useful mechanical power by the propulsion system. During the conversion process to useful mechanical power, part of the chemical power is lost as heat. The efficiency of this power conversion is given by the thermal efficiency (η_{th}). The mechanical power generated by the propulsor is then converted into propulsive power, with additional power lost from propulsor mechanical losses such as propeller efficiency and jet excess kinetic energy. The efficiency related to this power conversion is defined as the propulsive efficiency (η_{prop}). The breakdown between thermal and propulsive efficiency depends on the choice of the control volume around the propulsor. As a convention, the control volume around the propulsion system were defined as in Figure 1-3. For ducted propulsors, the control volume is bounded by the engine inlet and nozzle. For unducted propulsors, the control volume is bounded at the propeller surfaces. Mechanical loss generated outside the control volume is counted as part of the propulsive efficiency.

To propel the aircraft, the propulsive power generated by the propulsion system must balance the mechanical power consumed by the aircraft, which is ultimately dissipated. The power balance method described below allows determination of the magnitude of these mechanical power terms.

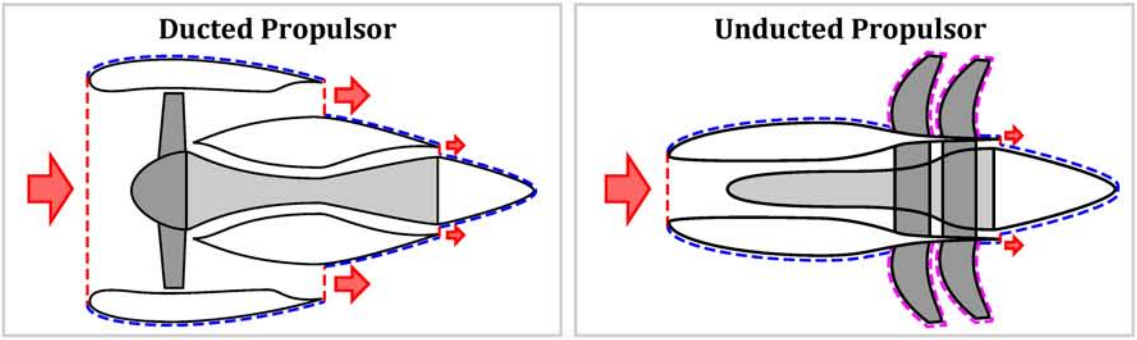

Figure 1-3: Control volume boundary for ducted (left) and unducted (right) propulsor. Ducted propulsor is bounded by the engine inlet and nozzle (red boundaries); unducted propulsor is bounded at the propeller surface (pink boundaries).

1.1.1 Formulation [9]

The fundamental equation in the power balance method is obtained by taking the dot product of each term in the Navier-Stokes equation with the local fluid velocity $\boldsymbol{V}$, defined as:

$$\boldsymbol{V} = (V_\infty + u)\hat{X} + v\hat{Y} + w\hat{Z}, \tag{1.1}$$

with V_∞ the magnitude of the freestream flow velocity, and u, v, w the velocity perturbations from the freestream velocity in the x, y and z directions respectively.

For a steady, compressible flow with no body forces, the differential form of the mechanical power balance equation is obtained by forming the dot product of $\boldsymbol{V}$ with the momentum equation and adding $1/2V^2$ times continuity:

$$\begin{align} \frac{1}{2}V^2\{\nabla\cdot(\rho\boldsymbol{V}) &= 0\} \tag{1.2}\\ +\boldsymbol{V}\cdot\{\rho\boldsymbol{V}\cdot\nabla\boldsymbol{V} &= -\nabla p+\nabla\cdot\overline{\overline{\tau}}\} \nonumber\\ \nabla\cdot\left(\rho\boldsymbol{V}\frac{1}{2}V^2\right) &= -\nabla p\cdot\boldsymbol{V}+\left(\nabla\cdot\overline{\overline{\tau}}\right)\cdot\boldsymbol{V}, \tag{1.3}\end{align}$$

with $\overline{\overline{\tau}}$ indicating the viscous stress tensor. Eq. 1.3 can be developed into an integral statement using the three dimensional control volume (CV) (2-D cutaway of the CV shown in Figure 1-4), which surrounds the flow around an aerodynamic body.

The CV boundary surface $\mathcal{S}$ is partitioned into the outer boundary $\mathcal{S}_O$, far from the body and the inner boundary $\mathcal{S}_B$, on the surface of the body. Gauss's theorem using these boundaries yields

$$\iiint \nabla\cdot\boldsymbol{A}\,d\mathcal{V} = \oiint \boldsymbol{A}\cdot\hat{n}\,d\mathcal{S}_O + \oiint \boldsymbol{A}\cdot\hat{n}\,d\mathcal{S}_B, \tag{1.4}$$

which holds for any continuous vector field $\boldsymbol{A}$.

Some outer boundary sections are defined to be oriented in a particular direction as follows:

- The downstream transverse plane boundary, $\mathcal{S}_O^{TP}$, is oriented normal to $\boldsymbol{V}_\infty$,
- The side cylinder boundary, $\mathcal{S}_O^{SC}$, is oriented parallel to $\boldsymbol{V}_\infty$.

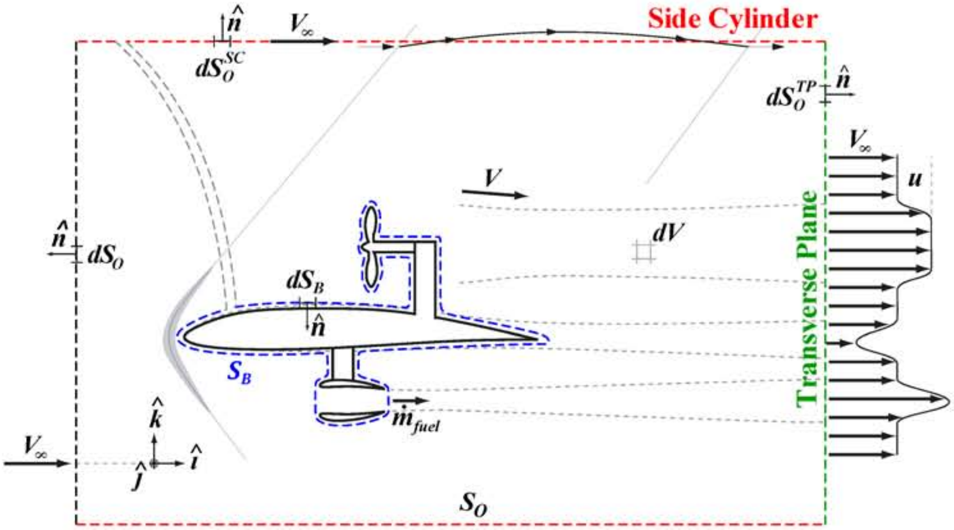

Figure 1-4: Two-dimensional cutaway view of 3-D CV surrounding an aerodynamic body (Adapted from [9]).

The transverse plane is a generalization of the Trefftz Plane[1] which does not have to be located far downstream of the airfoil.

The following is assumed:

- All vortical fluid leaves via $\mathcal{S}_O^{TP}$, linked with the orientation of the side cylinder boundary, $\mathcal{S}_O^{SC}$.
- Any oblique shock waves which are present in supersonic flow leave via $\mathcal{S}_O^{SC}$.
- The distance from the body to the side cylinder is several times (or more) the wing span of the body to ensure that the effect of pressure field generated by the aerodynamic body on the flow field at the side cylinder is negligible, i.e., $|\boldsymbol{V}|_{SC} \approx V_\infty$ for subsonic flow. The pressure disturbance of oblique waves may be present for supersonic flow.

The above assumptions are helpful in identifying the physical origin of various power terms in the equation. Integrating Eq. 1.3 over the control volume yields

$$\iiint \nabla \cdot \left(\rho \boldsymbol{V} \frac{1}{2} V^2\right) d\mathcal{V} = \iiint \left[-\nabla p \cdot \boldsymbol{V} + \left(\nabla \cdot \bar{\bar{\tau}}\right) \cdot \boldsymbol{V}\right] d\mathcal{V}. \tag{1.5}$$

Applying Eq. 1.4 to Eq. 1.5, the power balance equation is obtained:

---

[1] The Trefftz plane is defined as a plane downstream of an aerodynamic body, located sufficiently far from the body so the axial variation in the static pressure field is negligible.

$$P_S + P_V + P_K = W\dot{h} + \dot{E}_a + \dot{E}_v + \dot{E}_p + \dot{E}_w + \Phi. \tag{1.6}$$

The left hand side (LHS) of Eq. 1.6 represents the mechanical power supply, i.e., power production or inflow to the control volume. The right hand side (RHS) represents the mechanical power dissipation, conversion to potential energy and outflow from the control volume.

The terms on the LHS of Eq. 1.6 are defined as follows.

- P_S , the net propulsive shaft power, is defined as

  $$P_S \equiv \oiint [-(p - p_\infty)\hat{n} + \overline{\overline{\tau}} \cdot \hat{n}] \cdot \boldsymbol{V} \, d\mathcal{S}_B. \tag{1.7}$$

  P_S represents the power provided by components moving relative to the control volume. This term is non-zero only if the control volume wraps around a moving surface such as propeller blades, as depicted by the upper propulsor in Figure 1-4.

- P_V, the net pressure-volume "$p\,d\mathcal{V}$" power, is defined as

  $$P_V \equiv \iiint (p - p_\infty) \nabla \cdot \boldsymbol{V} \, d\mathcal{V}. \tag{1.8}$$

  P_V represents the volumetric mechanical power, provided by fluid expanding against atmospheric pressure. This term will be non-zero wherever heat is added to or removed from the flow.

- P_K represents the net propulsor mechanical energy flow rate into the control volume:

  $$P_K \equiv \oiint [(p - p_\infty) + \frac{1}{2}\rho(V^2 - V_\infty^2)] \cdot \boldsymbol{V} \cdot \hat{n} \, d\mathcal{S}_B. \tag{1.9}$$

  P_K indicates the net pressure power or work rate and kinetic energy inflow rate across the body surface boundary. P_K is non-zero when the control volume is defined around the inlet and outlet of the engine, as with the bottom propulsor shown in the Figure 1-4.

The terms on the RHS are defined as:

- $W\dot{h}$, the rate of change of potential energy, is the power used in increasing the potential energy of the body. It is calculated as the product of the aircraft weight W and the rate of altitude change $\dot{h}$,

  $$W\dot{h} = WV_\infty \sin\gamma, \tag{1.10}$$

  for a climb angle γ. During descent $\dot{h} < 0$, so this becomes a power source.

- $\dot{E}_a$ is the rate of streamwise kinetic energy being deposited into the flow out of the control volume through the transverse plane, caused by jets produced by propulsors or wakes generated by a body. It is defined as

  $$\dot{E}_a \equiv \iint \frac{1}{2}\rho u^2 (V_\infty + u)\, d\mathcal{S}_O^{TP}. \tag{1.11}$$

- $\dot{E}_v$ is the rate of transverse kinetic energy being deposited into the flow out of the control volume through the transverse plane. $\dot{E}_v$ is produced by the trailing vortex system from a lifting body. It is defined as

  $$\dot{E}_v \equiv \iint \frac{1}{2}\rho (v^2 + w^2)\,(V_\infty + u)\, d\mathcal{S}_O^{TP}. \tag{1.12}$$

- $\dot{E}_p$, the pressure defect work rate, is the rate of pressure work done on the fluid crossing the Trefftz Plane at a pressure different from its freestream value. It is defined as

  $$\dot{E}_p \equiv \iint (p - p_\infty) u\, d\mathcal{S}_O^{TP}. \tag{1.13}$$

- $\dot{E}_w$ is the pressure work and kinetic energy deposition rate of the fluid crossing the side cylinder and becomes important in supersonic flow. It is defined as

  $$\dot{E}_w \equiv \iint [p - p_\infty + \frac{1}{2}\rho (u^2 + v^2 + w^2)]\boldsymbol{V} \cdot \hat{n}\, d\mathcal{S}_O^{SC}. \tag{1.14}$$

- Φ is the viscous dissipation rate, accounting for all kinetic energy dissipated inside the control volume. It is defined as

  $$\Phi \equiv \iiint (\bar{\bar{\tau}} \cdot \nabla) \cdot \boldsymbol{V}\, d\mathcal{V}. \tag{1.15}$$

In actual flow situations, all forms of kinetic energy outflow are converted into dissipation as wakes, jets and vortices are convected downstream of the aircraft. Using this, the dissipation term in the power balance equation can be separated into various sources:

$$\begin{aligned} P_S + P_{V,\,prop} + P_K &= W\dot{h} + \left(\dot{E}_v + \Phi_{vortex}\right) \\ &+ \left(\dot{E}_w + \Phi_{wave}\right) + \left(\Phi_{surf} - P_{V,\,surf}\right) \\ &+ \left(\dot{E}_{a,wake} + \dot{E}_{p,wake} + \Phi_{wake} - P_{V,\,wake}\right) \\ &+ \left(\dot{E}_{a,jet} + \dot{E}_{p,jet} + \Phi_{prop} + \Phi_{jet} - P_{V,\,jet}\right). \end{aligned} \tag{1.16}$$

Φ_{surf} is the dissipation generated at the surface of the body. Φ_{vortex} , Φ_{wake}, Φ_{jet} and Φ_{wave} are dissipation caused by mixing out the velocity non-uniformity present in vortices, wakes, jets and shock waves inside the control volume. Φ_{prop} is the dissipation generated at the surface and wake of the moving component of the propulsor, e.g., propeller and flapping wings. The volumetric mechanical power, P_V was also divided into various components; the P_V terms inside the boundary layers and wakes are commonly referred to as recovery terms.

For a particular aircraft configuration, each quantity has a fixed value regardless of the choice of a control volume. To simplify Eq. 1.16, we can define the mechanical energy loss

$$\Phi^* \equiv \Sigma\dot{E} + \Sigma\Phi - \Sigma P_V. \tag{1.17}$$

An illustration of the mechanical energy loss Φ^* is shown in Figure 1-5, which shows the variation of the wake mechanical loss terms downstream of the airfoil. The total mechanical energy dissipated is unchanged, but it is made up of different terms depending on axial location. At the trailing edge, the velocity deficit in the wake has not dissipated, and the wake mechanical loss is made of $\dot{E}_a$, $\dot{E}_p$ and P_V. As the wake is convected downstream, $\dot{E}$ terms and P_V are ultimately converted to dissipation Φ.

Using Eq. 1.17, the power balance equation can be simplified as

$$P_S + P_{V,\,prop} + P_K = W\dot{h} + \Phi^*_{vortex} + \Phi^*_{wave} + \Phi^*_{surf} + \Phi^*_{wake} + \Phi^*_{prop}. \tag{1.18}$$

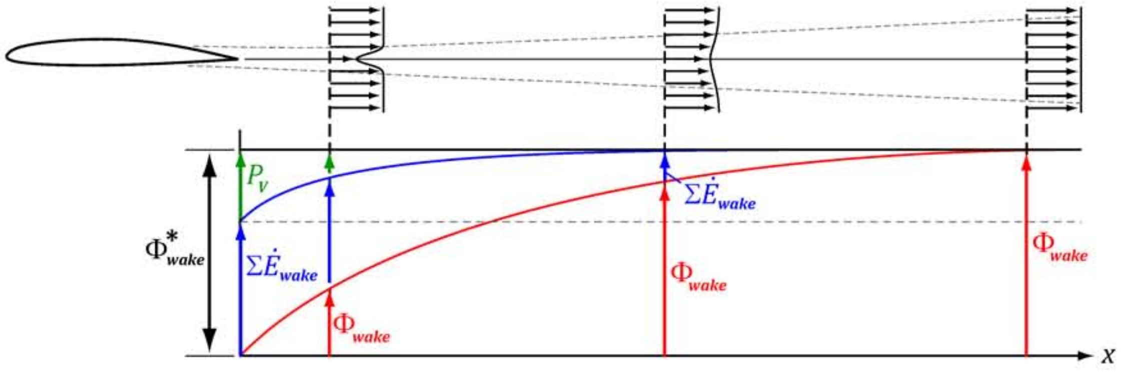

Figure 1-5: Variation in wake mechanical loss terms in Eq. 1.17 versus streamwise location. Total dissipated power sum is unchanged.

1.1.2 Application to Aircraft Performance Analysis

Figure 1-6 shows the flow of mechanical power from the propulsor. Among the terms in Eq. 1.18, all terms on the LHS and the jet mechanical energy loss $\left(\Phi^*_{prop}\right)$, are accounted as contributions from the propulsion system, while all other terms are accounted as part of the airframe losses.

The net propulsive power generated by the propulsor is defined as

$$P_P \equiv \Sigma P - \Phi^*_{prop}. \tag{1.19}$$

Using Eq. 1.19, the propulsive efficiency of the engine can be defined as

$$\eta_{prop} \equiv \frac{P_P}{\Sigma P} = 1 - \frac{\Phi^*_{prop}}{\Sigma P}. \tag{1.20}$$

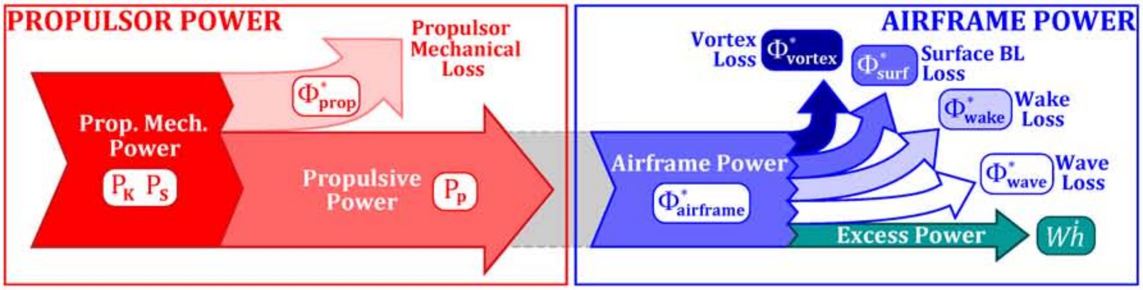

Figure 1-6: Power balance process between airframe and propulsor. All power provided to the airframe is eventually dissipated.

Propulsion system related terms are functions of propulsion system cycle parameters, and can be calculated from cycle analysis, which is a well established conceptual design process. The primary focus of this thesis is thus on the estimation of airframe losses. A main result of the thesis is to demonstrate that estimation of airframe losses using the power balance method has many advantages compared to drag estimation using the momentum balance method, especially for integrated aircraft configurations. This thesis therefore covers the development of an airframe performance estimation model using the power balance method, its application to integrated aircraft configurations, and its comparison against the momentum balance method to highlight the major advantages.

A focus of this thesis is to improve the wetted area method, a profile drag estimation commonly used in aircraft conceptual design. Profile drag calculation using the wetted area method has the general form

$$C_{D_p} = C_{f_{FP}} K_f \frac{S_{wet}}{S_{ref}}, \tag{1.21}$$

where the flat plate skin friction coefficient $C_{f_{FP}}$ is scaled by a component form factor K_f and normalized wetted area ${}^{S_{wet}}/{}_{S_{ref}}$. K_f is a quantity that depends on the geometry of the aerodynamic body, and is typically obtained from empirical correlations. Using the power balance method, an analytical expression for the form factor is derived in Chapter 4 as:

$$K_f = \frac{1}{\sum_{i=1}^{n} S_{wet_i}} \sum_{i=1}^{n} \frac{\iint_{wet_i} \rho_e U_e^3 \left(1 + \frac{\gamma-1}{2} M_e^2\right)^r dS_{wet_i}}{\rho_\infty V_\infty^3 \left(1 + \frac{\gamma-1}{2} M_\infty^2\right)^r}, \tag{1.22}$$

where n is the number of distinct surfaces on the aerodynamic body, and r is the temperature recovery parameter ($= \sqrt{\mathrm{Pr}}$). We will show in Chapter 4 that the expression in Eq. 1.22 is both as accurate as the empirical form factor correlations and is applicable to new geometries without the need for experimental data to estimate form factors.

Another focus of this thesis is the estimation of the aerodynamic performance of an integrated configuration, where two or more aerodynamic bodies have a significant[2] pressure field influence, without need for a viscous CFD solution. The loss estimation methodology is applied to representative integrated configurations: an airfoil coupled with a propulsor (modeled as an actuator disk), two closely positioned airfoils, and a nacelle with an actuator disk. Through these examples, the estimation methodology is shown to be accurate to within

---

[2] defined here as greater than 10% change in aerodynamic performance between integrated and non-integrated configuration

10% for configurations for which the average boundary layer kinematic shape parameter increases by no more than 0.04 as a result of interference. In this context we note there is no standard procedure to determine the performance of an integrated configuration using the momentum balance method apart from analyzing the entire configuration with a viscous computation. The development of these examples is presented in Chapter 5.

1.2 Boundary Layer Ingestion and Benefit Quantification

The concept of boundary layer ingestion for aircraft applications has been discussed since the 1940s [38] but has yet to be applied to commercial aircraft. Recently, however, there have been a growing interest in the application of BLI to improve the performance of civil aircraft.

The primary benefit of BLI comes from two effects:

1. Improvement of the propulsive efficiency. Ingestion of lower kinetic energy flow allows the engine to produce propulsive power with lower expenditure of kinetic energy in the exhaust jet compared to non-BLI configurations.

2. Reduction of airframe wake mechanical energy loss (Φ^*_{wake}). Ingestion of the boundary layer decreases the wake defect downstream of the airframe, reducing the total mechanical energy loss.

Performance calculation and design of aircraft using BLI was addressed in the Silent Aircraft Initiative [19]. The performance accounting was conducted using a momentum balance, where numerous assumptions about the viscous flow details needed to be made to evaluate the benefit of BLI. In this thesis, performance accounting based on the power balance method is employed in quantifying the benefit of BLI, with fewer assumptions being required compared to the momentum balance approach, as discussed in Chapter 6.

The following effects must be considered in assessing the system level impact of BLI:

1. Reduction of inlet pressure recovery due to the introduction of a boundary layer ingesting inlet duct system. In some designs, a long serpentine duct is required to divert the boundary layer into the engine, generating secondary flow and decreasing the duct inlet pressure recovery.

2. Reduction of fan efficiency due to ingestion of non-uniform flow. This thesis will not address the response of engines under non-uniform flow. The effect will be captured in the tradeoff analysis as a change in fan efficiency.

3. Performance variation due to change in engine installation. Wetted area of the nacelle changes depending on the type of the engine installation used on the aircraft, affecting the aircraft mechanical energy loss. This thesis assumes that no major flow separation and shock formation occurs from the changes in the engine installation; the impact is modeled as a change in profile mechanical energy loss due to wetted area and Reynolds number changes.

4. Performance variation due to change in the propulsion system and total fuel weight. Introduction of BLI affects the weight of both propulsion system and fuel carried on the aircraft. These weight changes affect the structural weight and the balance of the aircraft, changing the performance.

We will quantify the tradeoff between the amount of BLI and the increase in aircraft performance taking into account the effects listed above, by coupling an aircraft performance estimation method with an HWB aircraft design optimization program HWBOpt.

1.3 Contributions

The main contributions of this thesis are the following:

A. The derivation of an first-of-its-kind analytical expression for the component form factor used in the wetted area method:

$$K_f = \frac{1}{\sum_{i=1}^{n} S_{wet_i}} \sum_{i=1}^{n} \frac{\iint_{wet_i} \rho_e U_e^3 \left(1 + \frac{\gamma-1}{2} M_e^2\right)^r dS_{wet_i}}{\rho_\infty V_\infty^3 \left(1 + \frac{\gamma-1}{2} M_\infty^2\right)^r S_{wet_i}}. \tag{1.23}$$

Unlike other form factor correlations based on empiricism, this analytical expression allows calculating the component form factors of airfoils without experimental data. The accuracy of this analytical expression is shown to be as accurate as other form factor correlation based on empiricism and confirmed to be accurate within 2% for:

1. a D8.5[3] fuselage section with fineness ratio (l/d) greater than 5 at $M_\infty = 0.1$, and greater than 6.25 at $M_\infty = 0.85$,

2. a GAW1 low speed airfoil with lift coefficient between -0.5 and 1.0 at $M_\infty = 0.15$, and

3. a RAE2822 transsonic airfoil with $M_\infty \leqq 0.71$ at $\alpha = 3°$.

Aircraft operating at cruise typically are within the range of parameters examined in cases 1, 2, and 3 listed above. The analytical expression from the power balance method is therefore applicable for use at the conceptual design stage in estimating cruise performance, without relying on empiricism.

B. The estimation of performance of integrated configurations using the power balance method. The profile mechanical energy loss due to interference effect is shown to accurately scale as $\rho_e U_e^3 \left(1 + \frac{\gamma-1}{2} M_e^2\right)^r$, in line with the scaling developed from the boundary layer mechanical energy equation. The accuracy and limitation of this scaling law is demonstrated using the following examples: fuselage with actuator disk, two interfering airfoils and nacelle with actuator disk. The loss scaling breaks down when the boundary layer separates, but this is not a serious limitation since separated flow is not present at assumed design-point operating conditions. The interference effect, which no standard procedure were available using the momentum balance method apart from analyzing the entire configuration with a viscous computation, can therefore be estimated accurately using this scaling law during conceptual design.

C. The quantification of benefits of BLI on aircraft system performance. It is found that for the propulsion system configuration studied, the fuel burn of the aircraft decreased monotonically with increasing amount of BLI. Maximum fuel burn improvement thus comes from the design with the maximum allowable BLI on the HWB center body, giving an improvement of 11% from a non-BLI configuration. The performance gain from BLI, however, appeared to be problematic given the amount of technology challenge and risk associated with distributing the propulsor over the entire fuselage. It is concluded that BLI can have a larger impact in practice when applied to tube-and-wing configuration, where it can be achieved without a distributed propulsion system.

---

[3] Aircraft designed during the NASA N+3 Phase I project [14]

1.4 Thesis Outline

Chapter 2 surveys the relevant literature regarding the drag estimation correlations used in aircraft conceptual designs. This chapter also reviews the literature on BLI and describes its important physical features.

Chapter 3 extends on boundary layer integral equations using the power balance formulation introduced by Drela [9]. It also gives specifics of the fundamental advantages of the power balance method compared to the momentum balance method. Further the chapter develops a correlation of laminar and turbulent skin friction and dissipation coefficient for a flat plate.

Chapter 4 develops an analytical expression for the form factor used in the wetted area method (Contribution A). The advantages and limitation of this analytical model are explained and compared against current empirical form factor correlations, through three applications: bodies of revolution, a 2D low speed airfoil, and a 2D transonic airfoil.

Chapter 5 develops a methodology to estimate the performance of integrated configurations using the power balance method (Contribution B). The accuracy and limitation of this methodology are quantified using three canonical examples: an airfoil with an actuator disk, two interfering airfoils and a nacelle with actuator disk. The estimation method is compared against the methodology based on a momentum balance to highlight the key differences between power and momentum based approach.

Chapter 6 quantifies the tradeoff between BLI and the aircraft fuel burn for a hybrid wing body (HWB) aircraft using the power balance method (Contribution C). The analysis is conducted using an aircraft multidisciplinary design optimization model for the HWB coupled with the BLI performance estimation methodology based on the power balance method. The governing mechanism which links BLI to aircraft fuel burn is presented.

Chapter 7 presents a summary, conclusions, and a description of potential future work.

Chapter 2

Literature Review

This chapter presents a review of the literature relevant to the topics of this thesis. Section 2.1 surveys the drag estimation correlations used in aircraft conceptual design. Section 2.2 reviews the literature relevant to boundary layer ingestion (BLI) and describes its important features.

2.1 Profile Drag Correlations for Aircraft Conceptual Design

Current preliminary estimation methodologies for profile drag are based on wetted area, a flat plate skin friction coefficient and a component form factor. Methods currently employed by aircraft manufacturers have form factors calibrated based on extensive drag data obtained from in-house experiments or flight test data.[1] Details of these form factor formulations are proprietary.

The most recent profile drag estimation methods available in the literature are the ones implemented in aircraft configuration analysis programs, such as FLOPS [13] developed by NASA and PASS [25] developed by Stanford University. FLOPS, implemented based on the study by Feagin and Morrison [13], uses an empirically obtained form factor from Morrison [30], formulated using experimental data for the NACA 65-123 airfoil, a 9% thickness ratio state-of-the-art airfoil[2] , and 10% and 11% thickness ratio advanced airfoils[3]. Feagin notes that FLOPS is most accurate within the range of data from which it was derived, and that caution needs to be exercised if one wishes to analyze configurations outside the range

---

[1] per personal conversation with Prof. Mark Drela

[2] geometry not specified.

[3] geometry not specified.

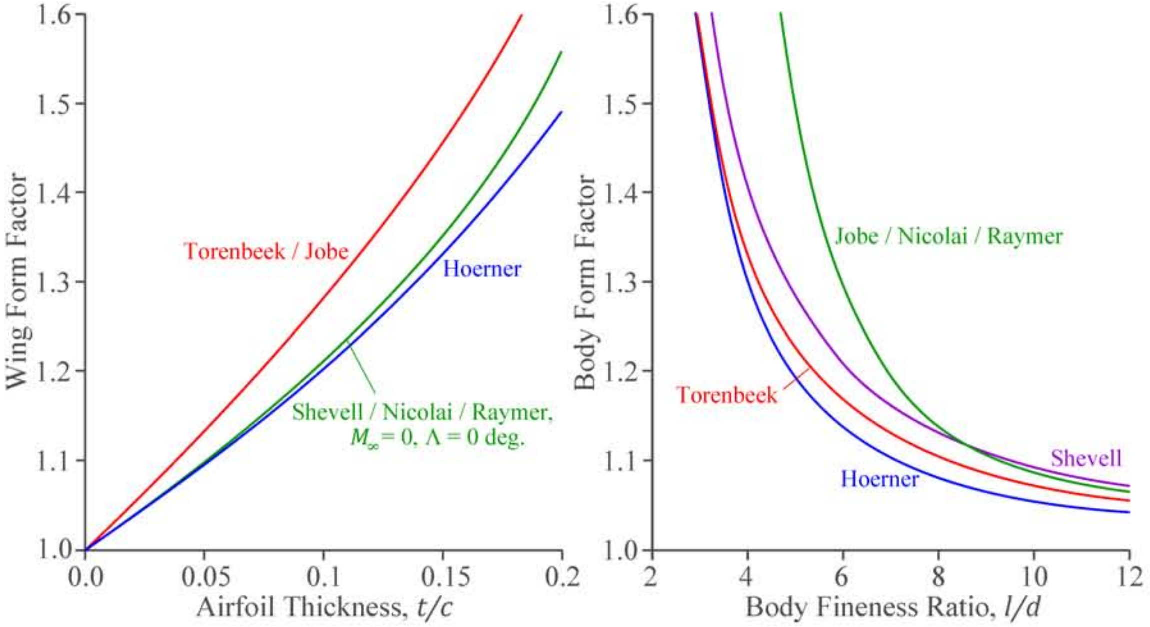

Figure 2-1: Comparison of form factor correlations for 2D wing sections (left) and bodies of revolution (right). (Adapted from [16]) Discrepancies exist between various form factor correlations.

of applicability.

PASS, developed by Kroo, employs a form factor derived analytically from the supervelocity due to thickness [24, 25]. This correlation is adjusted with an empirical calibration factor calculated from Shevell [37] and Schlichting [36].

A recent work by Gur [16] summarizes various form factor correlations and presents a comparison of empirical correlations of airfoils and body of revolution form factors, including Hoerner [20], Jobe [22], Nicolai [32], Raymer [34], Shevell [37] and Torenbeek [43]. The correlations are functions of geometric parameters: thickness to chord ratio, location of airfoil maximum thickness, and aircraft-quarter-chord sweep. Figure 2-1 shows comparisons of form factor correlations for 2D airfoils (left) and bodies of revolution (right). Discrepancies exist between the various form factor correlations and for a two-dimensional airfoil with thickness to chord ratio (t/c) of 0.12, the spread in drag between the correlations is up to 10%. In the correlations for axi-symmetric bodies, the spread is within 4% for high-fineness-ratio (length-to-diameter ratio) bodies ($l/d > 10$), and $\sim 50\%$ for lower-finess-ratio bodies ($l/d < 4$). These comparisons give indication of possible errors in the profile drag estimation, but there is no guidance as to which correlation works best for a particular airfoil.

2.2 Boundary Layer Ingestion Analysis

Boundary layer ingestion (BLI) is a concept that has been investigated since the 1940s. One of the first articles on this concept was by Smith and Roberts [38], who found a reduction of 5-10% in fuel consumption using BLI, although details of the derivation of these numbers were not presented.

A subsequent investigation of the effect of BLI on aircraft propulsive efficiency was conducted by Douglass [7]. Performance was examined for propulsion system configurations using an ideal diffuser (no losses in the inlet duct) and using a dump diffuser (dissipates inlet dynamic pressure). The calculations were conducted assuming incompressible flow and an inlet boundary layer with a one-seventh power profile, expanded to ambient pressure before being fed into the propulsor. The improvement in propulsive efficiency was calculated by relating power savings to thrust produced by the propulsor. Torpedoes with 100% wake ingestion were shown to achieve improvements in propulsive efficiency of 28%. For an aircraft configuration ingesting 25% of the wake, 13% improvement in propulsive efficiency was found. The thermal efficiency was impacted by the reduction of inlet pressure recovery, resulting in a cycle efficiency reduction of 6.1% for an ideal diffuser and 21% for the dump diffuser.

Smith [39] performed detailed analysis of BLI on an axisymmetric body with an unducted propeller. The flow was taken as incompressible, with the propulsor modeled as an actuator disk. A conceptual assumption was that the actuator disk was located far enough downstream of the body so there was no pressure field interaction between the airframe and the propulsor. As the figure of merit, Smith introduced a "power saving coefficient" (PSC), defined as the difference in propulsive power between the BLI and non-BLI configuration, normalized by "the propulsive power required to propel the part of the body whose wake is to be ingested, evaluated for a non-BLI configuration". The power saving coefficient was calculated from the required thrust and propulsive efficiency.

Smith examined effects on PSC of wake recovery parameter (R), boundary layer shape factor (H), amount of wake ingested (D/T, ratio between the "drag" of the part of the body whose wake is to be ingested and the total "thrust" generated by the propulsor), and propulsor thrust loading coefficient (C_{Th}). Figure 2-2 depicts the influence of propulsor thrust loading and boundary layer shape parameter on PSC for a configuration with fixed

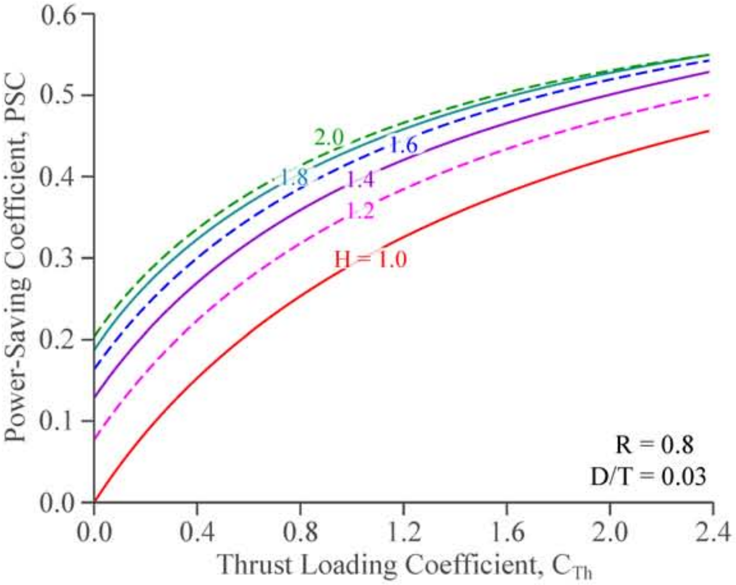

Figure 2-2: Effects of thrust loading coefficient and wake form factor on the power required to propel that part of the aircraft whose wake is being ingested. Amount of BLI $D/T = 0.03$ and wake recovery $R = 0.8$. (Adapted from [39]) Gain in PSC is larger for higher thrust loading coefficient and higher H.

amount of wake ingestion ($D/T = 0.03$). The benefit of BLI is higher when the boundary layer is close to separation, i.e., larger shape factor, with an increase of PSC of more than 0.2 between $H = 1.0$ and $H = 2.0$. Higher propulsor pressure rise also gave higher power savings, with an improvement of PSC close to 0.3 for $C_{Th} = 2.4$, relative to $C_{Th} = 0.0$.

Smith also examined the effect of BLI on propulsive efficiency for a higher level of wake ingestion, D/T. Figure 2-3 illustrates gains in propulsive efficiency for various amount of wake ingestion and thrust loading coefficient. The result showed a larger propulsive efficiency gain for a larger amount of wake ingestion combined with a lower thrust loading coefficient. At the best case, an improvement of approximately 20 percentage points in propulsive efficiency was observed between a non-ingesting configuration ($D/T = 0$) and a fully ingesting configuration ($D/T = 1$) for the same thrust loading coefficient.

Both Douglass [7] and Smith [39] offer thorough analyses of the performance benefits of boundary layer ingestion. However, they assume the wake was expanded to ambient pressure through an isentropic process and thus do not address the effect of pressure interaction between the airframe and the propulsor, a key aspect of the work in this thesis.

Other recent work by Daggett [4] and Kawai [23] examined BLI propulsion systems for a blended wing body aircraft, by calculating the benefit of BLI from the "reduction of ram

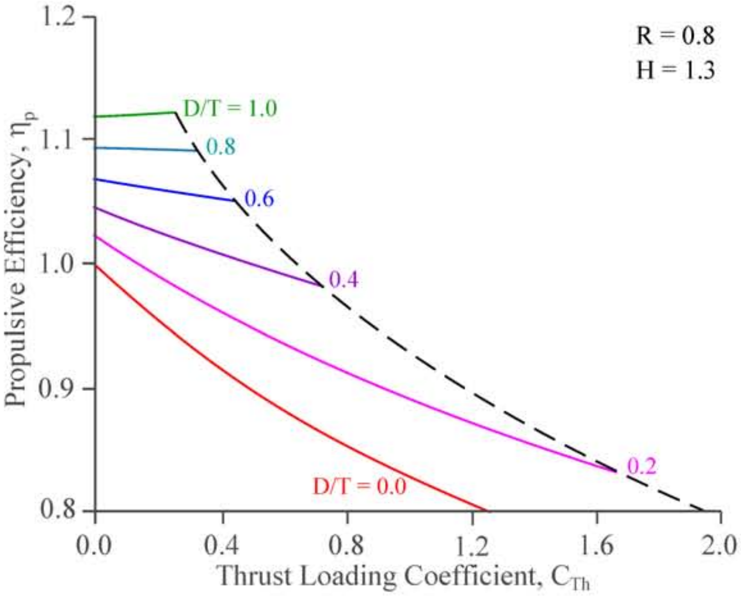

Figure 2-3: Propulsive efficiency gains from wake ingestion. (Adapted from [39]) Boundary layer shape factor $H = 1.3$ and wake recovery $R = 0.8$. Propulsive efficiency improves with larger D/T and lower C_{Th}.

drag" of the engine. Kawai points out that a challenge in the calculation of ram drag is to define separate control volumes for the internal and external flows and he approximated the reduction in ram drag by isentropically expanding the momentum captured by the engine to freestream static pressure.

Daggett estimated the performance benefit of a BLI configuration using a 3-D simulation. The BLI configuration considered featured active flow control inlets to improve the inlet pressure recovery. Compared to a podded, non-BLI design, the BLI configuration gave a 6.3% reduction in ram drag. Accounting for the reduction in engine efficiency, Daggett concluded that a 5.5% reduction in fuel burn can be achieved using BLI, assuming no effect of distortion because of the active flow inlet and neglecting the power to drive the flow-control system.

Sargeant [35] conducted an assessment of the benefit of BLI on the hybrid wing body aircraft designed during the Silent Aircraft Initiative [19], following the method used by Smith [39]. The propulsor was assumed to act at ambient pressure, and the ingested momentum defect was expanded to ambient conditions through an isentropic process. The benefit of BLI was calculated as an improvement of propulsive efficiency. Figure 2-4 shows the propulsive efficiency as a function of the amount of wake ingested (β), the normalized drag (equivalent to thrust loading coefficient), and the boundary layer kinetic energy shape factor (H^*). Improvement in propulsive efficiency from BLI increases with the amount of wake ingested, up to an improvement of 60 percentage points in propulsive efficiency with full BLI ($\beta = 100\%$), normalized drag of 1.0 and $H^* = 1.6$.

The propulsive efficiency improvement is also influenced by normalized drag (i.e. thrust loading), where the higher normalized drag configuration gives larger improvement in propulsive efficiency. A boundary layer with smaller H^* value (corresponding to a larger H) gave larger performance gain from BLI than boundary layer with larger H^*, consistent with Smith's results. For example, propulsive efficiency with $H^* = 1.6$ was more than 10 percentage points higher than that with $H^* = 1.8$ for a configuration with full BLI ($\beta = 100\%$).

For the HWB aircraft configuration designed in the Silent Aircraft Initiative, the introduction of BLI had the potential to realize a fuel burn improvement of 11% over a podded design. Taking into account the fan inefficiency in the presence of distorted flow and duct losses for the boundary layer ingesting inlets, Sargeant concludes that an improvement of 4.9% in fuel burn can be achieved with BLI compared to a podded engine design utilizing the same engine mass flow.

The works described in this section quantified the benefit of BLI using concepts of the momentum balance method. These require additional correction to evaluate the momentum defect ingested by the propulsor. This thesis will show that such correction is not needed if one uses the power balance method.

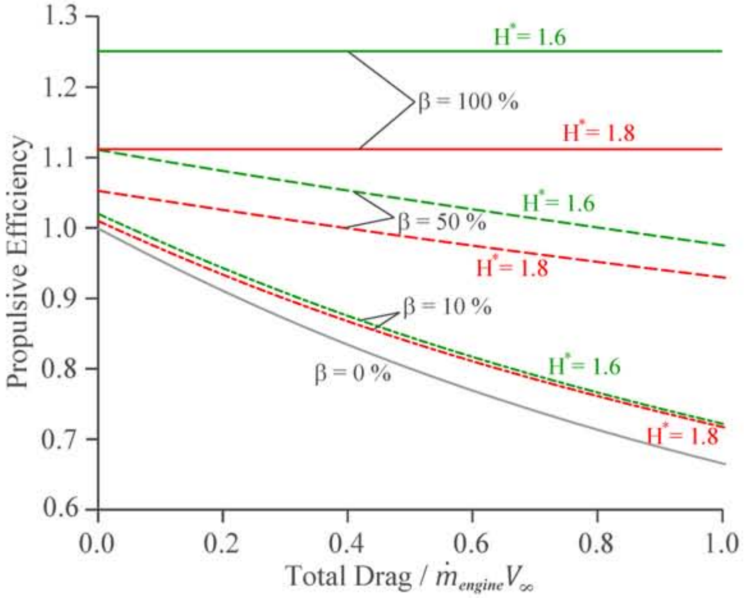

Figure 2-4: Propulsive efficiency as a function of BLI, normalized drag and H^*.(Adapted from [35]) Propulsive efficiency increases with β. Gain in propulsive efficiency with β is larger for larger normalized drag and lower H^*.

Chapter 3

Evaluation of Boundary Layer Mechanical Energy Loss

This chapter describes the evaluation of mechanical energy losses generated inside the boundary layer. The power balance equation derived by Drela [9] is extended based on the boundary layer integral equations and used to demonstrate the advantages of the power balance method for aerodynamic performance evaluation. The main advantages of this method come from a single observation: pressure forces do not explicitly affect the mechanical loss generation. The boundary layer mechanical energy equation is applied to a 2D fuselage section of the D8.5 aircraft to illustrate the evolution of various mechanical loss terms. A correlation for the flat plate skin friction and dissipation coefficient is also derived from boundary layer models and compared against experimental data.

Section 3.1 describes the key concepts and advantages of the power balance method. Section 3.2 presents the derivation of the mechanical power integral defect equation, and extends it to include the contribution of "baroclinic power[1]" for adiabatic compressible flow. Section 3.3 compares the boundary layer mechanical energy and momentum defect equations to highlight the differences. Section 3.4 derives a correlation for the flat plate skin friction and dissipation coefficients from the boundary layer equations. Section 3.5 summarizes the chapter findings.

---

[1] Buoyancy effect, described in Eq. 3.35 in Section 3.2.2.

3.1 Loss Generation and Pressure Forces

Eq. 3.1 is the power balance equation for the mechanical loss of an isolated airframe, without propulsor, in steady level flight:

$$\begin{aligned}\Phi^*_{airframe} &= \left(\dot{E}_v + \Phi_{vortex}\right) + \left(\dot{E}_w + \Phi_{wave}\right) \\ &+ \left(\dot{E}_{a,wake} + \dot{E}_{p,wake} + \Phi_{wake} - P_{V,wake}\right) \\ &+ \left(\Phi_{surf} - P_{V,surf}\right) \\ &= \Phi^*_{vortex} + \Phi^*_{wave} + \Phi^*_{surf} + \Phi^*_{wake}.\end{aligned} \tag{3.1}$$

Note that no propulsor related terms such as net propulsor shaft power (P_S), net propulsor mechanical energy flow rate (P_K), volumetric mechanical power ($P_{V,prop}$), and propulsor dissipation $\left(\Phi^*_{prop}\right)$ are included in this analysis.

The corresponding equation for airframe drag is:

$$D_{airframe} = D_i + D_w + D_p + F_{field}, \tag{3.2}$$

which consists of induced drag (D_i), wave drag (D_w), profile drag[2] (D_p) and force due to "potential" (or "field") effect (F_{field}). F_{field} is non-zero when the airframe is influenced by nearby bodies. Vortex loss (Φ^*_{vortex}) and induced drag (D_i) are generated by the velocity induced by the trailing vortices from a lifting body. They are related by

$$\Phi^*_{vortex} = D_i V_\infty. \tag{3.3}$$

In aircraft conceptual design, the induced drag (D_i) is evaluated using an assumed span efficiency, plus vortex-lattice or panel methods, together with a Trefftz plane analysis. The same can be used for the vortex loss (Φ^*_{vortex}).

Wave loss (Φ^*_{wave}) and wave drag (D_w) represent the effect of shock generated in the flow field. They are related to each other as follows:

$$\Phi^*_{wave} = D_w V_\infty. \tag{3.4}$$

For subsonic freestreams, D_w is associated with local shocks. which can be captured using

---

[2] which includes skin friction and pressure drag

Full-Potential, Euler or Navier-Stokes equations. For supersonic freestreams, D_w also includes the loss of the oblique wave system, which can be estimated via methods based on the linear Prantl-Glauert equation.

The evaluation of the remaining terms, losses and forces associated with the boundary layer viscous effects (Φ^*_{surf}, Φ^*_{wake}, and D_p) and "potential" effect (F_{field}) are different between the power balance method and the momentum balance method. The mechanical energy losses (Φ^*_{surf} and Φ^*_{wake}) are affected by the dissipation and the "baroclinic power", but are not directly affected by the pressure force on the body surface. The drag, on the other hand, is affected by the pressure. The difference between mechanical energy loss and drag gives the power balance method an important advantage in the estimation of the aerodynamic performance.

The independence of loss and pressure force can be seen as follows. From the first law of thermodynamics, a differential form of the total energy equation for an adiabatic flow can be derived:

$$\rho \frac{D}{Dt}\left[\left(e + \frac{1}{2}V^2\right)\right] = -\nabla \cdot \boldsymbol{q} - \nabla \cdot (p\boldsymbol{V}) + \nabla \cdot \left(\overline{\overline{\tau}} \cdot \boldsymbol{V}\right), \tag{3.5}$$

where e is the internal energy, $\boldsymbol{q}$ the heat flux vector, and $\overline{\overline{\tau}}$ the shear stress tensor. Body forces and volumetric heat sources are assumed to be zero in Eq. 3.5. Eq. 3.5 can be written in terms of the specific total enthalpy,

$$h_t = e + \frac{1}{2}V^2 + \frac{p}{\rho}, \tag{3.6}$$

$$\rho \frac{D}{Dt}(h_t) = -\nabla \cdot \boldsymbol{q} + \frac{\partial p}{\partial t} + \nabla \cdot \left(\overline{\overline{\tau}} \cdot \boldsymbol{V}\right). \tag{3.7}$$

Eq. 3.7 indicates that for a stationary surface, aside from direct heating, only unsteadiness in the pressure field can contribute to the increase in total enthalpy of the flow interior; the viscous terms can only redistribute the stagnation enthalpy. The mechanical energy equation is

$$\rho \frac{D}{Dt}\left[\frac{1}{2}V^2\right] = -\nabla p \cdot \boldsymbol{V} + \left(\nabla \cdot \overline{\overline{\tau}}\right) \cdot \boldsymbol{V}. \tag{3.8}$$

Subtracting Eq. 3.8 from Eq. 3.7 gives an equation for the static enthalpy:

$$\rho \frac{Dh}{Dt} = -\nabla \cdot \boldsymbol{q} + \frac{Dp}{Dt} + \Phi, \tag{3.9}$$

where $\Phi \equiv \left(\bar{\bar{\tau}} \cdot \nabla\right) \cdot \boldsymbol{V}$. The Gibbs equation can now be used to express the change in entropy,

$$\rho T \frac{Ds}{Dt} = -\nabla \cdot \boldsymbol{q} + \Phi, \tag{3.10}$$

which shows that the entropy is affected by viscous stresses and heat flux, and not by the pressure forces.

The main advantages of the power balance method are related closely to the independence of loss generation from pressure forces. These advantages are elaborated further in this chapter.

3.2 Integral Mechanical Energy Defect Equation

This section presents a derivation of the integral mechanical energy defect equation, used in the evaluation of the mechanical losses of aerodynamic bodies. Eq. 3.1 can be simplified by splitting the real viscous flow (RVF) into two flow fields as in Figure 3-1:

1. The equivalent inviscid flow (EIF). This flow is inviscid in all domains, and is the irrotational continuation of the outer RVF into the shear layer.
2. The boundary layer defect flow. This is the difference between the EIF and the real viscous flow (RVF). The boundary layer defect flow is zero outside the boundary layer, where RVF and EIF are equal.

In defining the EIF, a mass flux distribution ("wall transpiration") is imposed across the wall of the body to generate the same flow field outside the boundary layer as the real flow, as in Figure 3-2. Using this concept, the power consumption terms can be separated into terms that are present only in EIF and those that are only present in the boundary layer defect flow.

$$\Phi^*_{airframe} = \Phi^*_{EIF} + \Phi^*_{p}. \tag{3.11}$$

In the EIF, the only terms present are vortex and wave related terms:

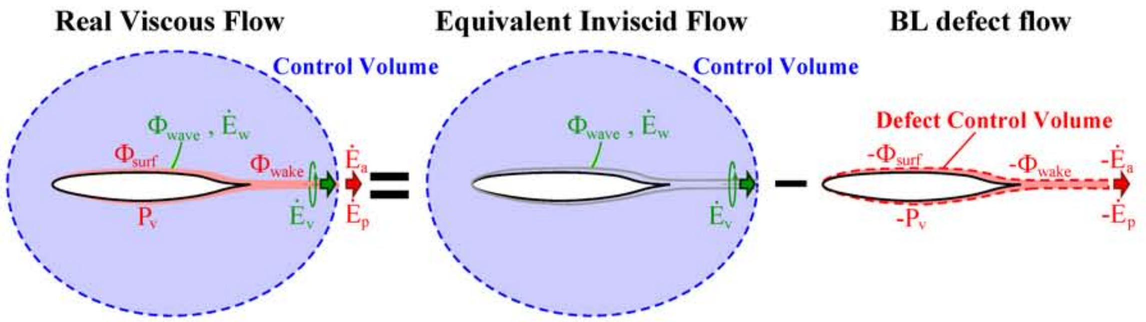

Figure 3-1: RVF, EIF and boundary layer defect flow. The analysis can be simplified by dividing the RVF into the two flow fields: i) EIF which is inviscid in all domains, and ii) the BL defect flow which is confined to the region inside the boundary layer.

$$\begin{aligned}\Phi^*_{EIF} &= \left(\dot{E}_v + \Phi_{vortex}\right) + \left(\dot{E}_w + \Phi_{wave}\right) \\ &= \Phi^*_{vortex} + \Phi^*_{wave}.\end{aligned} \tag{3.12}$$

The remaining terms make up the profile mechanical losses, which are

$$\begin{aligned}\Phi^*_p &= \left(\dot{E}_{a,wake} + \dot{E}_{p,wake} + \Phi_{wake} - P_{V,wake}\right) \\ &+ \left(\Phi_{surf} - P_{V,surf}\right) \\ &= \Phi^*_{surf} + \Phi^*_{wake}.\end{aligned} \tag{3.13}$$

The introduction of the boundary layer energy defect equation reduces the evaluation of these profile mechanical loss terms to a surface integral over the boundary layers, simplifying the calculation.

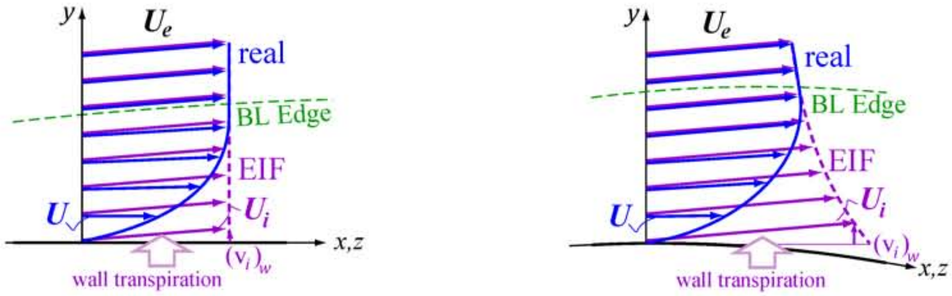

Figure 3-2: Difference between EIF and RVF. To obtain inviscid irrotational flow all the way to the wall, an artificial "wall transpiration" needs to be defined.

3.2.1 Boundary Layer Quantities

Density defect:

$$\mathrm{m} \equiv \rho_e \delta_\rho = \int_{y_w}^{y_e} (\rho_i - \rho)\, dy \tag{3.14}$$

Mass defect:

$$\mathbf{M} \equiv \rho_e U_e \boldsymbol{\delta^*} = \int_{y_w}^{y_e} (\rho_i \boldsymbol{U_i} - \rho \boldsymbol{U})\, dy \tag{3.15}$$

x-momentum defect:

$$\mathbf{P}_{\boldsymbol{x}} \equiv \rho_e U_e^2 \boldsymbol{\theta_x} = \int_{y_w}^{y_e} (u_i - u)\, \rho \boldsymbol{U}\, dy \tag{3.16}$$

z-momentum defect:

$$\mathbf{P}_{\boldsymbol{z}} \equiv \rho_e U_e^2 \boldsymbol{\theta_z} = \int_{y_w}^{y_e} (w_i - w)\, \rho \boldsymbol{U}\, dy \tag{3.17}$$

Kinetic energy defect:

$$\mathbf{K} \equiv \frac{1}{2} \rho_e U_e^3 \boldsymbol{\theta^*} = \frac{1}{2} \int_{y_w}^{y_e} \left(U_i^2 - U\right) \rho \boldsymbol{U}\, dy \tag{3.18}$$

Potential mixing dissipation:

$$\mathbf{E} \equiv \frac{1}{2} \rho_e U_e^3 \boldsymbol{\delta_k} = \frac{1}{2} \int_{y_w}^{y_e} (\boldsymbol{U_i} - \boldsymbol{U})^2\, \rho \boldsymbol{U}\, dy \tag{3.19}$$

Density-flux defect:

$$\mathbf{D} \equiv \rho_e U_e \boldsymbol{\delta^{**}} = \int_{y_w}^{y_e} (\rho_i - \rho)\, \boldsymbol{U}\, dy \tag{3.20}$$

Dissipation integral:

$$\mathcal{D} \equiv \int_{y_w}^{y_e} \left(\bar{\bar{\tau}} \cdot \nabla\right) \cdot \boldsymbol{V}\, dy \approx \int_{y_w}^{y_e} \left(\bar{\bar{\tau}} \cdot \nabla\right) \cdot \boldsymbol{U}\, dy \tag{3.21}$$

since the y component of $\bar{\bar{\tau}} \cdot \hat{n}$ is negligible.

$$c_{\mathcal{D}} \equiv \frac{\mathcal{D}}{\rho_e U_e^3} \tag{3.22}$$

3.2.2 Derivation of Integral Mechanical Energy Defect Equation

This section presents the derivation of the integral mechanical energy defect equation, which describes the loss generation inside the boundary layer. This equation is an important building block of this work and will be refered to multiple times throughout the thesis.

The starting point is the mechanical energy steady boundary-layer-defect equation in differential form,

$$\bar{\nabla} \cdot \mathbf{K} + \mathbf{D} \cdot \bar{\nabla} \frac{1}{2} U_e^2 = \mathcal{D} + (\boldsymbol{U} \cdot \vec{\tau})_w \tag{3.23}$$

applies to a solid wall and the dividing surface between the wakes generated from the upper and lower body surfaces, where the normal velocity on the surface is zero ($v_w = 0$). $\mathbf{K}$ is the kinetic energy defect (Eq. 3.18), $\mathbf{D}$ is the density flux defect (Eq. 3.20) and $\mathcal{D}$ is the dissipation integral (Eq. 3.21). Eq. 3.23 assumes no body forces. Detailed derivation of the differential form of the mechanical energy boundary layer defect equation is shown in Appendix A.

The integral form of Eq. 3.23 is

$$\begin{aligned} \Phi + \iint (\boldsymbol{U} \cdot \vec{\tau})_w \, d\mathcal{S} &= \iint \bar{\nabla} \cdot \mathbf{K} + \mathbf{D} \cdot \bar{\nabla} \frac{1}{2} U_e^2 \, d\mathcal{S} \qquad (3.24) \\ &= \oint \mathbf{K} \cdot \hat{n} \, d\ell + \iint \mathbf{D} \cdot \bar{\nabla} \frac{1}{2} U_e^2 \, d\mathcal{S}. \\ \Phi &\equiv \iint \mathcal{D} \, d\mathcal{S} \qquad (3.25) \end{aligned}$$

The surface and wake mechanical losses are calculated by evaluating Eq. 3.24 over the integration surfaces shown in Figure 3-3. These integration surfaces capture the upper and lower surface of the wing and the wake. Applying Eq. 3.24 over the control surface gives:

$$\begin{aligned} \int_{out} \mathbf{K} \cdot \hat{n} \, d\ell_{out} + 0 &= \Phi_p \qquad (3.26) \\ &- \iint \mathbf{D} \cdot \bar{\nabla} \frac{1}{2} U_e^2 \, d\mathcal{S}, \end{aligned}$$

where $()_{out}$ represents quantity evaluated at the outlet boundary of the control volume. Based on the choice of the integration surfaces shown in Figure 3-3, $\int \mathbf{K} \cdot \hat{n} \, d\ell = 0$ at the

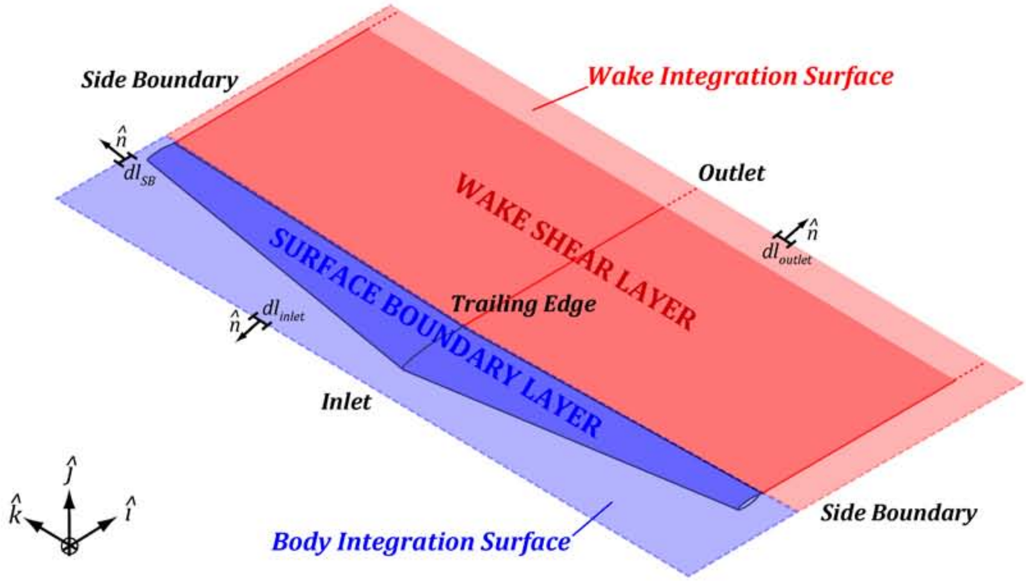

Figure 3-3: Integration surface used in analysis. The surfaces are split between the surface boundary layer and the wake shear layer, separated by the trailing edge (TE) boundary.

inlet and side boundaries, since these are in the inviscid domain.

Breaking down the terms in Eq. 3.26, the following expression for the defect in the kinetic energy flux across the control volume can be obtained:

$$-\Delta\dot{\mathcal{E}}_{out} = \Phi_p - \Pi_v. \tag{3.27}$$

where

$$-\Delta\dot{\mathcal{E}}_{out} \equiv \int_{out} \mathbf{K}\cdot\hat{n}\,d\ell_{out}. \tag{3.28}$$

For an isolated aerodynamic body without a propulsor, $\Delta\dot{\mathcal{E}}_{out}$ is negative. Its magnitude represents the net mechanical energy lost over the surface boundary layer and wake shear layer:

$$\Phi_p^* = -\Delta\dot{\mathcal{E}}_{out}. \tag{3.29}$$

Φ_p^* can be split into two components,

$$\Phi_p^* = \Phi_{surf}^* + \Phi_{wake}^*, \tag{3.30}$$

where

$$\Phi^*_{surf} = -\Delta\dot{\mathcal{E}}_{TE} = \int \mathbf{K} \cdot \hat{n}\, d\ell_{TE}, \tag{3.31}$$

$$\Phi^*_{wake} = \Delta\dot{\mathcal{E}}_{TE} - \Delta\dot{\mathcal{E}}_{out} = \int \mathbf{K} \cdot \hat{n}\, d\ell_{out} - \int \mathbf{K} \cdot \hat{n}\, d\ell_{TE}. \tag{3.32}$$

Φ^*_{surf} represent the mechanical loss generated over the surface of the airfoil, where the flow is brought to halt on the wall surface of the airfoil. Φ^*_{wake} represent the mechanical loss generated at the wake downstream of the airfoil, where the velocity deficit in the wake is mixed out to freestream condition. The distinction between Φ^*_{surf} and Φ^*_{wake} is important when assessing the benefit of BLI, which will be elaborated in Chapter 6.

The profile mechanical loss is generated through two different physical mechanisms, represented by the two terms in the RHS of Eq. 3.27. The first term represents the profile dissipation in the boundary and shear layer.

$$\Phi_p = \iint \mathcal{D}\, d\mathcal{S} \tag{3.33}$$

$$= \iint \rho_e U_e^3 c_{\mathcal{D}}\, d\mathcal{S}. \tag{3.34}$$

The second term represents the change in mechanical energy flux due to the pressure gradient acting on the boundary layer flow which has different density than in the EIF. This is referred to as "baroclinic power", defined as

$$\Pi_V = \iint \mathbf{D} \cdot \bar{\nabla} \frac{1}{2} U_e^2\, d\mathcal{S}. \tag{3.35}$$

While this term This quantity is zero when the flow is incompressible ($\mathbf{D} = 0$), yielding

$$\Phi^*_p = \Phi_p. \tag{3.36}$$

Eq. 3.36 shows that in incompressible flow the mechanical energy loss in the boundary layer is purely due to viscous dissipation. This result is useful in estimation of the airframe losses. In general,

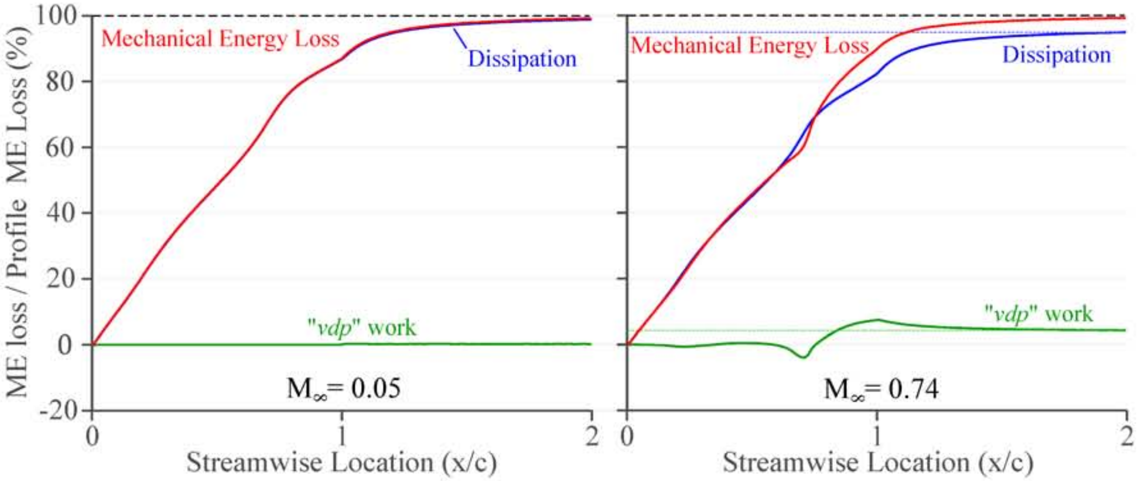

Figure 3-4: Evolution of mechanical energy loss terms for the D8.5 Fuselage at $M_\infty = 0.05$ (left) and $M_\infty = 0.74$ (right). While there is no contribution of pressure term in incompressible flow, the pressure term makes up for approximately 8% of the total mechanical energy loss at $M_\infty = 0.74$.

$$\begin{aligned} \Phi_p^* &= \Phi_p - \Pi_V, && (3.37) \\ &= \iint [\rho_e U_e^3 c_{\mathcal{D}} - \mathbf{D} \cdot \bar{\nabla} \frac{1}{2} U_e^2] \, d\mathcal{S}. && (3.38) \end{aligned}$$

Eq. 3.36 only holds when there is no pressure gradient. In an accelerating flow, Π_V (or "baroclinic power") is positive and $\Phi_p^* < \Phi_p$, while $\Phi_p^* > \Phi_p$ for decelerating flow. Figure 3-4 shows the evolution of the mechanical energy loss terms over an airfoil section with the same thickness distribution as the D8.5 aircraft fuselage section [14]. The figure on the left shows the evolution for a freestream Mach number of 0.05 (incompressible flow) and the figure on the right shows the evolution at the aircraft cruise Mach number of $M_\infty = 0.74$, both calculated using MSES[3] [8]. For incompressible flow the mechanical energy loss is equal to the dissipation, but there is a contribution of the baroclinic power at Mach number 0.74. The baroclinic power contribution can be approximated accurately using a function of edge velocity, as presented in the following section.

---

[3] MSES is a 2D code based on interacting boundary layer theory, with accuracy validated up to transonic speeds [11]. Its validation is presented in Appendix D.

3.2.3 Approximated Energy Defect Equation for Compressible Flow

As in Figure 3-4, the contribution of baroclinic power to the mechanical energy balance cannot be neglected at high[4] Mach number. Calculation of the baroclinic power term can be numerically challenging, as it involves the evaluation of the velocity gradient. The evaluation can be simplified, however, using the following assumptions:

1. Adiabatic wall;
2. Near-unity Prandtl number, $\mathrm{Pr} \simeq 1$; and
3. Small flow acceleration, $\frac{d|\boldsymbol{u_e}|}{ds}\frac{c}{V_\infty} \ll 1$.

Assumption 1 is valid for most aircraft which have insulated surfaces. Assumption 2 can be used because for turbulent flow, $\mathrm{Pr} \approx 0.85$ and for laminar flow, $\mathrm{Pr} \approx 0.7$. The validity of assumption 3 is discussed later in this section.

With these three assumptions, the boundary layer density profile can be expressed using the Crocco-Busemann enthalpy profile:

$$\frac{\rho_e}{\rho} = \frac{h}{h_e} \simeq 1 + \mathcal{R}\left(1 - \frac{U^2}{U_e^2}\right), \tag{3.39}$$

where $\mathcal{R}$ is the temperature recovery parameter, which is a function of the temperature recovery factor (r) and boundary layer edge Mach number (M_e):

$$\mathcal{R} \equiv r\frac{\gamma-1}{2}M_e^2, \ \left(r \simeq \mathrm{Pr}^{1/2}\right). \tag{3.40}$$

The density profile approximation in Eq. 3.39 is exact for flow with $\mathrm{Pr} = 1$ and $\frac{d|\boldsymbol{u_e}|}{ds}\frac{c}{V_\infty} = 0$. Using Eq. 3.39, an approximation for the density thickness ($\boldsymbol{\delta}^{**}$) is:

$$\begin{aligned}
\boldsymbol{\delta}^{**} &\equiv \int_{y_w}^{y_e}\left(\frac{\rho_i}{\rho} - 1\right)\frac{\rho\boldsymbol{U}}{\rho_e U_e}\,dy && (3.41)\\
&\approx \mathcal{R}\int_{y_w}^{y_e}\left(1 - \frac{U^2}{U_e^2}\right)\frac{\rho\boldsymbol{U}}{\rho_e U_e}\,dy \\
&= \mathcal{R}\boldsymbol{\theta}^{*}. && (3.42)
\end{aligned}$$

---

[4] $M_\infty > 0.74$ for the D8.5 aircraft fuselage. Most current transport aircraft operate roughly between $M_\infty = 0.7$ and 0.85

Substituting Eq. 3.42 into Eq. 3.23, gives a modified expression of the boundary layer mechanical energy equation:

$$\bar{\nabla} \cdot \mathbf{K} + r\frac{\gamma - 1}{a_e^2}\mathbf{K} \cdot \bar{\nabla}\frac{1}{2}U_e^2 = \mathcal{D}, \tag{3.43}$$

where a_e is the speed of sound at the edge of the boundary layer.

We now define a function $\mathcal{F}$ such that:

$$\mathcal{F}\left[\bar{\nabla} \cdot \mathbf{K} + r\frac{\gamma - 1}{a_e^2}\mathbf{K} \cdot \bar{\nabla}\frac{1}{2}U_e^2\right] = \bar{\nabla} \cdot \left(\mathcal{F}\mathbf{K}\right). \tag{3.44}$$

If such a function exists, Eq. 3.43 can be reduced to a perfect differential. Matching terms from Eq. 3.44, $\mathcal{F}$ obeys the following differential equation:

$$\bar{\nabla}\mathcal{F} = r\frac{\gamma - 1}{a_e^2}\mathcal{F}\bar{\nabla}\frac{1}{2}U_e^2. \tag{3.45}$$

Since $a_e^2 = (\gamma - 1)\left(h_{T\infty} - \frac{1}{2}q_e^2\right)$,

$$\bar{\nabla}\mathcal{F} = \mathcal{F}\frac{r}{\left(h_{t\infty} - \frac{1}{2}U_e^2\right)}\bar{\nabla}\frac{1}{2}qU_e^2. \tag{3.46}$$

Solving Eq. 3.46 for $\mathcal{F}$ gives:

$$\mathcal{F} = C\left[h_{t\infty}\left(1 + \frac{\gamma - 1}{2}M_e^2\right)^{-1}\right]^{-r}. \tag{3.47}$$

$\mathcal{F}$ satisfies Eq. 3.45 for an arbitrary choice of C. If $C = h_{t\infty}^r$, $\mathcal{F}$ can be non-dimensionalized as

$$\mathcal{F} = \left(1 + \frac{\gamma - 1}{2}M_e^2\right)^r. \tag{3.48}$$

Applying Eq. 3.48, the boundary layer mechanical energy defect equation in Eq. 3.23 can be expressed as:

$$\bar{\nabla} \cdot \left[\left(1 + \frac{\gamma - 1}{2}M_e^2\right)^r \mathbf{K}\right] \simeq \left(1 + \frac{\gamma - 1}{2}M_e^2\right)^r \mathcal{D}. \tag{3.49}$$

Integrating Eq. 3.49 over the integration surface in Figure 3-3,

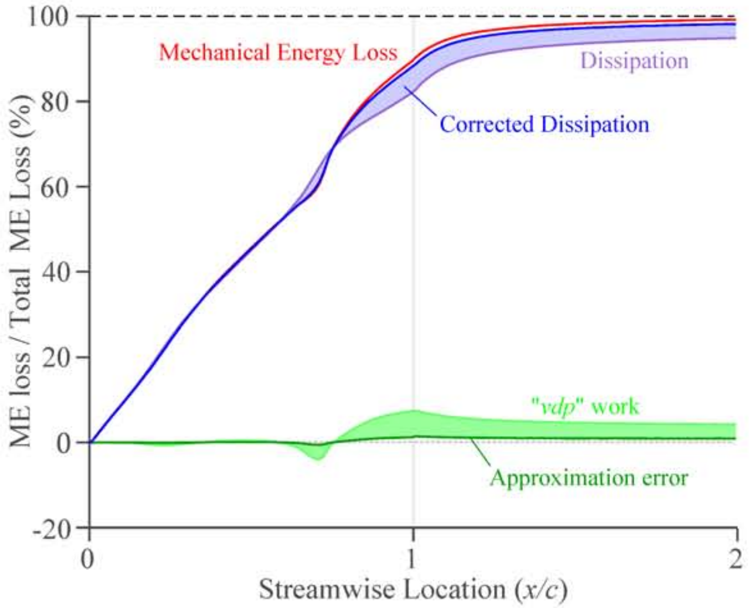

Figure 3-5: Accuracy of approximated mechanical energy defect equation (Eq. 3.50) for D8.5 Fuselage at $M_\infty = 0.74$. Maximum error between mechanical energy loss and corrected dissipation is less than 1%.

$$\Phi_p^* \approx \frac{\iint \rho_e U_e^3 \left(1+\frac{\gamma-1}{2}M_e^2\right)^r c_{\mathcal{D}}\, d\mathcal{S}}{\left(1+\frac{\gamma-1}{2}M_e^2\right)^r\Big|_{out}}. \tag{3.50}$$

With Eq. 3.50, the evaluation of profile mechanical loss is reduced to a function of the dissipation coefficient $c_{\mathcal{D}}$, the edge velocity U_e and the Mach number M_e. For low Mach number flow, Eq. 3.50 reduces to

$$\Phi_p^* = \Phi_p. \tag{3.51}$$

Figure 3-5 compares the mechanical loss terms from the actual mechanical energy equation, Eq. 3.38, and the approximated mechanical energy equation, Eq. 3.50, for the D8.5 fuselage at $M_\infty = 0.74$. The D8.5 fuselage airfoil has a chord Reynolds number of 1.2×10^8, and the boundary layer is taken as turbulent over the entire surface. For this airfoil, the approximated mechanical energy equation captures the contribution of the baroclinic power well, and the discrepancy between the mechanical energy loss curve (Eq. 3.38, red) the approximate mechanical loss curve (Eq. 3.50, blue) are within 1%. The result is encouraging, as the primary application of this methodology is for the estimation of aircraft performance at high Reynolds number $10^7 \sim 10^8$ turbulent flow at M_∞ between 0.7 to 0.85. The approximation of baroclinic power becomes inaccurate, however, when the boundary layer goes through a large pressure gradient such as in shocks and actuator disks, as will be quantified in Chapter 4 and 5. In summary, the introduction of the approximated mechanical energy defect equation can provide a powerful tool for evaluation of airframe losses. It is based on boundary layer edge velocity, Mach number and dissipation only, simplifying the required calculations as demonstrated through the examples in Chapters 4, 5 and 6.

3.3 Utilities of Mechanical Energy Defect Equation

This section describes the main advantages of using the mechanical energy defect equation, which come from two characteristics: 1) the dissipation coefficient is less sensitive to changes in boundary layer shape parameter than the skin friction coefficient (elaborated in Section 3.3.1), and 2) the kinetic energy thickness is a global quantity which is only weakly affected by the local pressure field (described in Section 3.3.2).

3.3.1 Behavior of Dissipation and Skin Friction Coefficients

The behavior of the dissipation coefficient is less sensitive to pressure gradients and to the boundary layer shape parameter H than is the skin friction coefficient. Figure 3-6 shows the dependence of $c_{\mathcal{D}}$ and ${}^{c_f}\!/_2$ on the boundary layer shape parameter (H) for laminar and turbulent flows [9]. H is a measure of the state of the boundary layer, which indicates how close the boundary layer is to separation. For laminar flow, $Re_\theta c_{\mathcal{D}}$ and $Re_\theta {}^{c_f}\!/_2$ are both independent of Re_θ which indicates that $c_{\mathcal{D}}$ and ${}^{c_f}\!/_2$ both scale as ${}^1\!/_{Re_\theta}$. $c_{\mathcal{D}}$ is nearly independent of H, while ${}^{c_f}\!/_2$ depends strongly on H, and goes to zero as the flow approaches separation ($H \to 4$).

For turbulent flow, the dependence of both $c_{\mathcal{D}}$ and ${}^{c_f}\!/_2$ has a weaker dependence on Re_θ. $c_{\mathcal{D}}$ has a minimum value which corresponds to a constant pressure flow, and increases for both accelerating and decelerating flow. As the flow nears separation, ${}^{c_f}\!/_2$ asymptotes to zero, whereas $c_{\mathcal{D}}$ increases monotonically. Even in separated flow $c_{\mathcal{D}}$ can be used to quantify the losses in separated flow, while ${}^{c_f}\!/_2$ is not useful in such circumstances.

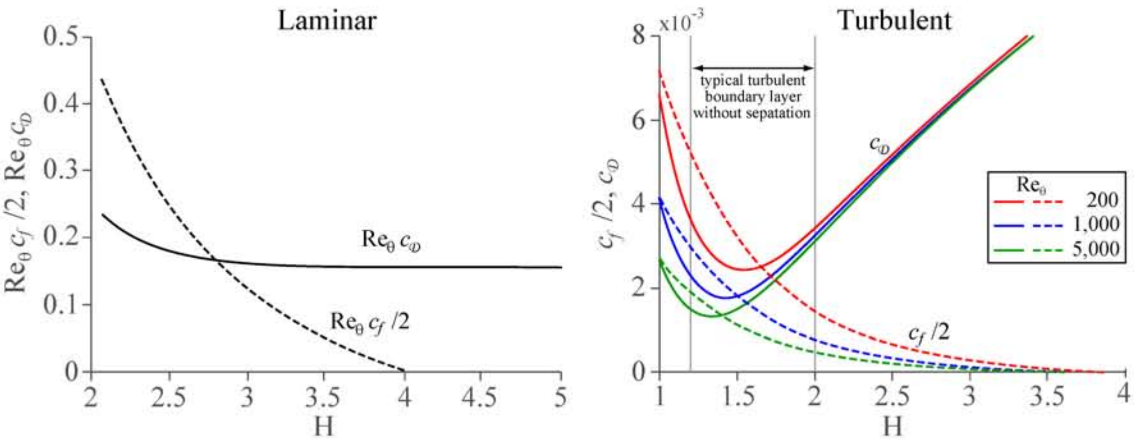

Figure 3-6: Dependence of $c_\mathcal{D}$ and c_f on H for laminar (left) and turbulent (right) flow. (Adapted from [9])

3.3.2 Comparison of Mechanical Energy and Momentum Defect Equations

the profile drag[5] on an aerodynamic body can be obtained by applying the x- and z-momentum boundary layer defect equation

$$x: \bar{\nabla}\cdot\mathbf{P_x} + \mathbf{M}\cdot\bar{\nabla}u_e = \tau_{x_w} \tag{3.52}$$

$$z: \bar{\nabla}\cdot\mathbf{P_z} + \mathbf{M}\cdot\bar{\nabla}w_e = \tau_{z_w} \tag{3.53}$$

($\mathbf{P_x}$ and $\mathbf{P_z}$ is the x and z momentum defect (Eq. 3.16 and 3.17) respectively) to the integration surfaces defined in Figure 3-3,

$$\begin{aligned} \boldsymbol{D_p} &= \iint \frac{1}{2}\rho_e U_e^2 \boldsymbol{c_f}\, d\mathcal{S}_{BL} \\ &- \iint \left(\mathbf{M}\cdot\bar{\nabla}\right)\boldsymbol{U_e}\, d\mathcal{S}_{BL}. \end{aligned} \tag{3.54}$$

In Eq. 3.54,

$$\boldsymbol{c_f} \equiv \frac{\tau_{x_w}\hat{\imath} + \tau_{z_w}\hat{k}}{{}^1\!/_2\rho_e U_e^2}. \tag{3.55}$$

---

[5] For an isolated aerodynamic body, $\boldsymbol{D_p}\cdot\boldsymbol{V_\infty} = \Phi_p^*$.

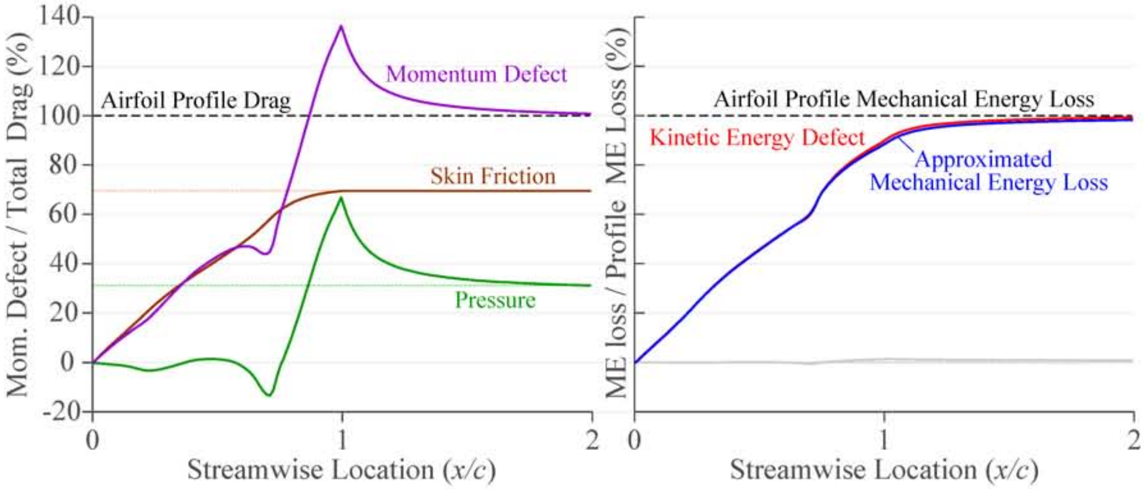

Figure 3-7: Evolution of momentum (left) and mechanical energy (right) defect over the D8.5 fuselage at $M_\infty = 0.74$. While momentum defect is affected by the local pressure term, mechancial energy loss is not.

The first RHS term in Eq. 3.54 represents skin friction drag, and the second represents pressure drag. Figure 3-7 shows the evolution of momentum defect (left) and mechanical energy defect (right) terms for the D8.5 fuselage section at $M_\infty = 0.74$. In the left hand figure, the momentum defect is broken into terms due to skin friction (brown) and pressure (green). In the right hand figure, the kinetic energy defect is plotted with the approximate mechanical loss (blue) derived in Section 3.2.3.

In Figure 3-7, the pressure term makes up to 50% of the local momentum defect. For a flat plate, on the other hand, the pressure term is zero, and the drag force equals the skin friction force applied to the body. The point is that the relative magnitude of the pressure term depends on the geometry of the aerodynamic body. This is why airfoil drag correlations rely heavily on empiricism to capture this pressure term.

The local value of the momentum defect is affected by the upstream pressure distribution, and does not represent the actual force acting on a part of the body. The kinetic energy defect, on the other hand, is a global quantity representing the mechanical energy loss generated up to the evaluation point. The contribution of mechanical losses can therefore be split into multiple sections on the aerodynamic body —- an aspect that is important in assessing the performance of an integrated configuration (such as a BLI configuration) where the boundary layer is ingested at non-ambient pressure. This will be demonstrated in Chapters 5 and 6.

3.3.3 Summary

Two advantages of the mechanical energy defect equations described above allow the following:

- Evaluating the aerodynamic body performance using a global quantity which is only weakly affected by the local pressure field. In adiabatic flow with no strong shocks, the dependence of the local pressure field can be separated from the calculation.
- Quantifying the increase in drag or dissipation due to potential-flow interactions between components, which historically has been viewed an "interference" drag.
- Expressing the boundary layer mechanical energy loss using an explicit function of edge velocity and dissipation coefficient.
- Calculating aerodynamic performance using the dissipation coefficient instead of the skin friction coefficient. The former varies much less than the former in pressure gradients and therefore gives more accurate estimates of the performance.

These benefits of the power balance method are displayed in three different applications: 1) derivation of analytial expression of profile drag estimates for conceptual design applications (Chapter 4), 2) aerodynamic performance estimation for three basic integrated configurations (Chapter 5), and 3) performance quantification of a hybrid wing body (HWB) with BLI propulsion system (Chapter 6).

3.4 Flat Plate Skin Friction and Dissipation Correlation

This section focuses on deriving the correlation of dissipation coefficients along with those for the skin friction coefficient, for laminar and turbulent flow, which are used in the preliminary performance calculation of aircraft configurations employing the wetted area method.

3.4.1 Laminar Boundary Layer

The laminar flat plate dissipation and skin friction coefficient can be obtained using the Blasius boundary layer equation, which yields

Flat plate local skin friction coefficient $c_{f_{FP}}$:

$$c_{f_{FP}} = \frac{0.664}{\sqrt{Re_x}}. \tag{3.56}$$

Flat plate local dissipation coefficient $c_{\mathcal{D}_{FP}}$:

$$c_{\mathcal{D}_{FP}} = \frac{0.261}{\sqrt{Re_x}}. \tag{3.57}$$

The skin friction coefficient averaged for a flat plate of length c is

$$C_{f_{FP}} \equiv \frac{1}{c}\int_0^c c_{f_0} dx. \tag{3.58}$$

The flat plate surface dissipation coefficient averaged for a flat plate of length c is

$$C_{\mathcal{D}_{surf_{FP}}} \equiv \frac{1}{c}\int_0^c c_{\mathcal{D}_0} dx. \tag{3.59}$$

The numerical expressions are:

Flat plate skin friction drag coefficient $C_{f_{FP}}$:

$$C_{f_{FP}} = \frac{1.328}{\sqrt{Re_c}}. \tag{3.60}$$

Flat plate surface dissipation coefficient $C_{\mathcal{D}_{FP}surf}$:

$$C_{\mathcal{D}_{surf_{FP}}} = \frac{0.522}{\sqrt{Re_c}}. \tag{3.61}$$

From Eq. 3.60 and Eq. 3.61, the ratio of wake to profile boundary layer dissipation are:

$$\begin{aligned} \varphi_w \equiv \frac{\Phi^*_{wake}}{\Phi^*_{BL}} &= 1 - 2\frac{C_{\mathcal{D}_{FP}surf}}{C_{f_{FP}}} \\ &= 0.214. \end{aligned} \tag{3.62}$$

For a laminar flat plate with trailing wake, 21% of the profile mechanical loss comes from wake dissipation. This ratio is independent of Reynolds number.

3.4.2 Turbulent Boundary Layer

For the derivation of the skin friction and dissipation coefficient in a turbulent boundary layer, the evolution of skin friction and dissipation were calculated by numerically integrating the Coles turbulent boundary layer profile [2] with constant edge velocity, using the G-β[6] locus of Clauser [1] as closure relations. Using this procedure, the distribution of the local skin friction and dissipation coefficients are obtained as a function of Reynolds number based on x (Re_x) and normalized wall effective roughness height (k^+), defined as

$$k^+ \equiv \frac{\rho u_\tau k}{\mu}, \tag{3.63}$$

where k is the wall roughness height and $u_\tau \equiv \sqrt{\tau_w/\rho}$. The detailed formulations of the turbulent boundary layer calculation are presented in Appendix B. Curves were fit to the numerically calculated local skin friction and dissipation resulting in correlations for the local skin friction and dissipation coefficient as:

$$c_{f_{FP}} = \frac{0.48}{\left[\ln\left(0.1729\frac{Re_x}{(1+0.3k^+)}\right)\right]^2}, \tag{3.64}$$

and

$$c_{\mathcal{D}_{FP}} = \frac{0.24}{\left[\ln\left(0.3833\frac{Re_x}{(1+0.3k^+)}\right)\right]^2}, \tag{3.65}$$

For integrated quantities such as skin friction drag coefficient $C_{f_{FP}}$ and surface dissipation coefficient $C_{\mathcal{D}_{FP}surf}$, it is useful to write the correlation in terms of wall roughness height Reynolds number $Re_k \equiv \rho_\infty V_\infty k/\mu$ and flat plate chord Reynolds number Re_c:

$$C_{f_{FP}} = \frac{0.48}{\left[\ln\left(0.0613\frac{Re_c}{(1+0.0123Re_k)}\right)\right]^2} \tag{3.66}$$

$$C_{\mathcal{D}_{surf_{FP}}} = \frac{0.24}{\left[\ln\left(0.1359\frac{Re_c}{(1+0.0123Re_k)}\right)\right]^2} \tag{3.67}$$

Figure 3-8 shows the local turbulent skin friction coefficient c_f as a function of local Reynolds

---

[6] $G \equiv \frac{\int(\Delta u^+)^2 d\eta}{\int(-\Delta u^+)d\eta} = \frac{1}{\sqrt{C_f/2}}\frac{H-1}{H}$, $\beta \equiv \frac{\delta^*}{\tau_w}\frac{dp}{d\xi} = H\frac{2}{C_f}\frac{\theta}{u_e}\frac{du_e}{d\xi}$

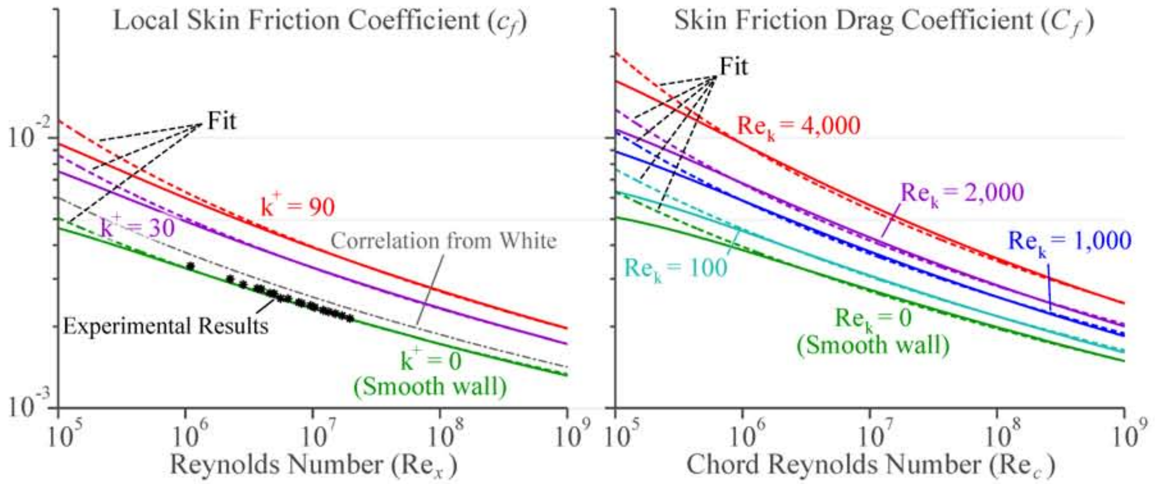

Figure 3-8: Local turbulent skin friction coefficient c_f vs. local Reynolds number Re_x (left, Eq. 3.64) and skin friction drag coefficient C_f vs. chord Reynolds number Re_c(right, Eq. 3.66) (Experimental results from [40]) c_f calculated numerically matches closely with experimental data for smooth wall.

number Re_x (left), and the skin friction drag coefficient, C_f as a function of flat plat chord Reynolds number Re_c (right). The left hand figure shows that Eq. 3.64 matches well with the experimental skin friction coefficient measurements by Österlund [40] conducted on a smooth flat plate at zero pressure gradient, over a range of Reynolds number between 1×10^6 and 2×10^7. Eq. 3.64 is also in line with the correlation of White [46],

$$c_{f_{FP}} = \frac{0.455}{\ln\left(0.06 Re_x\right)^2}. \tag{3.68}$$

The right hand figure represents the skin friction drag coefficient as a function of chord Reynolds number and wall roughness Reynolds number. The correlation developed has larger error at low Reynolds number (14% at $Re = 10^5$), but has high accuracy ($< 1\%$) for $Re_c > 10^6$.

The ratio of total to wake boundary layer loss is:

$$\begin{aligned} \varphi_w \equiv \frac{\Phi^*_{wake}}{\Phi^*_p} &= 1 - 2\frac{C_{\mathcal{D}_{surf_{FP}}}}{C_{f_{FP}}} \\ &= \frac{0.8}{\ln\left(0.1359\frac{Re_c}{(1+0.0123Re_k)}\right)}\left[2 - \frac{0.8}{\ln\left(0.1359\frac{Re_c}{(1+0.0123Re_k)}\right)}\right] \end{aligned} \tag{3.69}$$

For a flat plate with $Re_c = 10^7$ and $Re_k = 0$, Eq. 3.69 gives $\varphi_w = 11\%$. The fraction of wake loss is smaller for a turbulent boundary layer than for a laminar boundary layer.

3.4.3 Compressibility Effects

For a local edge Mach number comparable to or greater than unity, the kinetic energy of the flow is non-negligible compared to its thermal energy, and heat generation occurs inside the boundary layer as the flow is decelerated. The heat generated alters the density and the viscosity profiles and affects the skin friction and dissipation. To obtain accurate values of the skin friction and dissipation, the expressions in Section 3.4.1 and 3.4.2 need to be corrected for this effect.

Figure 3-9 illustrates the variation of flat plate skin friction drag coefficient as a function of freestream Mach number by van Driest [44]. As the freestream Mach number is increased, the skin friction drag coefficient is reduced.

Define the compressible to incompressible skin friction ratio as:

$$\frac{C_f}{C_{f_i}} \equiv \frac{1}{1 + K_\tau}, \tag{3.70}$$

then K_τ is expressed as

$$K_\tau = 0.0313 \ln (Re)^{1/3} M_\infty^{\frac{\gamma}{2(\gamma-1)}}. \tag{3.71}$$

3.5 Summary

In this chapter, equations to evaluate the profile mechanical energy loss of an aerodynamic body were derived from the mechanical energy defect equation.

The profile mechanical energy loss of an aerodynamic body is expressed as:

$$\Phi_p^* = \Phi_{surf}^* + \Phi_{wake}^*. \tag{3.72}$$

In Eq. 3.72, the surface mechanical energy loss is:

$$\Phi_{surf}^* = \int \mathbf{K} \cdot \hat{n} \, d\ell_{TE}. \tag{3.73}$$

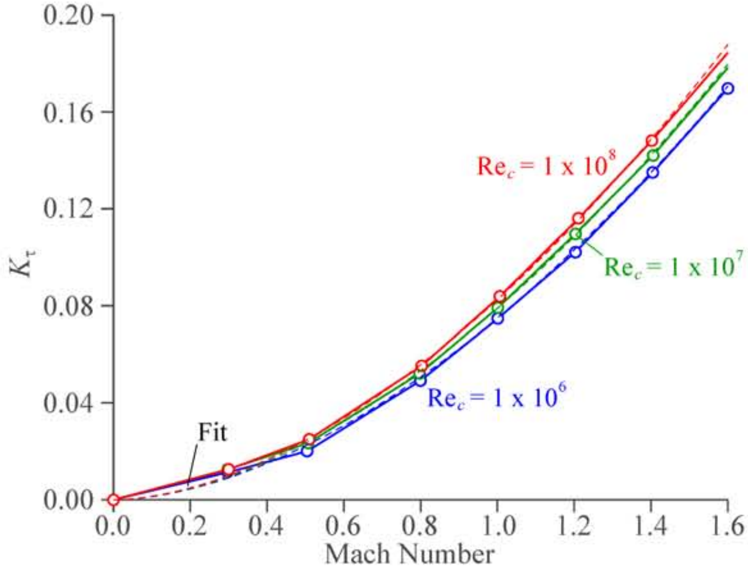

Figure 3-9: K_τ vs. chord Reynolds number for laminar (black) and turbulent boundary layer with various wall roughness [44]

The wake mechanical loss is:

$$\Phi^*_{wake} = \int \mathbf{K} \cdot \hat{n}\, d\ell_{out} - \int \mathbf{K} \cdot \hat{n}\, d\ell_{TE}. \tag{3.74}$$

For an incompressible turbulent boundary layer, these losses are due to viscous dissipation only,

$$\Phi^* = \Phi, \tag{3.75}$$

where

$$\Phi = \iint \rho_e U_e^3 c_{\mathcal{D}}\, d\mathcal{S}. \tag{3.76}$$

For a compressible adiabatic turbulent boundary layer, the mechanical loss can be approximated as a function of dissipation coefficient, edge velocity and edge Mach number,

$$\Phi^* \approx \frac{\iint \rho_e U_e^3 \left(1 + \frac{\gamma-1}{2} M_e^2\right)^r c_{\mathcal{D}}\, d\mathcal{S}}{\left.\left(1 + \frac{\gamma-1}{2} M_e^2\right)^r\right|_{out}}. \tag{3.77}$$

A correlation to calculate the flat plate skin friction coefficients ($c_{f_{FP}}$ and $C_{f_{FP}}$) and dissipation coefficients ($c_{\mathcal{D}_{PF}}$ and $C_{\mathcal{D}_{FP}}$) has been derived from boundary layer equations as tabulated in Table 3.1. The correlation for turbulent flow at $M_\infty = 0$ and $Re_k = 0$ was

Table 3.1: Flat plate skin friction and dissipation correlations

	Laminar:	Turbulent:
Local skin friction coefficient: $c_{f_{FP}}$	$\frac{0.664}{\sqrt{Re_x}}\frac{1}{1+K_\tau}$	$\frac{0.48}{\ln\left(0.1729\frac{Re_x}{(1+0.3k^+)}\right)^2}\frac{1}{1+K_\tau}$
Skin friction drag coefficient: $C_{f_{FP}}$	$\frac{1.328}{\sqrt{Re_c}}\frac{1}{1+K_\tau}$	$\frac{0.48}{\ln\left(0.0613\frac{Re_c}{(1+0.0123Re_k)}\right)^2}\frac{1}{1+K_\tau}$
Local dissipation coefficient: $c_{\mathcal{D}_{FP}}$	$\frac{0.261}{\sqrt{Re_x}}\frac{1}{1+K_\tau}$	$\frac{0.24}{\ln\left(0.3833\frac{Re_x}{(1+0.3k^+)}\right)^2}\frac{1}{1+K_\tau}$
Surface dissipation coefficient: $C_{\mathcal{D}_{surf_{FP}}}$	$\frac{0.522}{\sqrt{Re_c}}\frac{1}{1+K_\tau}$	$\frac{0.24}{\ln\left(0.1359\frac{Re_c}{(1+0.0123Re_k)}\right)^2}\frac{1}{1+K_\tau}$
Correction factor for compressibility effect:	$K_\tau = 0.0313\,\ln\left(Re\right)^{1/3} M_\infty^{\frac{\gamma}{2(\gamma-1)}}$	

shown to match experimental data by Österlund [40]. $C_{f_{FP}}$ for laminar and turbulent flow as a function of Re_c, Re_k is shown in Figure 3-10.

The rest of the thesis focuses on the different applications of the power balance method. Chapter 4 uses Eq. 3.77 to derive an analytical expression for the component form factor employed in the wetted area method. Chapter 5 applies Eq. 3.77 to estimate the interference effects in an integrated configuration. Chapter 6 applies the power balance method to quantify the system level benefit of BLI.

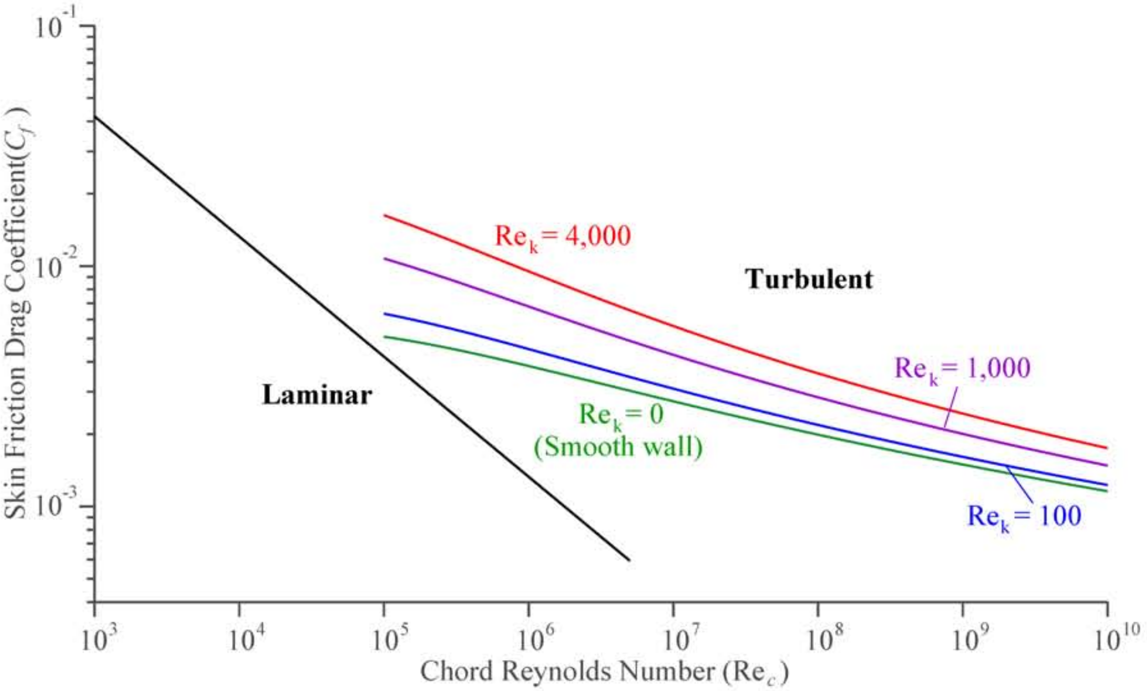

Figure 3-10: Skin friction drag coefficient vs. chord Reynolds number for laminar (black) and turbulent boundary layer with various wall roughness

Chapter 4

Improved Estimates for Airfoil Drag Using The Power Balance Method

In conceptual aircraft design, profile drag[1] is obtained through the wetted area method using a combination of a flat plate skin friction drag coefficient ($C_{f_{FP}}$) , a component form factor (K_f) and a wetted area (S_{wet}). The form factor, K_f, was correlated to geometric parameters such as airfoil thickness to chord ratio or body diameter to length ratio by Hoerner [20], Raymer [34], Shevell [37], and others. The main problem of such correlations is that the value of the form factor cannot be reliably applied to new geometries for which experimental data is not available. In this chapter, an analytical expression for the form factor is developed using the power balance method and its accuracy is quantified using CFD results. In this context we note that the results presented are extreme cases to illustrate the limitations of the developed form factor expression.

Section 4.1 introduces the wetted area method used in the profile drag estimation of aircraft during conceptual design. Section 4.2 derives an analytical expression of the form factor using the power balance method. Section 4.3 presents the accuracy and the limitation of the analytical expression through three examples, comparing it against other empirical form factor correlations. Section 4.4 summarizes the chapter findings.

4.1 Wetted Area Method For Profile Drag Estimation

The drag of an isolated aerodynamic body can be broken into three components:

---

[1] or equivalently profile mechanical energy loss for isolated bodies

1. Lift induced drag: drag force associated with trailing vorticity generated by a three dimensional lifting body, and its corresponding transverse velocities in the Trefftz Plane.

2. Wave drag: drag force due to changes in pressure distribution caused by formation of shockwaves around the body.

3. Profile drag: drag force caused by viscous effects in the boundary layer, which includes skin friction and pressure drag. This is related mainly to the axial velocity defect in the Trefftz Plane.

Lift induced drag and wave drag can be captured using computationally inexpensive methods such as Euler or panel methods, which could be employed during preliminary performance calculations. To estimate the profile drag of an aerodynamic body with minimum computation the wetted area method based on form factor and flat plate skin friction drag coefficient is used. The form factor is defined as:

$$K_f \equiv \frac{D_p}{D_{FP}}, \tag{4.1}$$

where D_p is the profile drag and

$$D_{FP} \equiv \frac{1}{2}\rho_\infty V_\infty^2 S_{wet} C_{f_{FP}}. \tag{4.2}$$

S_{wet} is the total wetted surface area of the body, and $C_{f_{FP}}$ is the flat plate skin friction coefficient, defined as

$$C_{f_{FP}} \equiv \frac{1}{S_{wet}} \iint c_{f_{FP}}\, dS_{wet}, \tag{4.3}$$

with $c_{f_{FP}}$ being the local skin friction coefficient at the Reynolds number of the actual body.

If K_f is assumed known (from external information) the profile drag coefficient, $C_{D_p} \equiv {}^{D_p}\!/\tfrac{1}{2}\rho_\infty V_\infty^2 S_{ref}$, can be estimated as

$$C_{D_p} = C_{f_{FP}} K_f \frac{S_{wet}}{S_{ref}}, \tag{4.4}$$

where S_{ref} is the reference area.

$C_{f_{FP}}$ can be reliably obtained from experimental results or boundary layer theory [1, 2], as presented in Section 3.4. The main challenge is the estimation of the form factor K_f, which relates the drag of an aerodynamic body to that of a flat plate by capturing two different effects:

1. Effect of local ${}^1\!/\!{}_2\rho_e U_e^2$. The skin friction drag of a body is higher than that of a flat plate, because of locally higher edge velocity around the body, on average.
2. Effect of pressure drag: The pressure drag is non-zero around an aerodynamic body with non-zero thickness.

The first effect can be captured using the edge velocity distribution around the body estimated from an inviscid calculation, but there is no simple way to estimate the pressure drag. The values of the form factor, therefore, are obtained from empirical correlations based on experimental data, such as those presented in Chapter 2.

4.2 Analytical Expression of Form Factor

In this section, an analytical expression relating the component form factor to the boundary layer edge quantities (density, velocity and Mach number) is derived by applying the power balance method. The boundary layer edge quantities are inputs in airfoil design, the derived expression can therefore be used in the profile drag estimation of newly designed airfoil. Calculation of profile drag over a three dimensional geometry can also be simplified using this expression, as the edge quantities can be calculated reliably using a source line model [14] or any other inviscid flow calculation method.

As mentioned in Section 3.3, the profile drag of an isolated airfoil can be related to the mechanical energy loss as:

$$\boldsymbol{D_p} \cdot \boldsymbol{V_\infty} = \Phi_p^*, \tag{4.5}$$

and the component form factor can also be expressed as:

$$K_f \equiv \frac{\Phi_p^*}{D_{FP} V_\infty}. \tag{4.6}$$

For each distinct surface i of an aerodynamic body, the profile mechanical loss over the surface i ($\Phi_{p_i}^*$) can be calculated as derived in Section 3.2.3:

$$\Phi^*_{p_i} = \iint_{tot_i} \left[\rho_e U_e^3 c_{\mathcal{D}} - \mathbf{D} \cdot \bar{\nabla} \frac{1}{2} U_e^2 \right] d\mathcal{S}_{tot_i}. \tag{4.7}$$

In Eq. 4.7, S_{tot} is the surface area of the flat plate surface and wake combined. Combining Eq. 4.6 and Eq. 4.7,

$$K_{f_i} = \frac{\iint_i \rho_e U_e^3 c_{\mathcal{D}} - \mathbf{D} \cdot \bar{\nabla} \frac{1}{2} U_e^2 \, d\mathcal{S}_i}{\frac{1}{2} \rho_\infty V_\infty^3 S_{wet_i} C_{f_{FP}}}. \tag{4.8}$$

Using the definition

$$C_{f_{FP}} = \frac{2}{S_{tot}} \iint c_{\mathcal{D}_{FP}} \, d\mathcal{S}_{tot}, \tag{4.9}$$

($c_{\mathcal{D}_{FP}}$ is the local dissipation coefficient) and the derivation given in Appendix C, Eq. 4.8 can be written as

$$K_{f_i} \approx \frac{\iint_{wet_i} \rho_e U_e^3 \left(1 + \frac{\gamma-1}{2} M_e^2\right)^r d\mathcal{S}_{wet_i}}{\rho_\infty V_\infty^3 \left(1 + \frac{\gamma-1}{2} M_\infty^2\right)^r S_{wet_i}}. \tag{4.10}$$

Using Eq. 4.10, an analytical expression for component form factor is:

$$\begin{aligned} K_f &\approx \frac{1}{\sum_{i=1}^n S_{wet_i}} \sum_{i=1}^n K_{fi} S_{wet_i} \\ &= \frac{1}{\sum_{i=1}^n S_{wet_i}} \sum_{i=1}^n \frac{\iint_{wet_i} \rho_e U_e^3 \left(1 + \frac{\gamma-1}{2} M_e^2\right)^r d\mathcal{S}_{wet_i}}{\rho_\infty V_\infty^3 \left(1 + \frac{\gamma-1}{2} M_\infty^2\right)^r}. \end{aligned} \tag{4.11}$$

Eq. 4.11 is a function of the edge density, the edge velocity, the edge Mach number and the component geometry. All of these can be obtained from potential-flow solutions and do not require empirical information.

Eq. 4.11, however, is derived based on the following assumptions for the flow around the body:

1. The approximation of baroclinic power[2] as

$$\Phi^*_{p_i} \approx \frac{\iint_{tot_i} \rho_e U_e^3 \left(1 + \frac{\gamma-1}{2} M_e^2\right)^r c_{\mathcal{D}} \, d\mathcal{S}_{tot_i}}{\left(1 + \frac{\gamma-1}{2} M_\infty^2\right)^r}. \tag{4.12}$$

---

[2] $\Pi_V = \iint \mathbf{D} \cdot \bar{\nabla} \frac{1}{2} U_e^2 \, d\mathcal{S}$.

2. The assumption that the boundary layer characteristics, in particular the shape parameter H (or kinematic shape parameter H_k for compressible flow), are within the range such that

$$c_{\mathcal{D}} \approx c_{\mathcal{D}_{FP}}. \tag{4.13}$$

The accuracy and limitation of Eq. 4.11 therefore depends on the validity of the above assumptions which are investigated in detail in this study for various airfoil geometry and operating conditions. It will be shown that:

1. assumption 1 breaks down when the boundary layer interacts with a shock with incoming Mach number higher than 1.15, and

2. assumption 2 breaks down when separation of boundary layer is observed, which can be caused by adverse pressure gradient or boundary layer/shock interaction.

It is emphasized that the breakdown of assumptions 1 and 2 only occurs on extreme cases which are not used in aircraft cruise condition. Eq. 4.11 is therefore applicable for use at the conceptual design stage in estimating cruise performance.

4.3 Accuracy and Limitation of Form Factor Calculation Method

To assess the accuracy of Eq. 4.11, the form factors of various aerodynamic bodies ($K_{f_{act.}} \equiv \frac{D_{P_{CFD}}}{D_{FP_{CFD}}}$) have been calculated using MSES [8] (for 2D airfoils) and MTFLOW[3] [10] (for body of revolution) and compared against the formula in Eq. 4.11 ($K_{f_{est.}}$) and various empirical correlations (K_{f_c}) presented in Chapter 2.

The comparison of three form factors ($K_{f_{act.}}$, $K_{f_{est.}}$ and $K_{f_{cor.}}$) is conducted for three common applications:

1. Bodies of revolution of various fineness ratio (l/d), used in the estimation of profile drag of an aircraft fuselage.

2. Low speed 2D airfoil at various angles of attack, used in the estimation of wing profile drag of a low speed aircraft.

3. Transonic 2D airfoil at various flight Mach numbers, used in the estimation of wing profile drag of a transonic aircraft.

---

[3] MTFLOW uses the same formulation as MSES, adapted for bodies of revolution.

4.3.1 Body of Revolution

In this estimation of profile drag of an aircraft fuselage, or its equivalent body of revolution, the area distribution was taken from the D8.5 aircraft design of the NASA N+3 project [14] as in Figure 4-1. The following parameters were varied:

- Free stream Mach number (M_∞): $M_\infty = 0.1$ to simulate incompressible flow and $M_\infty = 0.85$ to simulate transonic cruise condition for a commercial airliner (typical cruise Mach between 0.74 and 0.85).
- Airframe fineness ratio (l/d): varied from 2.5 (40% thick body) to 12 (8.3% thick body). D8.5 fuselage has a fineness ratio of 8.55.

The length Reynolds number (Re_l) was fixed at 1.0×10^7, with a boundary layer trip prescribed at $x/l = 0.10$.

Figure 4-2 shows the form factor from MTFLOW results (blue) which is taken as a true value and the estimated form factor from Eq. 4.11 (red), as a function of body fineness ratio (l/d) at $M_\infty = 0.1$. The Hoerner correlation [20], which was most accurate among available correlation, is also plotted. The Hoerner correlation (black) is given by

$$K_{f_{Hoerner}} = 1 + 1.5\left(\frac{l}{d}\right)^{-\frac{3}{2}} + 7\left(\frac{l}{d}\right)^{-3}. \tag{4.14}$$

The band highlighted in light blue indicates the region of 2% error from the actual form factor, defined as:

$$e_{K_f} \equiv \left(\frac{K_{f_{est.}}}{K_{f_{act.}}} - 1\right) \times 100\%. \tag{4.15}$$

The form factor estimated using Eq. 4.11 is accurate to within 2% for $l/d > 5$, which is as accurate as the correlation by Hoerner.

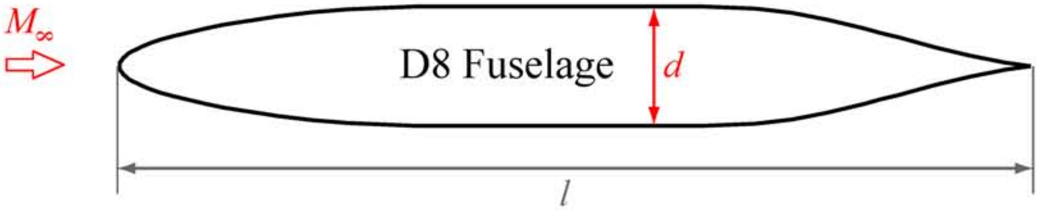

Figure 4-1: D8.5 fuselage section

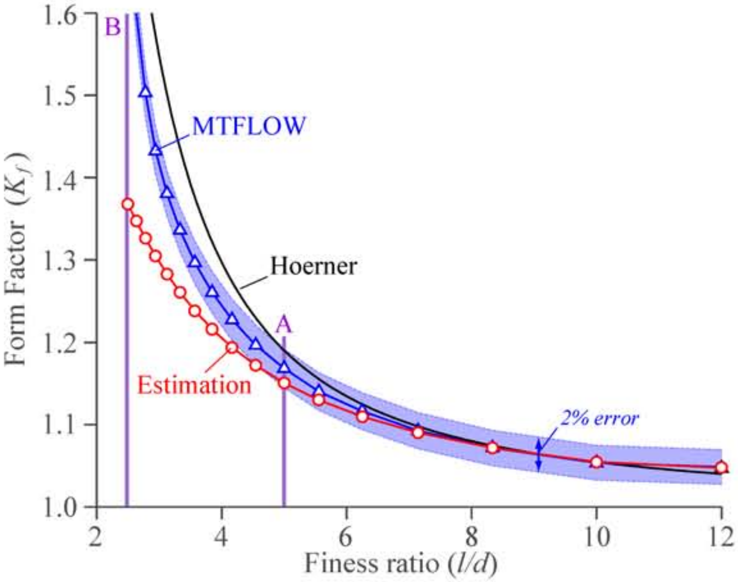

Figure 4-2: Form factor (K_f) vs. body fineness ratio (l/d), $M_\infty = 0.1$. The form factor estimation given by Eq. 4.11 is accurate to within 2% for the body fineness ratio greater than five, which is the case in typical fuselages.

Both the analytical model and Hoerner correlation have errors greater than 2% for $l/d < 5$. The correlation by Hoerner overpredicts the form factor, while the analytical model underpredicts it. To investigate the source of the estimation error, we analyze cases with $l/d = 5$ (Point A in Figure 4-2) and $l/d = 2.5$ (Point B in Figure 4-2). Figure 4-3 shows the C_p contours around the bodies with $l/d = 5$ (upper) and $l/d = 2.5$ (lower). The key difference between the two cases is the size of the wake downstream of the body. While the boundary layer over the upper body stays attached over the length of the body, the boundary layer of the thicker body separates and there is a large wake downstream of the body. The inaccuracy of the estimation occurs because the boundary layer is separated and the assumption that $c_{\mathcal{D}} \approx c_{\mathcal{D}_{FP}}$ is no longer accurate, causing the estimation to deviate from the actual value. To support this argument, we investigate the evolution of the local normalized loss generation ${}^{d\bar{C}_{\Phi^*}}/{}_{ds}$, which represents how closely the profile mechanical loss scales as $\rho_e U_e^3 \left(1 + \frac{\gamma-1}{2} M_e^2\right)^r$. $\bar{C}_{\Phi^*}$ is defined as,

$$\bar{C}_{\Phi^*} \equiv \frac{\left(1 + \frac{\gamma-1}{2} M_\infty^2\right)^r \Phi_p^*}{\left[\rho_e U_e^3 \left(1 + \frac{\gamma-1}{2} M_e^2\right)^r\right]_{ave} c}, \tag{4.16}$$

where

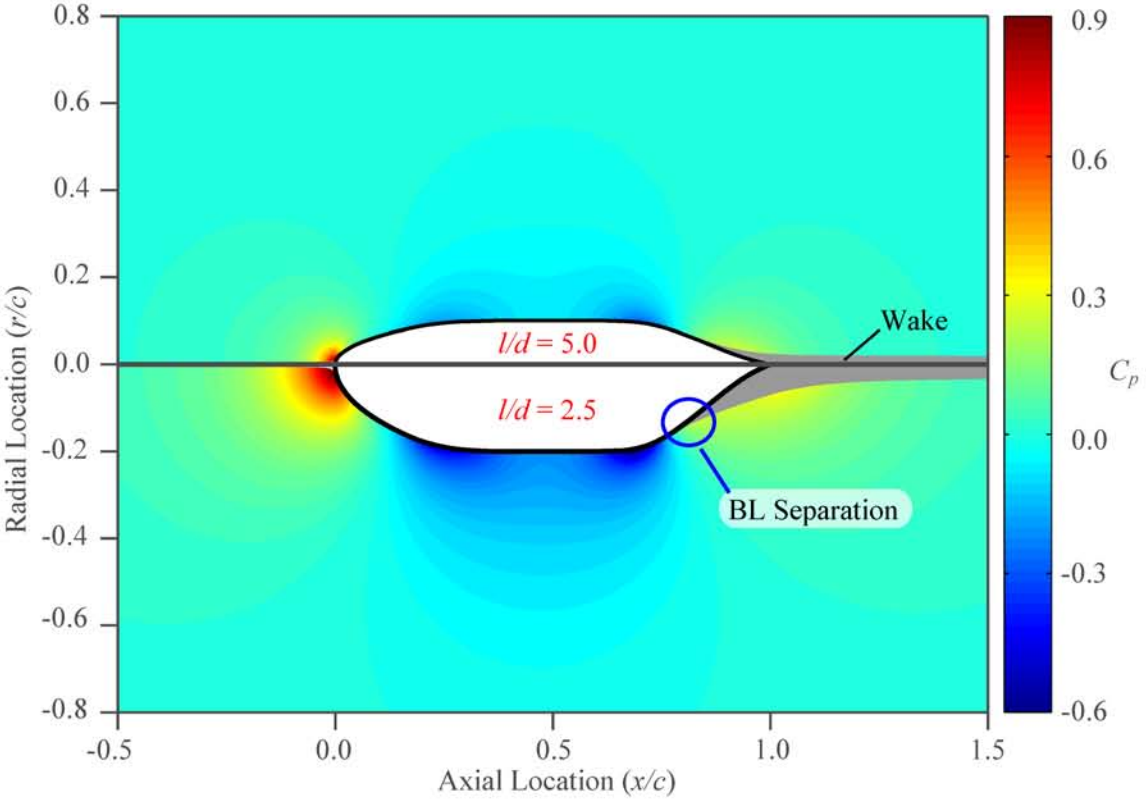

Figure 4-3: C_p contours of D8.5 fuselage with $l/d = 5$ (upper) and $l/d = 2.5$ (lower), $M_\infty = 0.1$. A significant change in the wake thickness is seen between the two bodies.

$$\left[\rho_e U_e^3 \left(1 + \frac{\gamma - 1}{2} M_e^2\right)^r\right]_{ave} \equiv \frac{\int_{LE}^{TE} \rho_e U_e^3 \left(1 + \frac{\gamma-1}{2} M_e^2\right)^r ds}{c}. \tag{4.17}$$

If the $d\bar{C}_{\Phi^*}/ds$ distribution of a body is the same as that for a flat plate, both assumptions made in deriving Eq. 4.11 are valid. Figure 4-4 shows a comparison of boundary layer properties between $l/d = 5.0$ (dashed purple lines) and $l/d = 2.5$ (solid red lines). The uppermost plot shows the evolution of the boundary layer kinematic shape parameter (H_k[4]) along the body, the middle plot shows the evolution of the local normalized loss generation $d\bar{C}_{\Phi^*}/ds$, and the lowermost plot shows the normalized edge velocity distribution. Figure 4-4 shows sharp increases in H_k and $d\bar{C}_{\Phi^*}/ds$ downstream of $x/c = 0.75$ on the $l/d = 2.5$ body, indicating separation has occurred as a result of the flow deceleration.

The CFD results at $M_\infty = 0.1$ show the analytical expression for the form factor is accurate to within 2% for bodies of fineness ratio greater than 5. For a body of revolution

---

[4] $H_k \equiv \delta_k^*/\theta_k$, $\theta_k \equiv \int \left(1 - \frac{U}{U_e}\right) \frac{U}{U_e}\, dy$, $\delta_k^* \equiv \int \left(1 - \frac{U}{U_e}\right) dy$

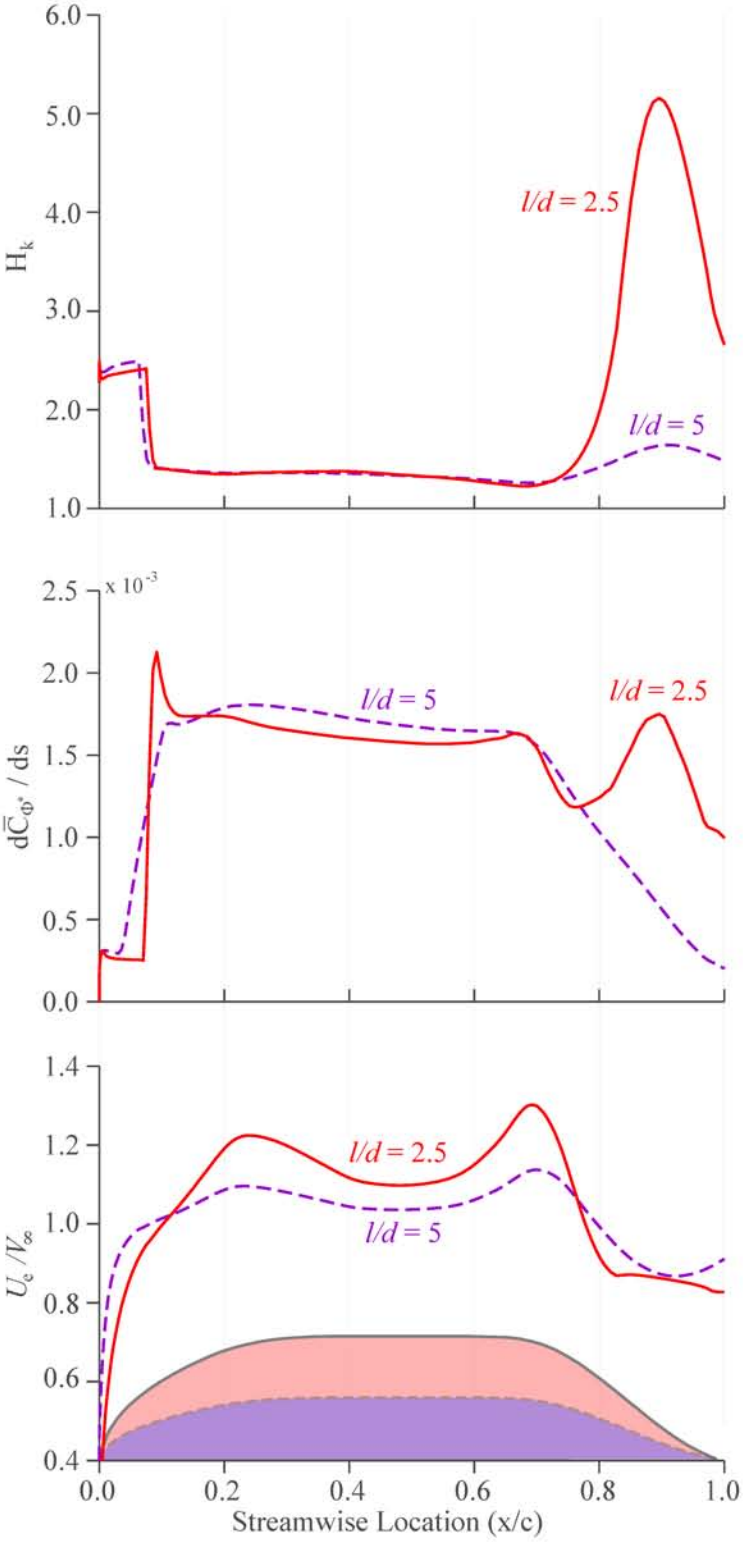

Figure 4-4: Evolution of H_k, $d\bar{C}_{\Phi^*}/ds$ and U_e/V_∞ over D8.5 fuselage, for $l/d = 5$ (purple dashed) and $l/d = 2.5$ (red solid), $M_\infty = 0.1$. $d\bar{C}_{\Phi^*}/ds$ increases by 1×10^{-3} when H_k increases by 4.

operating at a higher Mach number (e.g. cruise Mach number of 0.85), the derived form factor expression is less accurate, due to effects of compressibility. Figure 4-5 shows the form factor from MTFLOW results (blue) and the estimated form factor (red) as a function of body fineness ratio (l/d) at $M_\infty = 0.85$. For this Mach number, the form factor of Eq. 4.11 is accurate to within 2% for $l/d > 6.25$.

Following the same process as the low Mach number analysis, two body thicknesses ($l/d = 6.25$, point A and $l/d = 4.54$, point B) were analyzed further to investigate the source of the estimation error. Figure 4-6 shows the C_p contours around the $l/d = 6.25$ body (upper) and the $l/d = 4.54$ body (lower). Unlike the low Mach number cases, there is no significant difference in the downstream wake. The lower body, however, has a shock near $x/c = 0.75$, which is not present on the upper body. The presence of this shock is the primary cause of the estimation error.

Figure 4-7 shows a comparison of flow parameters between $l/d = 6.25$ body (dashed purple lines) and $l/d = 4.54$ body (solid red lines). The uppermost figure shows the boundary layer kinematic shape parameter H_k, the center plot shows the local normalized loss generation ${}^{d\bar{C}_{\Phi^*}}/_{ds}$, and the lowermost plot show the edge Mach number M_e. The main difference between the results for the two bodies analyzed is the sharp peak in ${}^{d\bar{C}_{\Phi^*}}/_{ds}$ at the location of the shock on the $l/d = 4.54$ body.

The cause of the peak in the normalized loss generation comes from the sudden increase in baroclinic power as a result of the large pressure rise across the shock, which is not captured in the approximation. Figure 4-8 illustrates this effect, showing the evolution of profile mechanical loss and approximated mechanical loss over the $l/d = 4.54$ body at $M_\infty = 0.85$. The approximation error has a sharp increase at the shock.

We can draw the following conclusions from this study:

1. For a body of revolution operating in a flow with $M_\infty^2 \ll 1$, Eq. 4.11 is accurate for flows without separation, or more precisely, for the fuselage geometry studied, a body with a fineness ratio larger than 5. This range covers typical aircraft fuselages, which have $l/d \sim 10$.

2. For a body of revolution operating at $M_\infty = 0.85$, the analytical model is affected by the error in the estimation of baroclinic power, caused by the pressure gradient generated by the shock. For a D8.5 fuselage body at $M_\infty = 0.85$, the fineness ratio

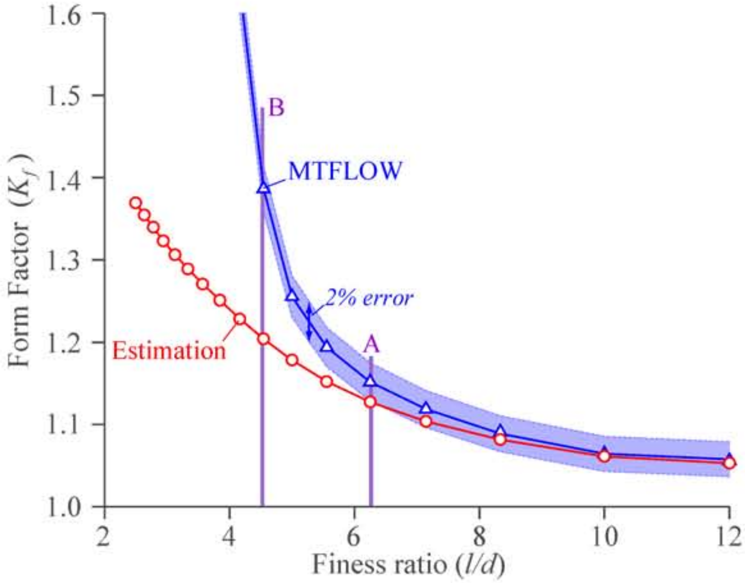

Figure 4-5: Form factor (K_f) vs. body fineness ratio (l/d), $M_\infty = 0.85$. The form factor estimation is accurate to within 2% for $l/d > 6.25$, which is the case in typical fuselages.

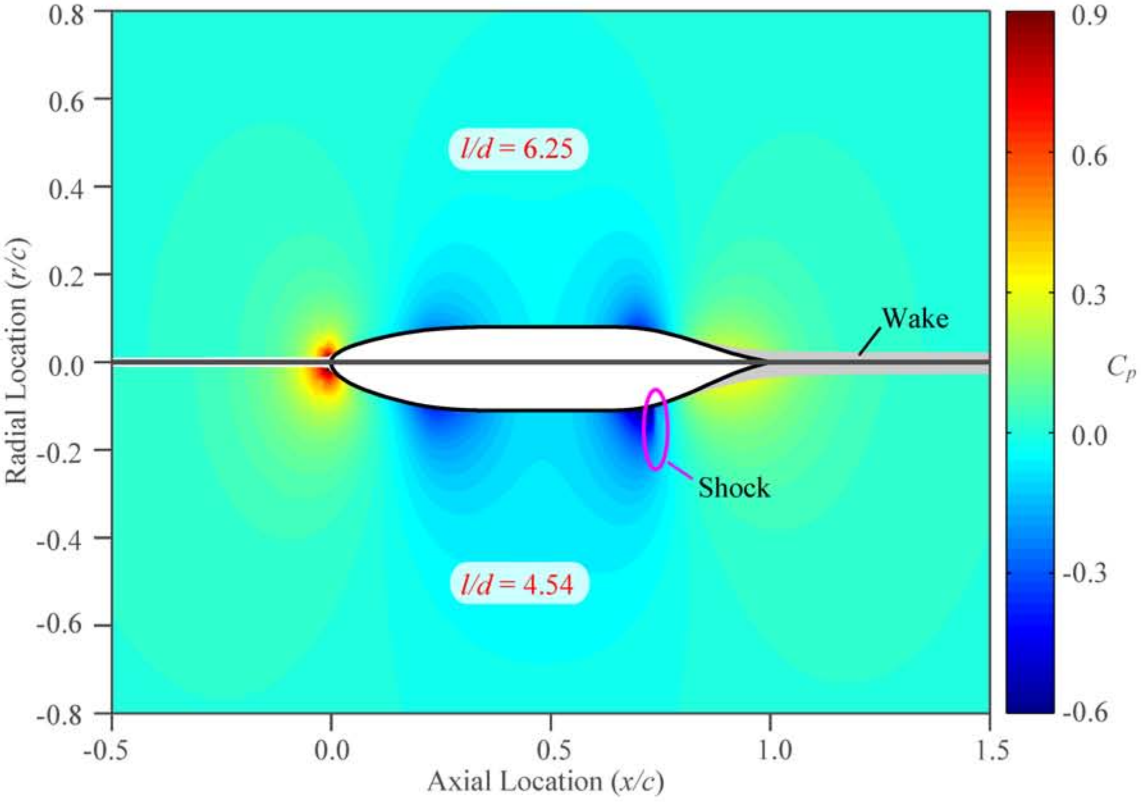

Figure 4-6: C_p contours of D8.5 fuselage with $l/d = 6.25$ (upper) and $l/d = 4.55$ (lower), $M_\infty = 0.85$. A shock forms over surface of the $l/d = 4.54$ body.

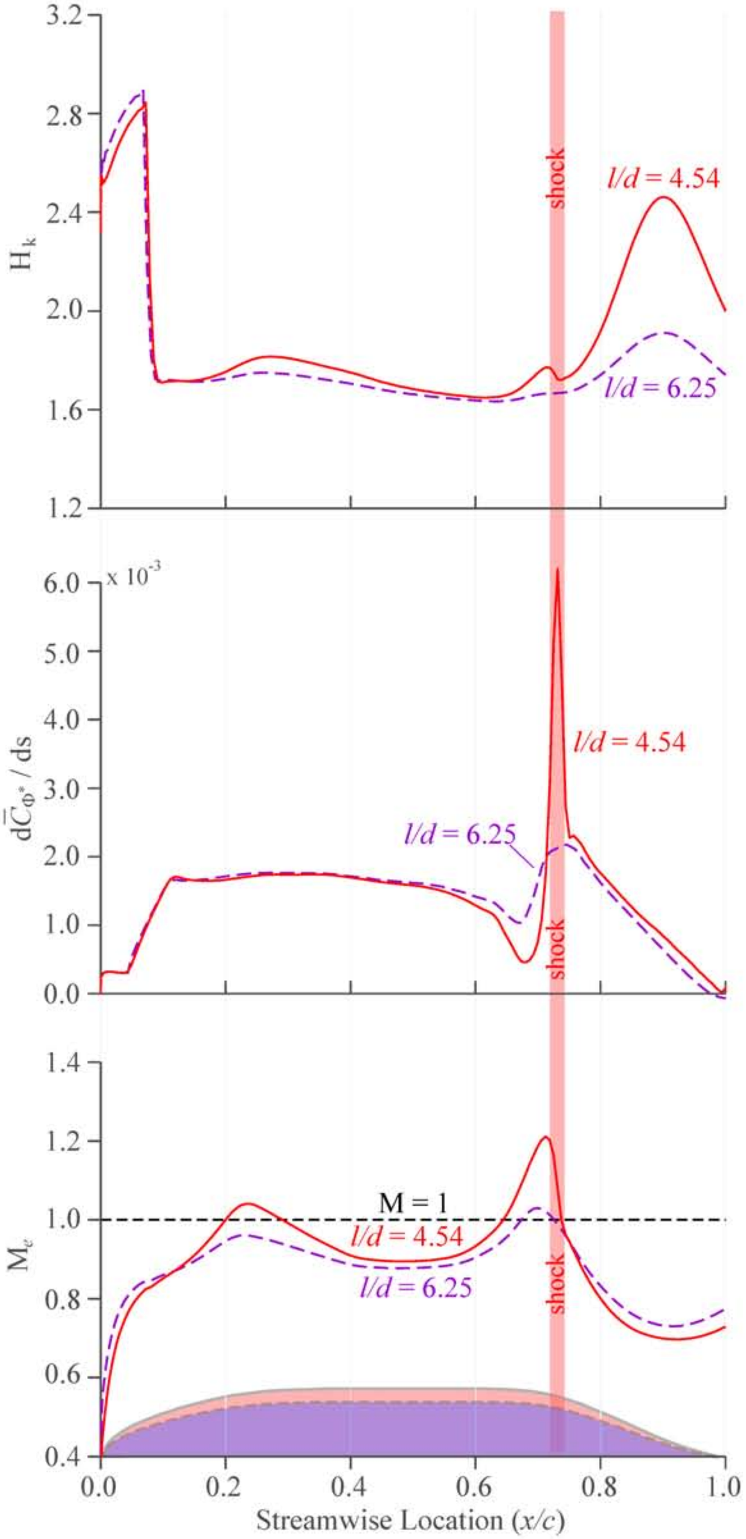

Figure 4-7: Evolution of H_k, $d\bar{C}_{\Phi^*}/ds$ and M_e over D8.5 fuselage, for $l/d = 6.25$ (purple dashed) and $l/d = 4.54$ (red solid), $M_\infty = 0.85$. A sharp peak in $d\bar{C}_{\Phi^*}/ds$ is seen at the location of the shock on the $l/d = 4.54$ body.

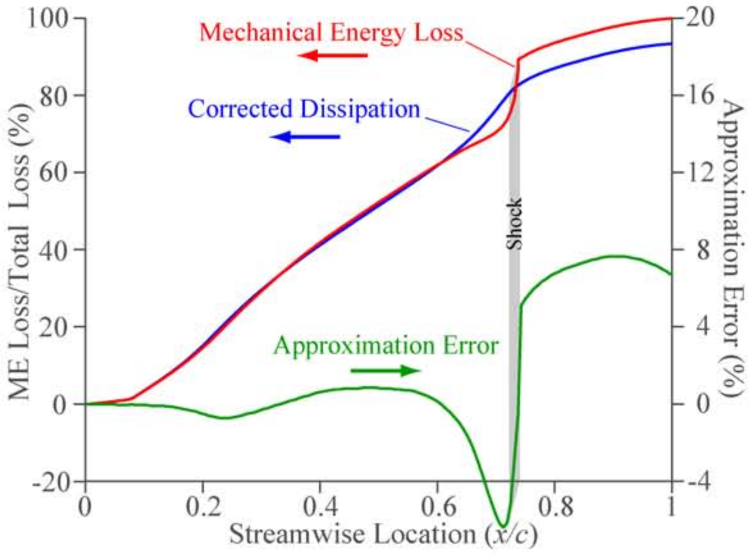

Figure 4-8: Evolution of mechanical energy loss, corrected dissipation and their difference for the $l/d = 4.54$ body at $M_\infty = 0.85$. The error between the mechanical energy loss and the approximation error increases sharply at the location of the shock over the body.

of the body should be kept over 6.25 to avoid shock formation over the body surface. The method should be applicable to a typical aircraft fuselage, which has $l/d \sim 10$.

In summary, the form factor estimation method developed is accurate for bodies of revolution without flow separation or strong shocks as defined above. This is always the case for fuselages at their design point, so the method is well-suited for fuselage drag estimation in conceptual design analysis and optimization.

4.3.2 Low Speed Airfoil

Another application of the wetted area method is the estimation of profile drag of a two-dimensional, low speed airfoil at various angles of attack. The profile drag of a typical[5] 2D low speed airfoil GAW1, Figure 4-9, is assessed for angles of attack between $\alpha = -4°$ and $18°$. The freestream Mach number was $M_\infty = 0.15$, the chord Reynolds number was fixed at the design value, $Re_c = 6.3 \times 10^6$, and the boundary layer was tripped at $s/c = 0.01$.

---

[5] per personal communication with Prof. Drela

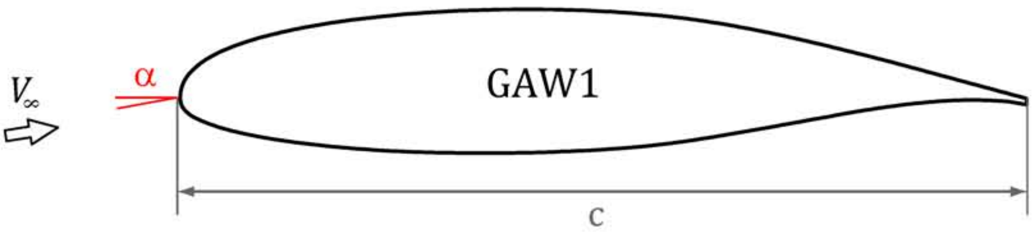

Figure 4-9: GAW1 airfoil section

Figure 4-10 shows the form factor calculated from MSES results (blue) and the estimation (red) as a function of airfoil lift coefficient C_ℓ. The figure also shows the empirical form factor correlation from Raymer [34] (black)

$$K_{f_{Raymer}} = \left(1 + \frac{(2 - M_\infty^2)}{\sqrt{1 - M_\infty^2}}\left(\frac{t}{c}\right) + 100\left(\frac{t}{c}\right)^4\right)\left(1 + \frac{1}{4}\left[C_{\ell_{des}} + (C_\ell - C_{\ell_{des}})^2\right]\right), \quad (4.18)$$

and correlation from Hoerner [20] (dashed black)

$$K_{f_{Hoerner}} = \left(1 + 2\left(\frac{t}{c}\right) + 60\left(\frac{t}{c}\right)^4\right)\left(1 + \frac{1}{4}\left[C_{\ell_{des}} + (C_\ell - C_{\ell_{des}})^2\right]\right), \quad (4.19)$$

where $C_{\ell_{des}}$ is the design lift coefficient of the airfoil. The band highlighted in light blue indicates the region of 2% error from the MSES form factor. The estimation using Eq. 4.11 is accurate to within 2% for $-0.5 < C_\ell < 1.0$, as accurate as the two empirical correlations.

The error in the analytical expression (and the correlations) grows beyond 2% for $C_\ell > 1.0$, as the airfoil operates closer to its stall condition.

To analyze the source of the estimation error in further detail, we compare the airfoil flow field at $\alpha = 0°$ (point A in Figure 4-10) and at $\alpha = 10°$ (point B in Figure 4-10). Figure 4-11 shows Mach number contours at $\alpha = 0°$ (upper) and at $\alpha = 10°$ (lower). The key difference between the two operating conditions is boundary layer separation on the suction surface at the higher angle of attack. As with the body of revolution examined earlier, separation is the primary cause of the error in form factor estimation.

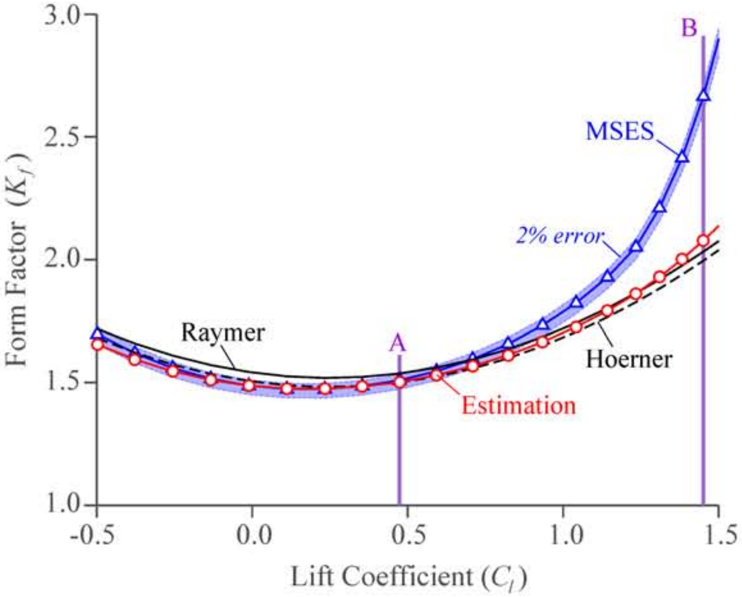

Figure 4-10: Form factor (K_f) vs. GAW-1 airfoil lift coefficient (C_ℓ), $M_\infty = 0.15$. The form factor estimation is accurate up to $C_\ell = 1.0$ for this airfoil.

Figure 4-12 shows the evolution of the boundary layer kinematic shape parameter H_k (uppermost), the local normalized loss generation $d\bar{C}_{\Phi^*}/ds$ (center), and the normalized edge velocity U_e/V_∞ (lower) for $\alpha = 0°$ (dashed lines) and $\alpha = 10°$ (solid line). The primary source of losses at high angle of attack comes from the increased loss generation towards the trailing edge of the suction surface, following the trend of the boundary layer kinematic shape parameter. The increase in the suction side boundary layer kinematic shape parameter is caused by the larger velocity gradient at higher angle of attack. The normalized loss generation over the pressure surface is unaffected by the change in the angle of attack, because the boundary layer sees only a weak adverse pressure gradient over the rear pressure side of the airfoil.

In summary, the analytical form factor expression is as accurate as the empirical form factors, and is within 2% for the GAW-1 airfoil with $-0.5 < C_\ell < 1.0$. The estimation breaks down when the airfoil operates near the stall condition. In an aircraft conceptual design stages, one is mainly concerned about the cruise performance of the airfoil, which would most likely be operating away from the stall condition, and for such application, the analytical expression is adequate.

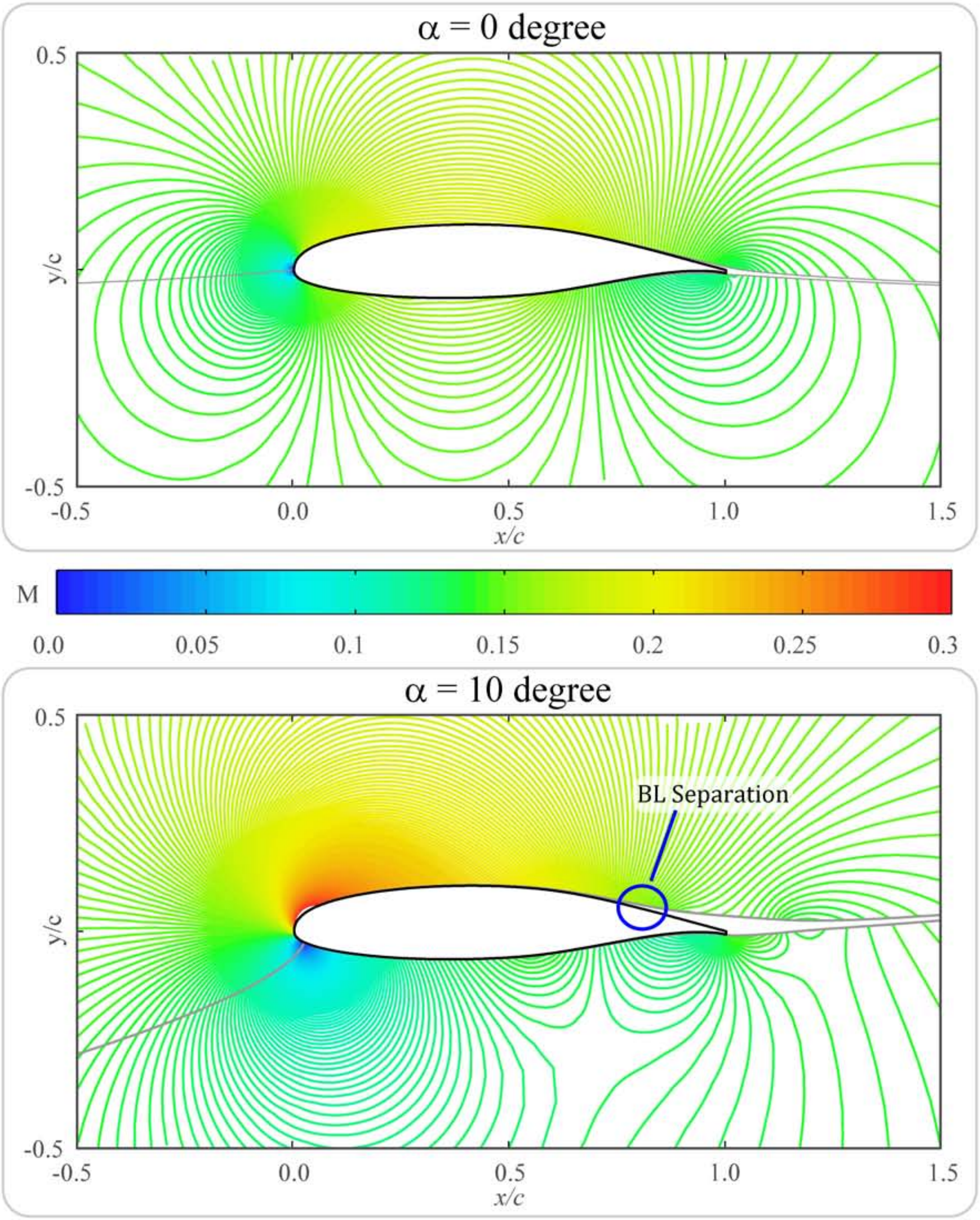

Figure 4-11: Mach contours of GAW1 airfoil at $\alpha = 0°$(upper) and $\alpha = 10°$(lower). Boundary layer separation occurs over the suction surface at high angle of attack.

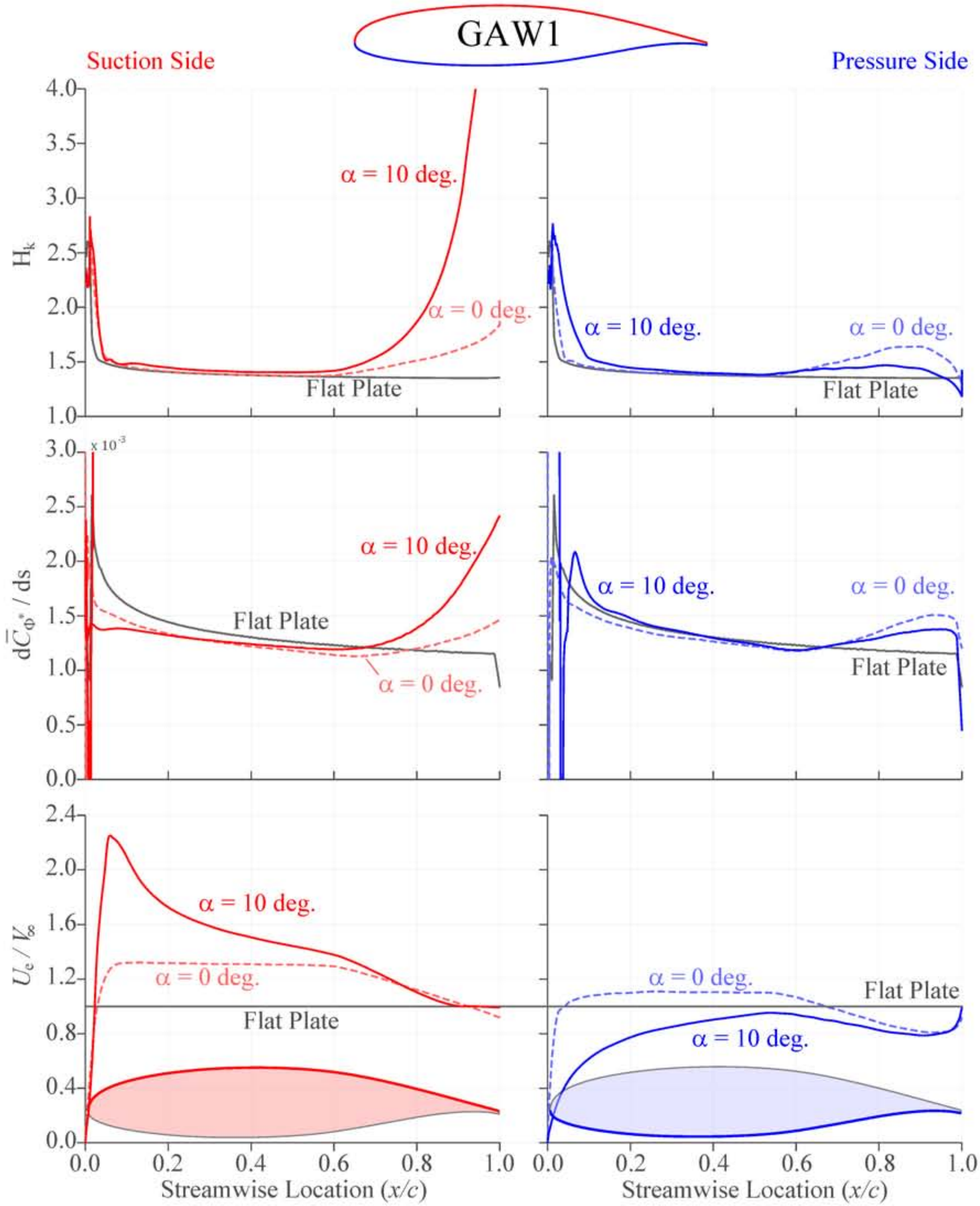

Figure 4-12: Evolution of H_k, $d\bar{C}_{\Phi^*}/ds$ and U_e/V_∞ over GAW1 airfoil, for $\alpha = 0°$ (dashed) and $\alpha = 10°$ (solid), suction surface (left), pressure surface (right). The trend of $d\bar{C}_{\Phi^*}/ds$ follows that of H_k.

4.3.3 High Speed Airfoil

The wetted area method is also used to estimate the profile drag of a two-dimensional, transonic airfoil RAE2822, shown in Figure 4-13. Analysis was conducted for freestream[6] Mach numbers between 0.3 and 0.79. As a reference, $M_\perp \sim 0.70$ is a typical perpendicular Mach number seen on the swept wing of a commercial airliner. The airfoil angle of attack was fixed at $\alpha = 3^\circ$, with chord Reynolds number of $Re_c = 1.0 \times 10^7$ and the boundary layer was tripped at $s/c = 0.01$.

Figure 4-14 shows the form factors calculated from MSES (blue) and from the analytical expression (red) as a function of freestream Mach number. The figure also shows the form factor calculated from the correlation of Shevell [37] (black),

$$K_{f_{Shevell}} = \left(1 + \frac{(2 - M_\perp^2)}{\sqrt{1 - M_\perp^2}}\left(\frac{t}{c}\right) + 100\left(\frac{t}{c}\right)^4\right)\left(1 + \frac{1}{4}\left[c_{L_{des}} + (c_L - c_{L_{des}})^2\right]\right), \quad (4.20)$$

and Nicolai [32] (dashed black),

$$K_{f_{Nicolai}} = \left(1 + \frac{0.6}{(x/c)_{max}}\left(\frac{t}{c}\right) + 100\left(\frac{t}{c}\right)^4\right)\left(1.34 M_\perp^{0.18}\right)\left(1 + \frac{1}{4}\left[c_{L_{des}} + (c_L - c_{L_{des}})^2\right]\right), \quad (4.21)$$

where $(x/c)_{max}$ is the location of the airfoil maximal thickness, which is at $x/c = 0.38$ for RAE2822. The band highlighted in light blue indicates the region of 2% error from the actual form factor. The form factor estimate of Eq. 4.11 is accurate to within 2% for freestream Mach numbers up to 0.71.

The error increases markedly above $M_\perp = 0.72$. The sharp increase in error is caused

---

[6] From infinite swept-wing theory, airfoil profile drag depends almost entirely on the perpendicular-plane Mach number $M_\perp \equiv M_\infty \cos \Lambda$, where Λ is the wing sweep angle. In this 2D airfoil section, the term "freestream Mach" will refer to $M_\perp$.

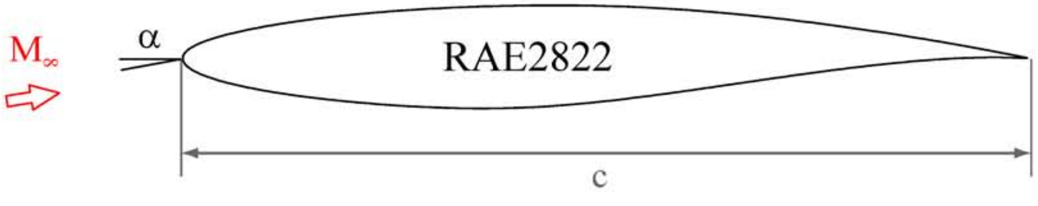

Figure 4-13: RAE2822 airfoil section

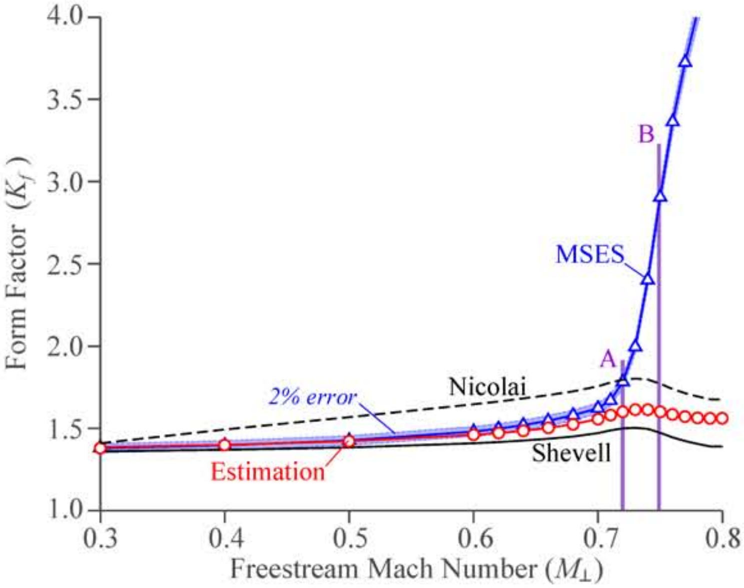

Figure 4-14: Form factor (K_f) vs. freestream Mach number, $\alpha = 3°$. The estimation error increases rapidly for $M_\perp > 0.72$, where a shock exists.

by the change in the shock strength over the airfoil suction surface as seen in comparison of flow around the airfoil at two operating conditions, $M_\perp = 0.72$ (point A in Figure 4-14) and $M_\perp = 0.75$ (point B in Figure 4-14).

Figure 4-15 shows the Mach number contours at $M_\perp = 0.72$ (upper) and at $M_\perp = 0.74$ (lower). The shock upstream Mach number is higher for $M_\perp = 0.74$ ($M = 1.4$ ahead of the shock), than for $M_\perp = 0.72$ ($M = 1.2$ ahead of the shock). As a result of this increase in shock strength at $M_\perp = 0.74$, the boundary layer downstream of the shock thickens noticeably compared to $M_\perp = 0.72$.

Figure 4-16 shows the evolution of the boundary layer kinematic shape parameter H_k (uppermost), the local normalized loss generation ${}^{d\bar{C}_{\Phi^*}}/_{ds}$ (center), and edge Mach number M_e (lowermost) for $M_\perp = 0.72$ (dashed lines) and $M_\perp = 0.74$ (solid line). An increase in the boundary layer kinematic shape parameter is seen downstream of the shock at $M_\perp = 0.74$, together with the increase in the normalized loss generation in this region. For $M_\perp = 0.72$, the loss generation downstream of the shock is affected less. The normalized loss generation over the pressure surface is unaffected by the change in the freestream Mach number as no shock exists.

To further investigate the effect of shock/boundary layer interaction on the accuracy of the form factor estimation, e_{K_f} is plotted against the local maximum Mach number over

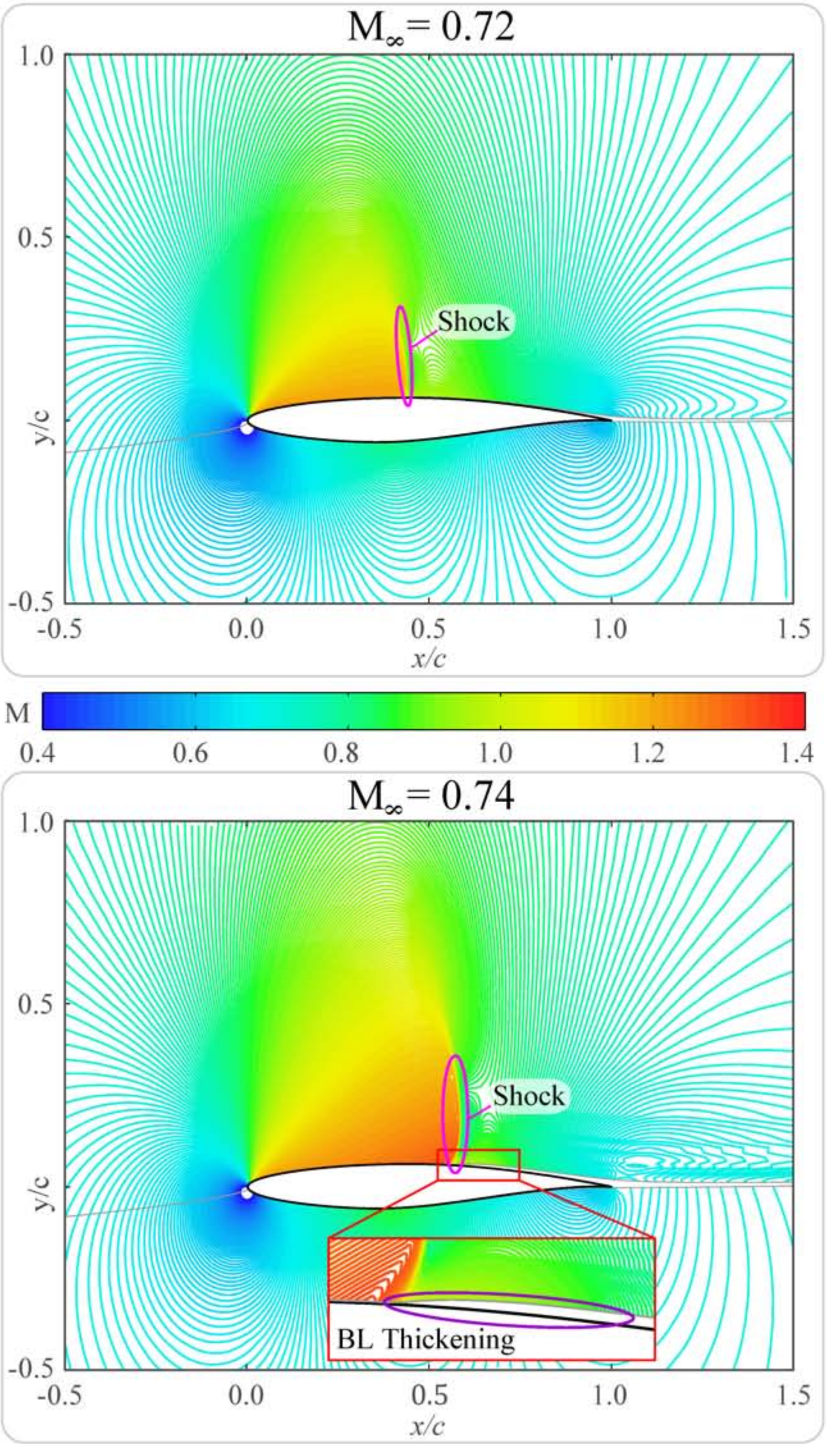

Figure 4-15: Mach contours of RAE2822 airfoil at $M_\perp = 0.72$ (upper) and $M_\perp = 0.74$ (lower). Boundary layer thickens downstream of the shock at $M_\perp = 0.74$.

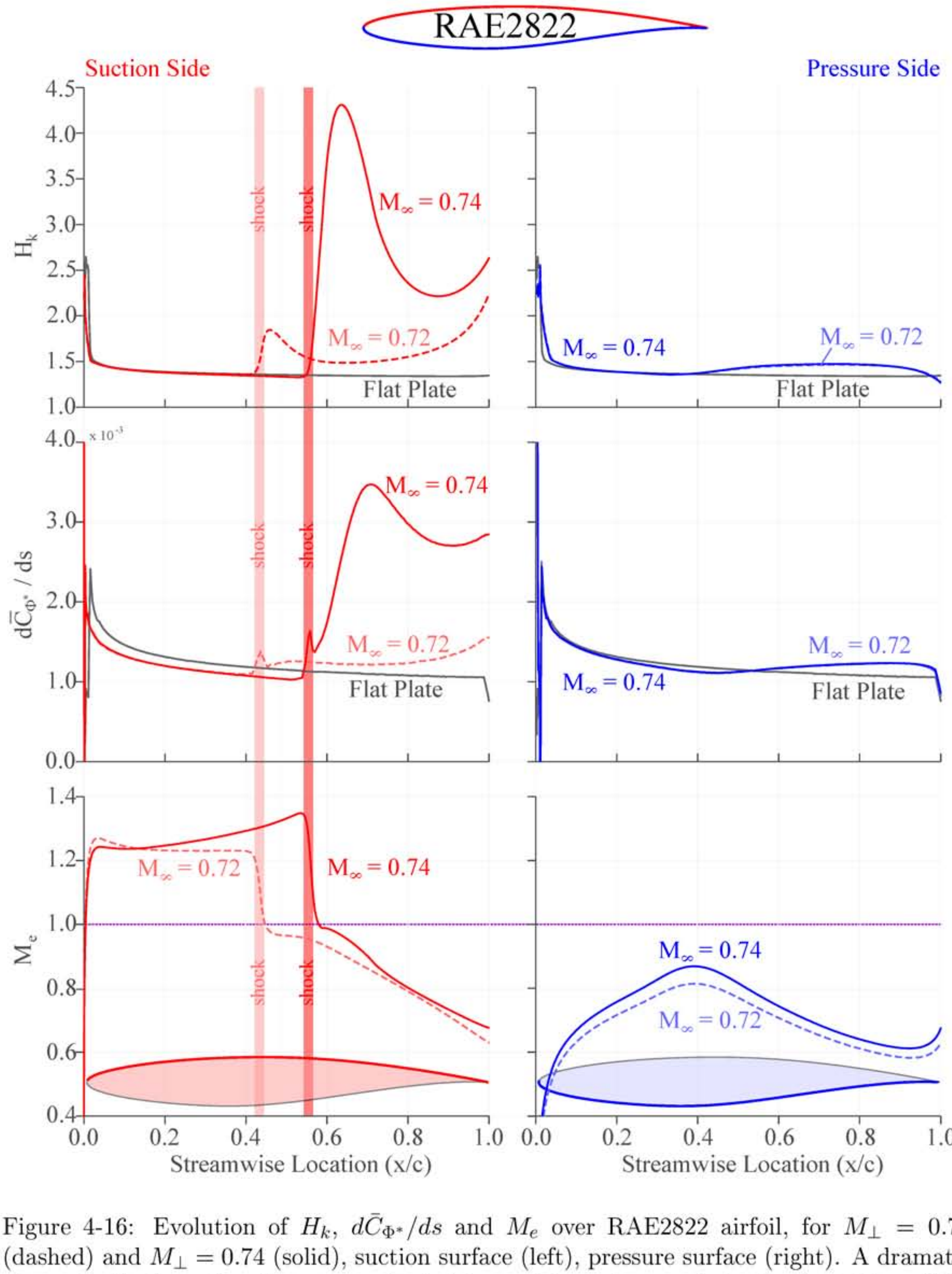

Figure 4-16: Evolution of H_k, $d\bar{C}_{\Phi^*}/ds$ and M_e over RAE2822 airfoil, for $M_\perp = 0.72$ (dashed) and $M_\perp = 0.74$ (solid), suction surface (left), pressure surface (right). A dramatic change in the boundary layer property is triggered downstream of the shock at $M_\perp = 0.74$.

the suction surface of the airfoil in Figure 4-17, for $\alpha = 2°$(green) and $\alpha = 3°$(purple). As shown, e_{K_f} increases rapidly for airfoils with $M_{max} > 1.15$. The estimation should therefore be limited to configurations with a peak Mach number over the airfoil surface less than $M_{max} = 1.15$. In a typical commercial airliner such as the Boeing 777, the perpendicular Mach number seen by the outer wing is about 0.7, and current design practice is not to have transonic airfoils operate with a suction surface peak Mach number greater than 1.15[7]. The present analytical method is therefore applicable in conceptual design of transonic airfoils used in commercial airliners.

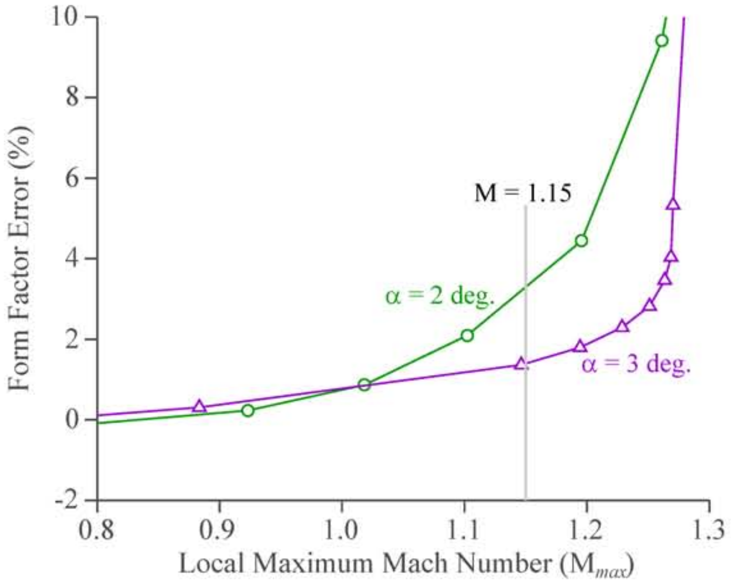

Figure 4-17: Error in form factor estimation vs. local maximum Mach number M_{max} for RAE2822 airfoil, at $\alpha = 2°$ (green) and $\alpha = 3°$ (purple). Magnitude of error exceeds 3% for $M_{max} > 1.15$.

4.3.4 Estimation of Form Factor Using Inviscid Calculations

The results presented in Section 4.3 focused on the accuracy of Eq. 4.11 assuming that the boundary layer edge velocity distribution is known *a priori*, which holds when the boundary layer edge velocity is given as design inputs. In many situations in aircraft conceptual design stages, however, the boundary layer edge velocity is not known and must be estimated using an inviscid calculation. This section presents the accuracy of the form factor estimates calculated based on the boundary layer edge velocity obtained from an inviscid calculation.

---

[7] per conversation with Prof. Drela

Figure 4-18 shows the form factor from MTFLOW results (blue), the estimated form factor using the boundary layer edge velocity from the viscous calculation (red) and the form factor obtained using the boundary layer edge velocity estimated from an inviscid calculation (green), as a function of body fineness ratio (l/d) at $M_\infty = 0.1$ (upper) and $M_\infty = 0.85$ (lower). Figure 4-19 shows the various form factors of GAW-1 airfoil as a function of lift coefficient (C_ℓ) at $M_\infty = 0.15$ and Figure 4-20 shows those for the RAE2822 airfoil for various perpendicular Mach number ($M_\perp$) at $\alpha = 3°$. The main takaway from Figures 4-18, 4-19 and 4-20 is that regardless of whether the form factor is calculated from the actual boundary layer edge velocity or from estimates based on inviscid calculation, the accuracy of the form factor obtained from Eq. 4.11 is not affected by more than 2% for the region of interest ($l/d > 5$, $C_\ell = -0.5 \sim 1.0$ and $M_\perp < 0.71$).

The fact that the accuracy of the form factor estimate is more accurate when calculated from the edge velocity estimates based on an inviscid calculation, is a result of contributions of different errors canceling. From the results in Sections 4.3.1, 4.3.1 and 4.3.1, the form factor estimates using Eq. 4.11 underpredict the actual form factor under the following conditions:

- when thickening / separation of boundary layer is observed: e.g., airfoil near stall condition and bluff bodies; and
- when the presence of shock with incoming Mach number greater than 1.15 is observed in the flow field,

where the loss generation inside the boundary layer is no longer similar to that over a flat plate.

When the form factor is calculated using an inviscid calculation, part of this error is canceled out by *overprediction* of the edge velocity from the elimination of the boundary layer displacement. The magnitude of overprediction increases with the magnitude of the boundary layer displacement, i.e. the edge velocity tends to be overpredicted more for flow with boundary layer closer to separation. The effect of elimination of boundary layer displacement is accentuated for flow with shocks, where the location and strength of the shock is affected by the presence of boundary layer displacement.

Figure 4-21 shows the comparison of the edge velocity distribution calculated from a viscous calculation (red) and that estimated from an inviscid calculation (green), for GAW-

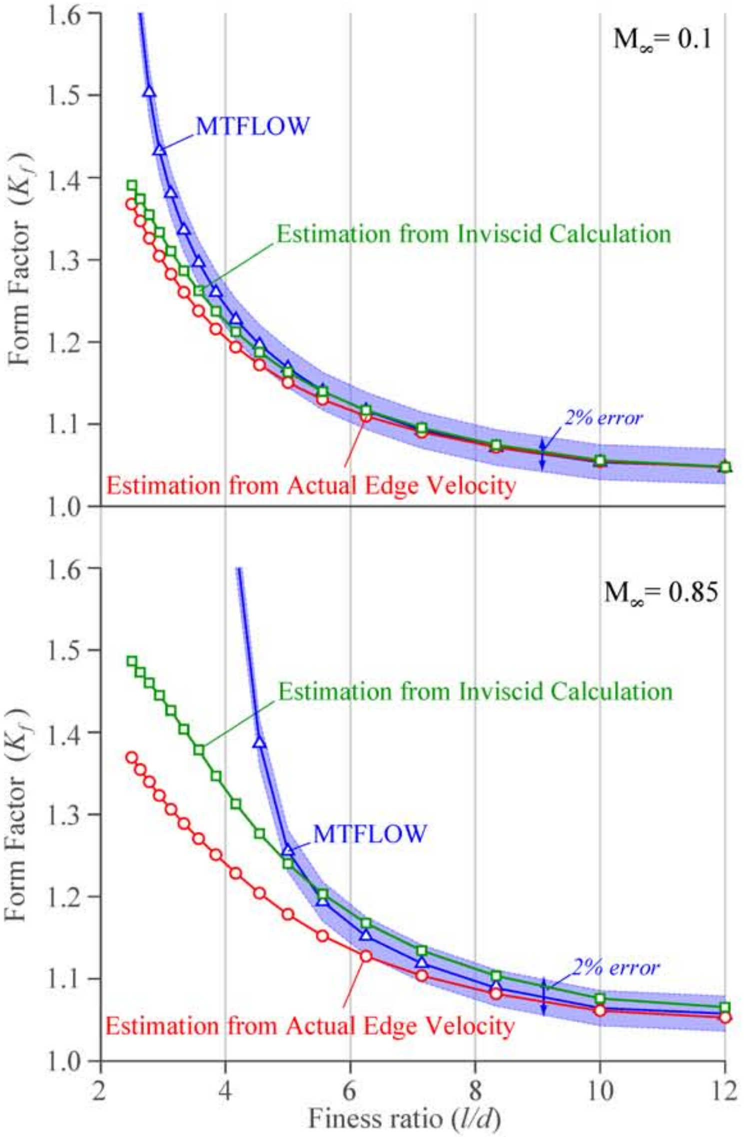

Figure 4-18: Form factor (K_f) vs. body fineness ratio (l/d), $M_\infty = 0.1$ (upper) and $M_\infty = 0.85$ (lower). The form factor estimated using the edge velocity obtained from inviscid calculations is more accurate than that estimated using the actual edge velocity.

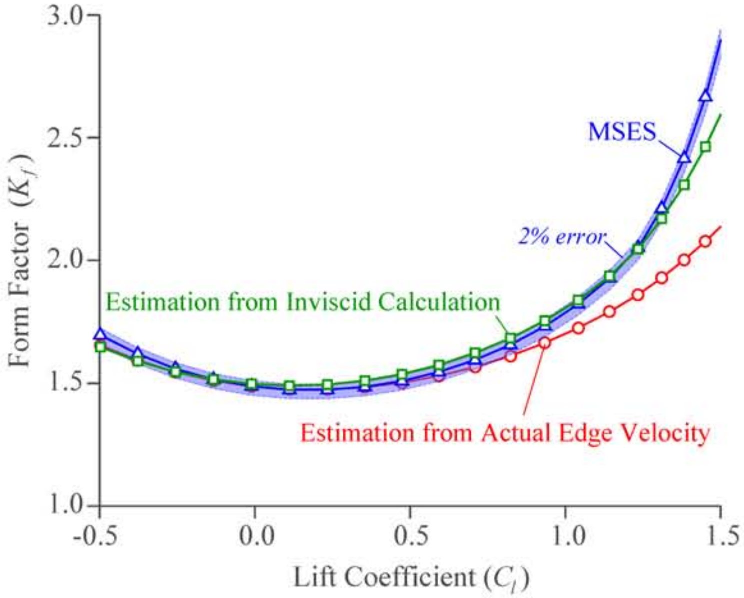

Figure 4-19: Form factor (K_f) vs. GAW-1 airfoil lift coefficient (C_ℓ), $M_\infty = 0.15$. The form factor estimated using the edge velocity obtained from inviscid calculations is more accurate than that estimated using the actual edge velocity.

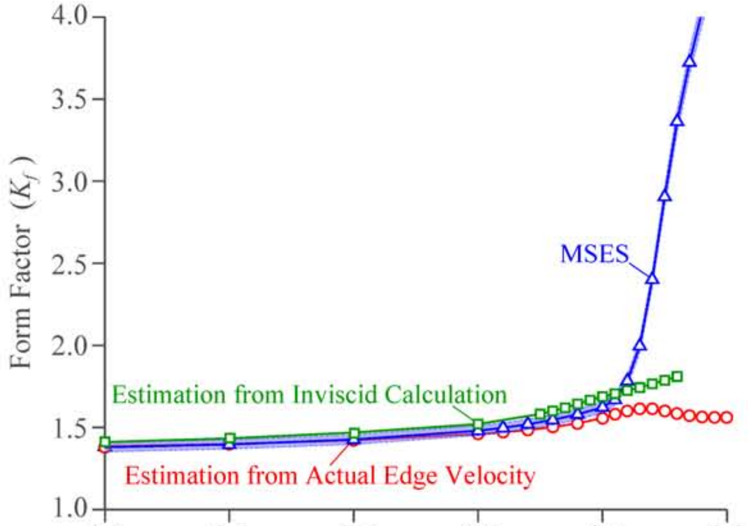

Figure 4-20: Form factor (K_f) vs. freestream Mach number, $\alpha = 3°$. The form factor estimated using the edge velocity obtained from inviscid calculations is more accurate than that estimated using the actual edge velocity.

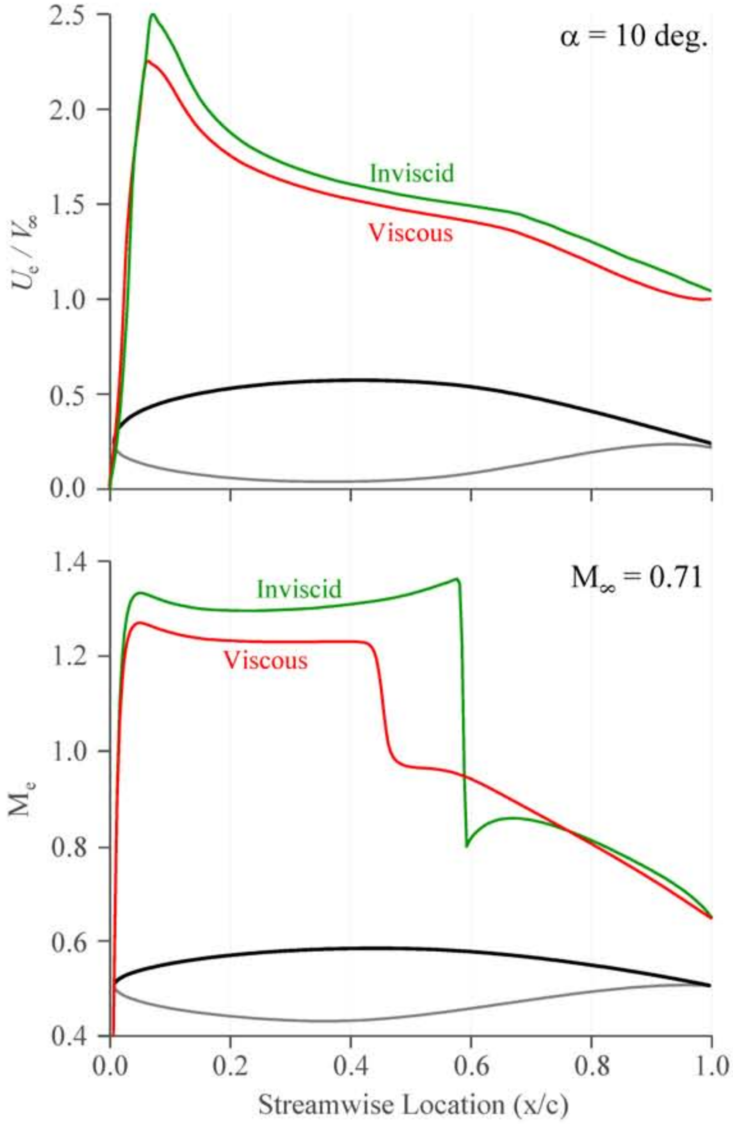

Figure 4-21: Edge velocity distributions over GAW-1 (upper, $\alpha = 10°$) and RAE2822 (lower, $M_\perp = 0.71$) airfoils.

1 airfoil at $\alpha = 10°$ and RAE2822 airfoil at $M_{\perp} = 0.71$. The edge velocity is overpredicted using the inviscid calculation in both cases. A large discrepancy is seen in the RAE2822 results, as the shock location is affected by the presence of the boundary layer displacement. Summary over the ranges of interest, there is no drawback in estimating the form factor with Eq. 4.11 using the edge velocity estimates from an inviscid calculation.

4.4 Summary

In this chapter, an analytical expression for the form factor used in the wetted area method was developed (Eq. 4.11). The expression is a function of edge density, velocity, Mach number and geometry. These quantities are either inputs for airfoil design, or obtained using a source line model [14] or other inviscid flow calculation methods. Unlike empirical form factor correlations, this form factor calculation method can be applied reliably to a new geometry for which experimental data is not available.

The accuracy of this form factor correlation were quantified by applying the method to three airfoil geometries where the wetted area method is commonly applied: a body of revolution at low and transonic Mach number, a low speed 2D airfoil and a transonic, 2D airfoil.

The results were compared against the form factors calculated from MSES and MTFLOW results. For all analyzed configurations, the developed form factor calculation method was accurate to within 2% for:

1. D8 fuselage section with fineness ratio (l/d) greater than 5 at $M_{\infty} = 0.1$, and greater than 6.25 at $M_{\infty} = 0.85$
2. GAW1 airfoil with lift coefficient between -0.5 and 1.0
3. RAE2822 airfoil with freestream Mach number up to $M_{\perp} = 0.71$ at $\alpha = 3°$

This result was as accurate as other empirical form factor correlations. The estimation error is found to increase under the following conditions (quantified in Section 4.3):

- when thickening / separation of boundary layer is observed: e.g., airfoil near stall condition and bluff bodies; and
- when the presence of shock with incoming Mach number greater than 1.15 is observed in the flow field.

This estimation method is applicable for preliminary performance calculation of transport aircraft at the cruise condition, as aircraft do not operate beyond the limiting conditions listed above at cruise: the aircraft fuselage typically have $l/d \sim 10$, low speed airfoils are operated at C_ℓ between 0.4 and 0.8 and transonic airfoils operate at $M_\perp \sim 0.7$, with a shock incoming Mach number less than 1.15.

Chapter 5

Effect of Interference on Mechanical Energy Loss

In this chapter we address the effect on airframe performance of interference effects, in other words the change in the mechanical loss when components are operated in interacting configurations. Interacting configurations are defined here as configurations which have separate aerodynamic bodies located close enough to each other so that the flow around each body, and hence the aerodynamic performance, is altered by the pressure field generated by other bodies by more than 10% from non-interacting configuration. The performance change due to interference effects is due to three sources: 1) change in profile mechanical loss; 2) change in induced drag due to variation in lift (and circulation) distribution, and 3)change in shock loss because of alteration of shock wave configurations.

Mechanisms 2 and 3 are related to losses in the equivalent inviscid flow (Φ^*_{EIF}) introduced in Chapter 3. These losses can be evaluated by simulating the entire configuration using an inviscid calculation and thus could be conducted during conceptual or conceptual design stages. Quantification of mechanism 1 using CFD in conceptual design, however, is challenging as viscous CFD is too computationally expensive to be run during early design and optimization and scaling laws are used to estimate the performance changes due to viscous effects.

In this chapter, we demonstrate that the change in the profile mechanical loss due to interference effects scales as $\rho_e U_e^3 \left(1 + \frac{\gamma-1}{2} M_e^2\right)^r$ as derived in Chapter 3, using results from CFD analysis of three basic interacting configurations: 1.) fuselage with actuator disk, 2.)

interfering airfoils and 3.) nacelle with actuator disk, to quantify the accuracy of the scaling law and to identify its limitations. The scaling law is also applied to estimate the profile mechanical loss of an interacting configuration based on the flow over a configuration with the same components in isolation.

Section 5.1 introduces the scaling law for mechanical loss due to interference effects and the parameters used to quantify its accuracy, explains the limitations of the scaling and describes the configurations analyzed to assess its accuracy. Section 5.2, 5.3, and 5.4 assess the accuracy of the mechanical energy scaling for the fuselage and actuator disk (Section 5.2), the interacting airfoils (Section 5.3), and the nacelle with actuator disk (Section 5.4). Section 5.5 introduces and assesses a method to estimate the profile mechanical loss of interacting configuration from the performance of non-interacting components. Section 5.6 summarizes the findings of this chapter.

5.1 Scaling of Interference Effects

One challenge in the performance estimation for an interacting configuration is the presence of the so-called "potential effect[1]" i.e. the changes in pressure distributions caused by component interaction. To illustrate the issue we show in figure 5-1, measurement of drag for a pair of strut sections in tandem [20]. The drag of the front strut (shown in blue) decreases as the two struts are brought together, because the static pressure between the two struts increases as they are brought together, resulting in a forward force on the front strut. Because of this pressure interaction, the individual force acting on each strut does not give meaningful information about its viscous drag. The only meaningful quantity for the configuration is the total drag, because the forces due to field effects mostly cancel out between the two bodies. Even further for a configuration where an airframe and a propulsor are interacting the total force over the entire configuration is not meaningful, because its value is zero for an aircraft at cruise condition. In contrast, performance assessment using the power balance method is quantified in terms of dissipation and kinetic energy defects, which are not explicitly affected by the local change in pressure distribution.

Another challenge is that the local skin friction coefficient (c_f) is affected by pressure gradient, as mentioned in Chapter 3. Conventional estimates of drag due to interference

---

[1] pressure "field effect"as termed by Smith [39]

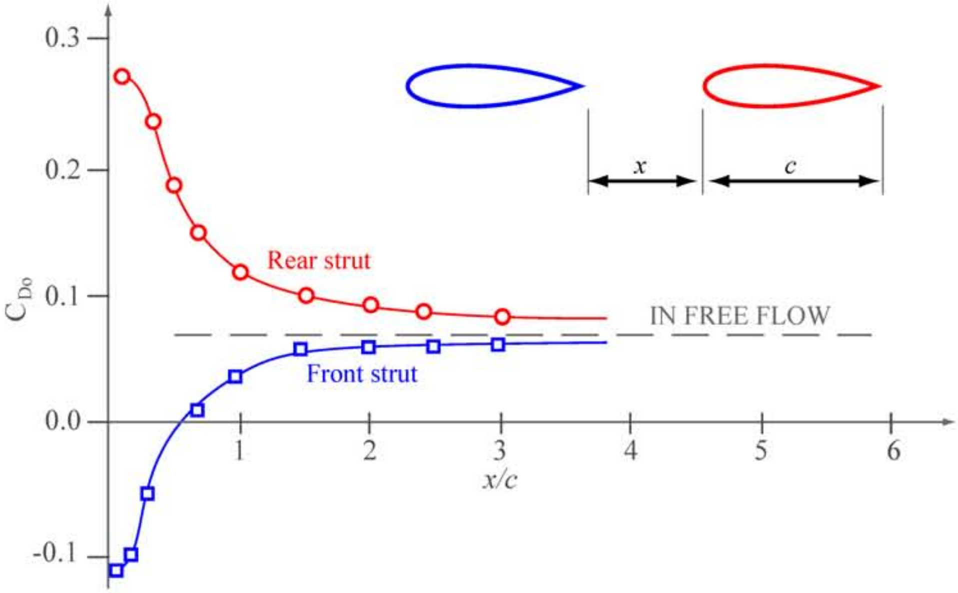

Figure 5-1: Drag of a pair of strut sections in tandem. (Adapted from [20]) Negative drag force acts on the front strut as the two struts are within 0.5 chord length away from each other.

effects which scale the individual drag contributions with $\rho_e U_e^2$, in other words with dynamic pressure, are thus inaccurate. The discrepancy between the calculated drag from this scaling and the actual drag is attributed to an additional "interference drag", which is calculated from empirical correlations [20]. The local dissipation coefficient, $c_{\mathcal{D}}$, used in the power balance method is less affected by the change in pressure gradient and is nearly unchanged between non-interacting and interacting configurations. The mechanical loss therefore scales with $\rho_e U_e^3 \left(1 + \frac{\gamma-1}{2} M_e^2\right)^r$ to a much greater accuracy, as derived in Chapter 3.

As such, the power balance method offers an advantage in assessing the performance of an interfering configuration. However, limitations exist in the use of the power balance method, which need to be quantified. The following section introduces the parameters used to quantify the accuracy of the scaling law, explains its limitations, and describes the configurations analyzed in this study.

5.1.1 Scaling Parameters

In comparing the performance between the interacting and the non-interacting configurations, we define the following quantities, the quantities with prime ($'$) representing values for the interacting configuration:

- Loss variation coefficient (LVC) represents the difference in profile mechanical loss between the non-interacting and interacting configurations

$$\mathrm{LVC} \equiv \frac{\Phi_p^{*\prime} - \Phi_p^*}{\Phi_p^*} \times 100\%. \tag{5.1}$$

- Drag variation coefficient (DVC) represents the difference in "profile drag" between the non-interacting and interacting configurations.

$$\mathrm{DVC} \equiv \frac{D_p' - D_p}{D_p} \times 100\%. \tag{5.2}$$

The results in this chapter focus on configurations with large interference effect, i.e., configurations with LVC and DVC greater than 10%.

In determining whether the interference effect scales with $\rho_e U_e^3 \left(1 + \frac{\gamma-1}{2} M_e^2\right)^r$ or with $\rho_e U_e^2$, we define the quantities below:

- The average mechanical loss coefficient $\bar{C}_{\Phi^*}$ is the mechanical loss of the configuration normalized using the loss scaling obtained from Chapter 3.

  $$\bar{C}_{\Phi^*} \equiv \frac{\left(1 + \frac{\gamma-1}{2} M_e^2\right)^r \Big|_{TE} \Phi^*}{\left[\rho_e U_e^3 \left(1 + \frac{\gamma-1}{2} M_e^2\right)^r\right]_{ave} c}, \tag{5.3}$$

  where

  $$\left[\rho_e U_e^3 \left(1 + \frac{\gamma - 1}{2} M_e^2\right)^r\right]_{ave} \equiv \frac{\int_{LE}^{TE} \rho_e U_e^3 \left(1 + \frac{\gamma-1}{2} M_e^2\right)^r ds}{c}. \tag{5.4}$$

- The average drag coefficient $\bar{C}_d$ is an overall quantity analogous to $\bar{C}_{\Phi^*}$, but based on drag and normalized by $\left[\rho_e U_e^2\right]_{ave} c$. It is defined as

  $$\bar{C}_d \equiv \frac{D}{[\rho_e U_e^2]_{ave}\, c}, \tag{5.5}$$

  where

  $$\left[\rho_e U_e^2\right]_{ave} \equiv \frac{\int \rho_e U_e^2 \, ds}{c}. \tag{5.6}$$

  This $\bar{C}_d$ is half of the usual drag coefficient definition, to allow direct comparison with $\bar{C}_{\Phi^*}$.

If $\bar{C}_{\Phi^*}$ is the same between interacting and non-interacting configurations, it indicates that the proposed scaling for the mechanical loss is appropriate. The same applies for $\bar{C}_d$.

5.1.2 Limitations

The scaling of mechanical loss used in this analysis is derived from the boundary layer mechanical energy equation described in Chapter 3, where two approximations were made:

1. The baroclinic power[2] is calculated assuming $\delta^{**} \approx \mathcal{R}\theta^*$ (adiabatic flow with small[3] pressure gradient).
2. $c'_{\mathcal{D}} \approx c_{\mathcal{D}}$ (normalized boundary layer dissipation does not vary between non-interacting and interacting configurations).

Assumption 1 breaks down when the boundary layer goes through a large pressure rise, such as the one caused by a shock or an actuator disk. Assumption 2 breaks down when the boundary layer separates due to the interference between the aerodynamic components. In the following sections, the accuracy of the mechanical loss scaling is evaluated using the CFD results of the interacting configurations described in Section 5.1.3.

5.1.3 Analyzed Configurations

The BLI aircraft of interest are highly interacting configurations in which the fuselage, propulsor and nacelle are tightly integrated. We assess the accuracy and the limitation of the mechanical loss scaling using three examples that include key features of the BLI configuration (shown in Figure 5-2):

1. Fuselage with actuator disk, to investigate changes in the fuselage profile mechanical loss due to interaction with propulsors of various size and strength.
2. Interfering airfoils, to investigate changes in the profile loss due to the mutual interaction of airfoils.
3. Nacelle with actuator disk, to investigate changes in nacelle external and internal duct mechanical loss caused by variation in the propulsor characteristics.

---

[2] $\Pi_V = \iint \mathbf{D} \cdot \bar{\nabla} \frac{1}{2} U_e^2 \, d\mathcal{S}$.

[3] to be quantified in Sections 5.2, 5.3 and 5.4

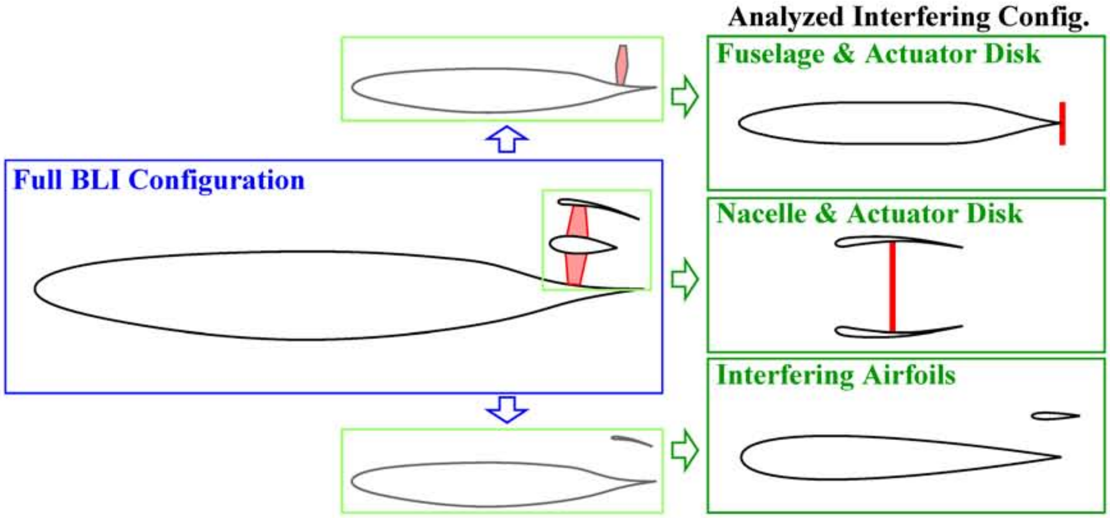

Figure 5-2: Canonical examples for BLI performance evaluation

For each example, MSES calculations of non-interacting components and the interacting configuration were conducted to quantify the magnitude of interference. In the analysis presented in this chapter, we focus solely on the effect of interference to the profile mechanical loss.

Although the examples in this section are two-dimensional for simplicity, the methodology presented is applicable to three-dimensional flow, although some consideration needs to be made to handle cross flow in the boundary layer.

5.2 Fuselage and Actuator Disk Configuration

Our goal is to quantify the change in surface mechanical loss $\left(\Phi^*_{surf}\right)$ between BLI and non-BLI configurations, and determine its scaling. We define a symmetric 2-D body, shown in Figure 5-3, with the thickness distribution taken from the D8.5 fuselage design of the NASA N+3 project [14]. The propulsor is modeled as a lossless actuator disk, with a prescribed uniform increase in stagnation pressure. The parameters varied are highlighted in red in Figure 5-3:

- Free stream Mach number (M_∞): D8.5 reference value $M_{\infty ref} = 0.74$.
- Propulsor stagnation pressure rise ($\Delta C_{p_t} \equiv \Delta p_t / \left(p_{t\infty} - p_\infty\right)$): D8.5 reference $\Delta C_{p_t} = 1.4$.

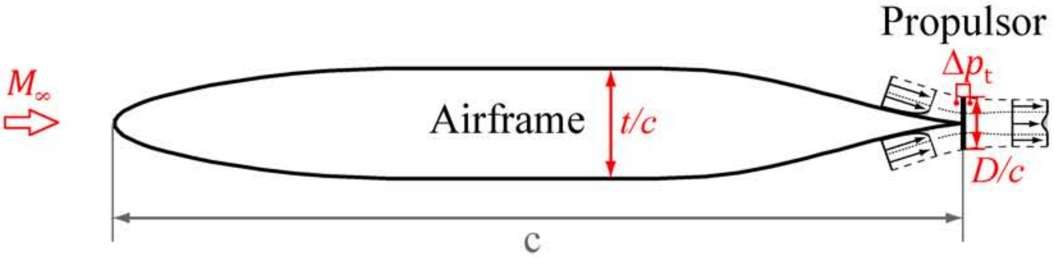

Figure 5-3: Airfoil with actuator disk configuration

- Airframe maximum thickness to chord ratio (t/c): D8.5 reference $(t/c)_{ref} = 11.7\%$. For freestream Mach numbers different than the cruise value, a Prandtl-Glauert transformation was used to give corresponding airframe thickness:

$$\left(\frac{t}{c}\right)_{@M_{\infty A}} = \frac{\sqrt{1 - M_{\infty ref}^2}}{\sqrt{1 - M_{\infty A}^2}} \left(\frac{t}{c}\right)_{D8.5}. \tag{5.7}$$

- Propulsor diameter to airframe chord ratio (D/c): D8.5 reference $(D/c)_{ref} = 0.08$.

The chord Reynolds number (Re_c) was fixed at 1.2×10^8, with boundary layer trips prescribed at $s/c = 0.01$ from the leading edge stagnation point. The principal quantity of interest is the airframe surface mechanical loss, Φ^*_{surf}, obtained by evaluating the airfoil trailing edge kinetic energy defect $\mathbf{K}_{TE}$.

5.2.1 Definition of "Drag"

To compare the power balance method and the momentum balance method, we need to define an equivalent performance metric using momentum. As mentioned the force on the body is influenced by the "potential" effect so the actual force acting on the body is not a suitable performance metric. The total force on the configuration is also not useful in quantifying the drag of the body, as there is no rigorous method to separate thrust and drag forces.

We will use a method developed by Sargeant [35] to define a performance metric for momentum balance. The momentum defect computed at the trailing edge of the airframe just in front of the propulsor is allowed to return to freestream pressure through the hypothetical process illustrated in Figure 5-4. We can find an approximate profile drag using the Squire and Young relation [47]:

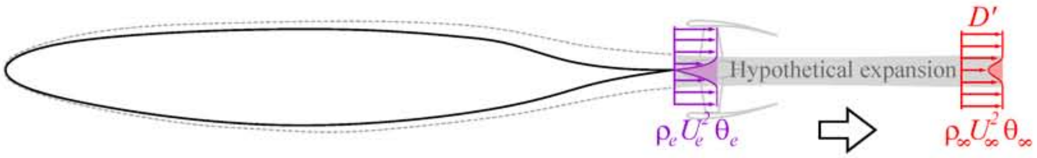

Figure 5-4: Trailing edge momentum defect returned to freestream pressure

$$D'_p = \rho_\infty U_\infty^2 \theta_\infty = \rho_e U_e^2 \theta_e \left(\frac{U_e}{U_\infty}\right)^{\bar{H}_k}, \tag{5.8}$$

where $\bar{H}_k$ is the average kinematic shape factor during the expansion process, approximated as an arithmetic mean between the kinematic shape factor at the trailing edge ($H_{k_{TE}}$) and the kinematic shape factor far downstream of the airframe (H_{k_∞}). The assumed expansion process is not required in the power balance method, as elaborated in Chapter 6.

5.2.2 Interference Effect

Figure 5-5 shows the loss variation coefficient (LVC from Eq. 5.1) as a function of actuator disk pressure rise ($\Delta C_{pt} \equiv \Delta p_t / (p_{t\infty} - p_\infty)$) for $M_\infty = 0.74$. Results are given for propulsor diameter to fuselage chord ratios (D/c) of 0.08 (green) and 0.5 (purple). In Figure 5-5 the loss variation coefficient, LVC, of the $D/c = 0.08$ configuration is smaller than 1%, because the region of influence of the propulsor is proportional to the actuator disk size [15] and for a typical BLI configuration with actuator disk much smaller than the airfoil chord length ($D/c < 0.1$), the variation of both loss and drag is negligible[4]. For the $D/c = 0.5$ configurations, on the other hand, the large propulsor accelerates the incoming flow over a large region of the fuselage, causing the mechanical loss to increase. At $\Delta C_{pt} = 1.4$, the increase in LVC is 25%. The rest of the analysis in this section will focus on the $D/c = 0.5$ configuration.

5.2.3 Scaling Accuracy

To assess the accuracy of the scaling law of the profile mechanical loss and the profile drag against the boundary layer edge quantities, we evaluate the relative change of the average mechanical loss ($\bar{C}_{\Phi^*}$, Eq. 5.3) and the average drag coefficient ($\bar{C}_d$, Eq. 5.5):

---

[4] Based on this result, the evaluation of BLI performance presented in Chapter 6 is conducted assuming that the fuselage surface mechanical loss is not affected by BLI.

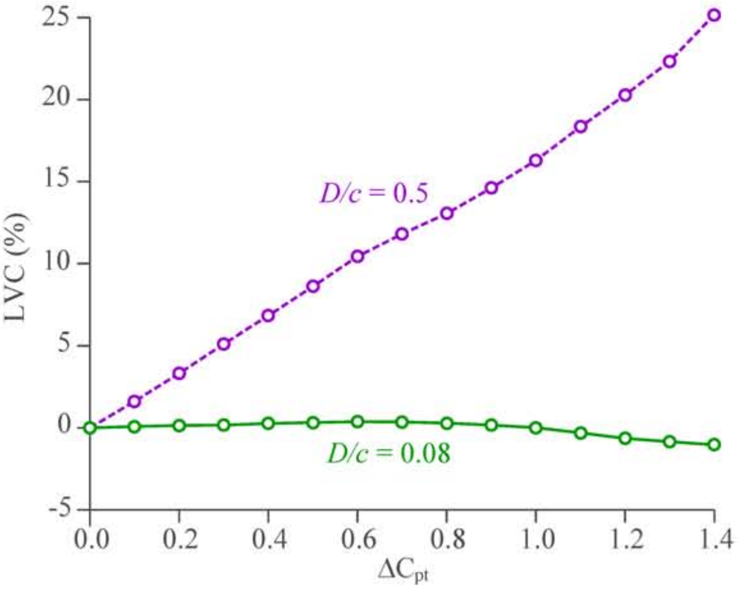

Figure 5-5: Loss variation coefficient (LVC, Eq. 5.1) vs. actuator disk pressure rise $\Delta C_{pt} \equiv \Delta p_t / (p_{t\infty} - p_\infty)$, for $M_\infty = 0.74$ for two different actuator disk diameters.

$$\Delta \bar{C}_{\Phi^*} \equiv \frac{\bar{C}'_{\Phi^*} - \bar{C}_{\Phi^*}}{\bar{C}_{\Phi^*}} \times 100\%, \tag{5.9}$$

$$\Delta \bar{C}_d \equiv \frac{\bar{C}'_d - \bar{C}_d}{\bar{C}_d} \times 100\%. \tag{5.10}$$

Figure 5-6 shows $\Delta \bar{C}_{\Phi^*}$ (red) and $\Delta \bar{C}_d$ (blue) as a function of actuator disk pressure rise for $M_\infty = 0.05$ (uppermost), $M_\infty = 0.60$ (center) and $M_\infty = 0.74$ (lowermost). The mechanical loss of the configuration scales accurately with $\rho_e U_e^3 \left(1 + \frac{\gamma-1}{2} M_e^2\right)^r$, as seen from the value of $\Delta \bar{C}_{\Phi^*}$ within 1% for $M_\infty = 0.05$ and $M_\infty = 0.60$, and within 6% for $M_\infty = 0.74$ at $\Delta C_{pt} = 1.4$. The profile drag does not scale with $\rho_e U_e^2$ as accurately, with a variation of 19% at $M_\infty = 0.74$.

Source of Error

Although the magnitude of $\Delta \bar{C}_{\Phi^*}$ is small (<6%), it increases rapidly as the freestream Mach number is increased from $M_\infty = 0.6$ to $M_\infty = 0.74$. For $\Delta C_{pt} = 1.4$, $\Delta \bar{C}_{\Phi^*}$ is 0.7% at $M_\infty = 0.60$, and 6% at $M_\infty = 0.74$. This is because the assumption used to estimate the baroclinic power, listed in Section 5.1.2, becomes inaccurate at $M_\infty = 0.74$ where shock have formed. Figure 5-7 presents the pressure coefficient (C_p), the mechanical loss terms and

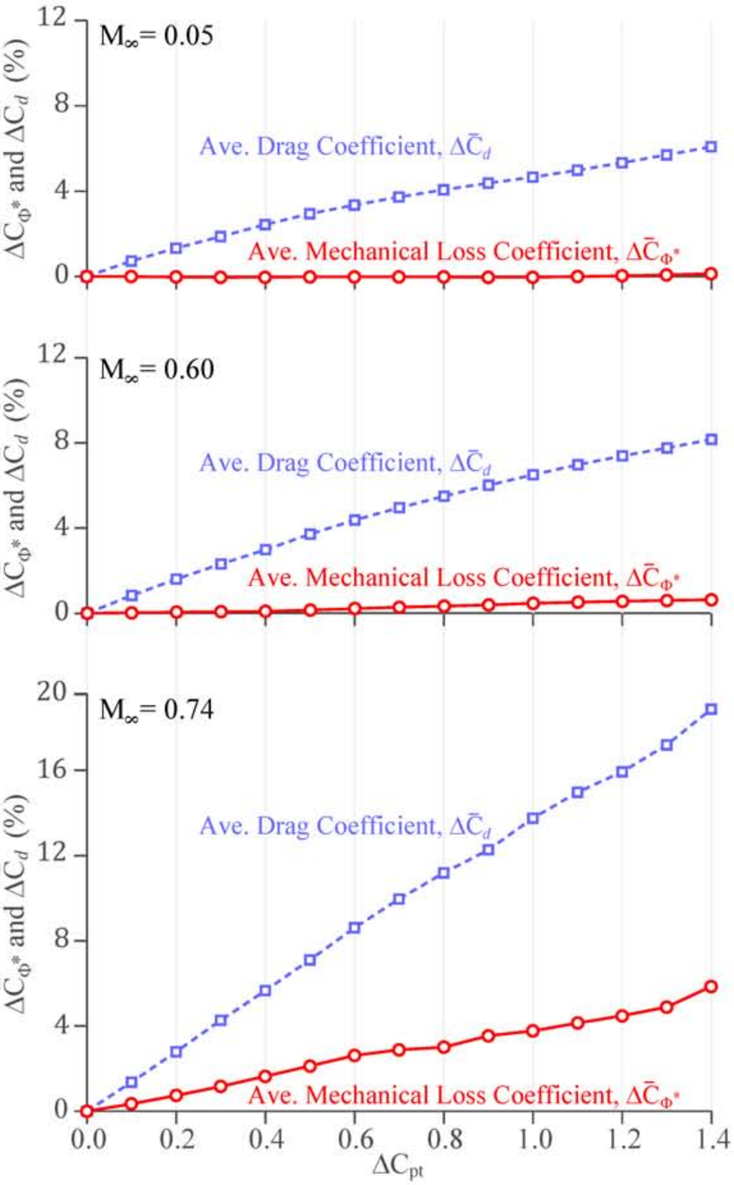

Figure 5-6: $\Delta\bar{C}_{\Phi^*}$ (red) and $\Delta\bar{C}_d$ (blue) vs. ΔC_{pt} for $M_\infty = 0.05$ (uppermost), $M_\infty = 0.60$ (center) and $M_\infty = 0.74$ (lowermost)

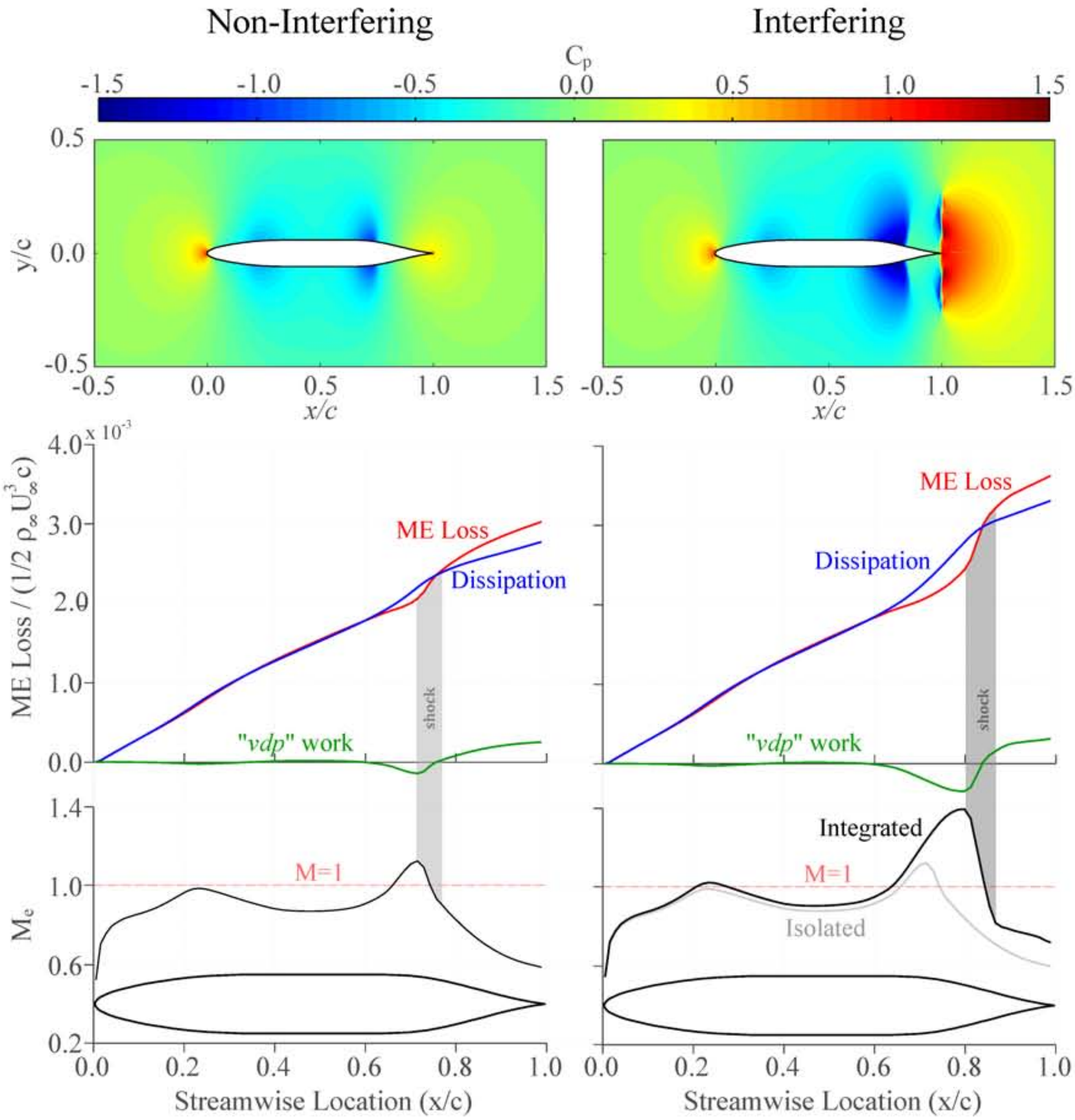

Figure 5-7: C_p contours, mechanical loss and boundary layer edge Mach number distribution of non-interacting (left) and interacting (right) configuration: propulsor $D/c = 0.5$, $\Delta C_{pt} = 1.4$, $M_\infty = 0.74$

the boundary layer edge Mach number profile around the non-interacting and interacting configuration at $M_\infty = 0.74$. Both configurations have a supersonic region near the trailing edge, but there is a much stronger shock for the interacting configuration (right), due to the flow acceleration caused by the propulsor. The shock generates a large pressure rise, which violates the assumption made in the baroclinic power calculation. This is also highlighted from the rapid change in the actual baroclinic power around the shock.

To support this argument, we compare the flow fields at $M_\infty = 0.6$ and $M_\infty = 0.74$ in Figure 5-8, for $\Delta C_{pt} = 1.4$. The uppermost plot shows the boundary layer kinematic shape parameter (H_k) along the airfoil. The middle plot shows the local normalized mechanical loss ${}^{d\bar{C}_{\Phi^*}}/_{ds}$, which is an important quantity for the assessment of the accuracy of the loss scaling. If the mechanical loss scaling using $\rho_e U_e^3 \left(1 + \frac{\gamma-1}{2} M_e^2\right)^r$ were perfect, the distribution of ${}^{d\bar{C}_{\Phi^*}}/_{ds}$ would be the same between non-interacting and interacting configuration. The lowermost plot shows the edge Mach number distribution.

For $M_\infty = 0.6$, there is little difference in the distribution of H_k and ${}^{d\bar{C}_{\Phi^*}}/_{ds}$ between non-interacting and interacting configurations. For $M_\infty = 0.74$, a spike in the local normalized mechanical loss occurs at $x/c = 0.84$, the location of the shock due to flow acceleration created by the propulsor.

The cause of the peak in the normalized loss generation comes from the increase in the baroclinic power across the shock which cannot be captured accurately from the $\delta^{**} \approx \mathcal{R}\theta^*$ approximation. This is illustrated in Figure 5-9, which shows the profile mechanical loss and the approximated mechanical loss, for $M_\infty = 0.74$ and $\Delta C_{pt} = 1.4$. The approximation error between the mechanical loss and the corrected dissipation has a sharp increase at the location of the shock in the interacting configuration. From Figure 5-6, the maximum value of $\Delta \bar{C}_{\Phi^*}$ was 6% from a shock with incoming Mach number of 1.4; if the Mach number over the fuselage is less than $M_e = 1.4$, the approximation error in baroclinic power will be less than 6%.

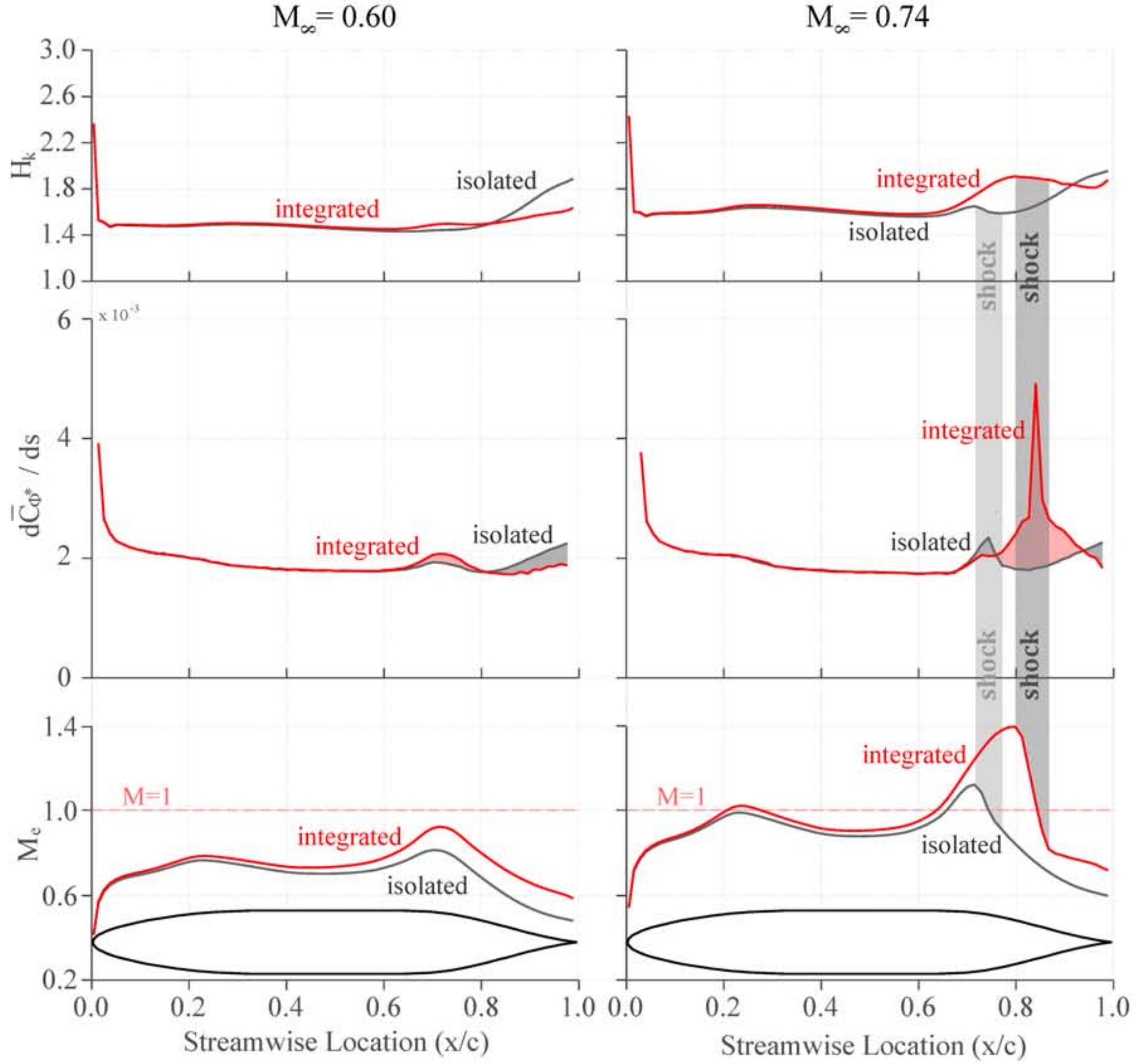

Figure 5-8: H_k, $d\bar{C}_{\Phi^*}/ds$ and M_e over D8.5 fuselage, for non-interacting and interacting configuration ($\Delta C_{pt} = 1.4$). Left: $M_\infty = 0.6$, right: $M_\infty = 0.74$. Gray lines represent values for the non-interacting configuration, and the red lines represent values for the interacting configuration. The strong shock causes large changes in the interacting $M_\infty = 0.74$ case.

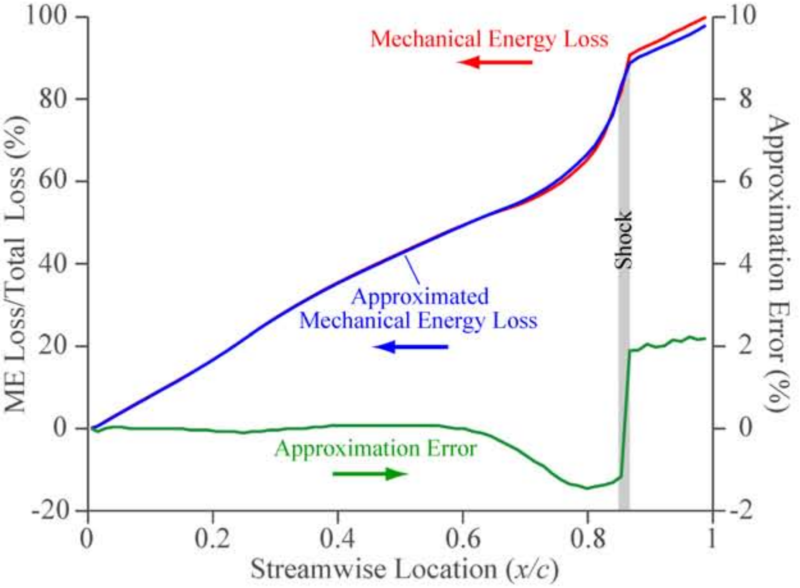

Figure 5-9: Mechanical energy loss, approximated mechanical loss and approximation error for interacting configuration, ($\Delta C_{pt} = 1.4$).

5.2.4 Summary

The following are the major findings from this analysis:

1. The interference effect is larger for larger propulsor (D/c). At $M_\infty = 0.74$ and propulsor $\Delta C_{pt} = 1.4$, the increase in the mechanical loss is less than 1% for $D/c = 0.08$ and about 25% for $D/c = 0.5$.

2. The change in the profile mechanical loss due to the interference effect scales as $\rho_e U_e^3 \left(1 + \frac{\gamma-1}{2} M_e^2\right)^r$. The maximum variation of $\Delta \bar{C}_{\Phi^*}$, which is a measure of how closely the mechanical loss scales as $\rho_e U_e^3 \left(1 + \frac{\gamma-1}{2} M_e^2\right)^r$, is within 6% for the configuration with $D/c = 0.5$ and $M_\infty = 0.74$. The "drag" does not scale with $\rho_e U_e^2$ as accurately, with a $\Delta \bar{C}_d$ of 19%.

3. The deviation of mechanical loss scaling from $\rho_e U_e^3 \left(1 + \frac{\gamma-1}{2} M_e^2\right)^r$ is due to the approximation error in baroclinic power, which assumes small pressure gradient and does not apply when the boundary layer interacts with shocks with incoming Mach number greater than 1.4. For the configurations analyzed, the error due to the approximation of baroclinic power term is within 6%. A shock of this strength would not be used in a design-point condition, however, so the error is of little concern in actual early design and optimization applications.

5.3 Interfering Airfoil Configuration

Changes in the profile mechanical loss between non-interacting and interacting airfoils are assessed using the 2-D configuration shown in Figure 5-10. The parameters varied are highlighted in red in the figure:

- Free stream Mach number (M_∞). Calculations are done at $M_\infty = 0.1$ to show features of incompressible flow, and at $M_\infty = 0.6$ to assess the effect of compressibility. A moderate Mach number was chosen in this analysis to avoid shock formation over the airfoil in non-interacting configuration.
- The relative size of airfoil 2, (c_2/c_1). Two values were examined: $(c_2/c_1) = 0.1$ and $(c_2/c_1) = 0.5$.
- Vertical distance between airfoils: (h/c_1). The smaller the distance, the larger the interference effect. In the simulation the distance was varied from 1.2 to 0.06 for $(c_2/c_1) = 0.1$ and from 1.2 to 0.12 for $(c_2/c_1) = 0.5$.
- Horizontal distance between airfoils: (d/c_1). Two values were examined:
    1. A mid-chord (MC) configuration with $d/c_1 = 0$, airfoil 2 located at mid chord of airfoil 1 where the local velocity is high.
    2. A trailing edge (TE) configuration with $d/c_1 = 0.5$, airfoil 2 located near the TE stagnation point of airfoil 1.

Both airfoils had $t/c = 12\%$ (NACA0012). The airfoil 1 chord Reynolds number (Re_{c_1}) was 1.2×10^8 with boundary layer trip at $s/c = 0.01$ from the leading edge stagnation point.

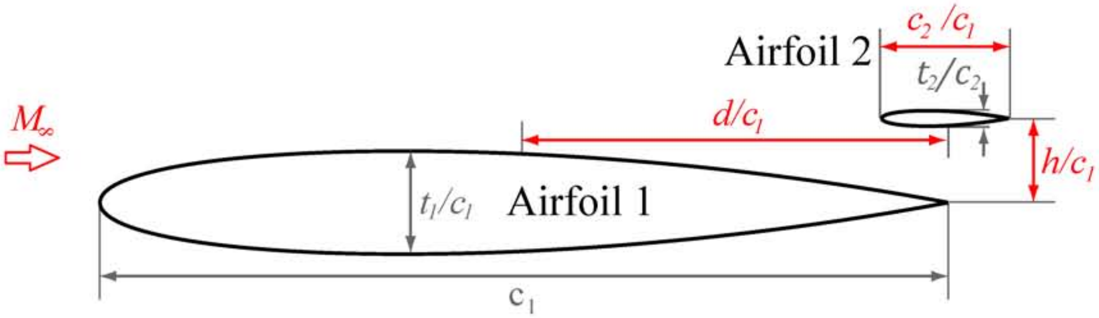

Figure 5-10: Interfering airfoil configuration

The quantity of interest in this example is the total profile mechanical loss of the entire configuration, the sum of the surface and the wake mechanical losses of both airfoils,

$$\Phi_p^* = \left(\Phi_{surf_1}^* + \Phi_{wake_1}^*\right) + \left(\Phi_{surf_2}^* + \Phi_{wake_2}^*\right). \tag{5.11}$$

An analogous quantity based on momentum is the total profile drag of the entire configuration (does not include wave drag),

$$D_p = D_{p_1} + D_{p_2}. \tag{5.12}$$

5.3.1 Mechanical Loss Scaling

Figure 5-11 shows the LVC as a function of the position of Airfoil 2 relative to Airfoil 1 for free stream Mach numbers of $M_\infty = 0.1$ (solid line) and $M_\infty = 0.6$ (dashed line). The geometry notation is as in Figure 5-10. The results are shown for the upper airfoil with $c_2/c_1 = 0.1$(upper plot) and $c_2/c_1 = 0.5$ (lower plot), at $d/c_1 = 0$ (purple line) and $d/c_1 = 0.5$ (green line). The region of pressure influence of each body scales with the relative size of the bodies [15], and the interference effect is larger for $c_2/c_1 = 0.5$ than for $c_2/c_1 = 0.1$. The rapid decay in pressure influence of aerodynamic bodies with the distance from the body [15] means that the magnitude of the interference effect has a sharp increase as two airfoils are brought together.

The reason for the smaller interference effects of the TE configuration compared to the MC configuration is explained by the flow feature differences. Figure 5-12 shows a comparison of Mach contours between the MC and TE configurations, for $M_\infty = 0.6$, $c_2/c_1 = 0.5$, and $h/c_1 = 0.24$. In the MC configuration, the location of maximum thickness of airfoil 1 and 2 occurs at approximately the same axial location ($x/c_1 \approx 0.45$), causing a contraction between the airfoils, the formation of a normal shock, and boundary layer separation. In the TE configuration, the maximum thickness of airfoil 2 occurs near the trailing edge of airfoil 1 and the flow passage is less affected. No shock is formed, and no boundary layer separation is observed. Although the magnitude of interaction varies with freestream Mach number and relative size of airfoil 2, the effect is always larger for MC configurations.

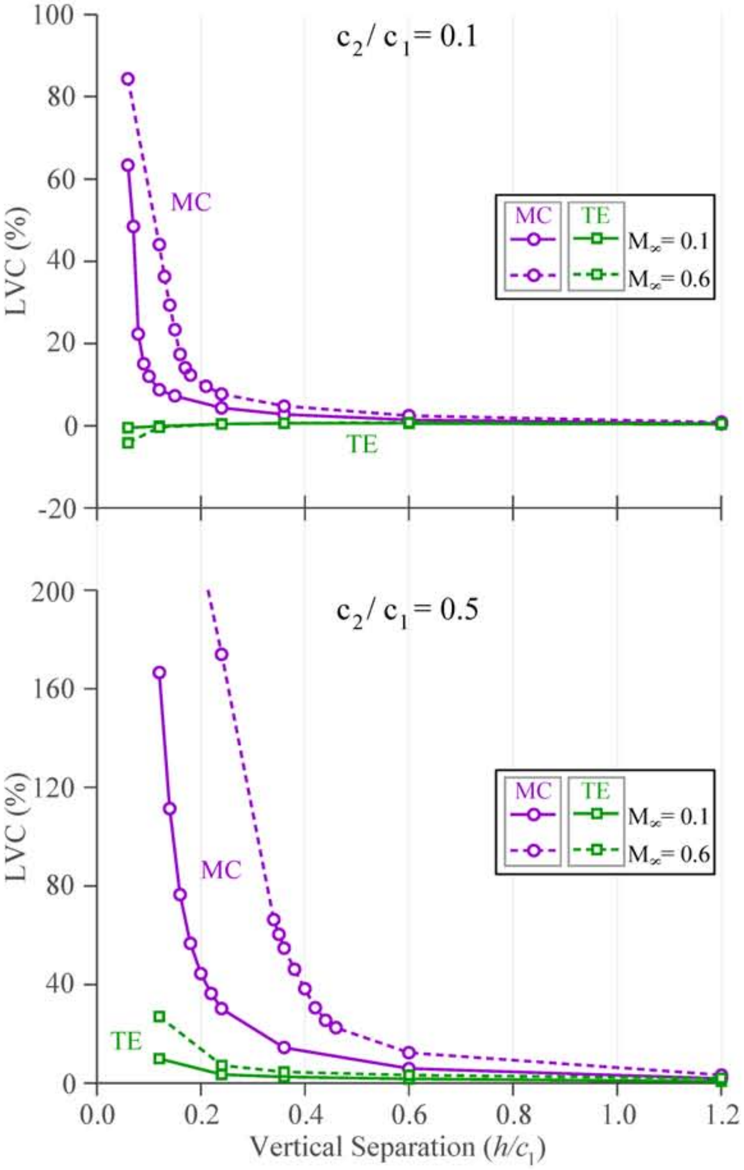

Figure 5-11: Loss variation coefficient (LVC) for various airfoil separations. $c_2/c_1 = 0.1$ (upper), $c_2/c_1 = 0.5$ (lower), for upper airfoil at mid-chord (MC, purple) and at trailing edge (TE, green).

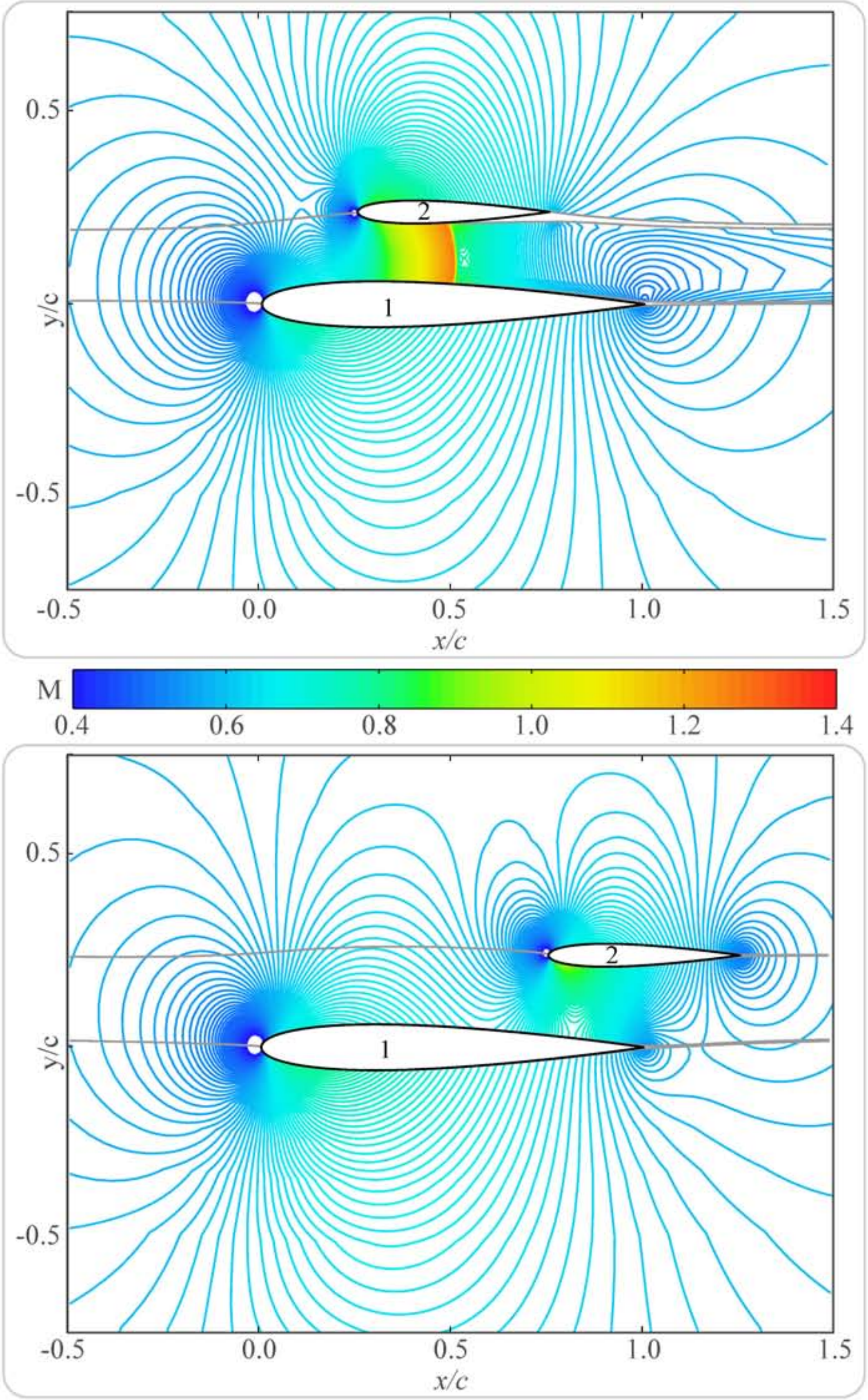

Figure 5-12: Mach contours of MC configuration (upper) and TE configuration (lower), $c_2/c_1 = 0.5$, $M_\infty = 0.6$. Stronger interference is seen in MC configuration in which there is a shock between the two airfoils due to a contraction.

5.3.2 Loss Scaling in Incompressible Flow

To visualize how the LVC scales with boundary layer edge quantities, the relative change of average mechanical loss and drag coefficient ($\Delta\bar{C}_{\Phi^*}$ and $\Delta\bar{C}_d$) were evaluated for MC configurations at $M_\infty = 0.1$. MC configurations were chosen because we are interested in cases with large interference effects. The boundary layer loss and drag are normalized by the average of edge quantities over the airfoil surface. Figure 5-13 shows $\Delta\bar{C}_{\Phi^*}$ (solid line) and $\Delta\bar{C}_d$ (dashed line) for $c_2/c_1 = 0.1$ (red) and $c_2/c_1 = 0.5$ (blue) configurations, as a function of vertical distance between the two airfoils (h/c_1).

Similar to the results in Section 5.2.3, the mechanical loss scales with $\rho_e U_e^3\left(1+\frac{\gamma-1}{2}M_e^2\right)^r$ better than the drag scales with $\rho_e U_e^2$, as seen from the larger variation of average drag coefficient ($\Delta\bar{C}_d$) than that of average loss coefficient ($\Delta\bar{C}_{\Phi^*}$). A sudden increase in $\Delta\bar{C}_{\Phi^*}$ is observed near $h/c_1 = 0.1$ for $c_2/c_1 = 0.1$ and $h/c_1 = 0.2$ for $c_2/c_1 = 0.5$, indicating the mechanical loss no longer scales with $\rho_e U_e^3\left(1+\frac{\gamma-1}{2}M_e^2\right)^r$. We show that the increase is caused by the change in boundary layer properties between the non-interacting and interacting configuration, by computations of the following four configurations:

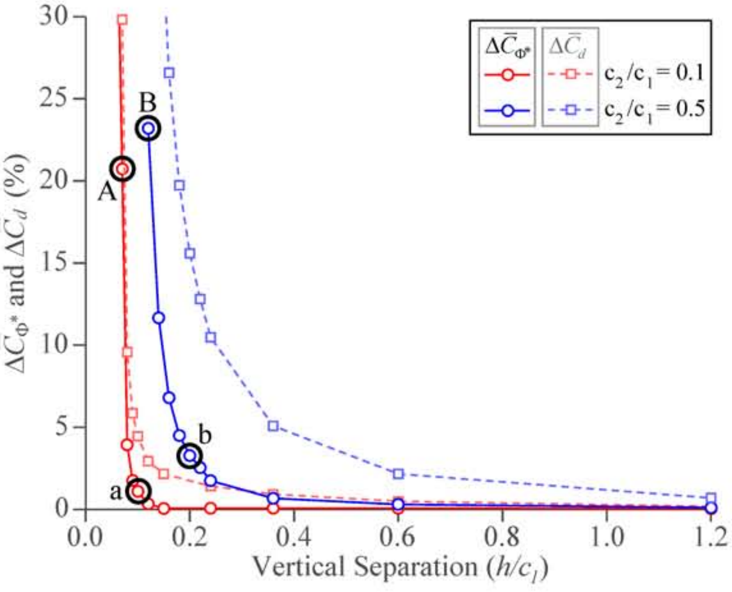

Figure 5-13: $\Delta\bar{C}_{\Phi^*}$ and $\Delta\bar{C}_d$ for MC configuration at $M_\infty = 0.1$

Configuration a: $c_2/c_1 = 0.1$, $h/c_1 = 0.1$. This configuration is the threshold case, just before the sharp increase in $\Delta\bar{C}_{\Phi^*}$ is observed in the $c_2/c_1 = 0.1$ configuration. ($\Delta\bar{C}_{\Phi^*} = 1\%$)

Configuration A: $c_2/c_1 = 0.1$, $h/c_1 = 0.07$. For this $c_2/c_1 = 0.1$ configuration the $\rho_e U_e^3 \left(1 + \frac{\gamma-1}{2} M_e^2\right)^r$ scaling is not appropriate. ($\Delta\bar{C}_{\Phi^*} = 21\%$)

Configuration b: $c_2/c_1 = 0.5$, $h/c_1 = 0.2$. This configuration is the threshold case, just before the sharp increase in $\Delta\bar{C}_{\Phi^*}$ is observed in the $c_2/c_1 = 0.5$ configuration. ($\Delta\bar{C}_{\Phi^*} = 4\%$)

Configuration B: $c_2/c_1 = 0.5$, $h/c_1 = 0.12$. For this $c_2/c_1 = 0.5$ configuration the $\rho_e U_e^3 \left(1 + \frac{\gamma-1}{2} M_e^2\right)^r$ scaling is not appropriate. ($\Delta\bar{C}_{\Phi^*} = 24\%$)

Source of Error

Figure 5-14 shows Mach number contours for configuration **a** ($c_2/c_1 = 0.1$, $h/c_1 = 0.10$) and configuration **A** ($c_2/c_1 = 0.1$, $h/c_1 = 0.07$), and Figure 5-15 shows Mach number contours for configuration **b** ($c_2/c_1 = 0.5$, $h/c_1 = 0.20$) and configuration **B** ($c_2/c_1 = 0.1$, $h/c_1 = 0.12$). The difference between the threshold (**a**, **b**) and extreme configurations (**A**, **B**) is the boundary layer separation observed in both **A** and **B** configurations which is generated by the strong adverse pressure gradient.

Figure 5-16 shows the boundary layer kinematic shape parameter H_k (uppermost), the local normalized loss generation $d\bar{C}_{\Phi^*}/ds$ (center), and the normalized edge velocity U_e/V_∞ (lower) over the airfoil surfaces for the $c_2/c_1 = 0.1$ configurations, Configuration **a** and **A**. Gray solid lines, colored dashed lines and colored solid lines represent values for the non-interacting configuration, configuration **a** and configuration **A** respectively. The primary cause of the increase in the mechanical loss is the change in the boundary layer properties, as seen in the change in H_k, caused by the flow deceleration seen near $x/c_1 = 0.48$. The loss generation follows the same trend as H_k, increasing sharply at the location of the flow deceleration. Unlike airfoil 1 where the flow acceleration and deceleration occurs over a short distance on the airfoil ($\sim$ 10% chord), airfoil 2, which is 10 times smaller than airfoil 1, sees a relatively mild flow deceleration over the entire airfoil. H_k and $d\bar{C}_{\Phi^*}/ds$ is therefore less affected on airfoil 2 than on airfoil 1.

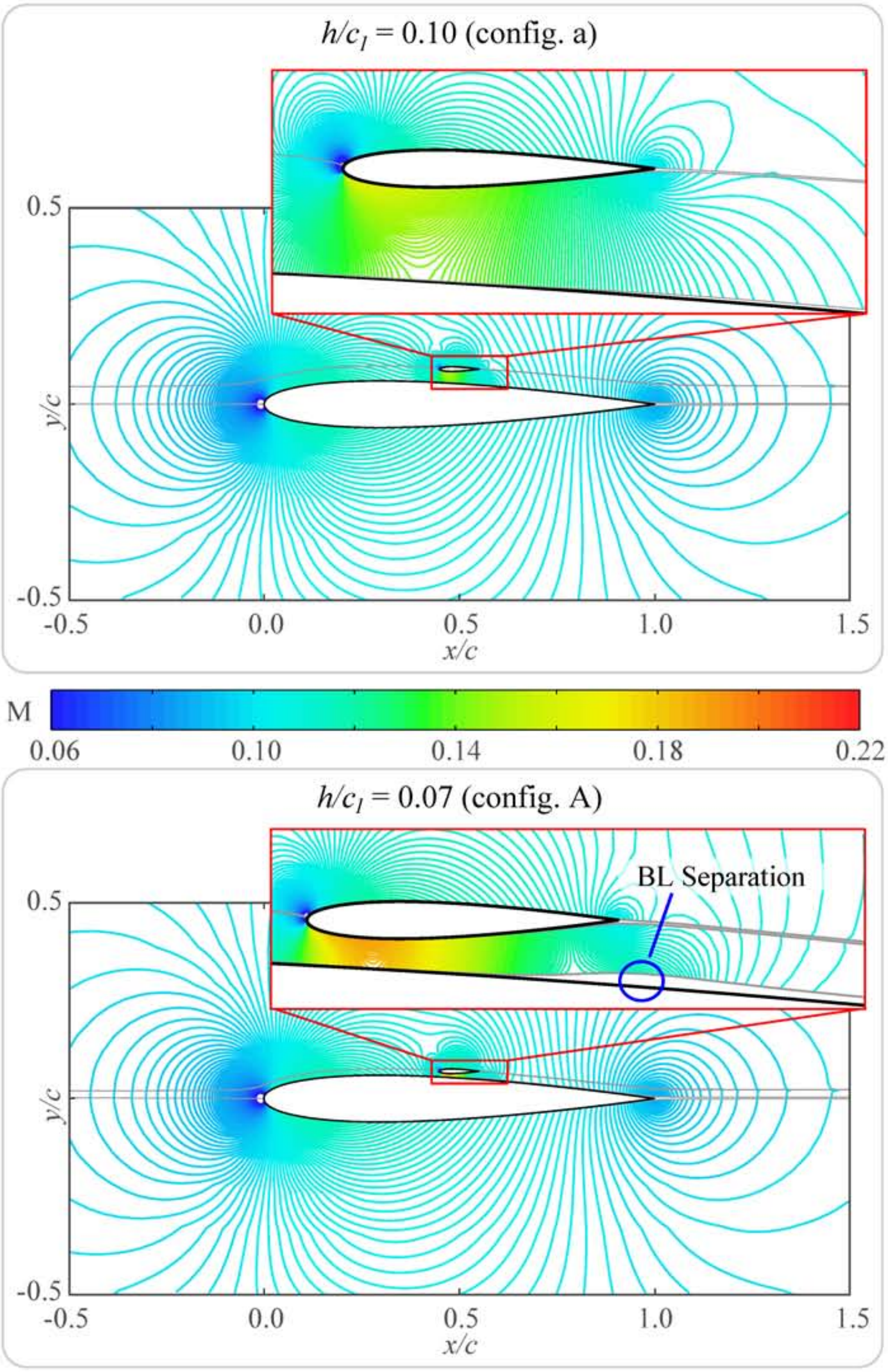

Figure 5-14: Mach contours of $c_2/c_1 = 0.1$ configurations at $M_\infty = 0.1$. Configuration **a** (upper, $h/c_1 = 0.10$) and **A** (lower, $h/c_1 = 0.07$)

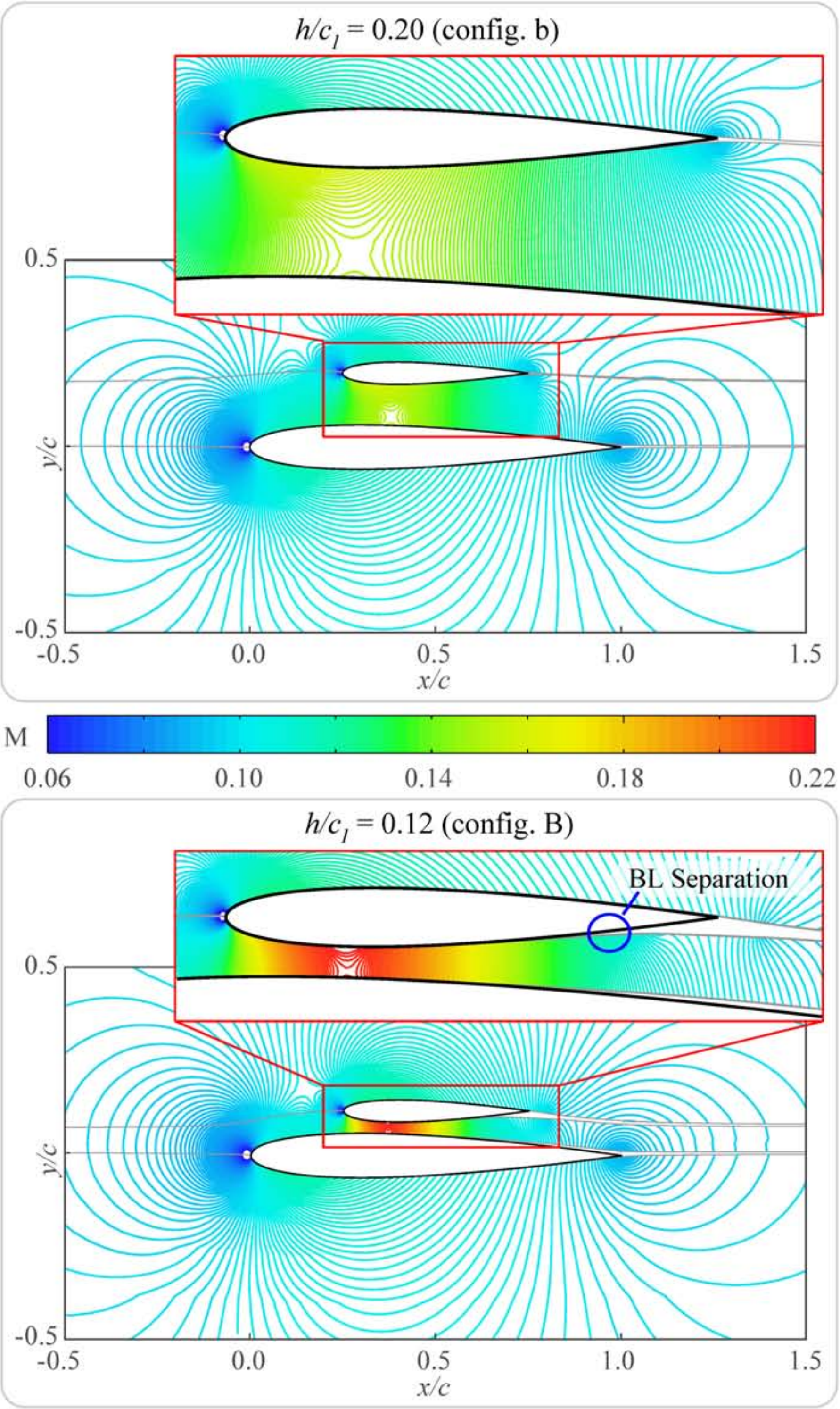

Figure 5-15: Mach contours of $c_2/c_1 = 0.5$ configurations at $M_\infty = 0.1$. Configuration **b** (upper, $h/c_1 = 0.20$) and **B** (lower, $h/c_1 = 0.12$)

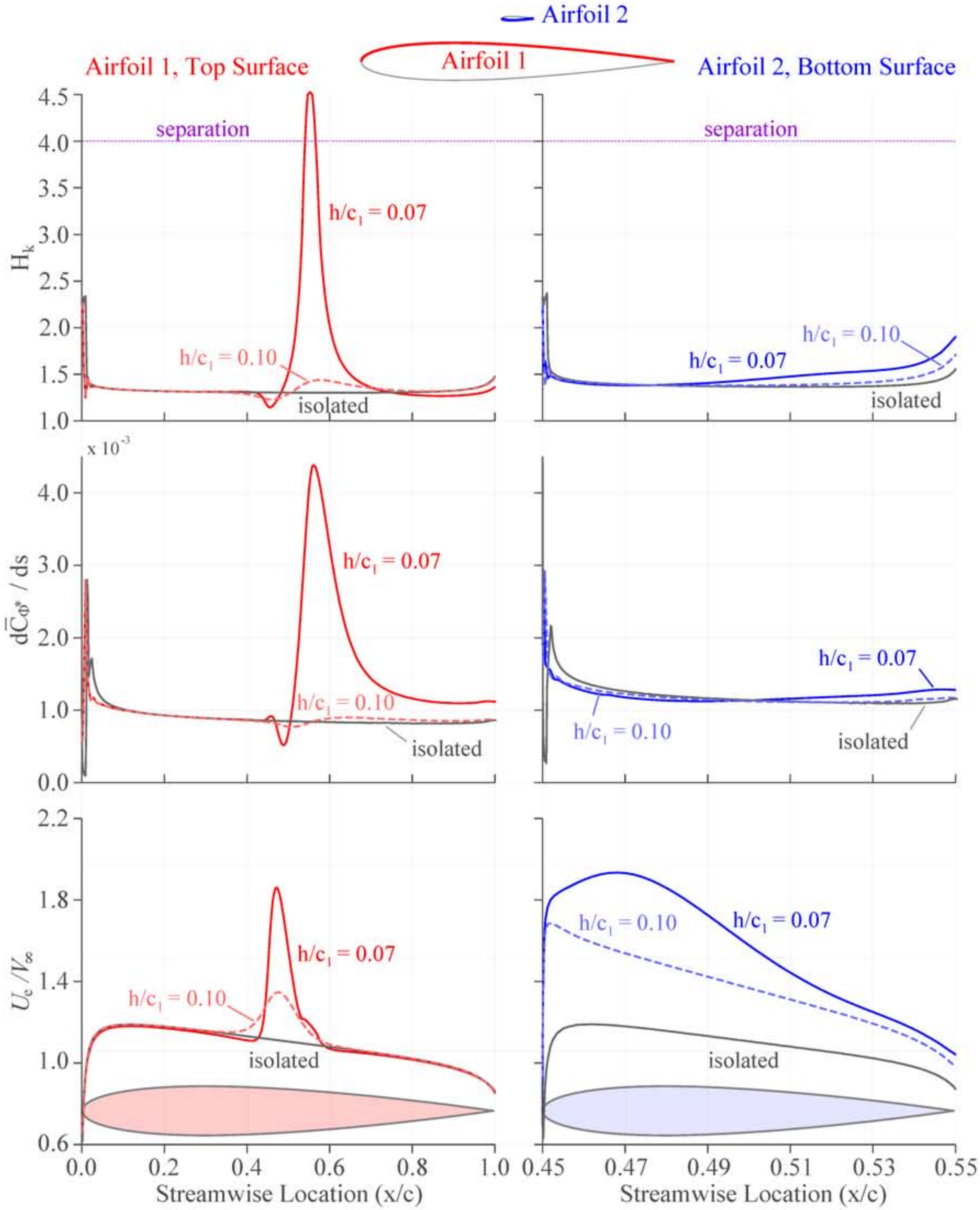

Figure 5-16: H_k, $d\bar{C}_{\Phi^*}/ds$ and U_e/V_∞ for $M_\infty = 0.1$, $c_2/c_1 = 0.1$ configurations. Left: Airfoil 1 upper surface, right: Airfoil 2 lower surface

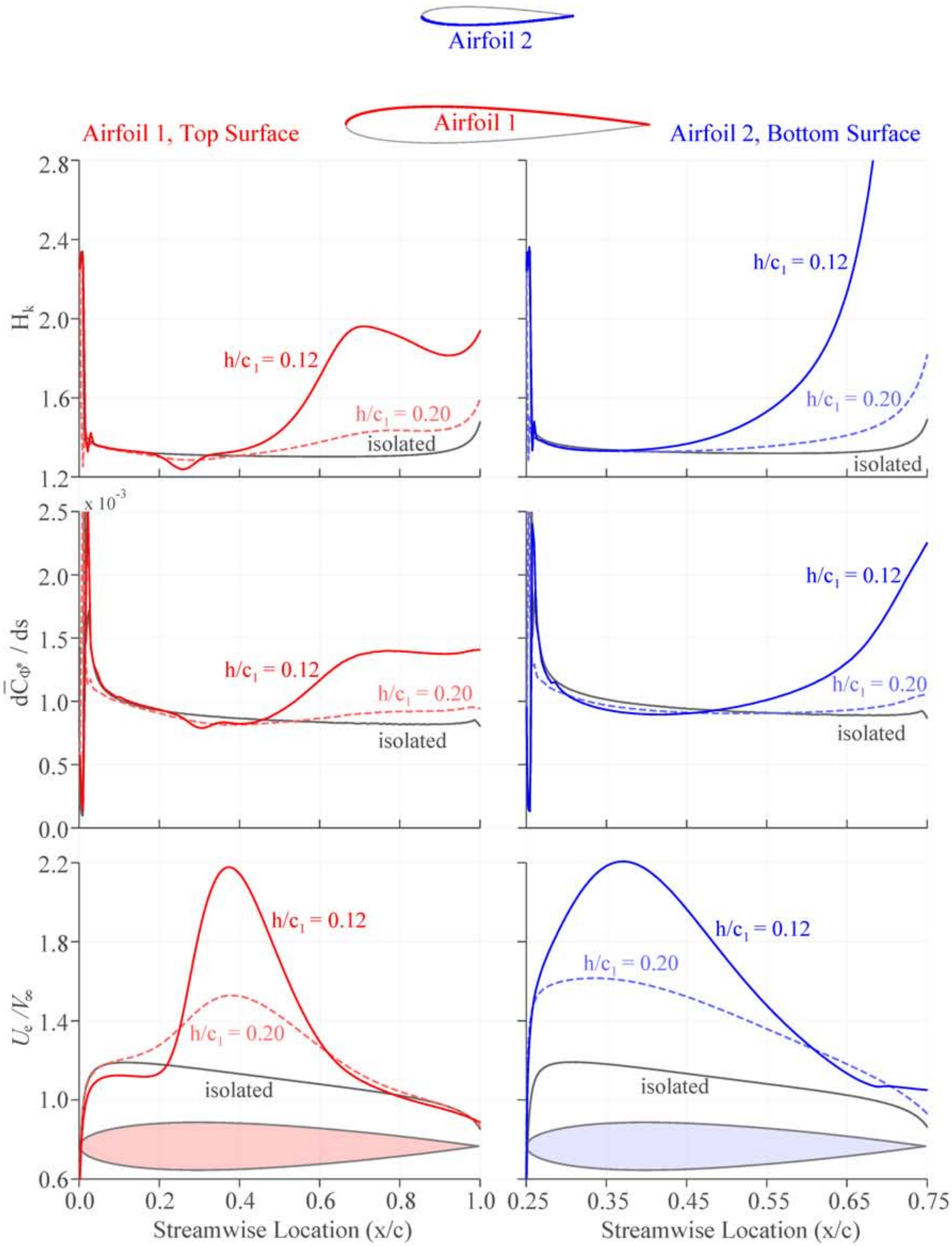

Figure 5-17: H_k, $d\bar{C}_{\Phi^*}/ds$ and U_e/V_∞ for $M_\infty = 0.1$, $c_2/c_1 = 0.5$ configurations. Left: Airfoil 1 upper surface, right: Airfoil 2 lower surface

A similar trend can be seen in Figure 5-17, which shows H_k, $d\bar{C}_{\Phi^*}/ds$ and U_e/V_∞ over the airfoil surfaces for the $c_2/c_1 = 0.5$ configurations (configurations **b** and **B**). With the larger airfoil 2, the velocity gradient is smaller than that in configurations **a** and **A**, so the relative change in H_k is not as pronounced. However, both H_k and $d\bar{C}_{\Phi^*}/ds$ are influenced over a larger region than configurations **a** and **A**, with changes in loss generation over 40% of the airfoil chord on both airfoil surfaces.

The results show that the error in mechanical loss scaling comes from the change in the boundary layer properties between the non-interacting and interacting configurations. Figure 5-18 shows $\Delta\bar{C}_{\Phi^*}$ plotted as a function of change in average boundary layer kinematic shape parameter $\Delta\bar{H}_k \equiv \bar{H}'_k - \bar{H}_k$, where

$$\Delta\bar{H}_k \equiv \frac{\sum_{i=1}^{n}\left[\int_{LE}^{TE} H_k ds_{n_{top}} + \int_{LE}^{TE} H_k ds_{n_{bot}}\right]}{\sum_{i=1}^{n}\left[s_{n_{top}} + s_{n_{bot}}\right]}. \tag{5.13}$$

$\bar{H}_k$ is the boundary layer kinematic shape parameter averaged over all airfoil surfaces in the interacting configuration and $\Delta\bar{C}_{\Phi^*}$ increases monotonically with $\Delta\bar{H}_k$. To keep $\Delta\bar{C}_{\Phi^*}$ smaller than 10%, $\Delta\bar{H}_k$ must be less than 0.04.

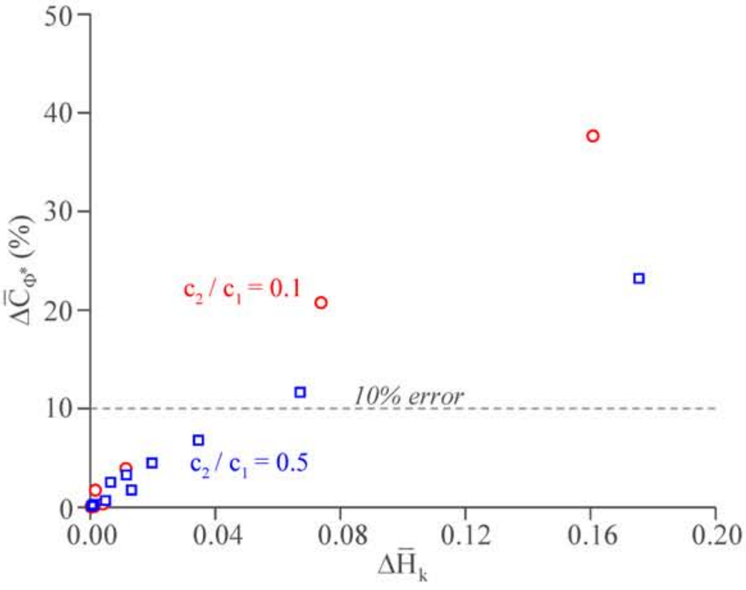

Figure 5-18: $\Delta\bar{C}_{\Phi^*}$ vs. $\Delta\bar{H}_k$, $M_\infty = 0.1$

5.3.3 Loss Scaling in Compressible Flow

Figure 5-19 shows the $\Delta\bar{C}_{\Phi^*}$ (solid line) and $\Delta\bar{C}_d$ (dashed line) for $c_2/c_1 = 0.1$ (red) and $c_2/c_1 = 0.5$ (blue) configurations, as a function of vertical distance between the two airfoils (h/c_1) at $M_\infty = 0.6$. The results are similar to the incompressible results in the previous section, with the mechanical loss scaling with $\rho_e U_e^3 \left(1 + \frac{\gamma-1}{2} M_e^2\right)^r$ better than drag does with $\rho_e U_e^2$. A sharp increase in $\Delta\bar{C}_{\Phi^*}$ is also seen as h/c_1 is reduced, but the increase happens at a larger h/c_1 than for incompressible flow: For $c_2/c_1 = 0.1$, the increase in $\Delta\bar{C}_{\Phi^*}$ starts at $h/c_1 = 0.18$ at $M_\infty = 0.6$ as opposed to $h/c_1 = 0.10$ at $M_\infty = 0.1$. For $c_2/c_1 = 0.5$, the increase starts at $h/c_1 = 0.44$ for $M_\infty = 0.6$, rather than $h/c_1 = 0.20$ for $M_\infty = 0.1$. This is due to two reasons:

1. For the same geometric thickness, the effective aerodynamic thickness is larger at higher Mach number due to compressibility.
2. Shock formation has a strong influence on the boundary layer properties.

The deviation of mechanical loss scaling from $\rho_e U_e^3 \left(1 + \frac{\gamma-1}{2} M_e^2\right)^r$ is caused by breakdown of the assumptions listed in Section 5.1.2 as demonstrated from results with the four configurations below:

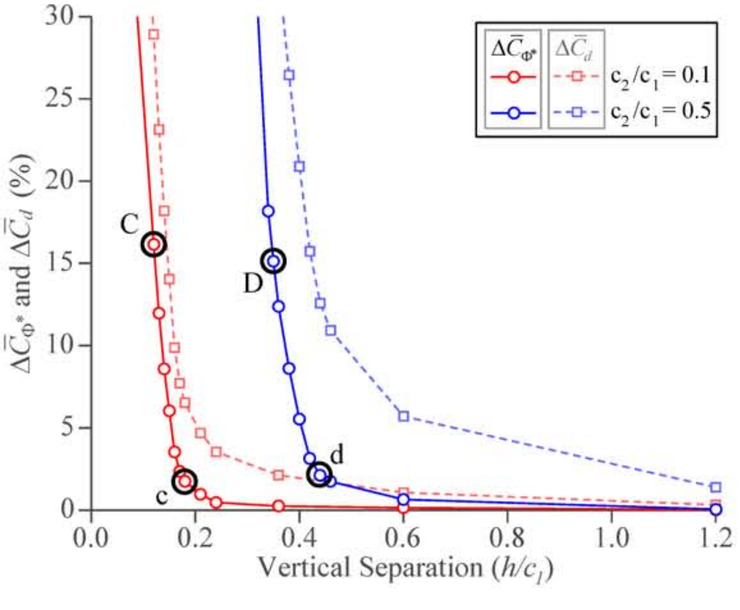

Figure 5-19: $\Delta\bar{C}_{\Phi^*}$ and $\Delta\bar{C}_d$ for MC configuration at $M_\infty = 0.6$

Configuration c: $c_2/c_1 = 0.1$, $h/c_1 = 0.18$. This is the threshold case, just before a sharp increase in $\Delta\bar{C}_{\Phi^*}$ is observed in the $c_2/c_1 = 0.1$ configuration. ($\Delta\bar{C}_{\Phi^*} = 2\%$)

Configuration C: $c_2/c_1 = 0.1$, $h/c_1 = 0.12$. For this $c_2/c_1 = 0.1$ configuration the $\rho_e U_e^3 \left(1 + \frac{\gamma-1}{2} M_e^2\right)^r$ scaling is not appropriate. ($\Delta\bar{C}_{\Phi^*} = 17\%$)

Configuration d: $c_2/c_1 = 0.5$, $h/c_1 = 0.44$. This is the threshold case, just before a sharp increase in $\Delta\bar{C}_{\Phi^*}$ is observed in the $c_2/c_1 = 0.5$ configuration. ($\Delta\bar{C}_{\Phi^*} = 2\%$)

Configuration D: $c_2/c_1 = 0.5$, $h/c_1 = 0.36$. For this $c_2/c_1 = 0.5$ configuration the $\rho_e U_e^3 \left(1 + \frac{\gamma-1}{2} M_e^2\right)^r$ scaling is not appropriate. ($\Delta\bar{C}_{\Phi^*} = 16\%$)

Source of Error

Figure 5-20 shows the Mach number contours for configuration **c** ($c_2/c_1 = 0.1$, $h/c_1 = 0.18$) and configuration **C** ($c_2/c_1 = 0.1$, $h/c_1 = 0.07$), and Figure 5-21 shows the Mach number contours for configuration **d** ($c_2/c_1 = 0.5$, $h/c_1 = 0.44$) and configuration **D** ($c_2/c_1 = 0.1$, $h/c_1 = 0.36$). Unlike the threshold cases (configuration **c** and **d**), with normal shocks only over the lower surface of airfoil 2, the extreme cases (configuration **C** and **D**) have normal shocks over the entire flow passage between the airfoils, causing the boundary layer to thicken or separate, the primary source of error in the mechanical loss scaling.

Figure 5-22 shows the boundary layer kinematic shape parameter H_k (uppermost), the local normalized loss generation $d\bar{C}_{\Phi^*}/ds$ (center), and the edge Mach number M_e (lowermost) over the airfoil surfaces of the $c_2/c_1 = 0.1$ configurations. Gray solid lines, colored dashed lines and colored solid lines represent values for the non-interacting configuration, configuration **c** (threshold) and configuration **C** (extreme) respectively. For $h/c_1 = 0.18$ (configuration **c**), only the lower surface of airfoil 2 is affected by the shock, and there is minimal effect on loss generation. In the extreme case (configuration **C**, $h/c_1 = 0.12$), the edge velocity increases up to $\sim 50\%$ due to the interference. The boundary layer is marked by the increase in H_k downstream of the normal shock. The local loss generation follows the same trend as H_k, almost doubling after the normal shock.

A peak in the normalized loss generation is also observed at the location of the shock ($x/c_1 = 0.5$) over airfoil 1, similar to that in Figure 5-8. Because of the sudden change in baroclinic power, however the integrated error in the mechanical loss due to the approximation of baroclinic power is less than 10% of the total error observed and it is the change in

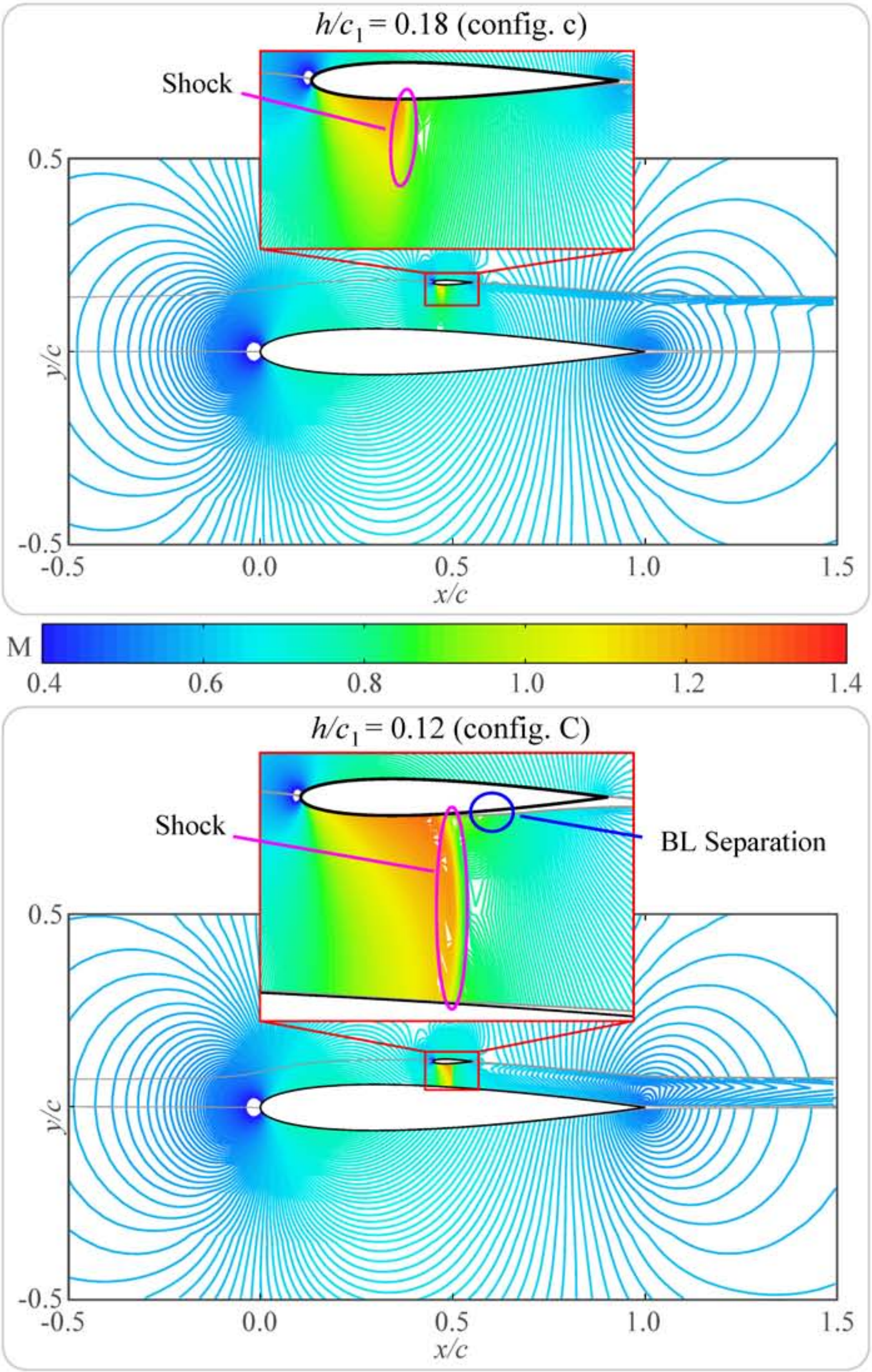

Figure 5-20: Mach contours of $c_2/c_1 = 0.1$ configurations at $M_\infty = 0.6$. Configuration **c**. (upper, $h/c_1 = 0.18$) and **C** (lower, $h/c_1 = 0.12$)

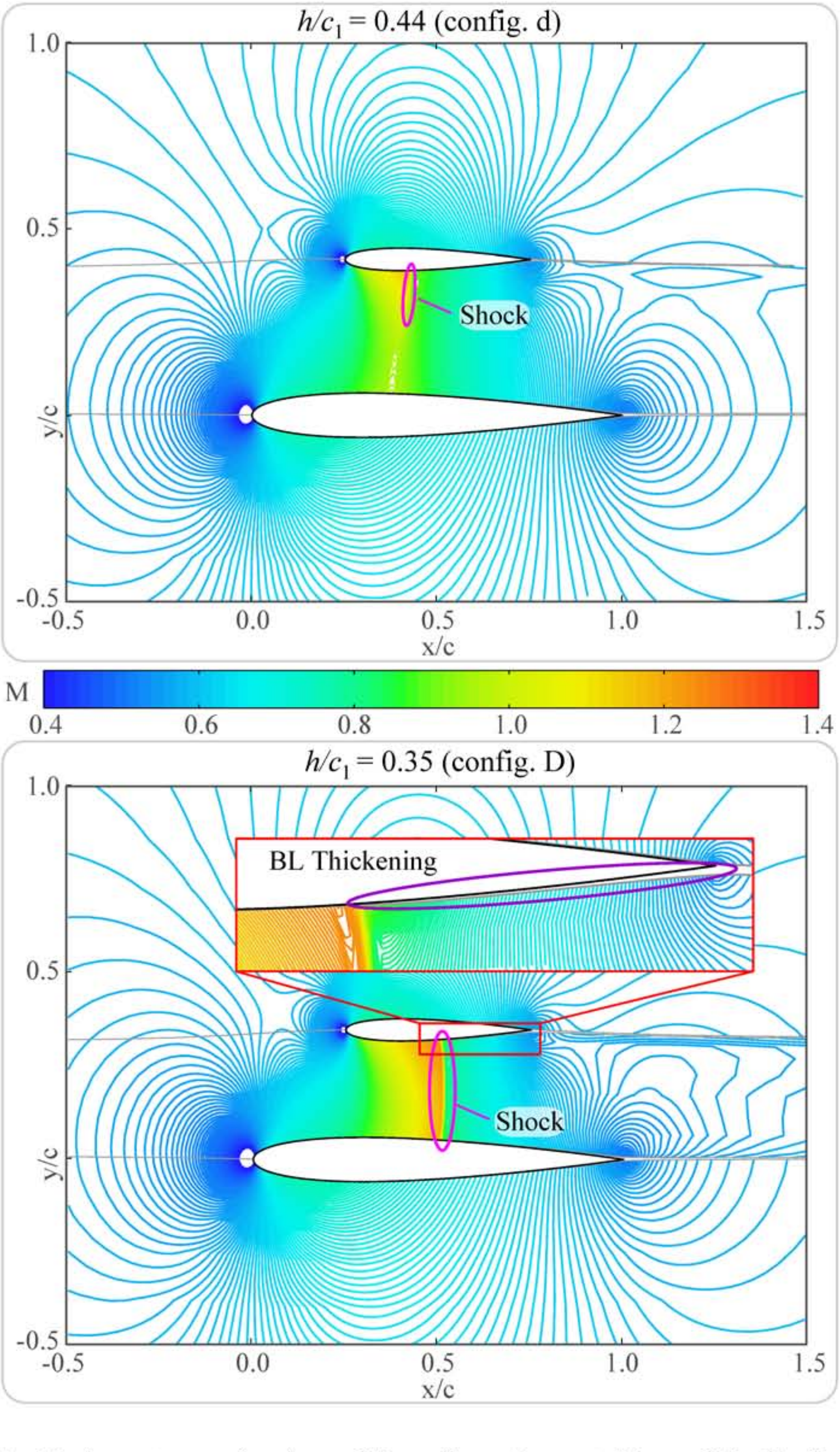

Figure 5-21: Mach contours of $c_2/c_1 = 0.5$ configurations at $M_\infty = 0.6$. Configuration **d**. (upper, $h/c_1 = 0.44$) and **D** (lower, $h/c_1 = 0.35$)

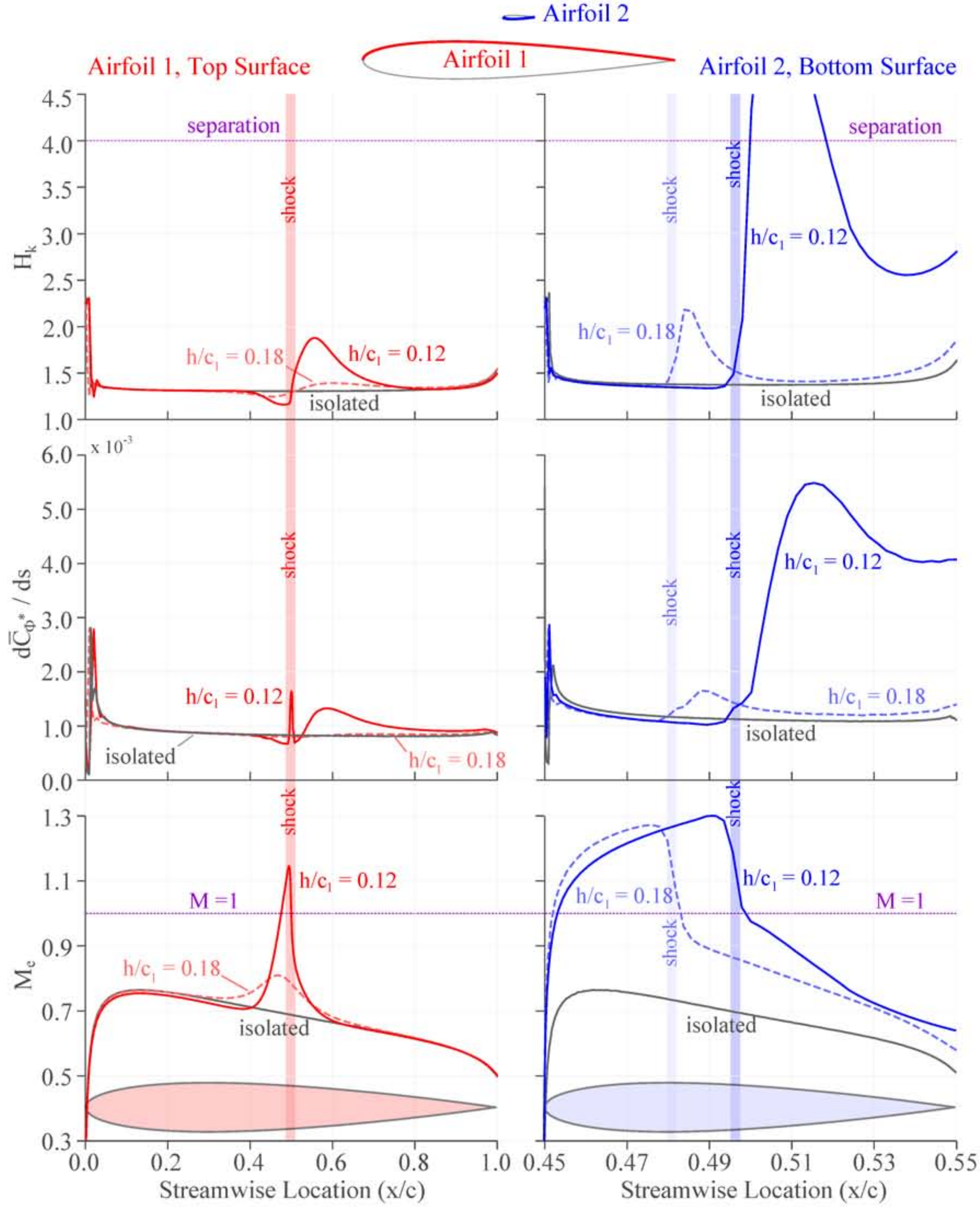

Figure 5-22: H_k, $d\bar{C}_{\Phi^*}/ds$ and M_e for $M_\infty = 0.6$, $c_2/c_1 = 0.1$ configurations. Left: Airfoil 1 upper surface. Right: Airfoil 2 lower surface.

the boundary layer property which is the primary source of the loss generation. The trend is similar for the $c_2/c_1 = 0.5$ configurations, with large variation in H_k and ${}^{d\bar{C}_{\Phi^*}}/_{ds}$ after the normal shock as in Figure 5-23.

Although both configurations **C** and **D** and the BLI configurations ($M_\infty = 0.74$, $D/c = 0.5$ and $\Delta C_{pt} = 1.4$) mentioned in Section 5.2.2 have shocks in the flow field, $\Delta\bar{C}_{\Phi^*}$, is smaller in the BLI configuration ($\sim 4\%$) compared to configuration C ($\sim 15\%$) and configuration D ($\sim 14\%$). Unlike the BLI configuration where the dominant source of error in the scaling law came from the baroclinic power approximation, configuration **C** and **D** has a large change in the boundary layer properties between the non-interacting and interacting configuration, which increased the profile loss of the interacting configuration over an extended region. We can explain this from the pressure distribution downstream of the shock structure between the two configurations. In Configuration **C** and **D**, the boundary layer is subject to an adverse pressure gradient (flow deceleration) downstream of the shock, which keeps the boundary layer kinematic shape parameter H_k at a high value (> 1.4 increase in H_k). The resulting change in the local dissipation coefficient is the primary cause of increase in $\Delta\bar{C}_{\Phi^*}$. In the BLI configuration, the presence of the actuator disk at the trailing edge alleviates the adverse pressure gradient, limiting the variation of H_k between isolated and interacting configuration. The increase in $\Delta\bar{C}_{\Phi^*}$ is thus mostly due to the approximation error in the baroclinic power.

Figure 5-24 shows $\Delta\bar{C}_{\Phi^*}$ plotted against the variation in average boundary layer kinematic shape parameter $\Delta\bar{H}_k$. $\Delta\bar{C}_{\Phi^*}$ increases monotonically with $\Delta\bar{H}_k$, and as in the incompressible calculation results, to keep $\Delta\bar{C}_{\Phi^*}$ smaller than 10%, $\Delta\bar{H}_k$ must be less than 0.04.

5.3.4 Summary

The key findings of this section are:

1. The effect of interference is larger for the configuration where airfoil 2 is located near the location of maximum thickness of airfoil 1.
2. The mechanical loss of the configuration scales with $\rho_e U_e^3 \left(1 + \frac{\gamma-1}{2} M_e^2\right)^r$ better than the drag scales with $\rho_e U_e^2$.
3. The scaling factor of $\rho_e U_e^3 \left(1 + \frac{\gamma-1}{2} M_e^2\right)^r$ is accurate to within 10% if the variation of

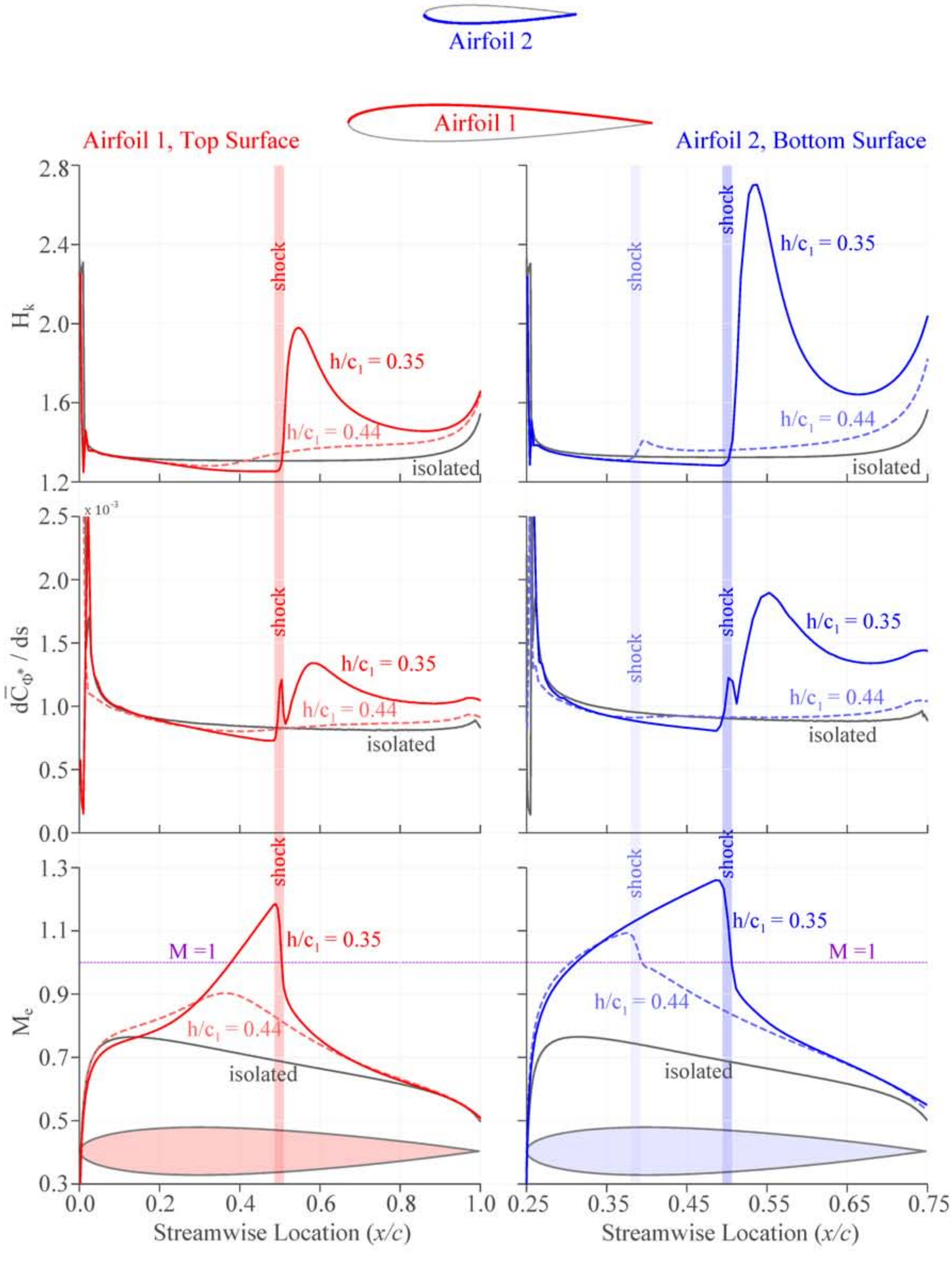

Figure 5-23: H_k, $d\bar{C}_{\Phi^*}/ds$ and M_e for $M_\infty = 0.6$, $c_2/c_1 = 0.5$ configurations. Left: Airfoil 1 upper surface. Right: Airfoil 2 lower surface.

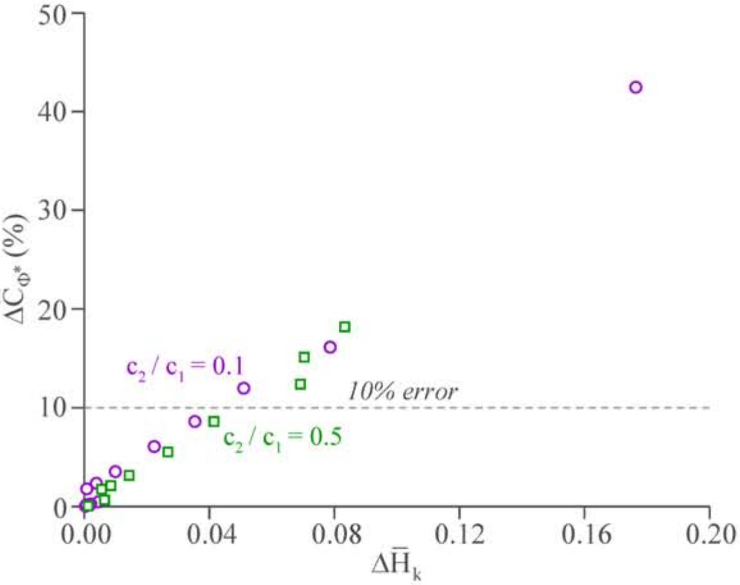

Figure 5-24: $\Delta\bar{C}_{\Phi^*}$ vs. $\Delta\bar{H}_k$, $M_\infty = 0.6$

the average BL kinematic shape parameter $\Delta\bar{H}_k$ is within 5% of the non-interfering configuration.

4. In incompressible flow, the mechanical loss scaling with $\rho_e U_e^3 \left(1 + \frac{\gamma-1}{2} M_e^2\right)^r$ breaks down when the boundary layer separates due to interference.

5. In compressible flow, shock formation from the interaction causes the mechanical loss scaling to break down, as both the baroclinic power and the boundary layer properties are altered by the shock in a way that is not accounted for.

Configurations in which the mechanical loss scaling broke down either had a strong normal shock, or a severe separation. Such situations would not be used for aircraft design points and for more realistic designs, the mechanical loss scaling will be applicable.

5.4 Nacelle and Actuator Disk Configuration

In this section we evaluate the change in the profile loss generated on the external surface and in the internal duct of a two-dimensional nacelle-propulsor combination. The propulsor is represented by an actuator disk. The nacelle and actuator disk configuration, shown in Figure 5-25, uses a nacelle design taken from an example MTFLOW case [10], with modified airfoil thickness ($t/c = 7.5\%$) and nozzle to actuator disk area ratio ($A_n/A_{disk} = 0.91$). The actuator disk was at $x/c = 0.4$, and the disk to nozzle area ratio was adjusted until no shock or severe duct losses were seen at an actuator disk strength of $\Delta C_{pt} = 1.0$. The chord Reynolds number of the nacelle airfoil (Re_c) was 1.2×10^7 with boundary layer trips at $s/c = 0.01$ from the leading edge stagnation point. The freestream Mach number was $M_\infty = 0.6$, the same as the velocity seen by the nacelle of the D8.5 aircraft. The actuator disk stagnation pressure rise $\left(\Delta C_{p_t} \triangleq \Delta p_t / \left(p_{t\infty} - p_\infty\right)\right)$, which ranged from $\Delta C_{pt} = 0.0$ to $\Delta C_{pt} = 1.6$.

The boundary layer losses of external and internal surfaces are treated separately for this analysis. The nacelle external loss is defined as:

$$\Phi^*_{ext} = \Phi^*_{surf_{ext.}} + \Phi^*_{wake_{ext.}}. \tag{5.14}$$

The nacelle duct loss is:

$$\Phi^*_{duct} = \Phi^*_{surf_{int.}} + \Phi^*_{wake_{int.}}. \tag{5.15}$$

The performance metric based on momentum is defined as:

$$D_{nac} + D_{duct} = \left(\rho_\infty U_\infty^2 \theta_\infty\right)_{ext.} + \left(\rho_\infty U_\infty^2 \theta_\infty\right)_{int.}. \tag{5.16}$$

5.4.1 Nacelle Losses Scaling

Figure 5-26 shows the nacelle external (upper) and duct internal (lower) LVC as a function of actuator disk pressure rise (ΔC_{pt}). In calculating LVC, values for $\Delta C_{pt} = 1.0$ were chosen as a reference, because the nacelle was designed for this actuator disk pressure rise. Variations in LVC up to 100% are observed for nacelle external loss, while variations from -70% to 80% are seen in duct loss. The nacelle external loss increases as the actuator disk pressure

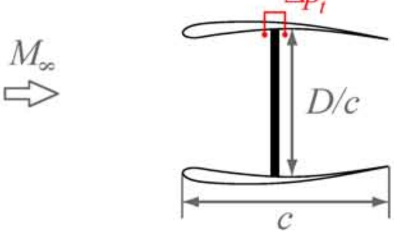

Figure 5-25: Nacelle with actuator disk configuration

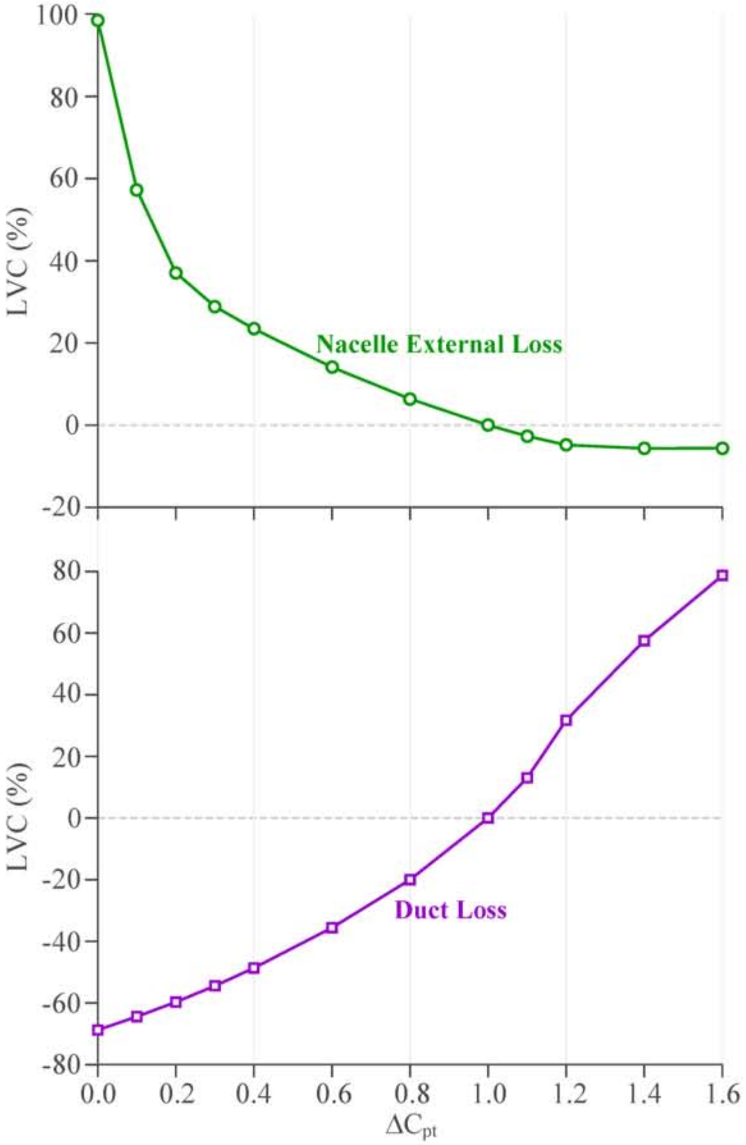

Figure 5-26: LVC for nacelle (upper) and duct (lower) losses vs. ΔC_{pt}, $M_\infty = 0.6$

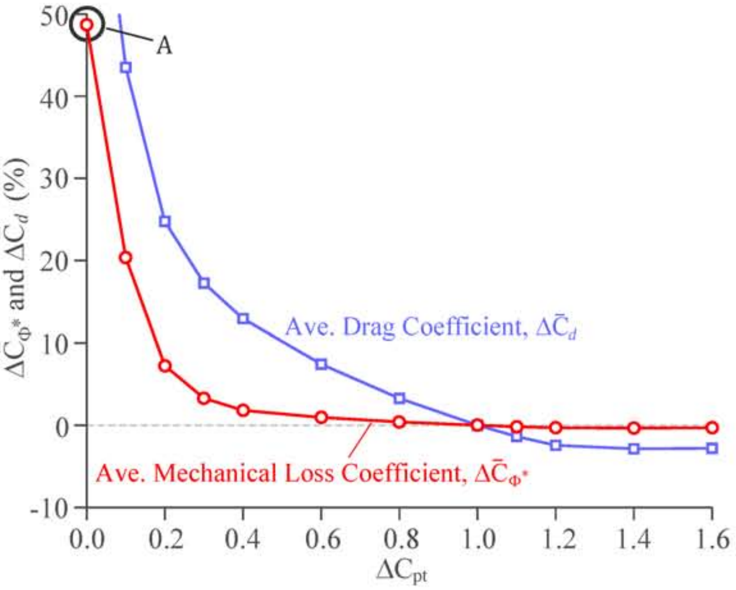

Figure 5-27: Nacelle $\Delta\bar{C}_{\Phi^*}$ and $\Delta\bar{C}_d$ vs. ΔC_{pt}

rise decreases because of acceleration around the nacelle lip, caused by flow spillage at low actuator disk pressure rise. The duct loss increases monotonically with ΔC_{pt}, because the edge velocity in the duct increases with ΔC_{pt}. The loss mechanisms of the nacelle external surfaces and the duct surfaces are presented in subsequent sections.

5.4.2 External Loss

Figure 5-27 shows the nacelle external $\Delta\bar{C}_{\Phi^*}$ (red) and $\Delta\bar{C}_d$ (blue) as a function of actuator disk stagnation pressure rise. The reference for calculating $\Delta\bar{C}_{\Phi^*}$ and $\Delta\bar{C}_d$ is the performance of the configuration at $\Delta C_{pt} = 1.0$. The mechanical loss scaling with $\rho_e U_e^3 \left(1 + \frac{\gamma-1}{2} M_e^2\right)^r$ has $\Delta\bar{C}_{\Phi^*}$ exceeding 10% for $\Delta C_{pt} \leq 0.1$, and maximum deviation of the mechanical loss scaling occurs at $\Delta C_{pt} = 0.0$ (Configuration A shown in Figure 5-27), from the shock generated at the nacelle lip due to spillage.

Figure 5-28 shows the boundary layer kinematic shape parameter H_k (uppermost), local normalized loss generation $d\bar{C}_{\Phi^*}/ds$ (center), and edge Mach number M_e (lower) over the nacelle surface. There is a shock at $x/c = 0.07$, causing the boundary layer kinematic shape parameter and normalized loss generation to increase.

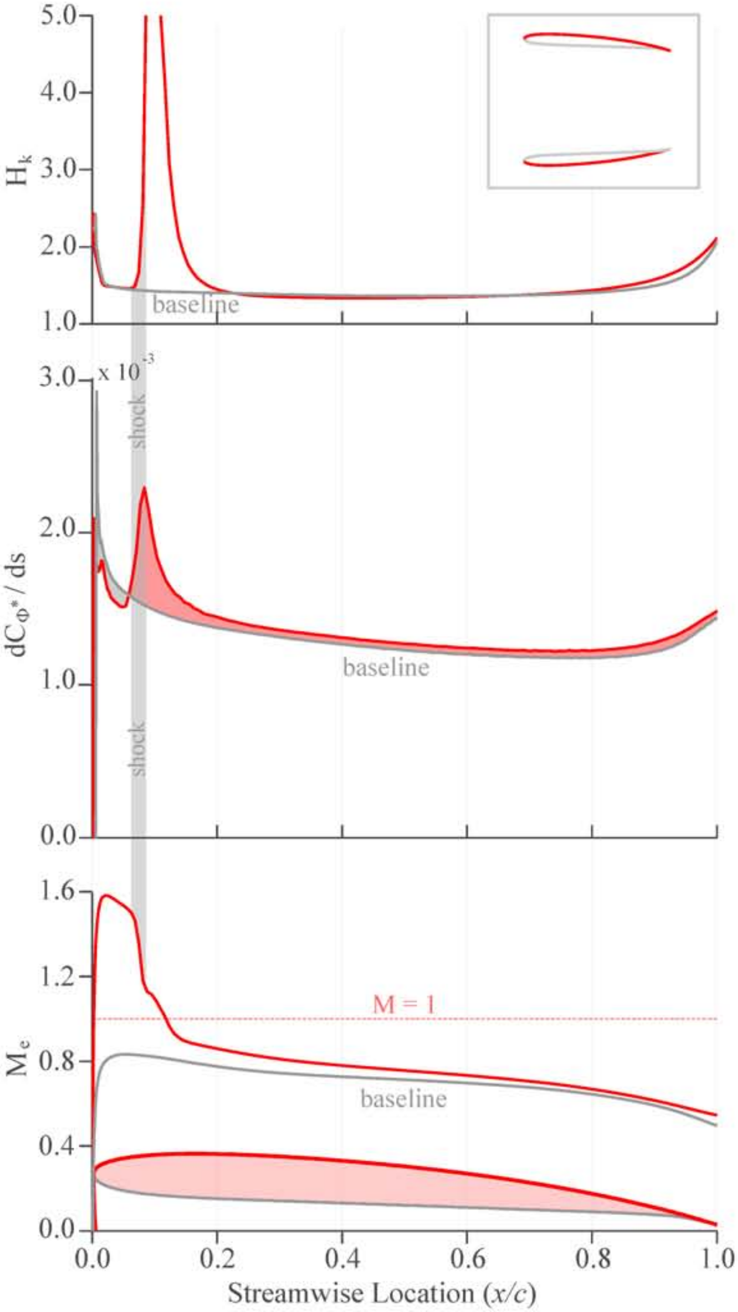

Figure 5-28: H_k, $d\bar{C}_{\Phi^*}/ds$ and M_e over nacelle surface for $\Delta C_{pt} = 0.0$. Gray lines represent the distribution for $\Delta C_{pt} = 1.0$, and red lines the distribution for $\Delta C_{pt} = 0.0$.

5.4.3 Duct Loss

Figure 5-29 shows the nacelle duct $\Delta\bar{C}_{\Phi^*}$ (red) and $\Delta\bar{C}_d$ (blue) as a function of actuator disk stagnation pressure rise. As with the nacelle external loss, the duct loss scales with $\rho_e U_e^3 \left(1 + \frac{\gamma-1}{2} M_e^2\right)^r$ more accurately than the drag does with $\rho_e U_e^2$. $\Delta\bar{C}_d$ varies monotonically between -30% to 40% but $\Delta\bar{C}_{\Phi^*}$ is within 10% for all $\Delta C_{pt} < 1.4$.

The deviation of the mechanical loss scaling from $\rho_e U_e^3 \left(1 + \frac{\gamma-1}{2} M_e^2\right)^r$ comes from two mechanisms: approximation of the baroclinic power, and boundary layer separation. At low ΔC_{pt}, error due to the approximation of the baroclinic power is dominant, while at high ΔC_{pt}, boundary layer separation has the major effect.

Figure 5-30 show H_k (uppermost), $^{d\bar{C}_{\Phi^*}}/_{ds}$ (center), and M_e (lowermost) for the nacelle duct, for $\Delta C_{pt} = 0.0$ (blue, configuration B shown in Figure 5-29), $\Delta C_{pt} = 1.0$ (purple, reference) and $\Delta C_{pt} = 1.6$ (red, configuration C shown in Figure 5-29). The actuator disk is located at $x/c = 0.4$, where there is a negative spike in the normalized loss generation for the $\Delta C_{pt} = 1.0$ and $\Delta C_{pt} = 1.6$ configurations, caused by the change in the boundary layer baroclinic power across the actuator disk, $\Delta\bar{C}_{\Phi^*}$ therefore decreases as ΔC_{pt} is increased from 0.0 to 1.0. The effect of ΔC_{pt} on $\Delta\bar{C}_{\Phi^*}$ has a maximum variation of 7% between ΔC_{pt} of 0.0 and 1.0.

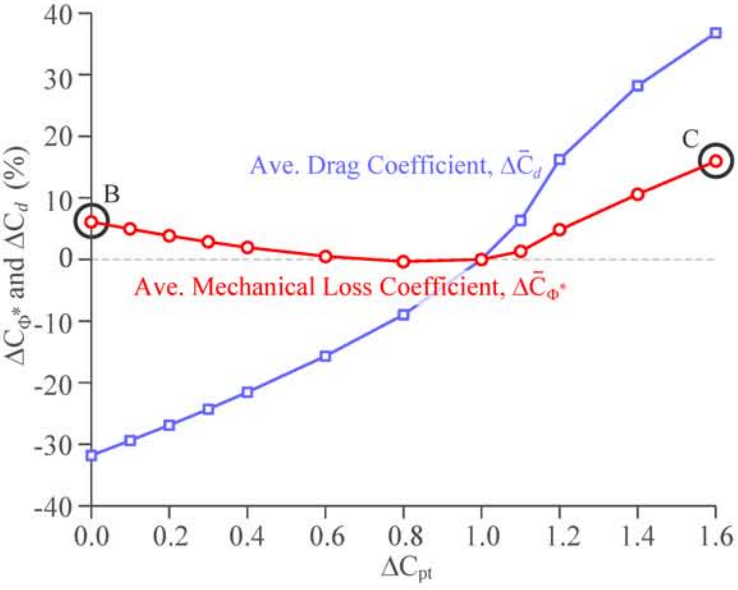

Figure 5-29: Duct $\Delta\bar{C}_{\Phi^*}$ and $\Delta\bar{C}_d$ vs. ΔC_{pt}

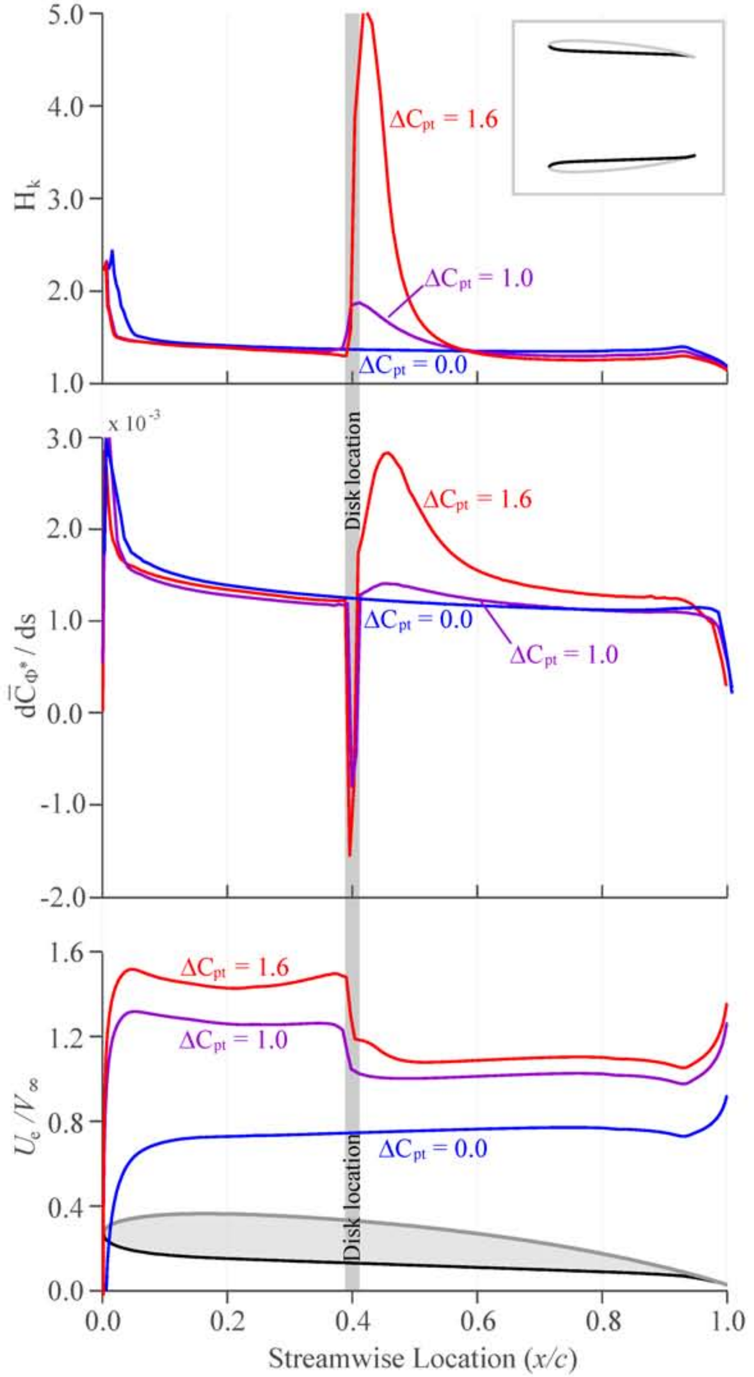

Figure 5-30: H_k, $d\bar{C}_{\Phi^*}/ds$ and U_e/V_∞ over the duct surface. $\Delta C_{pt} = 0.0$ (blue), $\Delta C_{pt} = 1.0$ (purple), $\Delta C_{pt} = 1.4$ (red)

Another feature in Figure 5-30 is the increase in the boundary layer kinematic shape parameter just downstream of the actuator disk, along with the increase in loss generation. The adverse pressure gradient generated by the actuator disk causes the boundary layer to thicken, increasing the loss generated. For $\Delta C_{pt} > 1.0$, this effect dominates the contribution of the baroclinic power, as demonstrated by the positive slope in $\Delta \bar{C}_{\Phi^*}$ for $\Delta C_{pt} > 1.0$. An actual propulsor fan would perform additional work on the slower boundary layer fluid if the fan did not stall locally, and thus mitigate the boundary layer thickening shown in Figure 5-30.

5.4.4 Summary

Key findings of this section are:

1. For the configuration analyzed, the mechanical loss scales with $\rho_e U_e^3 \left(1 + \frac{\gamma-1}{2} M_e^2\right)^r$.
2. The increase in loss due to changes in boundary layer kinematic shape parameter has a larger impact on the mechanical loss scaling than the effect on the baroclinic power.
3. The adverse pressure gradient generated by the actuator disk increases the boundary layer kinematic shape parameter, and hence the mechanical loss generation.
4. Work addition from the actuator disk causes the mechanical loss to decrease. The maximum magnitude of this effect is 7%, between $\Delta C_{pt} = 0.0$ and $\Delta C_{pt} = 1.0$.

5.5 Interacting Configuration Performance Estimation

As shown in Section 5.2, 5.3 and 5.4, $\bar{C}_{\Phi^*}$ is essentially constant for the configurations of interest here, so the boundary layer loss can be taken to scale with $\rho_e U_e^3 \left(1 + \frac{\gamma-1}{2} M_e^2\right)^r$. The performance of interacting configurations can thus be estimated from non-interacting component calculations using the process described in Figure 5-31.

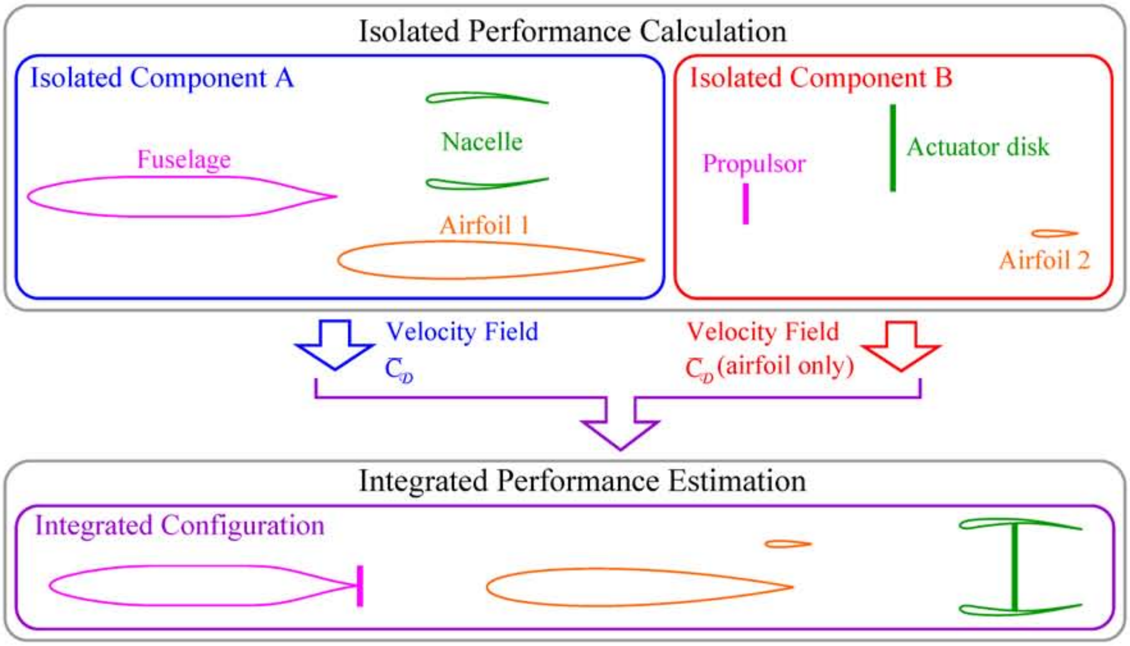

Figure 5-31: Performance estimation process of interacting configuration from non-interacting component calculation

The profile mechanical loss of the interacting configuration can be calculated by multiplying $\bar{C}_{\Phi^*}$ from an non-interacting configuration, by $\rho_e U_e^3 \left(1 + \frac{\gamma-1}{2} M_e^2\right)^r$ obtained from the inviscid calculation of the interacting configuration. Assumptions made in this estimation are the following:

- There is no change in shock structure between the non-interacting and interacting configuration.
- The change in the average boundary layer kinematic shape parameter, $\Delta\bar{H}_k$, is less than 0.04 between the non-interacting and interacting configurations.
- The boundary layers are thin (no separation, $Re_c > 1 \times 10^6$), so the boundary layer edge velocity can be approximated as the wall flow velocity in the inviscid calculation.

This calculation method has been applied to three examples to quantify the accuracy of this methodology. In assessing the accuracy of the calculation method, the calculation error was defined:

$$e = \frac{\Phi^{*\prime}_{est.} - \Phi^{*\prime}_{act.}}{\Phi^{*\prime}_{act.}} \tag{5.17}$$

where $\Phi^{*\prime}_{est.}$ is the boundary layer mechanical loss of the configuration using the calculation method described above, and $\Phi^{*\prime}_{act.}$ is the boundary layer mechanical loss obtained directly from CFD calculation of the interacting configuration, and serves as the reference.

Figure 5-32 summarizes the calculation accuracy of mechanical loss of interacting configurations, determined from non-interacting component losses and an overall inviscid calculation. The BLI configuration was assessed at $M_\infty = 0.6$ and $D/c = 0.5$. For the interfering airfoils, the MC configuration with $c_2/c_1 = 0.1$ and $M_\infty = 0.6$ was assessed. Figure 5-32 shows that all calculation errors are within 5% of the actual loss, apart from the cases where the $\rho_e U_e^3 \left(1 + \frac{\gamma-1}{2} M_e^2\right)^r$ scaling breaks down due to strong shocks or boundary layer separation. This demonstrates the utility of this methodology in assessing the performance of interacting configurations.

5.6 Summary

The analysis of the three basic examples leads to the following conclusions:

- The variation of the mechanical loss due to interference scales more accurately with $\rho_e U_e^3 \left(1 + \frac{\gamma-1}{2} M_e^2\right)^r$ than the drag does with $\rho_e U_e^2$.
- The limitations for the mechanical loss scaling arise from two assumptions that must be fulfilled:

  1. The flow must be adiabatic with pressure gradient small enough that the baroclinic power[5] can be calculated assuming $\delta^{**} \approx \mathcal{R}\theta^*$. The error due to this assumption is within 7% for the boundary layer interacting with a normal shock with upstream Mach number smaller than 1.4.

---

[5] $\Pi_V = \iint \mathbf{D} \cdot \bar{\nabla} \frac{1}{2} U_e^2 \, d\mathcal{S}$.

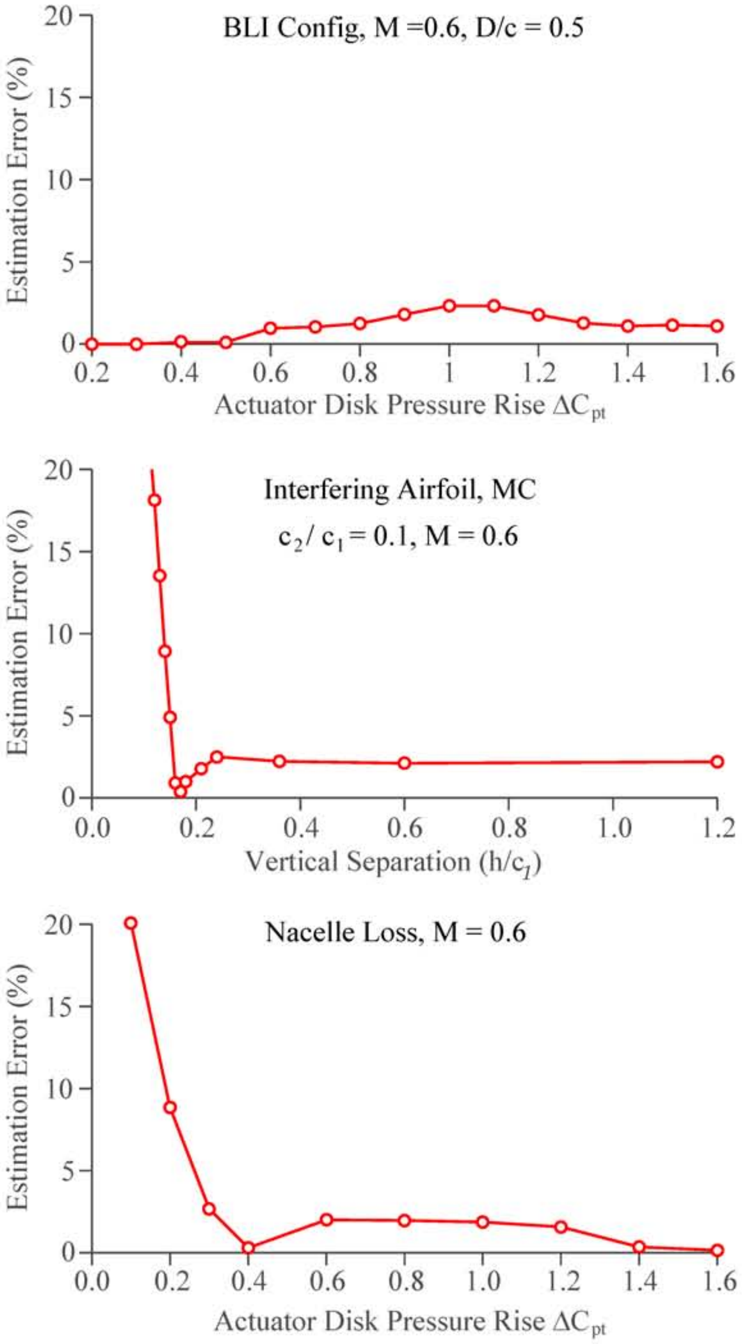

Figure 5-32: Estimation accuracy for BLI (uppermost), interfering airfoil (center) and nacelle configuration (lowermost)

2. $c'_{\mathcal{D}} \approx c_{\mathcal{D}}$ for non-interacting and interacting configurations. The error due to this can be kept within 10% if the variation of the averaged boundary layer kinematic shape parameters $\Delta \bar{H}_k$ between the interacting and the non-interacting configurations are within 0.04.

The mechanical loss scaling breaks down only for situations where a strong normal shock or a severe separation exist in the flow field. Such situations would not be used for aircraft design points. For realistic designs, therefore, the mechanical loss scaling procedure is applicable, and the methodology which is accurate to within 5% of the actual mechanical loss, has utility in estimating the performance of interacting configurations during conceptual design.

Chapter 6

Effect of BLI on HWB Fuel Efficiency

This chapter describes the effects of boundary layer ingestion (BLI) on the fuel burn performance of a Hybrid Wing Body (HWB) aircraft designed as part of the NASA N+3 Phase I project [14]. A performance estimation methodology for BLI configurations, based on the power balance method, is developed and applied to the multidisciplinary design optimization (MDO) of an HWB aircraft. The wide centerbody of the HWB can accommodate a highly integrated, distributed propulsion system, and the design space offers the possibility of performance improvements from BLI. Mechanically geared (planetary and beveled) and electrical transmissions systems are considered with varied numbers of turbogenerators and propulsors, and using either liquefied natural gas (LNG) or conventional jet fuel. The minimum fuel burn occurs with the largest BLI fraction, with a fuel burn reduction of 8% for jet fuel and 11% for LNG relative to the non-BLI configurations.

Section 6.1 presents power balance based performance metrics for aircraft configurations using BLI. Section 6.2 presents details of the design methodology for the HWB airframe: the HWB aircraft design requirement, the global optimization framework for the aircraft system design, the aerodynamic and propulsive performance model, the propulsion system configuration design space and the propulsion system weight model. Section 6.3 presents the results from the tradeoff analysis between BLI and HWB aircraft fuel burn. Section 6.4 summarizes the key findings.

6.1 Boundary Layer Ingestion

In this thesis, the fuel burn metric, referred to as Payload Fuel Energy Intensity (PFEI) [18], is defined as:

$$\text{PFEI} \equiv \frac{W_f h_f}{W_P R}. \tag{6.1}$$

In Eq. 6.1, h_f is the fuel heating value, R the range flown, W_f the total fuel weight, and W_P the weight of aircraft payload. PFEI can be expressed as a function of aircraft aerodynamics, propulsor thermodynamics and propulsive performance using a modified Breguet range equation:

$$\text{PFEI} = \frac{h_f}{R}\left(1 + \frac{W_E}{W_P} + \frac{W_R}{W_P}\right) exp\left(\frac{Rg}{h_f}\frac{1}{\eta_{th}}\frac{1}{\eta_{prop}}\frac{1}{{}^{C_L}/{}_{C_D}} - 1\right). \tag{6.2}$$

In Eq. 6.2, W_R is the weight of fuel reserve carried during a particular mission. Eq. 6.2 can also be written in terms of the power balance terms:

$$\text{PFEI} = \frac{h_f}{R}\left(1 + \frac{W_E}{W_P} + \frac{W_R}{W_P}\right) exp\left(\frac{Rg}{h_f}\frac{1}{\eta_{th}}\frac{1}{\eta_{prop}}\frac{1}{{}^{C_L}/{}_{C_{\Phi*}}} - 1\right). \tag{6.3}$$

For a fixed aircraft mission (fixed payload, range and fuel type), the following four non-dimensional parameters in Eq. 6.2 and 6.3 affect PFEI:

1. Empty weight fraction, ${}^{W_E}/{}_{W_P}$. Lower ${}^{W_E}/{}_{W_P}$ improves PFEI.
2. Propulsor thermal efficiency, η_{th}. Higher η_{th} improves PFEI.
3. Propulsor propulsive efficiency, η_{prop}. Higher η_{prop} improves PFEI.
4. Aircraft aerodynamic performance, ${}^{C_L}/{}_{C_D}$ or ${}^{C_L}/{}_{C_{\Phi*}}$. Higher ${}^{C_L}/{}_{C_D}$ or ${}^{C_L}/{}_{C_{\Phi*}}$ improves PFEI.

The main benefit of BLI comes in the improvement of η_{prop} and ${}^{C_L}/{}_{C_{\Phi*}}$ (or ${}^{C_L}/{}_{C_D}$) as we will show in the following sections.

6.1.1 Power and Force Accounting for a non-BLI Configuration

Figure 6-1 shows a schematic of the power and force terms for a non-BLI configuration at cruise condition. At cruise:

$$T = D_p + D_i, \tag{6.4}$$

$$P_K - \Phi^*_{jet} = \Phi^*_p + \Phi^*_{vortex}. \tag{6.5}$$

In a non-BLI configuration, aircraft performance accounting can be conducted using either the power balance or the momentum balance method, as there is a one-to-one match between the terms in the two methods. As defined in Chapter 3, the following relationships exist between mechanical energy losses and drag forces:

$$D_i V_\infty = \Phi^*_{vortex}, \tag{6.6}$$

and

$$D_p V_\infty = \Phi^*_p. \tag{6.7}$$

For a non-BLI configuration, therefore,

$$\frac{C_L}{C_D} = \frac{C_L}{C_{\Phi^*}}. \tag{6.8}$$

The definition of drag coefficient (C_D) and mechanical loss coefficient (C_{Φ^*}) are respectively:

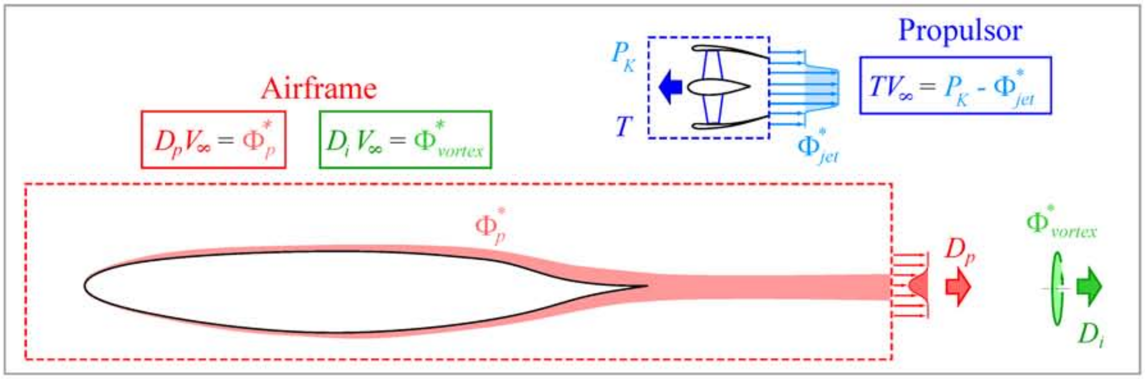

Figure 6-1: Power and force accounting for a non-BLI configuration. A one-to-one match exists between terms in the momentum and power balance methods.

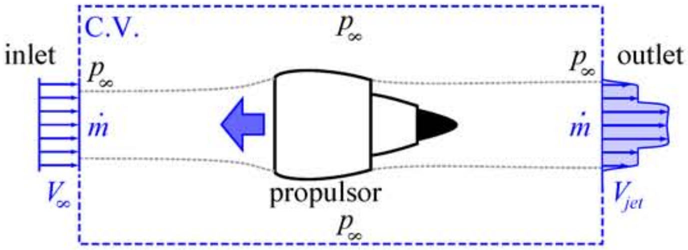

Figure 6-2: Control volume for thrust and propulsive power calculation. All boundaries are placed at ambient pressure.

$$C_D \equiv \frac{D}{1/2\rho V_\infty^2 S}, \tag{6.9}$$

$$C_{\Phi^*} \equiv \frac{\Phi^*}{1/2\rho V_\infty^3 S}. \tag{6.10}$$

For a BLI configuration, where thrust and drag cannot be separated, C_D is ambiguous. C_{Φ^*}, on the other hand, can be obtained unambiguously. This important advantage of the power balance method is elaborated further in Section 6.1.2.

A similar relation can also be obtained between $P_K - \Phi^*_{jet}$ and T. Using the control volume in Figure 6-2, the thrust generated by the propulsor is

$$T = \int (V_{jet} - V_\infty)\, d\dot{m}. \tag{6.11}$$

The quantities P_K (net propulsor mechanical power) and Φ^*_{jet} (propulsor jet dissipation) are defined as:

$$P_K = \int \frac{1}{2}\left(V_{jet}^2 - V_\infty^2\right) d\dot{m}, \tag{6.12}$$

$$\Phi^*_{jet} = \int \frac{1}{2}\left(V_{jet} - V_\infty\right)^2 d\dot{m}. \tag{6.13}$$

Thus,

$$P_K - \Phi^*_{jet} = \int \left(V_{jet}V_\infty - V_\infty^2\right) d\dot{m} = TV_\infty. \tag{6.14}$$

The propulsive efficiency η_{prop} is:

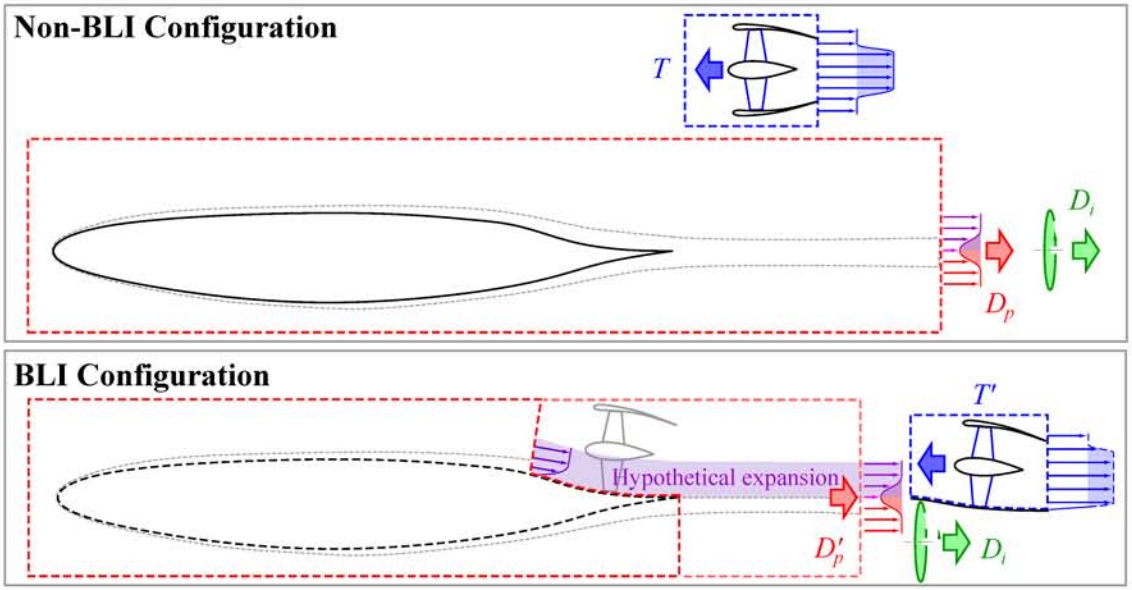

Figure 6-3: Non-BLI (upper) and BLI (lower) performance accounting using momentum balance. As described in Section 5.2, a hypothetical process in introduced to calculate the momentum defect ingested by the propulsor.

$$\eta_{prop} \equiv \frac{TV_\infty}{P_K} = 1 - \frac{\Phi^*_{jet}}{P_K}. \tag{6.15}$$

From Eq. 6.6, 6.7 and 6.14, for a non-BLI configuration, performance accounting using power and momentum balance is equivalent.

6.1.2 Challenge in Performance Accounting for a BLI Configuration

Figure 6-3 compares the momentum method applied to non-BLI and BLI configurations. Quantities with prime ($\prime$) represent quantities for a BLI configuration[1]. For a non-BLI configuration (upper Figure 6-3), the thrust generated by the propulsor is matched to the total drag generated by the airframe. In a BLI configuration, however, the pressure field interaction between airframe and the propulsion system affects the force acting on both[2].

In the power balance method, however, the accumulated mechanical energy loss is not explicitly affected by a local pressure variations whose interaction region is small compared to the overall length. Figure 6-4 shows the difference between a non-BLI and a BLI configuration based on the power balance method. Quantities with subscript "*int.*" represent

---

[1] For a small propulsor ($D/c \ll 1$), $D_i \approx D_i'$ can be assumed.

[2] Details presented in Chapter 5

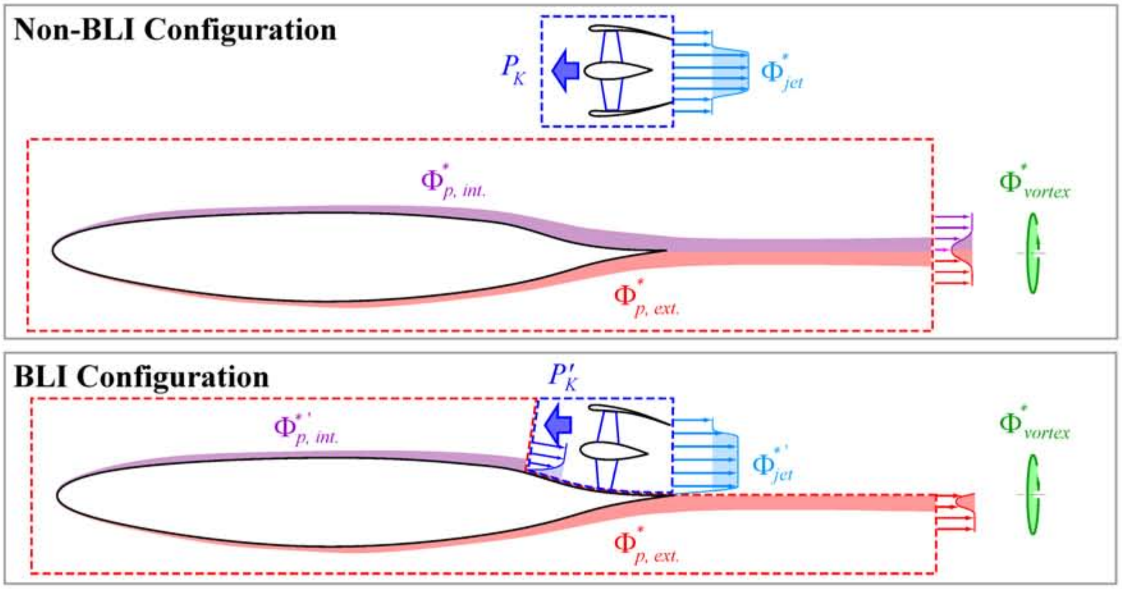

Figure 6-4: Non-BLI (upper) and BLI (lower) performance accounting using power balance. Unlike the momentum balance method, there is no need to approximate the value of profile loss via a hypothetical expansion to ambient pressure.

boundary layer quantities in the stream tube ingested by the propulsor, subscript "*ext.*" represent non-ingested boundary layer quantities. All quantities in the BLI configuration can be obtained without introducing further approximations or assumptions and the hypothetical expansion in Figure 6-3 is not needed. $\Phi^*_{p_{ext.}}$ is the profile mechanical loss of the stream tube that is not affected by the BLI propulsor, and is the same for both non-BLI and BLI configurations[3] (area shown in red in Figure 6-4). $\Phi^*_{p_{int.}}$ represents the profile mechanical loss of the non-BLI configuration, in the stream tube that would be ingested by the propulsor (area shown in purple on the upper part of Figure 6-4). $\Phi^{*\prime}_{p_{int.}}$ is the boundary layer mechanical loss of the ingested stream tube generated upstream of the BLI propulsor (area shown in purple on the lower part of Figure 6-4).

6.1.3 Quantification of BLI Benefit Using the Power Balance Method

In this section, we describe the source of BLI power savings using the power balance method. We define a metric which quantifies the overall power savings from BLI (η_{BLI}, BLI efficiency) as

---

[3] From Chapter 5, for a small propulsor $D/c \ll 1$ $\Phi^*_{BL,\,ext.} \approx \Phi^{*\prime}_{BL,\,ext.}$. Local distribution of $\Phi^*_{BL,\,int.}$ up to propulsor is approximately equal to $\Phi^{*\prime}_{BL,\,int.}$ for the same reason.

$$\eta_{BLI} \equiv \frac{D_{isolated} V_\infty}{P'_K}. \tag{6.16}$$

This relates the mechanical power output of the propulsor P'_K to the propulsive power required to propel an aircraft without BLI. The expression for η_{BLI} is equivalent to the definition of propulsive efficiency defined by Smith [39] and Sargeant [35]. Eq. 6.16 can be split into terms related to airframe power and those related to propulsor power as

$$\begin{aligned} \eta_{BLI} &= \frac{C_{\Phi^*}}{C'_{\Phi^*}} \frac{C'_{\Phi^*}}{P'_K} = \frac{C_{\Phi^*}}{C'_{\Phi^*}} \left(1 - \frac{\Phi^{*\prime}_{jet}}{P'_K}\right), \\ &= C_{BLI} \eta'_{prop}. \end{aligned} \tag{6.17}$$

Eq. 6.17 is derived by substituting $P'_K - \Phi^{*\prime}_{jet} = \Phi^{*\prime}_p$ to Eq. 6.16. $C_{BLI} \equiv {}^{C_{\Phi^*}}/_{C'_{\Phi^*}}$[4] is the ratio of required propulsive power between a non-BLI and a BLI aircraft, and $\eta'_{prop} \equiv 1 - {}^{\Phi^{*\prime}_{jet}}/_{P'_K}$ is the propulsive efficiency of the BLI propulsor.

We now derive how the amount of BLI affects C_{BLI} and η'_{prop}. In doing this, we define a few useful quantities:

$$\beta \equiv \frac{\Phi^*_{p_{int.}}}{\Phi^*_{p_{ext.}}}, \tag{6.18}$$

$$\varphi \equiv \frac{\Phi^{*\prime}_{p_{int.}}}{\Phi^*_{p_{int.}}}, \tag{6.19}$$

β is the ratio of the profile mechanical loss (sum of surface and wake losses) between the boundary layer streamtube that is ingested by the propulsor, and the loss in the boundary layer stream tube which is not ingested by the propulsor. $\beta = 0$ represents a design without BLI, and $\beta = 1$ is the design where all the boundary layer fluid is ingested by the propulsor.

φ is the mechanical loss of the ingested boundary layer stream tube upstream of the propulsor, normalized by the profile mechanical loss of that stream tube without BLI and is a measure of the axial location of the BLI propulsor. $\varphi = 0$ indicates the propulsor is located at the leading edge, and $\varphi = 1$ indicates that the propulsor is located infinitely downstream of the airframe, where the wake has mixed out to freestream conditions. A

---

[4] $C_{\Phi^*_p} \equiv C_{\Phi^*_{p_{int.}}} + C_{\Phi^*_{p_{ext.}}} + C_{\Phi^*_{vortex}}$, $C'_{\Phi^*_p} \equiv C'_{\Phi^*_{p_{int.}}} + C_{\Phi^*_{p_{ext.}}} + C_{\Phi^*_{vortex}}$

reasonable design choice would be to position the propulsor such that the propulsor jet does not interfere with the airframe[5]. In a such design, φ becomes a ratio between the surface boundary layer loss Φ^*_{surf} and the profile boundary layer loss Φ^*_p:

$$\varphi_{TE} = \frac{\Phi^*_{surf}}{\Phi^*_p} = \frac{\Phi^*_{surf}}{\Phi^*_{surf} + \Phi^*_{wake}}, \tag{6.20}$$

which is governed by the airframe aerodynamics. For an aircraft fuselage without separation $\varphi_{TE} \approx 0.91$ [6].

Substituting Eq. 6.18 and 6.19 into the definition of C_{BLI}, we obtain

$$C_{BLI} = \frac{\Phi^*_p + \Phi^*_{vortex}}{\left[1 - \beta\left(1 - \varphi\right)\right]\Phi^*_p + \Phi^*_{vortex}}. \tag{6.21}$$

Since $1 - \beta\left(1 - \varphi\right) < 0$ for non-zero BLI, $C_{BLI} > 1$. In 2D, $\Phi^*_{vortex} = 0$, and Eq. 6.21 simplifies to

$$C_{BLI} = \frac{1}{1 - \beta\left(1 - \varphi\right)}. \tag{6.22}$$

For a typical transport aircraft (Boeing 737 for example), the vortex loss (induced drag) is approximately 40% of the total aircraft mechanical energy loss [14], and the maximum achievable C_{BLI} is approximately 1.06 for $\varphi = \varphi_{TE} = 0.91$ and $\beta = 1$. For a 2D body the maximum C_{BLI} is approx. 1.1 for $\varphi = \varphi_{TE} = 0.91$ and $\beta = 1$.

Using Eq. 6.18 and 6.19, the net propulsor mechanical power of a BLI configuration (P'_K) can be expressed as:

$$P'_K = \iint \frac{1}{2}\left(V^2_{jet} - V^2_\infty\right) d\dot{m} + \beta\varphi\Phi^*_p. \tag{6.23}$$

The second term in Eq. 6.23 comes from the reduction of incoming kinetic energy due to BLI. Combining Eq. 6.23 with the definition of η_{prop}, we obtain an expression for the propulsive efficiency of a BLI configuration:

$$\eta'_{prop} = \frac{\iint V_\infty\left(V_{jet} - V_\infty\right) d\dot{m} + \beta\varphi\Phi^*_p}{\iint \frac{1}{2}\left(V^2_{jet} - V^2_\infty\right) d\dot{m} + \beta\varphi\Phi^*_p}. \tag{6.24}$$

---

[5] The body boundary layer loss generated by the jet passing over an airframe surface is much greater than the body boundary layer loss generated in the freestream

[6] From Chapter 3

Since $\iint V_\infty (V_{jet} - V_\infty)\, d\dot{m} \leqslant \iint \frac{1}{2}\left(V_{jet}^2 - V_\infty^2\right) d\dot{m}$, $\eta'_{prop} \leqslant 1$. For the same V_{jet} and V_∞, $\eta'_{prop} > \eta_{prop}$ and as $\beta\varphi\Phi_p^*$ increases relative to $\iint \frac{1}{2}\left(V_{jet}^2 - V_\infty^2\right) d\dot{m}$, η'_{prop} increases.

The power savings due to BLI comes from two effects. One is a reduction of airframe propulsive power due to the reduction of wake dissipation. The second is the improvement of propulsive efficiency due to ingestion of lower kinetic energy flow, which allows the engine to produce propulsive power with lower expenditure of kinetic energy in the exhaust jet than in a non-BLI configuration.

6.1.4 BLI Example

To illustrate the effect of BLI, we can work through the power savings for a 2D example (Figure 6-5), with incompressible flow, no pressure interaction between airframe and propulsor, uniform wake and jet velocity profile, constant pressure rise $\left(\Delta C_{pt} \equiv \frac{p_{t,\,out} - p_{t,\,in}}{1/2\rho_\infty V_\infty^2}\right)$ across the propulsor and no net thrust for the entire configuration.

The independent variables are: the fraction of wake ingested by the propulsor, β, and the propulsor pressure rise, ΔC_{pt}. φ_{TE} is fixed at 0.91 independent of the propulsor configuration.

Figure 6-6 shows the variation of BLI efficiency η_{BLI} as a function of BLI (β) and propulsor pressure rise (ΔC_{pt}); the detailed calculations are shown in Appendix E. The maximum BLI efficiency ($\eta_{BLI} = 1.11$) is achieved at 100% BLI, when the propulsor captures the entire wake, and accelerates it to the freestream velocity (Design B, $\beta = 1.0$, $\Delta C_{pt} = 0.64$). Design A ($\beta = 0.45$, $\Delta C_{pt} = 1.2$) corresponds to a design where propulsor does not ingest the entire wake, as the size of the propulsor is limited by the total thrust requirement. With a high pressure rise propulsor ($\Delta C_{pt} > 0.64$ in this example) the propulsor is smaller than the wake of the airframe. Design C ($\beta = 1.0$, $\Delta C_{pt} = 0.2$) corresponds to a design where the propulsor pressure rise is lower than the wake stagnation pressure defect. Some thrust therefore needs to be made up by the propulsor acting outside the wake.

Design D ($\beta = 0.0$, $\Delta C_{pt} = 1.2$) and F ($\beta = 0.0$, $\Delta C_{pt} = 0.2$) are non-BLI configurations. The lower power consumption of design F compared to design D is due to the reduction of jet dissipation. Design E is a design where the BLI efficiency is unity, i.e. the power consumption of the propulsor is equal to the isolated propulsive power of the airframe. This occurs when $C_{BLI} \times \eta'_{prop} = 1$, i.e., when the inefficiency in the propulsor from the jet excess kinetic energy is made up exactly by the reduction of the wake dissipation due to BLI.

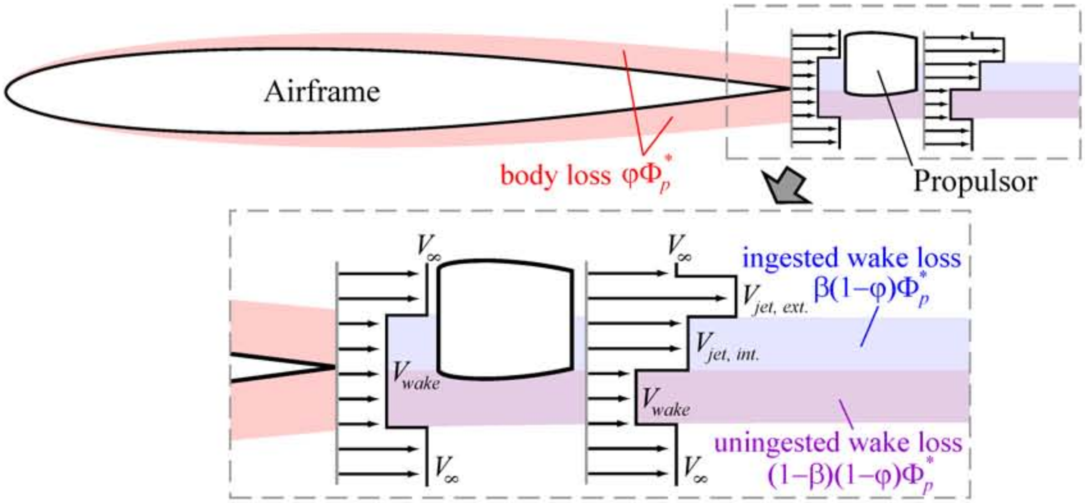

Figure 6-5: Simple 2D BLI problem. Airframe wake and propulsor jet are assumed to be uniform.Φ_p^* represent the total mechanical loss of the isolated airframe.

Figure 6-7 shows the reduction of airframe loss from the reduction in wake dissipation (C_{BLI}), and the improvement in propulsive efficiency (η_{prop}) from the reduction of jet dissipation, as functions of BLI fraction (β) and propulsor stagnation pressure rise (ΔC_{pt}). C_{BLI} increases linearly with β for a design with $\Delta C_{pt} \geqslant 0.64$ (designs A, B, D and E) where the propulsor has a larger stagnation pressure rise than the wake stagnation pressure defect. For design B, C_{BLI} has a maximum value of 1.10, which is $1/\varphi_{TE}$. For an aircraft with smaller φ_{TE} (larger wake loss), C_{BLI} is larger. For designs with pressure rise smaller than 0.64 (design C and F), the propulsor pressure rise cannot fill the wake completely, and a non-zero wake loss exists even at 100% BLI, resulting in a C_{BLI} smaller than for designs with $\Delta C_{pt} \geqslant 0.64$. In the limit of $\Delta C_{pt} \to 0$, $C_{BLI} = 1$, meaning that the propulsive power required to propel the airframe is the same as in non-BLI configuration.

$\eta_{prop} = 1$ can be achieved in two different ways. One is $\Delta C_{pt} \to 0$, where the propulsor accelerates an infinite amount of air to an infinitesimal velocity. A second is Design B, where the propulsor increases the wake velocity to the freestream value.

Table 6.1 summarizes the properties of Design B ($\beta = 1$, $\Delta C_{pt} = 0.64$) which has maximum BLI efficiency, design A ($\beta = 0.45$, $\Delta C_{pt} = 1.2$) and design D ($\beta = 0$, $\Delta C_{pt} = 1.2$), which has a non-dimensional propulsor pressure rise roughly representative of a geared turbofan. Compared to the non-BLI design (Design D), an improvement of 4% in C_{BLI} and an 13% in η_{prop} can be achieved by placing the propulsor in the wake (Design A). The

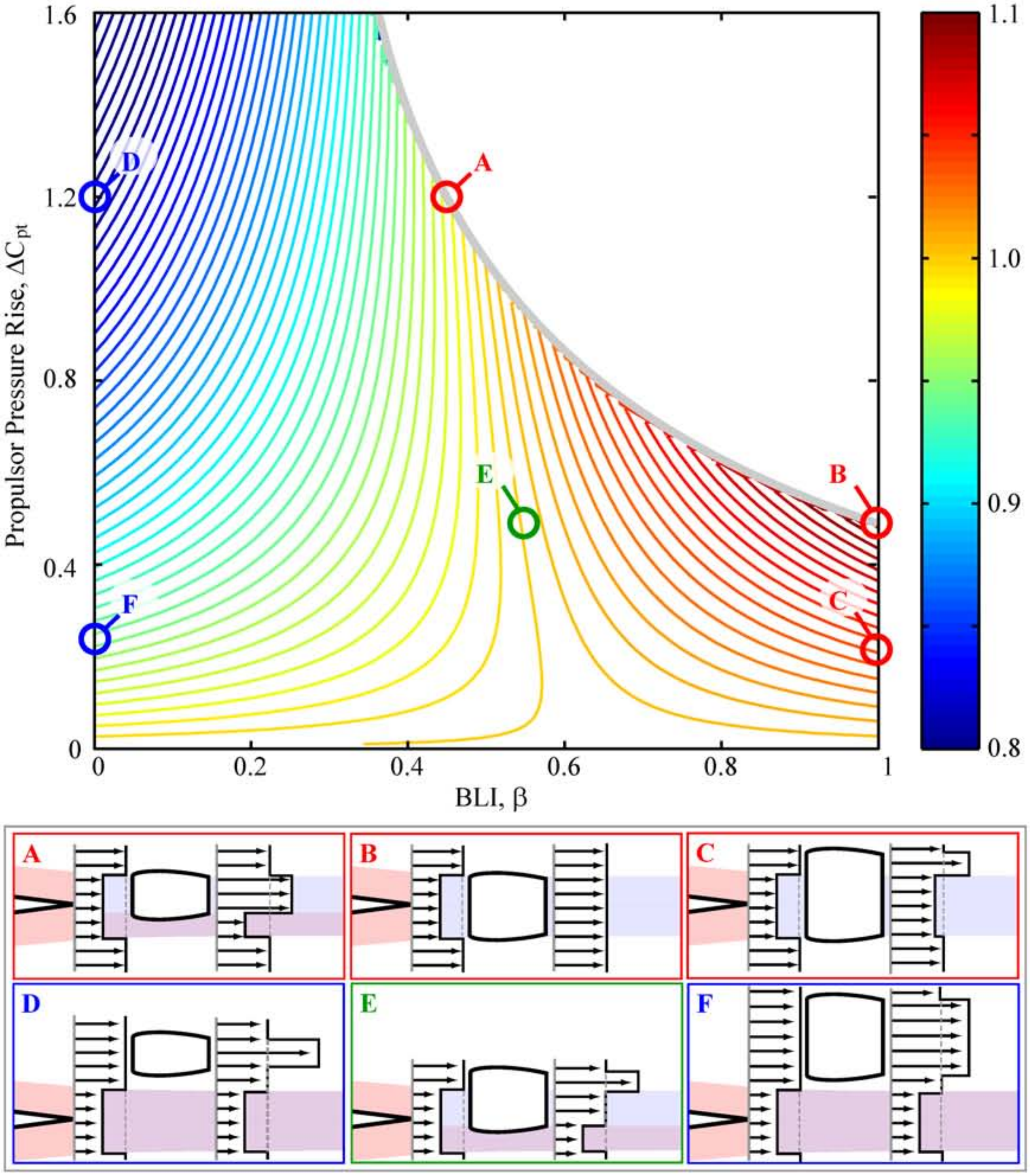

Figure 6-6: Contour of total BLI efficiency (η_{BLI}) as a function of BLI (β) and propulsor pressure rise (ΔC_{pt}), for an aircraft with $\varphi = 0.89$ and negligible induced drag. Case B is the best-possible situation.

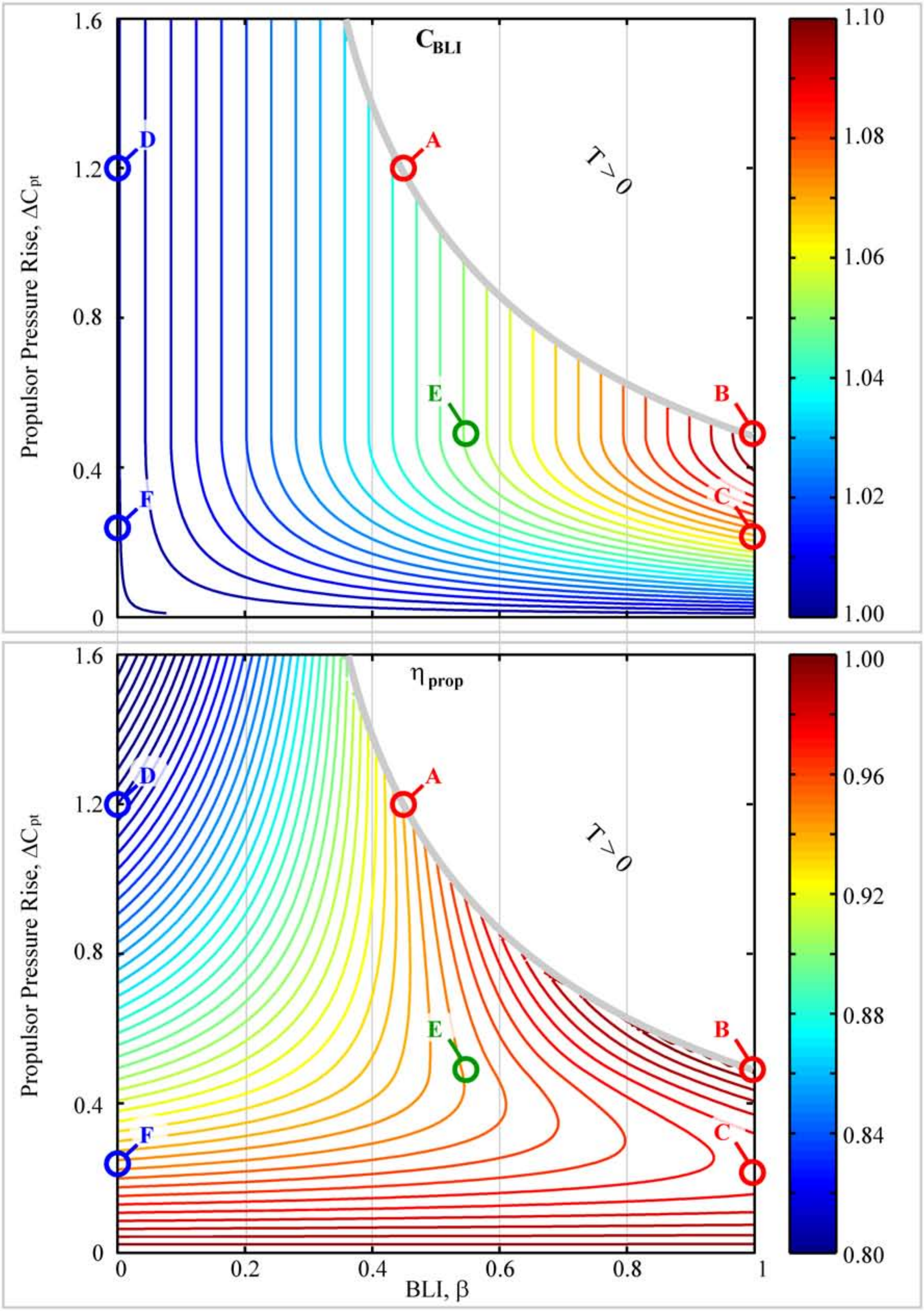

Figure 6-7: Contours of aicraft BLI power coefficient (C_{BLI}, upper) and propulsive efficiency (η_{prop}, lower) as functions of BLI (β) and propulsor pressure rise (ΔC_{pt}). Aircraft $\varphi = 0.91$, negligible induced drag. Cases A-F are the same as in Figure 6-6.

overall improvement in propulsor power consumption is 17%. For a maximum efficiency design (Design B), an improvement in 10% in C_{BLI} and 19% in η_{prop} can be achieved, an overall improvement of 29% compared to a non-BLI design (Design D).

For aircraft configuration employing BLI, this result suggests that the propulsor should be designed around an optimal ΔC_{pt} which depends on the amount of BLI and φ_{TE}. For a non-BLI configuration, such optimum do not exist since propulsive efficiency increases monotonically as $\Delta C_{pt} \to 0$. Additional considerations such as nacelle drag and engine weight must be included for a more realistic analysis.

Table 6.1: Parameters of various BLI configurations

Parameter		Design B	Design A	Design D
Boundary layer ingestion	β	100%	45%	0%
Propulsor pressure rise	ΔC_{pt}	0.64	1.2	1.2
BLI efficiency	η_{BLI}	1.10	0.98	0.81
BLI airframe power coefficient	C_{BLI}	1.10	1.04	1.00
Propulsive efficiency	η_{prop}	1.00	0.94	0.81
Normalized propulsor mass flow,	${}^{\dot{m}}/_{\dot{m}_B}$	1.0	0.45	0.37
Normalized propulsor area,	${}^{A}/_{A_B}$	1.0	0.45	0.31

6.2 HWB Conceptual Design

From Section 6.1, we see the use of BLI allows both reduction of airframe power consumption through reduction of the wake loss (improved C_{BLI}), and increase in the propulsive efficiency through the reduction of jet dissipation (improved η_{prop}), but the implementation of BLI also has additional secondary effects on aircraft performance, which need to be accounted for. One of these is additional duct loss in the inlet duct system (reduced inlet pressure recovery). For example, in some designs, a serpentine duct is required to divert the boundary layer into the engine, and can increase the duct inlet losses. A second is reduction of fan efficiency due to ingestion of non-uniform flow. A third is performance change due to change in engine installation, for example the nacelle wetted area. A fourth is performance change due to change in the propulsion system and total fuel weight. BLI affects the weight of both the propulsion system and the fuel carried, affecting the structural weight and the balance of the aircraft.

To capture these tradeoff, the HWB configuration has been designed in an optimization process built up from a combination of first principles and empirical data to incorporate the mission, airframe, operations, and propulsion system. The following sections present the global optimization framework of the aircraft system design, the aerodynamic and propulsive performance calculation methodology, the propulsion system configuration design space, and the weight model for the propulsion system.

6.2.1 Airframe Design Requirements

The HWB aircraft is designed around the performance goals set by NASA as part of the N+3 Phase I program [14]. The aircraft requirements summarized in Table 6.2 were chosen to meet the Long-Haul International mission selected by the MIT N+3 team, a mission currently flown by Boeing 777-200LR.

Table 6.2: Aircraft design requirements for the HWB design [14]

	Long-Haul International
Reference	Boeing 777-200LR
Capacity	350 passengers
Design Range	7,600 nm
Cruise Speed	> Mach 0.80
Runway Length	9,000 ft balanced field
Span Constraint	65 m
Compliance	FAA[7] and JAA[8] safety standards, NextGen compatibility
Technology	Technology available for entering service by 2035

6.2.2 Airframe Design and Aircraft System Level Optimization

The HWB airframe is a derivative of that created during the Silent Aircraft Initiative (SAI) [19], which was further explored in NASA sponsored N+2 research at MIT [31, 45]. The airframe was scaled and optimized to accommodate the change in mission and technology from the N+3 requirements using a HWB aircraft design methodology HWBOpt [28, 29]. HWBOpt utilizes a modular design framework executed from Matlab. Developed from methodology utilized during the SAI [19], it consists of an aircraft system design loop wrapped in a global optimization routine as in Figure 6-8. The objective function was aircraft fuel burn, calculated as PFEI. The optimized design variables define the airframe planform, engine cycle and initial flight altitude, with cruise Mach number fixed at 0.83.

The lack of *a priori* knowledge of the target design space favored the use of a stochas-

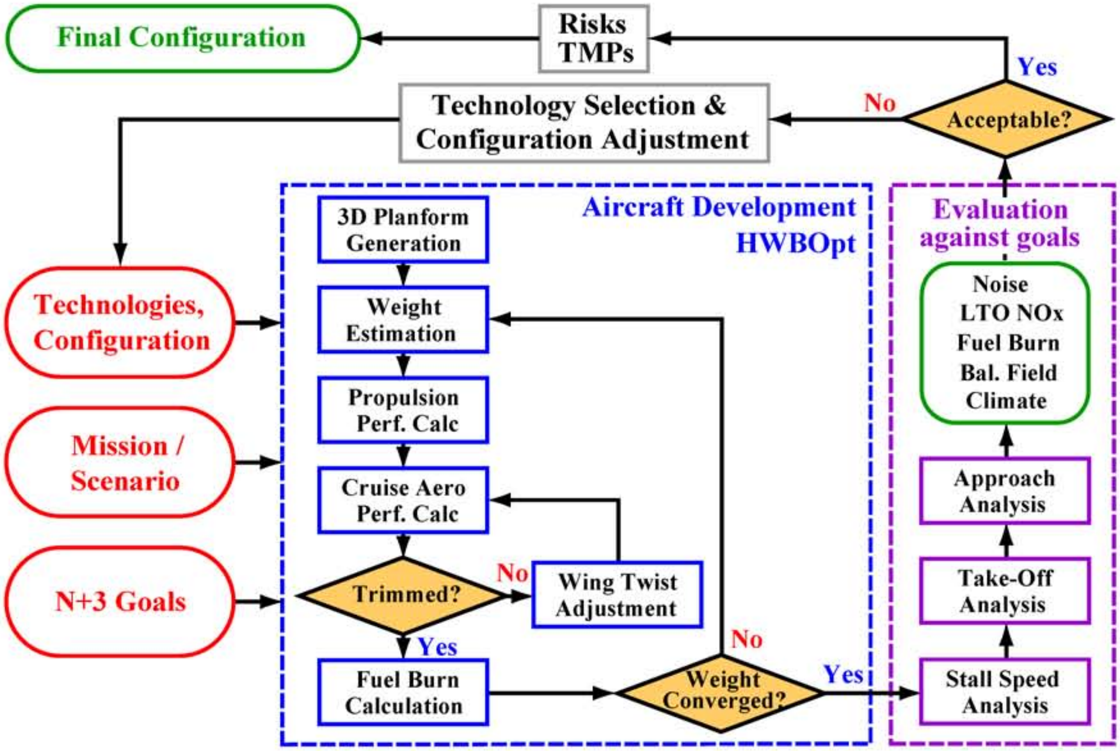

Figure 6-8: Design and optimization methodology

tic approach. The optimization was based on a two-tier hybrid heuristic/deterministic approach [28, 29], which combined the first tier multi-objective genetic algorithm (MOGA) and the second tier sequential quadratic programming (SQP) [28]. Constraints on the design included static stability and passenger comfort based on cabin angle during cruise. Beyond fuel volume restrictions, additional geometric constraints were imposed due to operational restrictions on aircraft span based on the ICAO[9] Annex 14 code E airports regulations [21], and balanced field takeoff length requirements.

To analyze the tradeoff of BLI and aircraft performance, the aircraft was optimized for various propulsion system configurations to be described in Section 6.2.5. The aircraft is designed for conventional fuel (JetA) and also liquefied natural gas (LNG). LNG enables the use of an electric transmission system by allowing for a reduction of the cryocooler weight required for the superconducting materials [14], giving a broader propulsion configuration design space.

The inputs to the design analysis include technologies, HWB airframe configuration, mission and scenario. For each input vector, the design process begins by lofting of the

---

[9] International Civil Aviation Organization

planform into a three-dimensional airframe that envelops the cabin[10]. An initial guess for the aircraft fuel weight is made and used along with initial aerodynamic analysis to size the propulsion system and estimate the fuel burn at cruise conditions as discussed in Section 6.2.4. The cruise analysis also requires adjustment of the wing twist to trim the aircraft at the start of cruise without control surface deflection or thrust vectoring. From the cruise fuel burn calculation, a new aircraft fuel weight is calculated, which is fed back to the next aircraft design loop until a converged statically stable design is achieved. The obtained aircraft design is then fed into an off-design analysis that involves stall speed estimation for takeoff and approach performance and is used to assess the aircraft field length.

6.2.3 Aerodynamic Performance

Figure 6-9 describes the power terms present in an HWB aircraft. In each design iteration, the following power balance equation is evaluated:

$$\left(P'_{K_{out}} - P'_{K_{inl}}\right) - \Phi^{*\prime}_{jet} = \Phi^{*\prime}_{p} + \Phi^{*\prime}_{vortex} + \Phi^{*\prime}_{wave} + \Phi^{*\prime}_{nacelle}, \tag{6.25}$$

where all primed ($\prime$) quantities are values for the BLI configuration. The terms on the left hand side are evaluated using the propulsion system performance calculation described in Section 6.2.4. The terms on the right hand side are evaluated using the aerodynamic performance calculation described in this section. The aerodynamic performance of the HWB aircraft is computed from[11]:

$$\Phi^{*\prime}_{airframe} = \left(1 - \beta\left(1 - \varphi\right)\right)\Phi^{*}_{p} + \Phi^{*}_{vortex} + \Phi^{*}_{wave} + \Phi^{*\prime}_{nacelle}. \tag{6.26}$$

In Eq. 6.26, all airframe mechanical energy loss terms are based on isolated airframes, except for $\Phi^{*\prime}_{nacelle}$. Φ^{*}_{vortex} is calculated from the induced drag (D_i) of the isolated aircraft using an inviscid two-dimensional panel method, AVL[12], as

$$\Phi^{*}_{vortex} = D_i V_{\infty}. \tag{6.27}$$

The boundary layer and shock loss of the airframe (Φ^{*}_{p} and Φ^{*}_{wave}) are calculated sep-

---

[10] The cabin was designed by geometrically scaling the design from the SAX-40 aircraft [19] to accommodate 350 passengers. [29]

[11] modified following the analysis from Section 6.1.2

[12] AVL, http://web.mit.edu/drela/Public/web/avl/

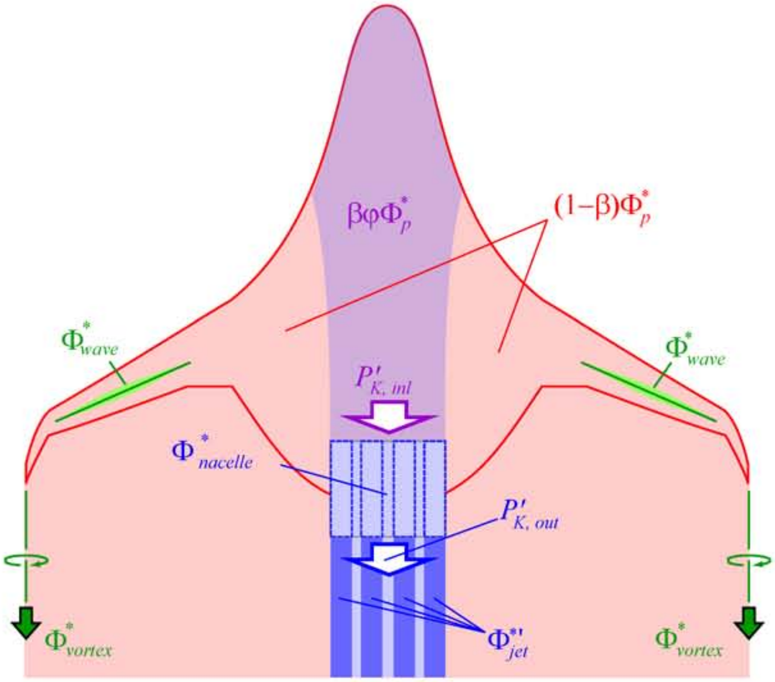

Figure 6-9: Various power terms present in a HWB BLI aircraft

arately for the centerbody and the outer wing. The HWB aircraft is a scaled version of the SAX-40F, so the boundary layer mechanical energy loss over the centerbody is obtained from a three-dimensional Navier-Stokes solution performed by Boeing using CFL3Dv6[13]. To capture Reynolds number effects, the mechanical loss of SAX-40F is adjusted based on the size of the designed aircraft using the correlation in Chapter 4:

$$\Phi^*_{p_{\text{HWB}}} = \Phi^*_{p_{\text{SAI}}} \left[\frac{\ln\left(0.1359 Re_{c_{\text{HWB}}}\right)}{\ln\left(0.1359 Re_{c_{\text{SAX}}}\right)} \right]^2, \tag{6.28}$$

where $Re_{c_{\text{HWB}}}$ is the chord Reynolds number of the designed HWB, and $Re_{c_{\text{SAX}}}$ is the SAX-40F chord Reynolds number. For the outer wing, the surface, wake and shock dissipation were calculated based on the airfoil section Mach number and angle of attack using a two-dimensional CFD program, MSES[14]. The amount of boundary layer ingested, parametrized by β and φ, is calculated based on the kinetic energy thickness distribution of the upper surface boundary layer of the centerbody, provided by the 3-D Navier-Stokes solution, and on the propulsion system configuration. The mechanical power P_K and the jet

---

[13] CFL3D Version 6, NASA Langley Research Center, http://cfl3d.larc.nasa.gov/Cfl3dv6/cfl3dv6.html

[14] A look-up table was created from this data for use during the design optimization process.

dissipation $\left(\Phi^*_{jet}\right)$ are calculated using the engine cycle model described in Section 6.2.4. The nacelle dissipation ($\Phi^{*\prime}_{nacelle}$) is calculated from the mechanical energy loss of a flat plate with the same Reynolds number and wetted area as the nacelle [19].

6.2.4 Propulsion System Performance

The propulsion system performance calculations was found from cycle analysis, with engine flows assumed to be a mixture of perfect gases with tabulated data for specific heat as a function of temperature [14, 17]. The engine powered by Jet A featured a Brayton cycle with improvements in turbine metal temperature and component efficiencies from current state-of-the-art engines. The turbine metal temperature was 1500K, with a film cooling effectiveness of 0.4 and a turbine Stanton number of 0.065. The component efficiencies were increased by 1 percentage point from current state-of-the-art compressors for the low and high-pressure compressor and low-pressure turbine, and 1.5 percentage points for the high-pressure turbine [14, 17]. The burner pressure loss was set at 0.955 [14]. To capture the effect of core size on engine performance, the polytropic efficiency of the high-pressure compressor (HPC) was scaled based on compressor exit corrected flow to account for Reynolds number and tip clearance effects[15]. The number of turbogenerators on the aircraft was limited to 9, to avoid the HPC exit corrected flow falling below 1 lbm/s [14]. For the engine using LNG as a fuel, a 2.2% improvement in normalized core work and a 4% improvement in normalized core work was assumed [14]. It was assumed that all of the turbogenerators were ingesting clean flow, i.e. all boundary layer ingested by the propulsion system were diverted to the fan bypass duct.

To capture the effect of BLI on fan performance, fan efficiency was kept at a current technology level; this assumes that technology advancement would be able to produce a distortion-tolerant fan having current efficiency levels [42]. In this study, the fan face Mach number was fixed at $M = 0.65$. Although a tradeoff exists between fan face Mach number and fan efficiency for BLI propulsion system, as described in the work by Plas [33], it was not considered in this study. Other effects of BLI such as aero-mechanical vibration of the fan blades and reduction of stability margin due to stagnation pressure distortion were also not considered.

---

[15] The HPC polytropic efficiency is calculated as $\eta_{poly,\,HPC} = \min\{0.93,\, 0.93 - 0.01\,(4 - \dot{m}_{corr,\,HPC})\}$, where $\dot{m}_{corr}$ is the HPC exit corrected flow in lbm/s. For $\dot{m}_{corr} \geqslant 4$ lbm/s, $\eta_{poly,\,HPC} = 0.93$, for $\dot{m}_{corr} < 4$, $\eta_{poly,\,HPC}$ decreases by 1% for every lbm/s reduction from 4 lbm/s.

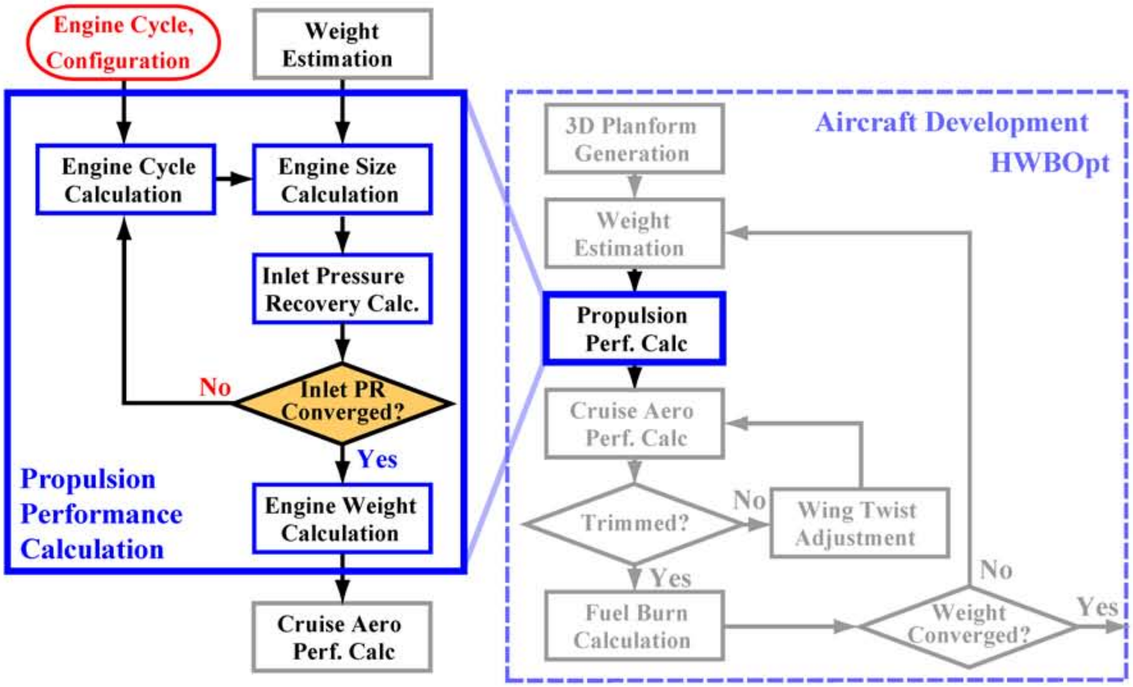

Figure 6-10: Propulsion system design process

Figure 6-10 illustrates how the propulsion system design process relates to Figure 6-8. For a given airframe configuration, the propulsion system is sized to meet the cruise propulsive power requirement. An iterative process was used to match the ingested kinetic energy defect assumed by the engine cycle calculation and the actual kinetic energy defect that can physically be captured by the propulsion system designed from the cycle calculation.

The propulsion performance calculation outputs specific fuel consumption and mechanical power production (P'_K) and jet loss ($\Phi^{*\prime}_{jet}$) fed into the aircraft cruise aerodynamic performance calculation to determine the size of the propulsion system and the total fuel consumption. Propulsion system sizing was only conducted at the cruise condition. Off-design calculations were conducted using the commercial software package Gasturb for the final aircraft design to check that the propulsion system met operational requirements.

6.2.5 Propulsion System Configurations and Weight Estimation

To increase the BLI fraction, the propulsion system must be distributed over the fuselage. Distribution can be achieved by employing multiple small engines, or through the use of a transmission system to allow more flexible positioning of turbogenerators relative to propulsors. The former leads to a reduction of engine core size, which decreases the efficiency of

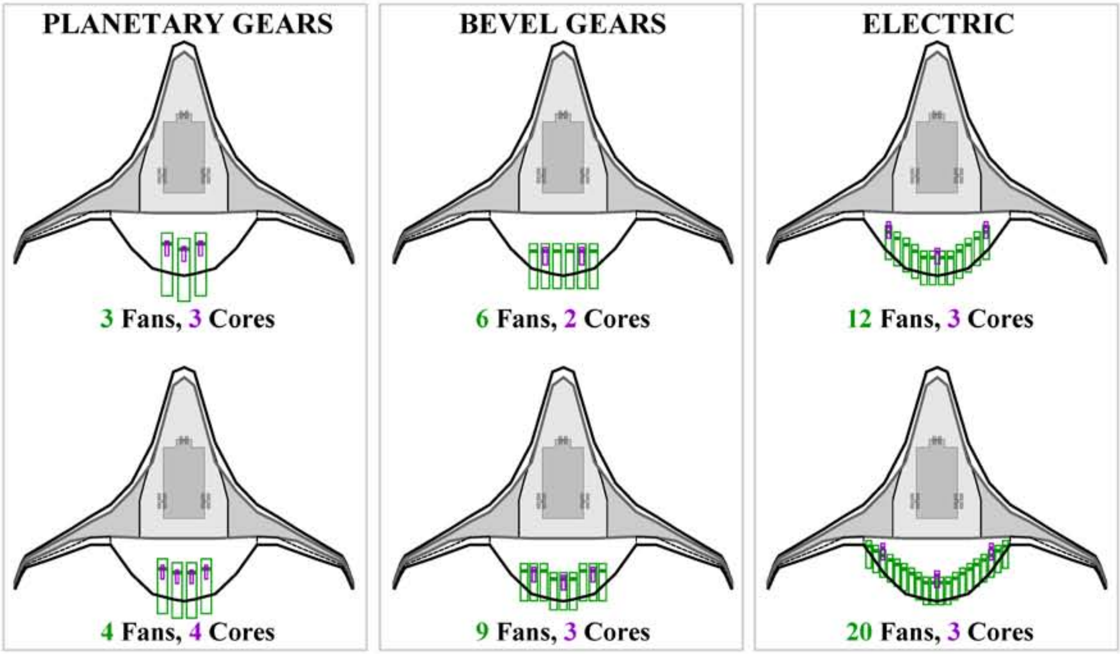

Figure 6-11: Example propulsion system configurations superimposed on the HWB planform

engine components. The latter leads to the introduction of transmission systems, (e.g., gears and electric transmission systems), which gives rise to additional complexity and weight. Different propulsion system configurations were thus considered in the global optimization.

The propulsion system configuration parameters are the number of cores, the number of fans, and the transmission system type, (i.e., direct drive, planetary gears, bevel gears or electrical transmission). Figure 6-11 depicts some of the propulsion systems examined with their corresponding transmission systems. The list of all propulsion system configurations examined is tabulated in Table 6.4.

The weight of a bare engine was calculated based on the fan diameter and the cruise propulsive power scaled from the Granta-3401 engine [5] of the SAX-40 aircraft. The weight of the nacelle and the exhaust duct was computed based on an empirical correlation from Raymer [34] that considers fan diameter, duct length to diameter ratio, and the inlet geometry. The weight of the heat exchanger used in the LNG configurations was calculated based on the fuel flow into the engine, 0.8kg of weight per (kg/hr) of fuel mass flow rate [26].

Different correlations were used to assess different transmission system weights. The planetary gear weight was based on the NASA GRC WATE++ model correlation [41]. This correlation relates the weight of the transmission system with the fan mass flow and core shaft power output at takeoff conditions. The bevel gear weight was based on the transmission system of Granta 3401 using the torque load as the scaling parameter. The bevel gear system included gears and transmission shafts, as well as the oil system [5]. The electric transmission system weight, which included the high temperature super conducting (HTSC) generator and motor, cryocooler, and the inverter was calculated using a correlation based on core shaft power and torque to define the weight of each component in the electric transmission system [14].

The electric transmission system was used only on aircraft configurations with LNG, as this propulsion system is most advantageous when coupled with cryogenic fuel, since it allows for a reduction of the cryocooler weight required for the superconducting materials. The weight of engine supports was scaled from that of the Granta-3401 based on the total propulsion system weight. The efficiency of the electric transmission system was calculated from an in-house model of the HTSC generator, motor and cryocooler developed during the N+3 program [14]. Table 6.3 summarizes the performance and characteristics of the transmission systems considered.

Table 6.3: Efficiency and characteristics of the transmission systems considered

	Planetary gears	Bevel Gears	Electric
Transmission efficiency	99.5%	95.5% [5]	98% [14]
Major components	Planetary gears Oil System	Bevel gears Transmission shafts Oil System	HTSC motor HTSC generator Cryocooler Inverter
System used with	Jet A and LNG	Jet A and LNG	LNG

6.3 Tradeoffs in Propulsion System Configuration and Fuel Type

The HWBOpt framework was used to explore fuel burn (PFEI) changes for a wide range of propulsion system configurations and two different fuel types (Jet A and LNG). For each combination of propulsion system configuration and fuel type, the HWB design was optimized to minimize PFEI, while meeting all design constraints. The PFEI examination was performed for the trades embedded in Eq. 6.29, the Breguet range equation modified from Eq. 6.3 to express PFEI in terms of the propulsive power specific fuel consumption

Table 6.4: List of propulsion system configuration evaluated. The letter denotes the transmission system, while the numbers denote the number of fans and cores.

Direct/Planetary Gear			Bevel Gears			Electric		
Config.	# of Fans	# of Cores	Config.	# of Fans	# of Cores	Config.	# of Fans	# of Cores
D03	3	3	B04/2	4	2	E12/3	12	3
D04	4	4	B06/2	6	2	E17/3	17	3
D05	5	5	B09/3	9	3	E22/3	22	3
D06	6	6	B12/4	12	4	-	-	-
D07	7	7	B15/5	15	5	-	-	-
D08	8	8	B18/6	18	6	-	-	-
D09	9	9	B21/7	21	7	-	-	-

(PSFC $= {}^{1}/_{h_f \eta_{th} \eta_{prop}}$),

$$\text{PFEI} = \frac{h_f}{R}\left(1 + \frac{W_E}{W_P} + \frac{W_R}{W_P}\right)\exp\left(R\,g\,\text{PSFC}\frac{1}{{}^{C_L}/_{C_{\Phi^*}}} - 1\right), \tag{6.29}$$

The propulsion system choice affects three terms in Eq. 6.29: propulsive power specific fuel consumption (PSFC), the ratio of empty to payload weight (${}^{W_E}/_{W_P}$), and the ratio of lift and airframe mechanical energy loss coefficients (${}^{C_L}/_{C_{\Phi^*}}$). The fuel type determines h_f and affects PSFC and the ratio of empty to payload weight indirectly.

For each type of transmission system, different numbers of turbogenerators (cores) and propulsors (fans) were investigated. The maximum number of turobogenerators was set by the minimum HPC exit corrected flow. For the configuration using the bevel gear transmission system, the number of propulsors was selected to avoid asymmetric positioning of turbogenerators and propulsors. For the configuration using the electric transmission system, performance results were calculated for three turbogenerators with different numbers of propulsors.

6.3.1 Propulsion System Configuration and BLI

Figure 6-12 summarizes the PFEI for the propulsion system configurations. Dashed lines indicate designs with Jet A fuel (H3J designs) while solid lines indicate LNG (H3L designs). Blue, red, and green lines represent direct/planetary gear, bevel gear, and electric transmission systems, respectively.

Two baseline designs, termed the H3J-Base and H3L-Base, were created with two podded, planetary gear-drive turbofan engines. These are configurations without BLI. The

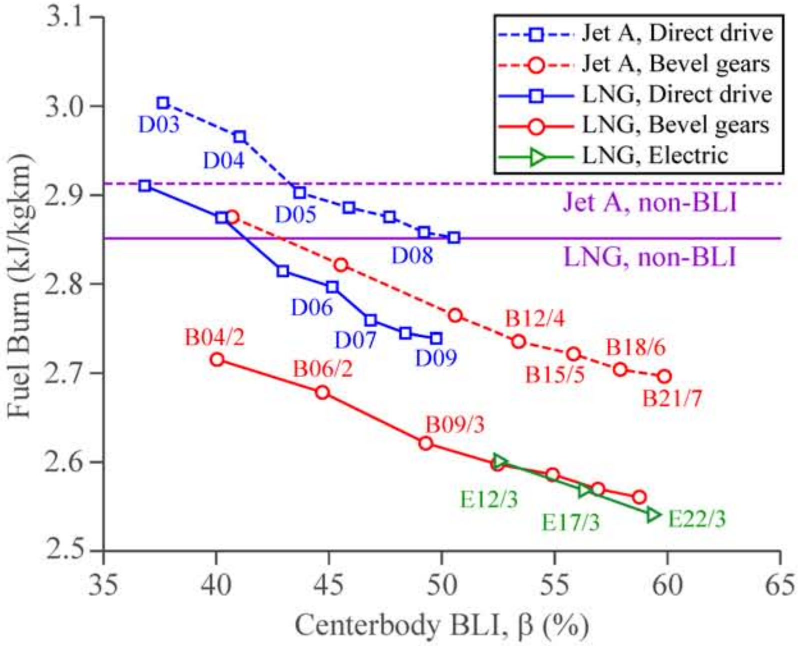

Figure 6-12: PFEI of HWB designs with various propulsion systems

calculated PFEI performance of these two designs is 2.93kJ/kg-km for the H3J-Base and 2.85kJ/kg-km for the H3LB. The general PFEI trends of the jet fuel and LNG designs are similar, with additional BLI resulting in reduced PFEI. The PFEI-optimal H3J design, the H3J-B21/7, had a PFEI of 2.70kJ/kg-km, an improvement of 8% from the H3J-Base. The PFEI-optimal H3L design, (H3L-E22/3) achieved a PFEI of 2.54kJ/kg-km, an 11% reduction from the H3L-Base. A minimum PFEI value was not reached because designs with additional cores and fans were not explored.

To illustrate the trends in PFEI with increasing boundary layer ingestion, PSFC, $^{C_L}/_{C_{\Phi*}}$ and the empty weight $(^{W_E}/_{W_P})$ were assessed separately using the H3L designs. The variations of these three parameters are shown in Figure 6-13. PSFC depends on the amount of BLI and the turbogenerator core size. An increase in BLI decreases PSFC, as shown in the overall decreasing trend of PSFC with BLI for all transmission system types in Figure 6-13 (uppermost). PSFC decreases with increasing BLI, as propulsive efficiency increases with the kinetic energy defect ingested by the propulsor.

The gray dashed lines in Figure 6-13 (uppermost) indicate propulsion configurations with the same number of turbogenerators. Larger number of turbogenerators means smaller turbogenerator core size. In Figure 6-13 (uppermost), the gray dashed lines shift upward as the number of turbogenerators is increased, because the reduction of turbogenerator

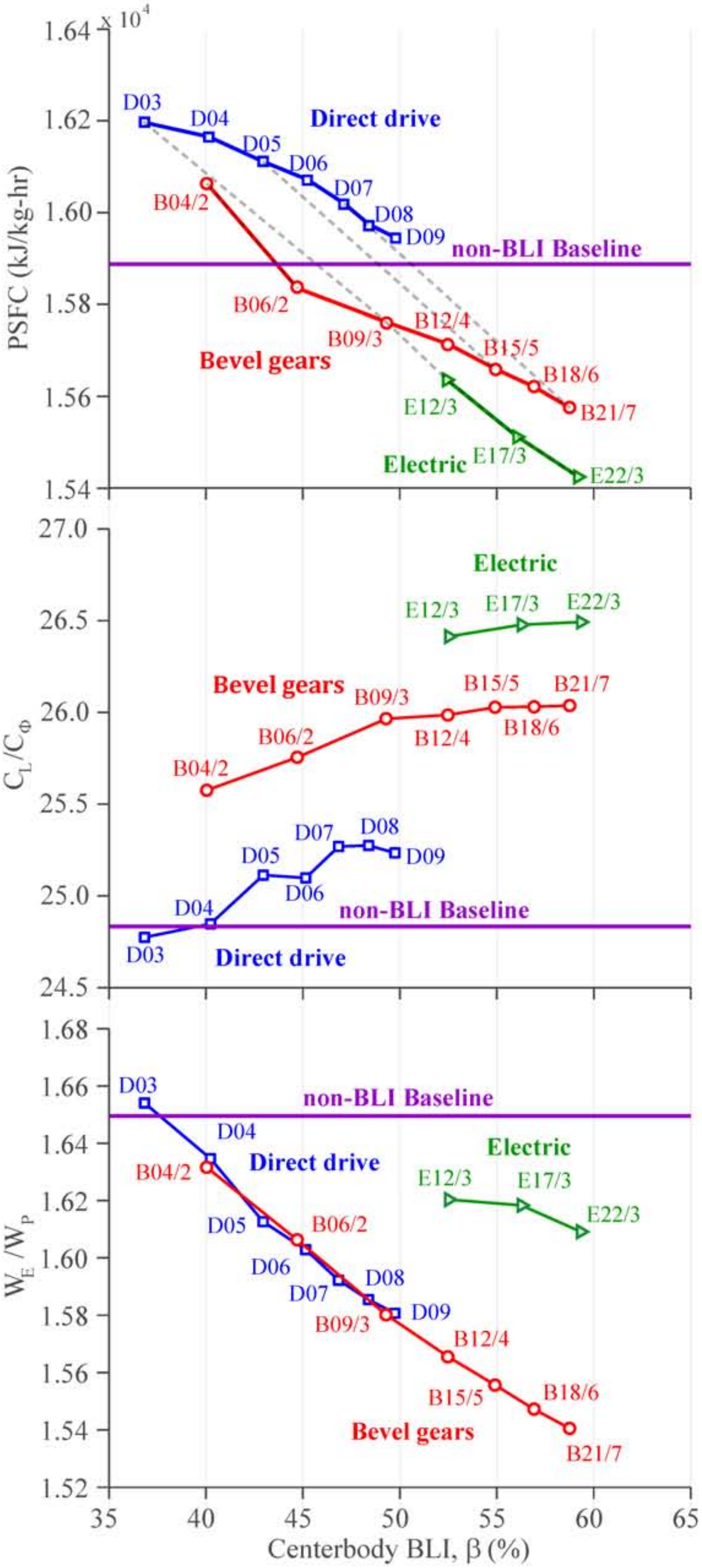

Figure 6-13: PSFC (uppermost), C_L/C_{Φ^*} (center) and W_E/W_P (lowermost) of H3L designs. Note that for the non boundary layer ingesting case, $C_L/C_{\Phi^*} = C_L/C_D$

core size increases PSFC. This is directly related to the polytropic efficiency of the HPC, which decreases[16] as the size of the turbogenerator is reduced. The introduction of electric transmission allows the propulsion system to ingest more boundary layer, without increasing the number of turbogenerators, thus giving the best PSFC among all types of transmission systems examined.

$^{C_L}/_{C_{\Phi *}}$ is affected by changes in span loading due to changes in aircraft balance; nacelle dissipation due to the nacelle size; and the airframe wake dissipation which is determined by the amount of BLI. The result is that $^{C_L}/_{C_{\Phi *}}$ increases with increased BLI (see Figure 6-13 (center)). This, like the PSFC trend, indicates an improvement in PFEI with increased BLI. For a given transmission system, improvements in $^{C_L}/_{C_{\Phi *}}$ from increased BLI result from a decrease in nacelle dissipation as the number of fans is increased and from the reduction of wake dissipation which scales linearly with the amount of boundary layer ingested. Because the nacelle length to diameter ratio ($^L/_D$) was fixed, increasing the number of fans results in shorter nacelles, reducing the overhang of the nacelle beyond the airframe and the nacelle wetted area. The change in transmission system also impacts $^{C_L}/_{C_{\Phi *}}$ through span loading.

The change in span loading occurs mainly from the change in aircraft CG location, which results from a change in the propulsion system weight and the amount of fuel carried by the aircraft. For example, although both D09 and B09/3 ingest approximately the same amount of boundary layer, D09 has a lower $^{C_L}/_{C_{\Phi *}}$ than B09/3 (79 for the D09 versus 82 for the B09/3). While the propulsion system weight of the two configurations are similar (43,177lbs for D09, 43,675lbs for B09/3), the higher PSFC of the D09 propulsion system requires the aircraft to carry more fuel, which degrades its span loading efficiency.

There is also a change in aerodynamic performance between the beveled gears and the electric configuration due to the change in propulsion system weight. For example, the E12/3 design has a heavier propulsion system than the B12/4 design (51,760lbs compared to 41,500lbs). Because it is added in an area that does not negatively impact the aircraft balance, the added propulsion system weight improves the ratio of lift to parasitic drag, increasing the aerodynamic efficiency of the aircraft. The result is higher aerodynamic performance for the E12/3 design.

The empty weight of the aircraft is affected directly by propulsion system weight. As in Figure 6-13 (lowermost), the choice of transmission system impacts the ratio of operating

---

[16] from Reynolds number and tip clearance increase

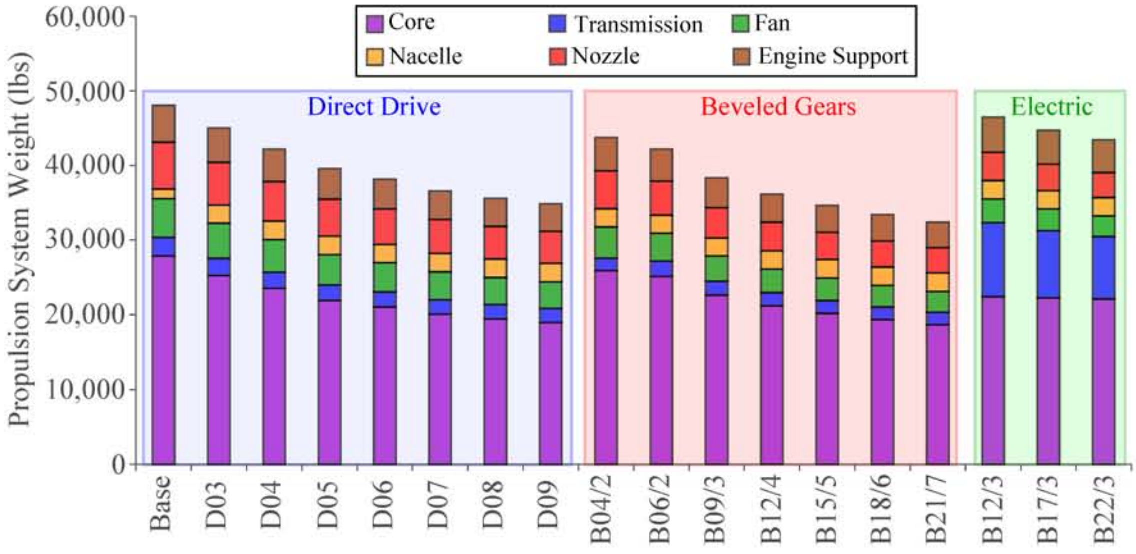

Figure 6-14: Weight breakdowns of H3L propulsion system

empty weight to payload weight. The electric transmission system is heavier than the beveled gear transmission system. For a given BLI fraction, the weight of the direct drive propulsion system is the lightest, followed by bevel gears, while the electric transmission system is the heaviest. However, the empty weight fraction of the direct drive and beveled gear configurations are essentially equal. This is a coincidence arising from opposing factors; the direct drive propulsion system is lighter, yielding a lower empty weight fraction, while its higher PSFC increases the amount of required fuel, increasing the empty weight fraction.

The estimate for weight variation is further seen in Figure 6-14, which shows the weight breakdown of the propulsion system. The weight of the electric transmission system accounts for almost 20% of the total propulsion system weight. The essential weight of the electric transmission system might be optimistic as it does not include the power transmission wires or a redundant cooling system, which could be required to ensure safe operation of the HTSC generator and motors.

6.3.2 HWB Aircraft Design Summary

Figure 6-15 shows four different HWB designs. The H3J-Base configuration is the baseline, lowest technological risk design, without BLI. A total fuel burn reduction of 50% relative to the baseline Boeing 777-200LR aircraft is suggested from this baseline configuration.

The H3J-B04/2 configuration, with two engine clusters, each consisting of two fans driven

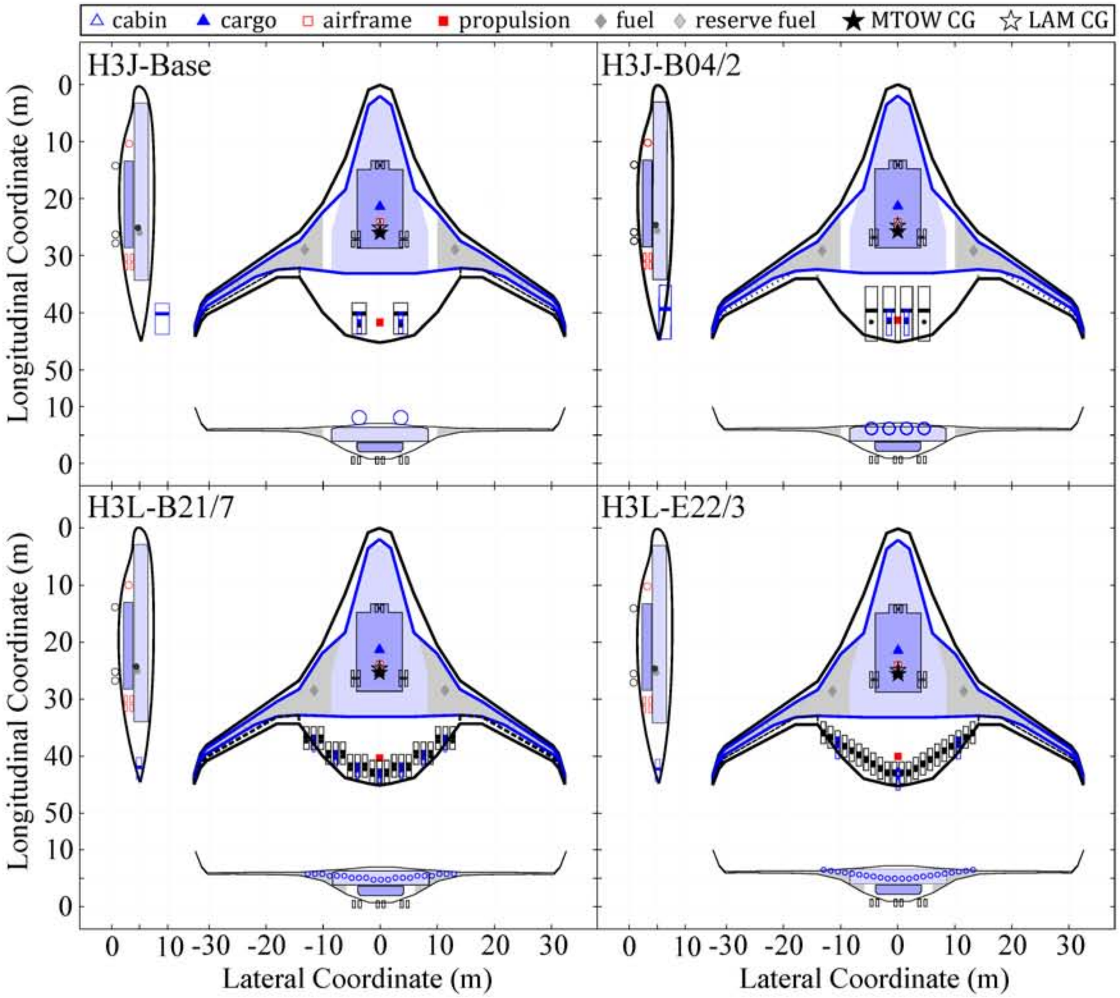

Figure 6-15: Three view schematic of H3J-Base (upper left), H3J-B04/2 (upper right), H3L-B21/7 (lower left) and H3L-E22/3 (lower right) with details for the cabin, cargo, engines, undercarriage, and internal spars.

by one turbogenerator, takes one step further in the use of advanced technology, featuring a beveled gear transmission system to increase the amount of BLI using only two cores. This configuration has a PFEI reduction of 52% from the baseline aircraft. The largest risk of this configuration is the beveled gear transmission system.

The H3L-B21/7 configuration, which uses seven engine clusters, each consisting of one turbogenerator driving three fans with a beveled gear transmission system, is the lowest PFEI design using a mechanical transmission system. This has a PFEI reduction of 57% compared to the reference aircraft, but it is more complex. This design relies on the use of LNG, which has risk associated with airport infrastructure and aircraft thermal management. The use of seven turbogenerators introduces further risk due to the high efficiency

Table 6.5: H-Series Aircraft Parameters

	H3J-Base	H3J-B04/2	H3L-B21/7	H3L-E22/3
PFEI and Key Terms from Modified Breguet Range Equation				
PFEI (kJ/kg-km)	2.93	2.87	2.56	2.54
PFEI improvement (%)	49.5%	51.7%	56.9%	57.2%
H (MJ/kg)	43.2	43.2	50.0	50.0
PSFC (g/kW-hr)	0.182	0.184	0.156	0.154
$C_L/C_{\Phi*}$	24.2	24.9	26.0	26.5
β, fuselage	0.0%	40.6%	58.8%	59.3%
W_E/W_{MTOW}	0.448	0.450	0.467	0.479
W_E/W_P	1.65	1.63	1.54	1.61
Geometric Parameters				
Span (m)	65.0	65.0	65.0	65.0
Planform area (m^2)	946.9	949.5	944.6	944.6
Fuselage length (m)	45.1	45.1	45.1	45.1
Aspect ratio, b2/S	4.5	4.5	4.5	4.5
Mid chord sweep (degree)	31.4	30.9	31.5	31.5

small cores (HPC exit corrected mass flow 1.3lbm/s, polytropic efficiency 90%) that would be required and the possibility of distorted flow entering the center turbogenerator.

The configuration using the electric transmission system, the H3L-E22/3 design, has the lowest PFEI (2.54kJ/kg-km) among all the designs, with a PFEI reduction 57% relative to the B777-200LR. As discussed, this design has considerable risk.

Table 6.5 lists the aircraft parameters of the four designs examined. As one goes from left-to-right from the H3J-Base to the H3L-E22/3, the designs increase in technological risk. The aerodynamic performance of the aircraft ($C_L/C_{\Phi*}$) and the PSFC improve, primarily due to the increased BLI fraction. The empty weight fraction increases due to the added complexity associated with the transmission system and the type of fuel being used. The ultimate choice is a tradeoff between risk, cost and performance.

6.4 Summary

The impact of propulsion system configuration and fuel type on the fuel burn performance of an HWB aircraft was evaluated using the design methodology HWBOpt. The wide center-body of the HWB can accommodate a highly integrated, distributed propulsion system, and the large design space offers the possibility of performance improvements from the extensive use of BLI. Furthermore, the large internal volume of a HWB aircraft can accommodate low density, high specific energy fuels like LNG. Weight and performance models of mechanically geared (planetary and beveled) and electrical transmissions systems were developed, and various propulsion system configurations with different numbers of turbogenerators and propulsors were assessed. The performance assessment of the integrated airframe and propulsion system was carried out using a power balance method. A maximum PFEI reduction of 57% was found relative to a Boeing 777-200LR.

The primary tradeoffs in the propulsion system design of the HWB aircraft exist between the amount of BLI and the complexity and weight of the propulsion system configuration. BLI improves the aircraft aerodynamics and propulsion system through a reduction of wake dissipation and the ingestion of lower kinetic energy flow. Distribution of the propulsion system adds weight to the aircraft, which increases the empty weight fraction of the aircraft. Increased propulsion system weight also introduces secondary impacts on the aerodynamic performance of the aircraft through a shift in the center of gravity, which can improve aerodynamic efficiency. Increasing the number of turbogenerators leads to a reduction of HPC polytropic efficiency, which reduces engine PSFC.

Designs with increased BLI give better PFEI, but the incremental performance gains diminish as BLI is increased. For an equal amount of BLI, the use of an electric transmission system yielded a PFEI improvement of less than 1% relative to designs using a beveled gear transmission system with multiple turbogenerators. At the maximum BLI span coverage considered here, both the H3L-E22/3 aircraft and the H3L-B21/7 aircraft concept had 57% reduction in PFEI.

The HWB designs analyzed have PFEI improvement, relative to the reference aircraft, between 50% (low-risk, direct drive design) and 57% (high risk, LNG-electric design). A preliminary assessment of relative preference among these configurations has been provided, but the ultimate choice of the propulsion system should come from a broader consideration of tradeoffs among fuel burn, cost, environmental performance, and relative risk. Given the technology challenge and risk associated with distributing the propulsor over the entire fuselage, it appears that the performance gain of BLI is marginal for the HWB configuration studied. BLI will have a much bigger impact when applied to a tube-and-wing configuration, where large amount of BLI can be achieved without a distributed propulsion system configuration.

Chapter 7

Summary, Conclusions and Suggestions for Further Research

7.1 Summary and Conclusions

The capability to rapidly estimate the aerodynamic performance of an aircraft configuration is critical in conceptual design, as the performance is evaluated thousands of times during the optimization studies. Such studies currently use methods based on a momentum balance, with drag of the airframe matched against the thrust generated by the propulsor. For configurations in which the airframe and the propulsion system are tightly integrated, however, the pressure field interactions between the propulsor and the fuselage, as well as the ingestion of boundary layers, makes the concept of thrust and drag less well defined, and insert possible arbitrariness into the accounting of thrust and drag. For these configurations, the power balance method has been shown to be more useful for performance estimation, because the mechanical energy loss is cumulative, not affected explicitly by pressure forces, and allows clear bookkeeping of loss generation from different components.

In the power balance method, the mechanical energy production and the power consumption of the aircraft are balanced. This allows:

- Evaluating the aerodynamic body performance using a global quantity which is only weakly affected by the local pressure field. In an adiabatic flow with no strong[1] shocks, the dependence of the local pressure field can be eliminated.

---

[1] Shock upstream Mach number less than 1.2

- Quantifying the increase in drag or dissipation due to potential-flow interactions between components, which historically has been viewed as some uncertain "interference" drag.

- Expressing the boundary layer mechanical energy loss using an explicit function of edge velocity and dissipation coefficient.

- Calculating aerodynamic performance using the dissipation coefficient instead of the skin friction coefficient. The former varies much less than the latter in pressure gradients and therefore gives more accurate estimates of the performance.

The thesis demonstrated the major benefits of the power balance method for three different applications: 1) derivation of analytical expression of profile drag estimates for conceptual design applications, 2) aerodynamic performance estimation for three basic integrated configurations, and 3) performance quantification of a hybrid wing body (HWB) with BLI propulsion system.

7.1.1 Improved Estimates for Profile Drag Using the Power Balance Method

In conceptual aircraft design, profile drag is estimated from the wetted area method, where a flat plate skin friction coefficient is scaled by a form factor specific to an airfoil or body geometry. The value of the form factor relies on empirical data, and is not applicable to a new geometry without such data. Using the power balance method, an analytical expression for the form factor was derived, allowing calculation of the form factor without empiricism.

The accuracy of the derived analytical form factor formula was quantified using three examples: bodies of revolution, low speed 2D airfoil, and transonic 2D airfoil. For all configurations analyzed, the form factor model was shown to be as accurate as the empirical form factor correlations. The accuracy was within 2% for:

1. D8 fuselage section with fineness ratio (l/d) greater than 5 at $M_\infty = 0.1$, and greater than 6.25 at $M_\infty = 0.85$.

2. GAW1 airfoil with lift coefficient between -0.5 and 1.0 at $M_\infty = 0.15$.

3. RAE2822 airfoil with freestream Mach number up to $M_\infty = 0.71$ at $\alpha = 3°$.

Aircraft operating at cruise typically are within the range of parameters examined in cases 1, 2, and 3 listed above. The analytical expression from the power balance method is therefore applicable for use at the preliminary design stage in estimating cruise performance.

7.1.2 Effect of Interference on Boundary Layer Loss

Traditional estimates of the total drag due to interference effects, e.g. [20], scale the individual drag contributions with local $\rho_e U_e^2$. Discrepancies between the estimated and actual drag are attributed to "interference drag", which is estimated from correlations. To determine the effect of interference on the boundary layer, the mechanical energy loss was evaluated numerically, using MSES, for three integrated configurations: a fuselage with actuator disk, two interfering airfoils, and a nacelle with actuator disk. The results show that the effect of interference on boundary layer mechanical energy loss scales as $\rho_e U_e^3 \left(1 + \frac{\gamma-1}{2} M_e^2\right)^r$, in line with the scaling developed from the boundary layer mechanical energy equation. The scaling is accurate to within 10% for configurations satisfying $\Delta \bar{H}_k < 0.04$, where $\Delta \bar{H}_k \equiv \left(\bar{H}'_k - \bar{H}_k\right)$, $\bar{H}_k$ is the average boundary layer kinematic shape parameter of the configuration, and quantities with prime represent those from the integrated configuration. The loss scaling breaks down when the boundary layer separates, but this is not a serious limitation since separated flow is not present in an assumed design-point operating condition.

7.1.3 Effect of BLI on HWB Fuel Efficiency

The power balance method was applied to conduct a Multidisciplinary Design Optimization (MDO) of an BLI HWB aircraft. The study included a number of different propulsion system configurations. Each system had a different amount of BLI, a different number of propulsors and turbogenerators, and a different choice of transmission system: coaxial planetary gear, beveled gear or electrical transmission systems.

For the propulsion system configurations studied, the aircraft fuel burn decreased monotonically with increasing amounts of BLI. The design with BLI on the entire HWB center body gives an improvement of 11% from a non-BLI aircraft. It appears, however, that the performance gain from BLI is problematic given the amount of technology challenge and risk associated with distributing the propulsor over the entire fuselage. BLI can have a larger impact when applied to tube-and-wing configuration, where it can be achieved without a distributed propulsion system.

7.2 Suggestions for Further Research

This section presents suggestions for further research on the topics presented in this thesis. It is emphasized that these suggestions are only a part of many possible applications of the power balance method.

The form factor correlation presented in Chapter 4 has errors whose major cause is the change in boundary layer properties due to separation. One could improve the form factor correlation by developing a secondary correction factor to account for the change in the boundary layer properties. For example, one could relate the velocity gradient over the airfoil surface to adjust the mechanical loss production. One could also develop a correlation between the mechanical loss production and the strength of the normal shock interacting with the boundary layer.

The drag correlations were only assessed for two-dimensional and axisymmetric flow. Analysis of a fully three dimensional flow should be conducted to assess the effect of cross flow and other three dimensional flow features.

No simulations were conducted for freestream Mach number close to unity and an analysis could be carried out to define how boundary layer loss scales in supersonic flow.

The analysis of integrated configurations has been conducted for two-dimensional geometries and this should be extended to three dimensional flow. An interesting geometry to investigate would be one with intersections, such as wing/fuselage or strut/wing junctions. Intersections of this type appear in many aircraft configurations, for which performance estimation is currently done through empirical correlations.

Another suggested field of study is the investigation of the applicability of the power balance method to flow fields in which heat transfer has a substantial effect in the flow, such as ramjets.

Appendix A

Integral Defect Equations

The derivation of the mass, momentum and mechanical energy boundary layer defect equations is presented here.

A.1 Nomenclature

A.1.1 Definition of Local Coordinate System

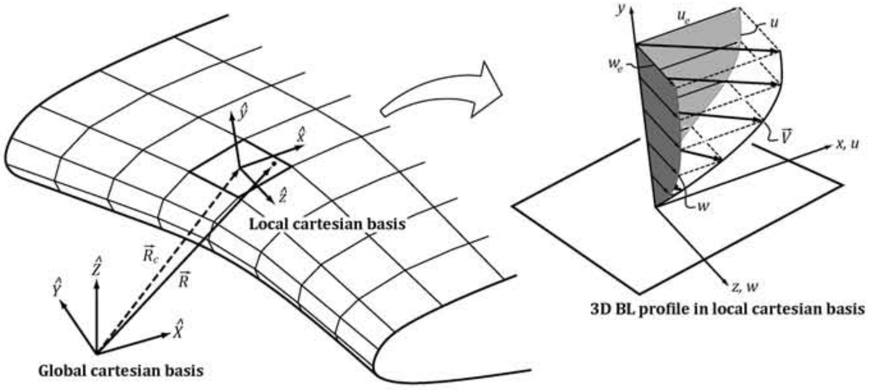

Figure A-1: Definition of local cartesian coordinate system

$$
\begin{aligned}
x &= (\boldsymbol{R} - \boldsymbol{R_O}) \cdot \hat{\imath} \quad & u &= \boldsymbol{u} \cdot \hat{\imath} \\
y &= (\boldsymbol{R} - \boldsymbol{R_O}) \cdot \hat{\jmath} \quad & v &= \boldsymbol{u} \cdot \hat{\jmath} \\
z &= (\boldsymbol{R} - \boldsymbol{R_O}) \cdot \hat{k} \quad & w &= \boldsymbol{u} \cdot \hat{k}
\end{aligned}
$$

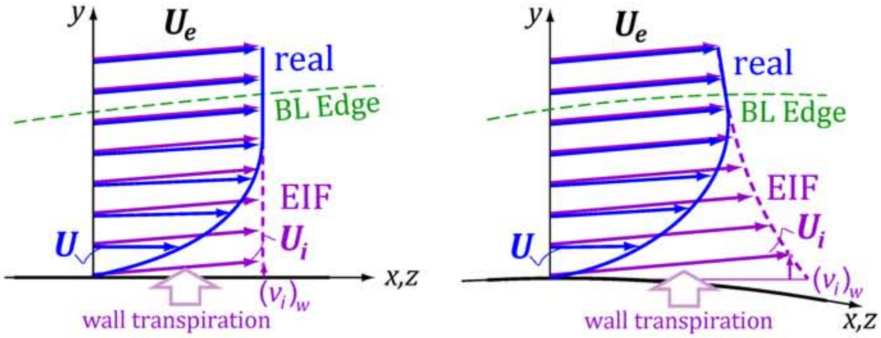

Figure A-2: Real viscous flow and equivalent inviscid flow over curved (left) and flat (right) shear layer

A.1.2 Gradient and Divergence Relations and Identities

$$\nabla() = \hat{\imath}\frac{\partial}{\partial x} + \hat{\jmath}\frac{\partial}{\partial y} + \hat{k}\frac{\partial}{\partial z} \tag{A.1}$$

$$\bar{\nabla}() = \hat{\imath}\frac{\partial}{\partial x} + \hat{k}\frac{\partial}{\partial z} \tag{A.2}$$

$$\begin{aligned} \int_{y_w}^{y_e} \nabla \cdot \boldsymbol{f}\, dy \quad &= \quad \bar{\nabla} \cdot \int_{y_w}^{y_e} \left(f_x \hat{\imath} + f_z \hat{k} \right) dy + \left[f_y \right]_{y_w}^{y_e} \\ &\quad - \left[\left(f_x \hat{\imath} + f_z \hat{k} \right) \cdot \bar{\nabla} y_e \right]_{y_w}^{y_e} \end{aligned} \tag{A.3}$$

$$\nabla \cdot (a\boldsymbol{B}) \quad = \quad \nabla a \cdot \boldsymbol{B} + a \nabla \cdot \boldsymbol{B} \tag{A.4}$$

$$\nabla \cdot (\bar{\bar{\alpha}} \cdot \boldsymbol{B}) \quad = \quad \left(\nabla \cdot \bar{\bar{\alpha}} \right) \cdot \boldsymbol{B} + \left(\bar{\bar{\alpha}} \cdot \nabla \right) \cdot \boldsymbol{B} \tag{A.5}$$

A.2 Integral Defect and Thickness Definitions

Density defect:

$$\mathrm{m} = \rho_e \delta_\rho = \int_{y_w}^{y_e} \left(\rho_i - \rho \right) dy \tag{A.6}$$

Mass defect:

$$\mathbf{M} = \rho_e U_e \boldsymbol{\delta^*} = \rho_e U_e \left(\delta_x^* \hat{\imath} + \delta_z^* \hat{k}\right) = \int_{y_w}^{y_e} \left(\rho_i \boldsymbol{U_i} - \rho \boldsymbol{U}\right)\, dy \tag{A.7}$$

$$\mathrm{M}_x = \rho_e U_e \delta_x^* = \int_{y_w}^{y_e} \left(\rho_e u_e - \rho u\right)\, dy \tag{A.8}$$

$$\mathrm{M}_z = \rho_e U_e \delta_z^* = \int_{y_w}^{y_e} \left(\rho_e w - \rho w\right)\, dy \tag{A.9}$$

x-momentum defect:

$$\mathbf{P}_{\boldsymbol{x}} = \rho_e U_e^2 \boldsymbol{\theta_x} = \rho_e U_e \left(\theta_{xx} \hat{\imath} + \theta_{xz} \hat{k}\right) = \int_{y_w}^{y_e} \left(u_i - u\right) \rho \boldsymbol{U}\, dy \tag{A.10}$$

$$\mathrm{P}_{xx} = \rho_e U_e^2 \theta_{xx} = \int_{y_w}^{y_e} \left(u_i - u\right) \rho u\, dy \tag{A.11}$$

$$\mathrm{P}_{xz} = \rho_e U_e^2 \theta_{xz} = \int_{y_w}^{y_e} \left(u_i - u\right) \rho w\, dy \tag{A.12}$$

z-momentum defect:

$$\mathbf{P}_{\boldsymbol{z}} = \rho_e U_e^2 \boldsymbol{\theta_z} = \rho_e U_e^2 \left(\theta_{zx} \hat{\imath} + \theta_{zz} \hat{k}\right) = \int_{y_w}^{y_e} \left(w_i - w\right) \rho \boldsymbol{q}\, dy \tag{A.13}$$

$$\mathrm{P}_{zx} = \rho_e U_e^2 \theta_{xx} = \int_{y_w}^{y_e} \left(w_i - w\right) \rho u\, dy \tag{A.14}$$

$$\mathrm{P}_{zz} = \rho_e U_e^2 \theta_{zz} = \int_{y_w}^{y_e} \left(w_i - w\right) \rho w\, dy \tag{A.15}$$

Scalar kinetic energy defect:

$$\mathrm{k} = \frac{1}{2} \rho_e U_e^2 \delta_E = \frac{1}{2} \int_{y_w}^{y_e} \left(\rho_i U_i^2 - \rho U^2\right)\, dy \tag{A.16}$$

Kinetic energy defect:

$$\mathbf{K} = \frac{1}{2}\rho_e U_e^3 \boldsymbol{\theta^*} = \frac{1}{2}\rho_e U_e^3 \left(\theta_x^* \hat{\imath} + \theta_z^* \hat{k}\right) = \frac{1}{2}\int_{y_w}^{y_e} \left(U_i^2 - U^2\right) \rho \boldsymbol{U}\, dy \tag{A.17}$$

$$\mathrm{K}_x = \frac{1}{2}\rho_e U_e^3 \theta_x^* = \frac{1}{2}\int_{y_w}^{y_e} \left(U_i^2 - U^2\right) \rho u\, dy \tag{A.18}$$

$$\mathrm{K}_z = \frac{1}{2}\rho_e U_e^3 \theta_z^* = \frac{1}{2}\int_{y_w}^{y_e} \left(U_i^2 - U^2\right) \rho w\, dy \tag{A.19}$$

Potential mixing dissipation:

$$\mathbf{E} = \frac{1}{2}\rho_e q U_e^3 \boldsymbol{\delta_k} = \frac{1}{2}\rho_e U_e^3 \left(\delta_{k_x} \hat{\imath} + \delta_{k_z} \hat{k}\right) = \frac{1}{2}\int_{y_w}^{y_e} \left(U_i - U\right)^2 \rho \boldsymbol{U}\, dy \tag{A.20}$$

$$\mathrm{E}_x = \frac{1}{2}\rho_e U_e^3 \delta_{k_x}^* = \frac{1}{2}\int_{y_w}^{y_e} \left(U_i - U\right)^2 \rho u\, dy \tag{A.21}$$

$$\mathrm{E}_z = \frac{1}{2}\rho_e U_e^3 \delta_{k_z}^* = \frac{1}{2}\int_{y_w}^{y_e} \left(U_i - U\right)^2 \rho w\, dy \tag{A.22}$$

Density flux defect:

$$\mathbf{D} = \rho_e U_e \boldsymbol{\delta^{**}} = \rho_e U_e \left(\delta_x^{**} \hat{\imath} + \delta_z^{**} \hat{k}\right) = \int_{y_w}^{y_e} \left(\rho_i - \rho\right) \boldsymbol{U}\, dy \tag{A.23}$$

$$\mathrm{D}_x = \rho_e U_e \delta_x^{**} = \int_{y_w}^{y_e} \left(\rho_i - \rho\right) u\, dy \tag{A.24}$$

$$\mathrm{D}_z = \rho_e U_e \delta_z^{**} = \int_{y_w}^{y_e} \left(\rho_i - \rho\right) w\, dy \tag{A.25}$$

Volume flux defect:

$$\mathbf{Q} = U_e \boldsymbol{\delta_k^*} = U_e \left(\delta_{k_x}^* \hat{\imath} + \delta_{k_z}^* \hat{k}\right) = \int_{y_w}^{y_e} \left(\boldsymbol{U_i} - \boldsymbol{U}\right)\, dy \tag{A.26}$$

$$\mathrm{Q}_x = U_e \delta^*_{k_x} = \int_{y_w}^{y_e} (u_i - u)\, dy \tag{A.27}$$

$$\mathrm{Q}_z = U_e \delta^*_{k_z} = \int_{y_w}^{y_e} (w_i - w)\, dy \tag{A.28}$$

Dissipation integral:

$$\mathcal{D} = \int_{y_w}^{y_e} \left(\bar{\bar{\tau}} \cdot \nabla\right) \cdot \boldsymbol{u}\, dy \approx \int_{y_w}^{y_e} \left(\tau_{xy} \frac{\partial u}{\partial y} + \tau_{zy} \frac{\partial w}{\partial y}\right) dy. \tag{A.29}$$

A.3 Approximations

A.3.1 Thin Shear Layer Approximations

$$()_i \approx ()_e\,, \tag{A.30}$$

$$\nabla p_i \approx \nabla p, \tag{A.31}$$

$$\nabla \cdot \bar{\bar{\tau}} \approx \frac{\partial \boldsymbol{\tau}}{\partial y} = \frac{\partial \tau_x}{\partial y}\hat{\imath} + \frac{\partial \tau_z}{\partial y}\hat{k}. \tag{A.32}$$

A.3.2 Other assumptions

- No body forces
- No heat addition

A.4 Defect Integral Equations

A.4.1 Mass Relations

Mass conservation:

$$\frac{\partial \rho}{\partial t} + \nabla \cdot (\rho \boldsymbol{u}) = 0. \tag{A.33}$$

Taking the defect integral:

$$\int_{y_w}^{y_e} \left\{ \frac{\partial \left(\rho_i - \rho\right)}{\partial t} + \nabla \cdot \left(\rho_i \boldsymbol{u_i} - \rho \boldsymbol{u}\right) = 0 \right\} dy. \tag{A.34}$$

Using identity in Eq. A.3,

$$\frac{\partial m}{\partial t} + \bar{\nabla} \cdot \mathbf{M} - \left(\rho_i v_i - \rho v\right)_w = 0. \tag{A.35}$$

A.4.2 Momentum Relations

$$\begin{aligned} x: \frac{\partial \rho u}{\partial t} + \nabla \cdot \left(\rho \boldsymbol{u} u\right) &= -\nabla \cdot \left(p \hat{\imath}\right) + \nabla \cdot \left(\bar{\bar{\tau}} \cdot \hat{\imath}\right), && \text{(A.36)} \\ z: \frac{\partial \rho w}{\partial t} + \nabla \cdot \left(\rho \boldsymbol{u} w\right) &= -\nabla \cdot \left(p \hat{k}\right) + \nabla \cdot \left(\bar{\bar{\tau}} \cdot \hat{k}\right). && \text{(A.37)} \end{aligned}$$

Forming the defect integral,

$$\begin{aligned} x: \quad & \int_{y_w}^{y_e} \left\{ \frac{\partial \left(\rho_i u_i - \rho u\right)}{\partial t} + \nabla \cdot \left(\rho_i \boldsymbol{u_i} u_i - \rho \boldsymbol{u} u\right) = -\nabla \cdot \left(\bar{\bar{\tau}} \cdot \hat{\imath}\right) \right\} dy, && \text{(A.38)} \\ z: \quad & \int_{y_w}^{y_e} \left\{ \frac{\partial \left(\rho_i w_i - \rho w\right)}{\partial t} + \nabla \cdot \left(\rho_i \boldsymbol{u_i} w_i - \rho \boldsymbol{u} w\right) = -\nabla \cdot \left(\bar{\bar{\tau}} \cdot \hat{k}\right) \right\} dy, && \text{(A.39)} \end{aligned}$$

which leads to:

$$\begin{aligned} x: \frac{\partial \mathrm{M}_x}{\partial t} + \bar{\nabla} \cdot \left(\mathbf{P}_x + u_e \mathbf{M}\right) - \left(\rho_i v_i u_i - \rho v u\right)_w &= \tau_{x_w}, && \text{(A.40)} \\ z: \frac{\partial \mathrm{M}_z}{\partial t} + \bar{\nabla} \cdot \left(\mathbf{P}_{\boldsymbol{z}} + w_e \mathbf{M}\right) - \left(\rho_i v_i w - \rho v w\right)_w &= \tau_{z_w}. && \text{(A.41)} \end{aligned}$$

Form [Eq. A.40]$-u_e$[Eq. A.35] and [Eq. A.41]$-w_e$[Eq. A.35]:

$$\begin{aligned} x: \frac{\partial \mathrm{M}_x}{\partial t} - u_e \frac{\partial m}{\partial t} + \bar{\nabla} \cdot \mathbf{P}_{\boldsymbol{x}} + \mathbf{M} \cdot \bar{\nabla} u_e - \left(\rho v \left(u_i - u\right)\right)_w &= \tau_{x_w}, && \text{(A.42)} \\ z: \frac{\partial \mathrm{M}_z}{\partial t} - w_e \frac{\partial m}{\partial t} + \bar{\nabla} \cdot \mathbf{P}_{\boldsymbol{zx}} + \mathbf{M} \cdot \bar{\nabla} w_e - \left(\rho v \left(w_i - w\right)\right)_w &= \tau_{z_w}. && \text{(A.43)} \end{aligned}$$

A.4.3 Mechanical Energy Relations

The mechanical energy relation can be obtained by calculating the dot product between the momentum equation and $\boldsymbol{u}$, and simplify $|\boldsymbol{u}^2| \simeq U^2$:

$$\frac{\partial\left(\rho^{1}/_{2}q^{2}\right)}{\partial t}+\nabla\cdot\left(\rho\boldsymbol{u}\frac{1}{2}q^{2}\right)=-\boldsymbol{u}\cdot\nabla p+\boldsymbol{u}\cdot\left(\nabla\cdot\overline{\overline{\tau}}\right). \tag{A.44}$$

Forming the defect integral:

$$\int_{y_w}^{y_e}\left\{\frac{\partial\left(^{1}/_{2}\left(\rho_i U_i^2-\rho U^2\right)\right)}{\partial t}+\nabla\cdot\left(\frac{1}{2}\left(\rho_i\boldsymbol{u_i}U_i^2-\rho\boldsymbol{u}U^2\right)\right)=-\left[\boldsymbol{u_i}\cdot\nabla p_i-\boldsymbol{u}\cdot\nabla p\right]-\boldsymbol{u}\cdot\left(\nabla\cdot\overline{\overline{\tau}}\right)\right\}dy, \tag{A.45}$$

$$\frac{\partial k_E}{\partial t}+\bar{\nabla}\cdot\left(\mathbf{K}+\frac{1}{2}U_e^2\mathbf{M}\right)-\left(\frac{1}{2}\left(\rho_i v_i U_i^2-\rho v U^2\right)\right)_w=-\mathbf{M}_k\cdot\bar{\nabla}p_e+\mathcal{D}+\left(\boldsymbol{u}\cdot\vec{\tau}\right)_w. \tag{A.46}$$

Form [Eq. A.46]$-\frac{1}{2}U_e^2$[Eq. A.35] and substitute $\bar{\nabla}p_e=-\rho_e\bar{\nabla}\frac{1}{2}U_e^2$ and $\mathbf{M}-\rho_e\mathbf{Q}=\mathbf{D}$

$$\frac{\partial k_E}{\partial t}-\frac{1}{2}U_e^2\frac{\partial m}{\partial t}+\bar{\nabla}\cdot\mathbf{K}+\mathbf{D}\cdot\bar{\nabla}\frac{1}{2}U_e^2=\mathcal{D}+\left(\boldsymbol{U}\cdot\vec{\tau}\right)_w. \tag{A.47}$$

Vector identity in Eq. A.5 was used to simplify the equation.

A.4.4 Summary

Differential version of the boundary layer defect equations derived in this section:

Mass conservation:

$$\frac{\partial m}{\partial t}+\bar{\nabla}\cdot\mathbf{M}-\left(\rho_i v_i-\rho v\right)_w=0. \tag{A.48}$$

x- and z-momentum conservation:

$$x:\ \frac{\partial \mathrm{M}_x}{\partial t}-u_e\frac{\partial m}{\partial t}+\bar{\nabla}\cdot\mathbf{P}_{\boldsymbol{x}}+\mathbf{M}\cdot\bar{\nabla}u_e-\left(\rho v\left(u_e-u\right)\right)_w = \tau_{x_w}, \tag{A.49}$$

$$z:\ \frac{\partial \mathrm{M}_z}{\partial t}-w_e\frac{\partial m}{\partial t}+\bar{\nabla}\cdot\mathbf{P}_{\boldsymbol{z}}+\mathbf{M}\cdot\bar{\nabla}w_e-\left(\rho v\left(w_e-w\right)\right)_w = \tau_{z_w}. \tag{A.50}$$

Mechanical energy:

$$\frac{\partial k}{\partial t} - \frac{1}{2} U_e^2 \frac{\partial m}{\partial t} + \bar{\nabla} \cdot \mathbf{K} + \mathbf{D} \cdot \bar{\nabla} \frac{1}{2} U_e^2 = \mathcal{D} + (\boldsymbol{u} \cdot \tau)_w \, . \tag{A.51}$$

Appendix B

Numerical Calculation of Flat Plate Turbulent Boundary Layer Profile

This section describes the boundary layer calculation used to calculate the flat plate skin friction and dissipation. A fourth order Runge-Kutta iteration is used at discreet points along the surface, marching forward to calculate the evolution of the boundary layer over a constant edge velocity, assuming incompressible, fully turbulent flow. The boundary layer velocity distribution at each discreet point (referred through index i) is calculated using the combination of Spalding turbulent wall layer profile and Coles turbulent outer layer profile [2], coupled with the G-beta locus of Clauser [1] as closure relations.

B.1 Integral Boundary Layer Formulation

B.1.1 Governing Equations

The boundary layer profile is governed by the integral boundary layer momentum equations for incompressible flow,

$$\frac{d\theta}{d\xi} = \frac{C_f}{2}\left(1 - \frac{(H+2)}{H}\beta\right). \tag{B.1}$$

where β is the Clauser pressure gradient paramter,

$$\beta \triangleq \frac{\delta^*}{\tau_w}\frac{dp}{d\xi} = H\frac{2}{C_f}\frac{\theta}{u_e}\frac{du_e}{d\xi}. \tag{B.2}$$

For a flat plate, the edge velocity gradient is zero ($\beta = 0$) and yields

$$\frac{d\theta}{d\xi} = \frac{C_f}{2}. \tag{B.3}$$

B.1.2 Turbulent Boundary Layer Velocity Profile

The boundary layer profile at each point is calculated from a combination of Spalding turbulent wall layer profile and Coles turbulent outer layer profile [2], which expresses the boundary layer velocity profile in terms of skin friction coefficient (C_f) and the boundary layer thickness Reynolds number (Re_δ) as

$$U\left(Re_\delta,\, C_f\right) \triangleq \frac{u}{u_e} = \sqrt{\frac{C_f}{2}}\left[\frac{1}{\kappa}\ln\left(\eta Re_\delta\sqrt{C_f/2}\right) + (B + \Delta B) + A\, W(\eta)\right], \tag{B.4}$$

where κ and B are two log law constants, obtained by fitting the Spalding wall layer profile, and are given as $\kappa = 0.40$ and $B = 5.5$. ΔB is a correction factor to account for wall roughness, given by

$$\Delta B = \frac{1}{\kappa}\ln\left(1 + 0.3k^+\right). \tag{B.5}$$

k^+ is the normalized effective roughness height, defined as

$$k^+ \triangleq \frac{k}{\ell_\tau} = \frac{k}{\nu}\sqrt{\frac{C_f}{2}}. \tag{B.6}$$

A is the wake amplitude parameter, obtained as

$$A = \frac{1}{\sqrt{C_f/2}} - (B + \Delta B) - \frac{1}{\kappa}\ln\left(Re_\delta\sqrt{C_f/2}\right). \tag{B.7}$$

$W(\eta)$ is the Coles wake function,

$$W(\eta) = \sin^2\left(\frac{\pi}{2}\eta\right). \tag{B.8}$$

All boundary layer quantities such as Eq. B.4 δ^*,θ, θ^*, H and H^* are calculated by numerically integrating the velocity profile from Eq. B.4 from $\eta = 0$ to $\eta = 1$:

$$\delta^* \triangleq \int_0^1 (1-U)\, d\eta, \tag{B.9}$$

$$\theta \triangleq \int_0^1 (1-U)\, U\, d\eta \tag{B.10}$$

$$\theta^* \triangleq \int_0^1 \left(1-U^2\right) U\, d\eta \tag{B.11}$$

$$H \triangleq \frac{\delta^*}{\theta} \tag{B.12}$$

$$H^* \triangleq \frac{\delta^*}{\theta} \tag{B.13}$$

The dissipation coefficient is obtained as

$$2C_{\mathcal{D}} = H^* \frac{C_f}{2} \left(1 - \frac{H-1}{H}\beta\right). \tag{B.14}$$

To obtain the boundary layer velocity profile for each discrete point, a newton iteration is required to calculate $U(Re_\delta,\, C_f)$ for a specified momentum thickness θ, which requires two closure relations. The first relation is trivial, which relates the thickness of the boundary layer (Re_δ) to the momentum thickness (θ),

$$Re_\delta = \frac{Re_\theta}{\theta}. \tag{B.15}$$

The second relation relates the distribution of the skin friction coefficient C_f with the edge velocity distribution and the boundary layer shape parameter, using the G-beta locus from Clauser:

$$\frac{1}{C_f/2} \left(\frac{H-1}{H}\right)^2 = \mathcal{A}^2 \left[1 + \mathcal{B}\beta\right], \tag{B.16}$$

where $\mathcal{A}$ and $\mathcal{B}$ are constants obtained from experimental results, $\mathcal{A} = 6.7$ and $\mathcal{B} = 0.75$. Eq. B.16 simplifies to

$$\frac{1}{C_f/2} \left(\frac{H-1}{H}\right)^2 = \mathcal{A}^2 \tag{B.17}$$

for a flat plate where $\beta = 0$.

By combining Eq. B.4 with the two closure relations in Eq. B.15 and B.17, the flat plate boundary layer velocity profile U can be calculated as a function of the boundary layer momentum thickness θ as described in the following section.

B.2 Calculation Procedure

To obtain the flat plate boundary layer profile U_i at each discreet point i, U_i must be calculated from θ_i using a Newton iteration. The equation for the boundary layer profile (Eq. B.4) is be closed by two equations (Eq. B.15 and Eq. B.17). Equations B.15 and B.17 can be rearranged in residual form,

$$\begin{aligned} \mathcal{R}_1 &= Re_{\theta_i} - Re_{\delta_i}\theta_i, && \text{(B.18)} \\ \mathcal{R}_2 &= \left(\frac{H_i - 1}{H_i}\right)^2 - \mathcal{A}^2\frac{C_{f_i}}{2}. && \text{(B.19)} \end{aligned}$$

Solution of Eq. B.18 and B.19 is solved by Newton iteration. A good initial guess for Re_{δ_i} and C_{f_i} are the values at the previous station $Re_{\delta_{i-1}}$ and $C_{f_{i-1}}$. The values are updated via Newton iteration of the 2 × 2 system.

$$\begin{bmatrix} \frac{\partial \mathcal{R}_1}{\partial Re_{\delta\,i}}\left(Re_{\delta}{}_i^j,\, C_f{}_i^j\right) & \frac{\partial \mathcal{R}_1}{\partial \theta_i}\left(Re_{\delta}{}_i^j,\, C_f{}_i^j\right) \\ \frac{\partial \mathcal{R}_2}{\partial Re_{\delta\,i}}\left(Re_{\delta}{}_i^j,\, C_f{}_i^j\right) & \frac{\partial \mathcal{R}_2}{\partial \theta_i}\left(Re_{\delta}{}_i^j,\, C_f{}_i^j\right) \end{bmatrix} \begin{bmatrix} \delta\, Re_{\delta}{}^j \\ \delta\, C_f{}^j \end{bmatrix} = \begin{bmatrix} -\mathcal{R}_1\left(Re_{\delta}{}_i^j,\, C_f{}_i^j\right) \\ -\mathcal{R}_2\left(Re_{\delta}{}_i^j,\, C_f{}_i^j\right) \end{bmatrix} \tag{B.20}$$

$$\begin{aligned} Re_{\delta}{}_i^{j+1} &= Re_{\delta}{}_i^j + \delta\, Re_{\delta}{}^j\,, && \text{(B.21)} \\ C_f{}_i^{j+1} &= C_f{}_i^j + \delta\, C_f{}^j\,, && \text{(B.22)} \end{aligned}$$

where j is the number of Newton iterations.

Using the calculation of the velocity profile at each discreet point, the momentum thickness distribution over the flat plate is obtained by of the boundary layer is integrated numerically from the governing equation Eq. B.3 using a initial momentum thickness $Re_{\theta_0} = 150$. The numerical integration is done using a fourth order Runge-Kutta method:

$$\theta_{i+1} = \theta_i + \frac{1}{6}\left(k_1 + 2k_2 + 2k_3 + k_4\right) \tag{B.23}$$

where

$$\begin{aligned}
k_1 &= \frac{d\theta}{d\xi}\left(\theta_i\right)\Delta\xi, && \text{(B.24)}\\
k_2 &= \frac{d\theta}{d\xi}\left(\theta_i + \frac{1}{2}k_1\right)\Delta\xi, && \text{(B.25)}\\
k_3 &= \frac{d\theta}{d\xi}\left(\theta_i + \frac{1}{2}k_2\right)\Delta\xi, && \text{(B.26)}\\
k_4 &= \frac{d\theta}{d\xi}\left(\theta_i + k_3\right)\Delta\xi. && \text{(B.27)}
\end{aligned}$$

and

$$\frac{d\theta}{d\xi}\left(\theta\right) = \frac{1}{2}C_f\left(\theta\right), \tag{B.28}$$

where C_f is an implicit function of θ calculated from the velocity profile U obtained using the Newton iteration described above.

Appendix C

Derivation of Analytical Form Factor Expression

This section presents the derivation of the analytical form factor formula using the power balance method in Eq. 4.11.

C.1 Derivation of Form Factor Using Power Balance

The form factor is defined as:

$$K_f \triangleq \frac{D_p}{D_{FP}}, \tag{C.1}$$

where D_p is the profile drag and

$$D_{FP} \triangleq \frac{1}{2}\rho_\infty V_\infty^2 S_{wet} C_{f_{FP}}. \tag{C.2}$$

S_{wet} is the total wetted surface area of the body, and $C_{f_{FP}}$ is the flat plate skin friction coefficient, defined as

$$C_{f_{FP}} \triangleq \frac{1}{S_{wet}} \iint c_{f_{FP}} \, dS_{wet}, \tag{C.3}$$

with $c_{f_{FP}}$ being the local skin friction coefficient at the Reynolds number of the actual body. As mentioned in Section 3.3, the profile drag of an isolated airfoil can be related to the mechanical energy loss as:

$$\boldsymbol{D_p} \cdot \boldsymbol{V_\infty} = \Phi_p^*, \tag{C.4}$$

and the component form factor can also be expressed as:

$$K_f \triangleq \frac{\Phi_p^*}{D_{FP} V_\infty}. \tag{C.5}$$

For each distinct surface i of an aerodynamic body, the profile mechanical loss over the surface i ($\Phi_{p_i}^*$) can be calculated as derived in Section 3.2.3:

$$\Phi_{p_i}^* = \iint_{tot_i} \left[\rho_e U_e^3 c_\mathcal{D} - \mathbf{D} \cdot \bar{\nabla} \frac{1}{2} U_e^2 \right] d\mathcal{S}_{tot_i}. \tag{C.6}$$

In Eq. C.6, S_{tot} is the surface area of the flat plate surface and wake combined. Applying the approximation for the "baroclinic power" to Eq. C.6 yields

$$\Phi_{p_i}^* \approx \frac{\iint \rho_e U_e^3 \left(1 + \frac{\gamma - 1}{2} M_e^2\right)^r c_\mathcal{D} \, d\mathcal{S}_{tot_i}}{\left(1 + \frac{\gamma-1}{2} M_\infty^2\right)^r}. \tag{C.7}$$

This approximation holds for adiabatic flow with small flow acceleration, $\frac{d|\boldsymbol{u_e}|}{ds} \frac{c}{V_\infty} \ll 1$ and near-unity Prandtl number, $\mathrm{Pr} \simeq 1$. Substituting Eq. C.7 to Eq. C.5,

$$\begin{aligned} K_{f_i} &\approx \frac{\iint \rho_e U_e^3 \left(1 + \frac{\gamma - 1}{2} M_e^2\right)^r c_\mathcal{D} \, d\mathcal{S}_{tot_i}}{\frac{1}{2} \rho_\infty V_\infty^3 \left(1 + \frac{\gamma-1}{2} M_\infty^2\right)^r S_{wet_i} C_{f_{FP_i}}}, & \text{(C.8)} \\ &= \frac{\iint \rho_e U_e^3 \left(1 + \frac{\gamma - 1}{2} M_e^2\right)^r c_\mathcal{D} \, d\mathcal{S}_{wet_i} + \iint \rho_e U_e^3 \left(1 + \frac{\gamma - 1}{2} M_e^2\right)^r c_\mathcal{D} \, d\mathcal{S}_{wake_i}}{\frac{1}{2} \rho_\infty V_\infty^3 \left(1 + \frac{\gamma-1}{2} M_\infty^2\right)^r S_{wet_i} C_{f_{FP_i}}}. & \text{(C.9)} \end{aligned}$$

Define k_ϕ such that

$$\iint \rho_e U_e^3 \left(1 + \frac{\gamma - 1}{2} M_e^2\right)^r c_\mathcal{D} \, d\mathcal{S}_{wake_i} = k_\phi \iint \rho_e U_e^3 \left(1 + \frac{\gamma - 1}{2} M_e^2\right)^r c_\mathcal{D} \, d\mathcal{S}_{wet_i} \tag{C.10}$$

Using k_ϕ, Eq. C.9 can be re-written as

$$K_{f_i} \approx \frac{(1 + k_\phi) \iint \rho_e U_e^3 \left(1 + \frac{\gamma - 1}{2} M_e^2\right)^r c_\mathcal{D} \, d\mathcal{S}_{wet_i}}{\frac{1}{2} \rho_\infty V_\infty^3 \left(1 + \frac{\gamma-1}{2} M_\infty^2\right)^r S_{wet_i} C_{f_{FP_i}}}. \tag{C.11}$$

We now assume that the boundary layer characteristics, in particular the shape parameter H (or kinematic shape parameter H_k for compressible flow), are within the range such that

$$c_{\mathcal{D}} \approx c_{\mathcal{D}_{FP}}, \tag{C.12}$$

and

$$k_{\phi} \approx k_{\phi_{FP}}. \tag{C.13}$$

Substituting Eq. C.12, C.12 to Eq. C.11, we obtain

$$K_{f_i} \approx \frac{(1 + k_{\phi_{FP}}) \iint \rho_e U_e^3 \left(1 + \frac{\gamma-1}{2} M_e^2\right)^r c_{\mathcal{D}_{FP}} \, d\mathcal{S}_{wet_i}}{\frac{1}{2} \rho_\infty V_\infty^3 \left(1 + \frac{\gamma-1}{2} M_\infty^2\right)^r S_{wet_i} C_{f_{FP_i}}}. \tag{C.14}$$

Since $c_{\mathcal{D}_{FP}}$ is a weak function of the streamwise arc length s,

$$\begin{aligned} \iint \rho_e U_e^3 \left(1 + \frac{\gamma - 1}{2} M_e^2\right)^r c_{\mathcal{D}_{FP}} \, d\mathcal{S}_{wet_i} \quad &\approx \quad \iint \rho_e U_e^3 \left(1 + \frac{\gamma - 1}{2} M_e^2\right)^r d\mathcal{S}_{wet_i} \\ &\times \quad \frac{1}{S_{wet_i}} \iint c_{\mathcal{D}_{FP}} \, d\mathcal{S}_{wet_i}, \end{aligned} \tag{C.15}$$

then Eq. C.11 can be expressed as

$$K_{f_i} \approx \frac{\iint \rho_e U_e^3 \left(1 + \frac{\gamma-1}{2} M_e^2\right)^r c_{\mathcal{D}} \, d\mathcal{S}_{wet_i} \times (1 + k_{\phi_{FP}}) \frac{1}{S_{wet_i}} \iint c_{\mathcal{D}_{FP}} \, d\mathcal{S}_{wet_i}}{\frac{1}{2} \rho_\infty V_\infty^3 \left(1 + \frac{\gamma-1}{2} M_\infty^2\right)^r S_{wet_i} C_{f_{FP_i}}}. \tag{C.16}$$

Finally, using the identity

$$C_{f_{FP_i}} = (1 + k_{\phi_{FP}}) \frac{2}{S_{wet_i}} \iint c_{\mathcal{D}_{FP}} \, d\mathcal{S}_{wet_i}, \tag{C.17}$$

with Eq. C.16, we obtain

$$K_{f_i} \approx \frac{\iint_{wet_i} \rho_e U_e^3 \left(1 + \frac{\gamma-1}{2} M_e^2\right)^r d\mathcal{S}_{wet_i}}{\rho_\infty V_\infty^3 \left(1 + \frac{\gamma-1}{2} M_\infty^2\right)^r S_{wet_i}}, \tag{C.18}$$

which ultimately gives:

$$
\begin{aligned}
K_f &\approx \frac{1}{\sum_{i=1}^{n} S_{wet_i}} \sum_{i=1}^{n} K_{fi} S_{wet_i} \\
&= \frac{1}{\sum_{i=1}^{n} S_{wet_i}} \sum_{i=1}^{n} \frac{\iint_{wet_i} \rho_e U_e^3 \left(1+\frac{\gamma-1}{2} M_e^2\right)^r \, d\mathcal{S}_{wet_i}}{\rho_\infty V_\infty^3 \left(1+\frac{\gamma-1}{2} M_\infty^2\right)^r}.
\end{aligned}
\tag{C.19}
$$

Appendix D

Validation of MSES CFD Program

This section shows the validation of the MSES CFD program used throught the analysis of this work. MSES is a compressible, two-dimensional airfoil analysis tool which employes a viscous, inviscid interaction method.

D.1 GAW-1 Airfoil

MSES results were compared against experimental data of 2D low speed airfoil GAW-1 [27]. Table D.1 shows the test condition.

Table D.1: GAW-1 Airfoil Test Condition [27]

Parameter		Value
Freestream Mach number	M_∞	0.15
Chord Reynolds Number	Re_c	6.3×10^6
Suction side trip	x_{tr_s}	$0.08c$
Pressure side trip	x_{tr_p}	$0.1c$
Angle of attack	α	$-4^\circ \sim 21^\circ$

Figure D-1 shows the comparison of drag polars (left) and lift coefficient vs. airfoil angle of attack (right) between experimental data from [27] and results from MSES simulated at the same operating conditions. While MSES predicts lift coefficient accurately up to near-stall condition, the profile drag is underpredicted compared to experimental data.

The discrepancy between the experimental data and MSES could be due to multiple reasons. Firstly, the experimental data was gathered on low aspect ratio airfoil ($AR = 1.5$) with circular endplates at the wingtip, and did not have any sidewall boundary layer control.

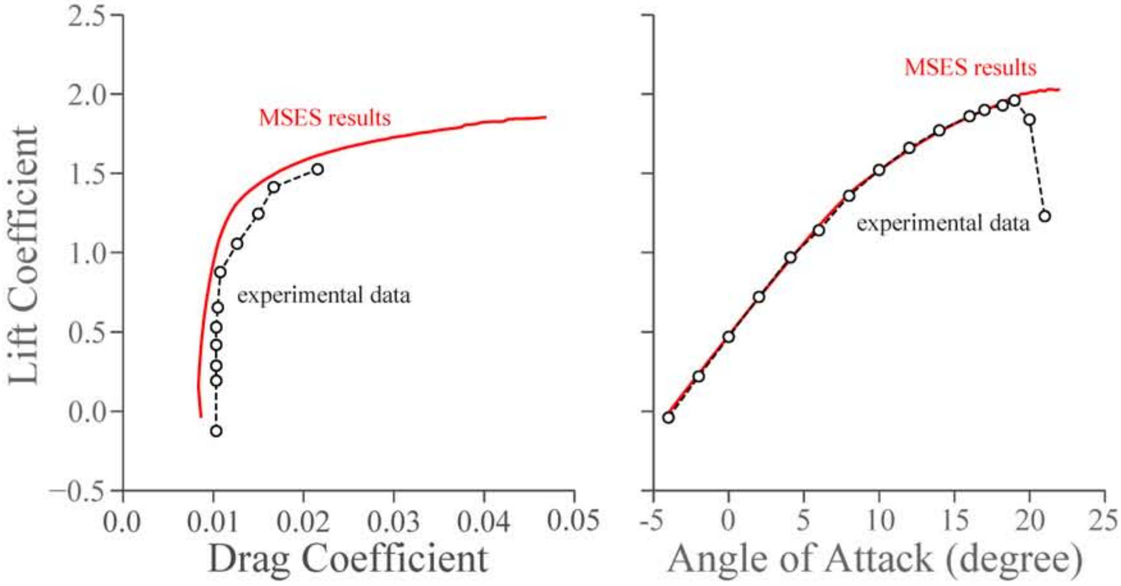

Figure D-1: Comparison of MSES and experimental [27] drag polar (left) and C_ℓ vs. α (right) of GAW-1 Airfoil at $M_\infty = 0.15$, $Re = 6.3 \times 10^6$.

The flow contraction due to blockage generated on the endplates could have affected the data. Furthermore, MSES does not model unsteady wake shedding from the blunt trailing edge which increases the wake dissipation of the airfoil.

Although discrepancy were seen between the MSES result and the experimental data, the general trend of the drag polar and the lift coefficient are properly captured.

D.2 RAE2822 Airfoil

Drela and Giles [11] present detailed validation of MSES on the RAE2822 airfoil by comparing the CFD results to experimental data by Cook et al. [3]. In the work, Drela presents the results on “case 10” of the series of transonic tunnel experiments, which corresponds to a freestream Mach number of 0.75, and a lift coefficient of 0.743. This case involves limited shock induced separation immediately behind the strong suction surface shock wave, which was visualized in the experiment using the oil flow technique. The work showed good agreement in pressure distribution and drag coefficient between experimental data and MSES calculation, as illustrated in Figure D-2.

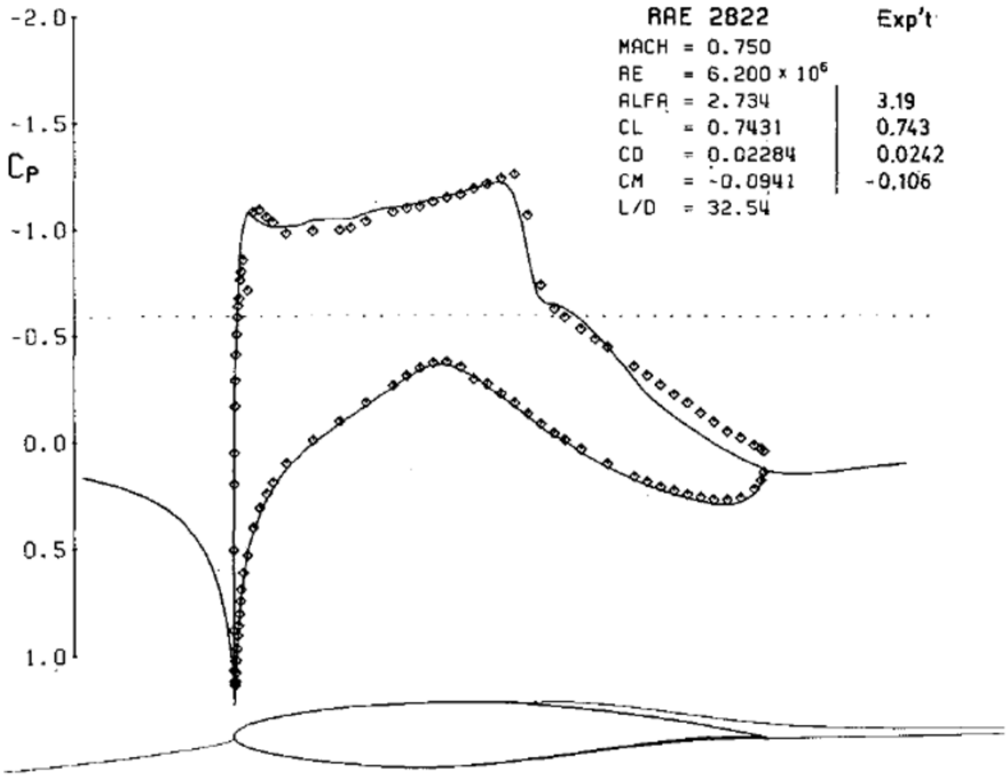

Figure D-2: Comparison of MSES and experimental pressure distribution of RAE2822 Airfoil at $M_\infty = 0.75$ [11]

D.3 Summary

Although some discrepancy is seen between experimental and MSES results, MSES captures well the physical trend of the airfoil performance. Further, the analysis presented in this thesis focused explicitly on the scaling and trends of airfoil profile mechanical losses, which does not require MSES to exactly predict the airfoil profile drag.

Appendix E

Calculation of η_{BLI} for a Simple 2D BLI Problem

This section describes detailed derivation of the BLI efficiency η_{BLI} as a function of BLI (β) and propulsor pressure rise (ΔC_{pt}), for the simple 2D example (Figure E-1) presented in Chapter 6. This example assumes incompressible flow, no pressure interaction between airframe and propulsor, uniform wake and jet velocity profile, constant stagnation pressure rise $\left(\Delta C_{pt} \triangleq \frac{p_{t,\,out}-p_{t,\,in}}{1/2\rho_\infty V_\infty^2}\right)$ across the propulsor regardless of the incoming flow velocity, and no net thrust for the entire configuration.

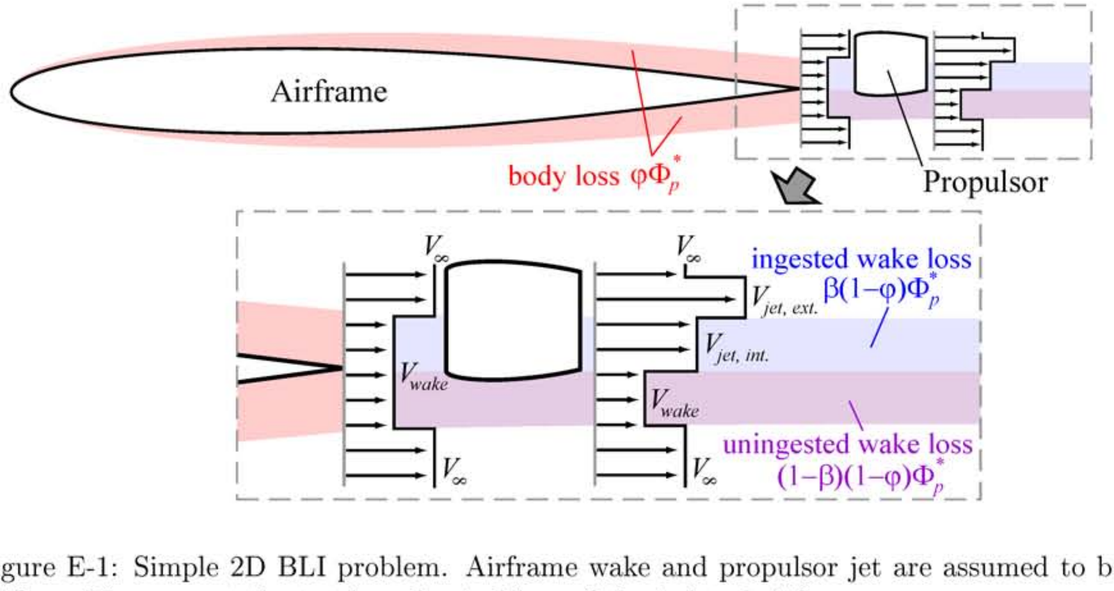

Figure E-1: Simple 2D BLI problem. Airframe wake and propulsor jet are assumed to be uniform.Φ_p^* represent the total mechanical loss of the isolated airframe.

Fixed parameters:

- Ratio between the surface boundary layer loss Φ^*_{surf} and the profile boundary layer loss Φ^*_p (Non-BLI configuration):

$$\varphi_{TE} \triangleq \frac{\Phi^*_{surf}}{\Phi^*_p} = \frac{\Phi^*_{surf}}{\Phi^*_{surf} + \Phi^*_{wake}}. \tag{E.1}$$

Variable parameters:

- Amount of BLI, β
- Propulsor stagnation pressure rise,

$$\Delta C_{pt} \triangleq \frac{p_{t,\,out} - p_{t,\,in}}{{}^1\!/_2 \rho_\infty V_\infty^2}. \tag{E.2}$$

E.1 Preliminary Considerations

This section lists a few relations used extensively in the derivation.

- The non-BLI airfoil profile mechanical loss,

$$\Phi^*_p = DV_\infty = \dot{m}_{wake} \left(V_\infty - V_{wake}\right) V_\infty, \tag{E.3}$$

  where $\dot{m}_{wake}$ is the mass flow of the airfoil wake.

$$\dot{m}_{wake} = \rho_\infty V_{wake} A_{wake}. \tag{E.4}$$

- The non-BLI airfoil wake mechanical loss,

$$\Phi^*_{wake} = \frac{1}{2}\dot{m}_{wake} \left(V_\infty - V_{wake}\right)^2. \tag{E.5}$$

- The wake velocity can be expressed as

$$V_{wake} = \left(2\varphi_{TE} - 1\right) V_\infty, \tag{E.6}$$

  by combining Eq. E.3 and E.5 with the definition of E.1.

- The propulsor jet velocities can be expressed as

$$V_{j_i} = \sqrt{1+\Delta C_{pt}}V_w, \tag{E.7}$$

for the jet velocity of the propulsor acting inside the airframe wake, and

$$V_{j_e} = \sqrt{1+\Delta C_{pt}}V_\infty, \tag{E.8}$$

for the jet velocity of the propulsor acting outside the wake. Both expressions in Eq. E.7 and E.8 are derived using Eq. E.2.

E.2 Derivation

The objective of this section is to derive an expression for the BLI efficiency (η_{BLI}). Since η_{BLI} can be expressed as

$$\eta_{BLI} = C_{BLI}\eta'_{prop}, \tag{E.9}$$

we need to derive the expression for C_{BLI} and η'_{prop}.

E.2.1 Derivation of C_{BLI}

C_{BLI} is the ratio of required propulsive power between a non-BLI and a BLI aircraft, defined as

$$C_{BLI} \triangleq \frac{\Phi_p^*}{\Phi_p^{*\prime}}. \tag{E.10}$$

If $\sqrt{1+\Delta C_{pt}} \geqslant {}^{V_\infty}/_{V_{wake}}$, the propulsor pressure rise is high enough to accelerate the wake velocity beyond freestream velocity. In such case, the airframe wake dissipation of the ingested streamtube is eliminated, and the expression for C_{BLI} is

$$C_{BLI} = \frac{1}{1-\beta\left(1-\varphi_{TE}\right)}. \tag{E.11}$$

If $\sqrt{1+\Delta C_{pt}} < {}^{V_\infty}/_{V_{wake}}$, on the other hand, the propulsor pressure rise cannot accelerate the wake to freestream velocity, and the airframe wake dissipation cannot be fully eliminated:

$$C_{BLI} = \frac{1}{1 - \beta\left(1 - \varphi_{TE}\right) R_w}, \tag{E.12}$$

where R_w is the wake recovery parameter,

$$\begin{aligned} R_w &= \left[\frac{\sqrt{1 + \Delta C_{pt}} - 1}{{}^{V_\infty}\!/\!{}_{V_{wake}} - 1}\right]^2, & \text{(E.13)} \\ &= \left[\left(\sqrt{1 + \Delta C_{pt}} - 1\right)\left(1 - \frac{1}{2\left(1 - \varphi_{TE}\right)}\right)\right]^2. & \text{(E.14)} \end{aligned}$$

For $\sqrt{1 + \Delta C_{pt}} < {}^{V_\infty}\!/\!{}_{V_{wake}}$, $R < 1$.

E.2.2 Derivation of η'_{prop}

η'_{prop} is the propulsive efficiency of the BLI propulsor, and is defined as

$$\eta'_{prop} \triangleq 1 - \frac{\Phi^{*\prime}_{jet}}{P'_K}. \tag{E.15}$$

Since no net thrust is generated for the entire configuration (propulsor and airframe combined), the following relation must hold:

$$P'_K - \Phi^{*\prime}_{jet} = \Phi^{*\prime}_p = \frac{1}{C_{BLI}} \Phi^*_p. \tag{E.16}$$

The propulsor net mechanical power is

$$P'_K = \frac{1}{2} \beta \dot{m}_{wake} V^2_{wake} \Delta C_{pt} + \frac{1}{2} \dot{m}_{ext} V^2_\infty \Delta C_{pt}, \tag{E.17}$$

where $\dot{m}_{ext}$ is the mass flow through the propulsor outside the wake.

For $\sqrt{1 + \Delta C_{pt}} \geqslant {}^{V_\infty}\!/\!{}_{V_{wake}}$, the propulsor jet loss is

$$\Phi^*_{jet} = \frac{1}{2} \beta \dot{m}_{wake} \left(\sqrt{1 + \Delta C_{pt}} V_{wake} - V_\infty\right)^2 + \frac{1}{2} \dot{m}_{ext} V^2_\infty \left(\sqrt{1 + \Delta C_{pt}} - 1\right)^2, \tag{E.18}$$

and the airframe profile mechanical loss is

$$\Phi^{*\prime}_p = \left[1 - \beta\left(1 - \varphi_{TE}\right)\right] \Phi^*_p. \tag{E.19}$$

For $\sqrt{1+\Delta C_{pt}} < {}^{V_\infty}/{}_{V_{wake}}$, the propulsor jet loss is

$$\Phi^*_{jet} = \frac{1}{2}\dot{m}_{ext} V_\infty^2 \left(\sqrt{1+\Delta C_{pt}} - 1\right)^2, \tag{E.20}$$

and the airframe profile mechanical loss is

$$\Phi^{*\prime}_p = \left[1 - \beta\left(1 - \varphi_{TE}\right) R_w\right] \Phi^*_p. \tag{E.21}$$

Solving Eq. E.16, the ratio of propulsor mass flow outside the wake to the wake mass flow (R_m) can be obtained:

$$R_m \triangleq \frac{\dot{m}_{ext}}{\dot{m}_{wake}} = \frac{1 - \left[1 + \beta\left(\sqrt{1+\Delta C_{pt}} + 1\right)\right]\left(2\varphi_{TE} - 1\right)}{\left(\sqrt{1+\Delta C_{pt}} - 1\right)}. \tag{E.22}$$

This expression holds for both $\sqrt{1+\Delta C_{pt}} \geqslant {}^{V_\infty}/{}_{V_{wake}}$ and $\sqrt{1+\Delta C_{pt}} < {}^{V_\infty}/{}_{V_{wake}}$.

Combing Eq. E.15, Eq. E.16 and Eq. E.22 we obtain an expression for the propulsive efficiency for this example. For $\sqrt{1+\Delta C_{pt}} \geqslant {}^{V_\infty}/{}_{V_{wake}}$,

$$\eta'_{prop} = 1 - \frac{\beta\left(\sqrt{1+\Delta C_{pt}}\left(2\varphi_{TE} - 1\right) - 1\right)^2 + R_m\left(\sqrt{1+\Delta C_{pt}} - 1\right)^2}{\left[\beta\left(2\varphi_{TE} - 1\right)^2 + R_m\right]\Delta C_{pt}}. \tag{E.23}$$

For $\sqrt{1+\Delta C_{pt}} < {}^{V_\infty}/{}_{V_{wake}}$,

$$\eta'_{prop} = 1 - \frac{R_m\left(\sqrt{1+\Delta C_{pt}} - 1\right)^2}{\left[\beta\left(2\varphi_{TE} - 1\right)^2 + R_m\right]\Delta C_{pt}}. \tag{E.24}$$

E.2.3 Summary

The expression for C_{BLI} and η'_{prop} was derived for the simple 2D example presented in Chapter 6.

C_{BLI} is expressed as:

$$C_{BLI} = \frac{1}{1 - \beta\left(1 - \varphi_{TE}\right) R_w} \tag{E.25}$$

where R_w is the wake recovery parameter,

$$R_w = \begin{cases} 1 & \text{, if } \sqrt{1+\Delta C_{pt}} \geqslant {}^{V_\infty}/_{V_{wake}} \\ \left[\left(\sqrt{1+\Delta C_{pt}}-1\right)\left(1-\frac{1}{2(1-\varphi_{TE})}\right)\right]^2 & \text{, if } \sqrt{1+\Delta C_{pt}} < {}^{V_\infty}/_{V_{wake}} \end{cases}. \tag{E.26}$$

η'_{prop} is expressed as:

$$\eta'_{prop} = 1 - \frac{\beta\left(\sqrt{1+\Delta C_{pt}}\,(2\varphi_{TE}-1)-1\right)^2 + R_m\left(\sqrt{1+\Delta C_{pt}}-1\right)^2}{\left[\beta\,(2\varphi_{TE}-1)^2 + R_m\right]\Delta C_{pt}}, \tag{E.27}$$

for $\sqrt{1+\Delta C_{pt}} \geqslant {}^{V_\infty}/_{V_{wake}}$, and

$$\eta'_{prop} = 1 - \frac{R_m\left(\sqrt{1+\Delta C_{pt}}-1\right)^2}{\left[\beta\,(2\varphi_{TE}-1)^2 + R_m\right]\Delta C_{pt}}, \tag{E.28}$$

for $\sqrt{1+\Delta C_{pt}} < {}^{V_\infty}/_{V_{wake}}$. R_m is the ratio of propulsor mass flow outside the wake to the wake mass flow,

$$R_m = \frac{1-\left[1+\beta\left(\sqrt{1+\Delta C_{pt}}+1\right)\right](2\varphi_{TE}-1)}{\left(\sqrt{1+\Delta C_{pt}}-1\right)}. \tag{E.29}$$

The total BLI efficiency is calculated as

$$\eta_{BLI} = C_{BLI}\eta'_{prop}, \tag{E.30}$$

which, combining Eq. E.25, Eq. E.27 and Eq. E.28, reduces to:

$$\eta_{BLI} = \frac{4\,(1-\varphi_{TE})}{\left[\beta\,(2\varphi_{TE}-1)^2 + R_m\right]\Delta C_{pt}}. \tag{E.31}$$

Bibliography

[1] Clauser, F. H. Turbulent boundary layers in adverse pressure gradients. *J. Aeron. l Sci.*, pages 91–108, 1954.

[2] Coles, D. The law of the wake in the turbulent boundary layer. *Journal of Fluid Mechanics*, 1(2):191–226, 1956.

[3] Cook, P. H., McDonald, M.A. and Firmin, M.C.P. Test Cases for Inviscid Flow Field Methods. Technical Report AR-211, AGARD Working Group 7, 1985.

[4] Daggett, D. L., Kawai, R. and Friedman, D. Blended Wing Body Systems Studies: Boundary Layer Ingestion Inlets With Active Flow Control. Technical Report CR-2003-212670, NASA, 2003.

[5] De la Rosa Blanco, E., Hall, C. and Crichton, D. Challenges in the silent aircraft engine design. *45th AIAA Aerospace Sciences Meeting and Exhibit*, (AIAA-2007-0454), January 2007.

[6] Denton, J. D. Loss Mechanicsms in Turbomachines - The 1993 IGTI Scholar Lecture. *Journal of Turbomachinery*, 115:621–656, Oct. 1993.

[7] Douglass, W. M. Propulsive efficiency with boundary layer ingestion. Technical Report MDC J0860, McDonnell Douglas, August 1970.

[8] Drela, M. MSES 3.05. MSES multielement airfoil design/analysis program, Massachusetts Institute of Technology, 2007.

[9] Drela, M. Power balance in aerodynamic flows. *AIAA Journal*, 47(7):1761–1771, July 2009.

[10] Drela, M. MTFLOW 2.03. Multi-passage ThroughFLOW Design/Analysis Program, Massachusetts Institute of Technology, 2010.

[11] Drela, M. and Giles, M. B. Viscous-Inviscid Analysis of Transonic and Low Reynolds Number Airfoil. *AIAA Journal*, 25(10):1347–1355, 1986.

[12] Emmons, H. W. *Fundamentals of Gas Dynamics.* Princeton University Press, 1958.

[13] Feagin, R. C. and Morrison, D. Delta Method, An Empirical Drag Buildup Technique. Technical Report NASA-CR-151971, NASA, 1978.

[14] Greitzer, E. M. et al. Aircraft and technology concepts for an N+3 subsonic transport. NASA Grant/Cooperative Agreement NNX08AW63A, NASA, 2010.

[15] Greitzer, E. M., Tan, C. S. and Graf, M. B. *Internal Flow Concepts and Applications.* Cambridge University Press, The Edinburgh Building, Cambridge CB2 2Ru, UK, First Edition edition, 2004.

[16] Gur, O., Mason, W. H. and Schwartz, J. A. Full-Configuration Drag Estimation. *Journal of Aircraft*, 47(4):1356–1367, 2010.

[17] Hall, D. K. Performance Limint of Axial Turbomachine Stages. Master's thesis, Massachusetts Institute of Technology, Department of Aeronautics and Astronautics, December 2010.

[18] Hileman, J. I., Katz, J. B., Mantilla, J. and Fleming, G. Payload Fuel Energy Efficiency as a Metric for Aviation Environmental Performance. *Proceedings of the 26th International Congress of the Aeronautical Sciences*, 2008.

[19] Hileman, J. I., Spakovszky, Z. S., Drela, M., Sargeant, M. A. and Jones, A. Airframe design for silent fuel-efficient aircraft. *Journal of Aircraft*, 47(3):956–969, 2010.

[20] Hoerner, S. F. *Fluid-Dynamic Drag.* Hoerner Fluid Dynamics, Vancouver, WA, 1965.

[21] International Civil Aviation Organization (ICAO), editor. *Annex 14: Aerodromes Volume I: Aerodrome Design and Operation.* New York, fourth edition, 2004.

[22] Jobe, C. E. *Thrust and Drag: Its Prediction and Verification.* Progress in Aeronautics and Astronautics. AIAA, New York, 1985.

[23] Kawai, R. T., Friedman, D. M. and Serrano, L. Blended Wing Body (BWB) Boundary Layer Ingestion (BLI) Inlet Configuration and System Studies. Technical Report CR-2006-214534, NASA, 2006.

[24] Kroo, I. *Aircraft Design: Synthesis and Analysis.* Desktop Aeronautics, Inc., Stanford, CA, 1.2 edition, September 2006.

[25] Kroo, I. and Takai, M. A Quasi-Procedural, Knowledge Based System for Aircraft Synthesis. *AIAA Aircraft Design Meeting*, (AIAA-88-6502), 1988.

[26] Lundbladh, A. and Sjunnesson, A. Heat Exchanger Weight and Efficiency Impact on Jet Engine Transport Applications. *International Symposium of Air Breathing Engines*, (ISABE-2003-1122), 2003.

[27] McGhee, R. J. et al. Low-Speed Aerodynamic Characteristics of a 17-Percent-Thick Airfoil Section Designed for General Aviation Applications. Technical Report NASA-TN-D-7428, NASA, Dec 1973.

[28] Mody, P. C. Impact of Liquefied Natural Gas Usage and Payload Size on Hybrid Wing Body Aircraft Fuel Efficiency. Master's thesis, Massachusetts Institute of Technology, Department of Aeronautics and Astronautics, June 2010.

[29] Mody, P. C., Sato, S., Hall, D. K., De la Rosa Blanco, E., Hileman, J. I. and Wen, E. Conceptual Design of an N+3 Hybrid Wing Body Subsonic Transport. *28th AIAA Applied Aerodynamics Conference*, (4812), July 2010.

[30] Morrison, W. D. Advanced Airfoil Design Empirically Based Transonic Aircraft - Drag Buildup Technique. Technical Report NASA CR-137928, NASA, Jan 1976.

[31] Ng, L. Design and acoustic shielding prediction of hybrid wing-body aircraft. Master's thesis, Massachusetts Institute of Technology, Department of Aeronautics and Astronautics, June 2009.

[32] Nicolai, M. L. *Fundamentals of Aircraft Design.* E. P. Domincone, Fairborn, OH, 1975.

[33] Plas, A. Performance of a Boundary Layer Ingesting Propulsion System. Master's thesis, Massachusetts Institute of Technology, Department of Aeronautics and Astronautics, June 2006.

[34] Raymer, D. *Aircraft Design: A Conceptual Approach.* AIAA Education Series. American Institute of Aeronautics and Astronautics Inc., New York, NY, 2006. ISBN 1-56347-829-3.

[35] Sargeant, M. A. *Boundary Layer Ingestion for Advanced Airframes.* Ph.D. disseration, University of Cambridge, Trinity College, December 2007.

[36] Schlighting, H. and Gersten, K. *Boundary Layer Theory.* Springer, Germany, 8 edition, 2000.

[37] Shevell, R. S. *Fundamentals of Flight.* Prentice-Hall, Upper Saddle River, NJ, 1989.

[38] Smith, A. M. O. and Roberts, H. E. The jet airplane utilizing boundary layer air propulsion. *Journal of the Aeronautical Sciences*, 14(2):97–109, 1947.

[39] Smith, L. H. Wake ingestion propulsion benefit. *Journal of Propulsion and Power*, 9(1):74–82, 1993.

[40] Österlund, J. M. Experimental Studies of Zero Pressure-Gradient Turbulent Boundary-Layer Flow. Technical Report, Royal Institute of Technology, SE-100 44 Stockholm Sweden, December 1999.

[41] Tong, M. and Naylor, B. An Object-Oriented Computer Code for Aircraft Engine Weight Estimation. Technical Report 215656, NASA, 2009.

[42] Tong, M., Jones, S. and Handschuh, W. H. Engine Conceptual Design Studies for a Hybrid Wing Body Aircraft. *ASME Turbo Expo*, (GT2009-59568), 2009.

[43] Torenbeek, E. *Synthetisis of Subsonic Airplane Design.* Delft Univ. Press, The Netherlands, 1982.

[44] Van Driest, E. R. Turbulent Boundary Layer in Compressible Fluids. *Journal of Aeronautical Science*, 18:145–160, 1951.

[45] Weed, P. Hybrid Wing-Body Aircraft Noise and Performance Assessment. Master's thesis, Massachusetts Institute of Technology, Department of Aeronautics and Astronautics, June 2009.

[46] White, F. M. *Viscous fluid flow.* McGraw-Hill, New York, 3rd edition edition, 2006.

[47] Young, A. D. *Boundary Layers.* BSP Professional Books, 1989.